Development of Al alloy composites by powder metallurgy routes

Xia Jiang

Linacre College

A thesis submitted for the degree of

Doctor of Philosophy

Department of Materials, University of Oxford

Trinity Term 2014

Abstract

Xia Jiang D.Phil. Thesis

Linacre College Trinity term, 2014

Development of Al alloy composites by powder metallurgy routes

Particulate reinforced Al alloy composites (AlMCs) are recognized as important structural materials due to their lightweight, high modulus and strength and high wear resistance. In order to understand the effect of matrix, reinforcement and secondary processing techniques on the microstructure development and mechanical properties of AlMCs produced by powder metallurgy routes, Al alloy composites reinforced with three types of reinforcements by different secondary processing techniques have been produced and examined.

Fabrication of Al or 6061Al alloy based composites reinforced with nano-sized SiC particles (~500nm), micro-sized (<25μm) quasicrystalline alloy particles (hereinafter referred to as "NQX") and micro-sized Nb particles (~130μm) has been carried out by powder metallurgy routes followed by extrusion or cold rolling. After extrusion, a homogeneous distribution of secondary particles has been obtained with rare interfacial reaction products. The 6061Al/SiC composites exhibit superior mechanical properties than either monolithic alloys or composites reinforced with micro-sized particles with retained ductility while the 6061Al/NQX and 6061Al/Nb composites show limited improvement in tensile strength mainly due to their reinforcement size and poor interfacial bonding.

After cold rolling, the evolution in microstructure, texture and strength has been analysed. A typical near β fibre texture with highest intensities near Copper and Brass orientations has been developed for 6061Al/NQX and 6061Al/Nb composites. For 6061Al/SiC composites, a randomized texture with very small grains has achieved due to the presence of the non-deformable SiC particles. Mechanical property tests including microhardness, three-point bending tests and tensile tests have been carried out on cold rolled samples and the results exhibit some level of improvement when compared with as-extruded samples due to work hardening.

Finally, the work moves on to the general discussion based on the previous result chapters. The microstructural development related to reinforcement, matrix and interfacial areas during extrusion and cold rolling has been summarised and the correlation between microstructure and mechanical properties has been discussed.

The thesis provides a thorough understanding of AlMCs produced by powder metallurgy routes in terms of matrix, reinforcement and processing techniques. It can provide reference to the future development of AlMCs for high strength applications.

Preface

The work described in this thesis was carried out by the author in the Department of Materials, University of Oxford under the supervision of Dr. Marina Galano and Prof. Fernando Audebert. No part of this thesis has been previously submitted for a degree at this or any other university. The work of others has been freely drawn upon and is duly acknowledged in the text. Some of the work described in this thesis has been submitted or published in the following journals and conference proceedings:

1. X. Jiang, M. Galano, F. Audebert, "Extrusion textures in Al, 6061 alloy and 6061/SiCp composites", Materials Characterization, 88 (2014) 111-118.
2. A.J. Knowles, X. Jiang, M. Galano and F. Audebert, "Microstructure and mechanical properties of 6061 Al alloy based composites with SiC nanoparticles", Journal of Alloys and Compounds, 2014, http://dx.doi.org/10.1016/j.jallcom.2014.01.134.
3. X. Jiang, M. Galano, F. Audebert, "Microstructure and mechanical behavior of 6061 Al alloy reinforced with SiC nanoparticles processed by extrusion and cold rolling", Proceedings of the 19th International Conference on Composite Materials, Montreal, Canada, edited by S.V. Hoa and P. Hubert (2013), 6435-6443.
4. M. Mostafavi, Y. Vertyagina, C. Reinhard, R. Bradley, X. Jiang, M. Galano and J. Marrow, "3D studies of indentation by combined X-ray tomography and digital volume correlation", Key Engineering Materials, 592-593 (2014) 14-21.

Acknowledgements

This thesis is a heavy and long-time work during which I have constantly received helpful advice and warm support. Special thanks goes to:

Dr. Marina Galano and Prof. Fernando Audebert for their supervision, advice and thesis correction;
The technicians in Materials department, especially Bob Lloyd, Laurie Walton, Steve Lett and Robin Vincent for their help and advice through the whole project;
The EM group in Materials department, especially Gabriella Chapman who has helped me with sample preparations and SEM images the whole time;
Dr. Susie speller for her training and help with texture xrd;
Dr. Igor Dyson for the access to his mechanical lab and patient training with tensile equipment;
Dr. Singh Ubhi from Oxford instrument for his help with EBSD mapping;
Co-workers in my office, especially Stella pedrazzini and Nick Rounthwaite for their help and advice on my project and also for keeping the office quite relaxed and entertained.

I would also like to thank all the friends I met at Oxford. The frequently organized gatherings and poker nights have kept me relaxing and happy during the weekends so that I have all the positive energy to solve scientific problems in weekdays.

Finally, I want to thank for the support and encouragement from my family, especially my boyfriend, Guo Wu, who has always been standing by my side, helping with my project as if it were his own, cheering me up with his funny jokes or body languages or mixed accents from time to time, etc. His accompany has made the D.Phil. time much easier and happier.

Table of contents

Chapter 1 Introduction

1. Introduction - 1 -
1.1 Objective - 1 -
1.2 Outline of the thesis - 1 -
1.3 References - 4 -

Chapter 2 Literature review

2. Literature review - 5 -
2.1 Particulate reinforced Al alloy composites - 6 -
  2.1.1 Fabrication process - 6 -
  2.1.2 Reinforcement selection - 8 -
    2.1.2.1 Ceramic particles and intermetallics - 8 -
    2.1.2.2 Nanoquasicrystals - 9 -
  2.1.3 Mechanical properties of particulate reinforced Al alloy composites - 11 -
    2.1.3.1 Effect of reinforcement size - 12 -
    2.1.3.2 Effect of reinforcement volume fraction - 16 -
    2.1.3.3 Effect of secondary processing - 17 -
  2.1.4 Problems existing so far hindering mechanical behaviour - 19 -
    2.1.4.1 Inhomogeneous distribution of reinforcements - 19 -
    2.1.4.2 Undesirable reactions at interface - 20 -
    2.1.4.3 Weak interfacial bonding - 21 -
2.2 Plastic deformation of Al alloy composites - 22 -
  2.2.1 Deformation microstructure - 22 -
  2.2.2 Deformation texture - 25 -
  2.2.3 Deformation processed metal-metal composites (DPMMCs) - 32 -
2.3 Summary - 34 -
2.4 References - 36 -

Chapter 3 Experimental details

3. Experimental details - 46 -
3.1 Billet production - 47 -
  3.1.1 Production of 6061Al/SiC billets - 47 -
  3.1.2 Production of 6061Al/$Al_{93}Fe_3Cr_2Ti_2$ billets - 47 -
    3.1.2.1 Sieving of $Al_{93}Fe_3Cr_2Ti_2$ powders - 47 -
    3.1.2.2 Mixing - 48 -
    3.1.2.3 Compaction - 48 -
  3.1.3 Production of Al/Nb and 6061Al/Nb billets - 49 -
    3.1.3.1 Mixing and Compaction - 49 -

3.2 Secondary processing - 50 -
    3.2.1 Extrusion into bars - 50 -
    3.2.2 Extrusion into strips - 51 -
    3.2.3 Heat treatment - 51 -
    3.2.4 Cold rolling - 52 -
3.3 Characterization techniques - 55 -
    3.3.1 Optical Emission Spectroscopy (OES) - 55 -
    3.3.2 Density measurement - 55 -
    3.3.3 Grain size estimation - 56 -
    3.3.4 X-ray diffraction (XRD) - 56 -
    3.3.5 Optical Microscope (OM) - 56 -
    3.3.6 Scanning electron microscope (SEM) and Energy dispersive X-ray (EDX) - 57 -
    3.3.7 Transmission electron microscope (TEM) - 57 -
    3.3.8 Texture X-ray diffraction - 58 -
    3.3.9 Electron backscatter diffraction (EBSD) - 60 -
3.4 Mechanical testing - 62 -
    3.4.1 Microhardness - 62 -
    3.4.2 Compression tests - 62 -
    3.4.3 Tensile tests - 63 -
    3.4.4 Load-controlled fatigue tests - 63 -
    3.4.5 Three-point bending tests - 63 -
3.5 References - 65 -

Chapter 4 Extruded bars of 6061Al/SiC composites

4. Extruded bars of 6061Al/SiC composites - 67 -
4.1 Microstructural characterization of 6061Al alloy and 6061Al/SiC composites - 68 -
    4.1.1 Chemical analysis - 68 -
    4.1.2 Density measurements - 68 -
    4.1.3 X-ray diffraction analysis - 69 -
    4.1.4 Scanning electron microscopy analysis - 71 -
    4.1.5 Transmission electron microscopy analysis - 73 -
4.2 Mechanical properties of 6061Al alloy and 6061Al/SiC composites - 80 -
    4.2.1 Microhardness analysis - 80 -
    4.2.2 Room temperature compression tests - 81 -
    4.2.3 Room temperature tensile tests - 82 -
    4.2.4 Fracture surface analysis of tensile samples - 85 -
    4.2.5 Load-controlled fatigue tests - 87 -
    4.2.6 Fracture surface analysis of fatigue samples - 88 -
4.3 Discussion - 96 -
    4.3.1 Effect of extrusion process - 96 -
    4.3.2 Effect of aging heat treatment - 98 -
    4.3.3 Effect of the additions of nano-sized SiC particles - 99 -
    4.3.4 Effect of SiC volume fractions - 102 -

4.4 Summary - 104 -
4.5 References - 106 -

Chapter 5 Cold rolling of 6061Al/SiC composites

5. Cold rolling of 6061Al/SiC composites - 112 -
5.1 Microstructural characterization of as-extruded and cold rolled 6061Al alloy and 6061Al/SiC composites - 113 -
  5.1.1 X-ray diffraction analysis - 113 -
  5.1.2 Scanning electron microscopy analysis - 115 -
  5.1.3 Macroscopic texture development during extrusion, solution heat treatment and cold rolling - 117 -
  5.1.4 Electron backscatter diffraction analysis of as-extruded strips - 125 -
  5.1.5 Electron backscatter diffraction analysis of cold rolled samples - 129 -
5.2 Mechanical properties and work hardening of as-extruded and cold rolled 6061Al alloy and 6061Al/SiC composites - 132 -
  5.2.1 Microhardness analysis - 132 -
  5.2.2 Three-point bending tests of as-extruded, solution heat treated and cold rolled samples - 133 -
5.3 Discussion - 137 -
  5.3.1 Effect of extrusion parameters - 137 -
  5.3.2 Effect of rolling process and rolling strain - 138 -
  5.3.3 Effect of SiC particles - 139 -
5.4 Summary - 144 -
5.5 References - 146 -

Chapter 6 Cold rolling of 6061Al/$Al_{93}Fe_3Cr_2Ti_2$ alloy particle composites

6. Cold rolling of 6061Al/$Al_{93}Fe_3Cr_2Ti_2$ alloy particle composites - 149 -
6.1 Microstructural characterization of as-extruded and cold rolled 6061Al/$Al_{93}Fe_3Cr_2Ti_2$ alloy particle composites - 150 -
  6.1.1 X-ray diffraction analysis - 150 -
  6.1.2 Scanning electron microscopy and optical microscopy analysis - 152 -
  6.1.3 Transmission electron microscopy analysis - 158 -
  6.1.4 Macroscopic texture development during extrusion and cold rolling - 160 -
  6.1.5 Electron backscatter diffraction analysis - 167 -
6.2 Mechanical properties and work hardening of as-extruded and cold rolled 6061Al/$Al_{93}Fe_3Cr_2Ti_2$ alloy particle composites - 173 -
  6.2.1 Microhardness analysis - 173 -
  6.2.2 Three-point bending tests of cold rolled samples - 174 -
  6.2.3 Tensile tests of as-extruded and cold rolled samples - 177 -
6.3 Discussion and future work - 184 -
  6.3.1 Effect of rolling strain - 184 -
  6.3.2 Effect of NQX particles - 185 -
  6.3.3 Future work - 186 -

6.4 References - 187 -

Chapter 7 Cold rolling of Al/Nb and 6061Al/Nb composites

7. Cold rolling of Al/Nb and 6061Al/Nb composites - 191 -
7.1 Microstructural Characterization of as-extruded and cold rolled Al/Nb and 6061Al/Nb composites - 192 -
    7.1.1 X-ray diffraction analysis - 192 -
    7.1.2 Scanning electron microscopy and Optical microscopy analysis - 194 -
    7.1.3 Macroscopic texture development during extrusion and cold rolling - 198 -
    7.1.4 Electron backscatter diffraction analysis of Al matrix - 211 -
    7.1.5 Electron backscatter diffraction analysis of Nb particles - 216 -
7.2 Mechanical properties and work hardening of as-extruded and cold rolled Al/Nb and 6061Al/Nb composites - 219 -
    7.2.1 Microhardness analysis - 219 -
    7.2.2 Three-point bending tests of cold rolled samples - 220 -
    7.2.3 Tensile tests of as-extruded and cold rolled samples - 223 -
7.3 Discussion and future work - 230 -
    7.3.1 Effect of rolling strain - 230 -
    7.3.2 Effect of Nb particles - 231 -
    7.3.3 Future work - 233 -
7.4 References - 234 -

Chapter 8 General discussion

8. General discussion - 237 -
8.1 Summary of the produced composites - 237 -
8.2 Microstructural development during extrusion and cold rolling - 239 -
    8.2.1 Microstructural development related to the reinforcement - 239 -
    8.2.2 Microstructural development related to the matrix - 241 -
    8.2.3 Microstructural development related to interface - 248 -
8.3 Mechanical properties after extrusion and cold rolling - 249 -
    8.3.1 Mechanical properties after extrusion into bars - 249 -
    8.3.2 Mechanical properties after cold rolling - 255 -
        8.3.2.1 Texture strengthening - 255 -
        8.3.2.2 Substructure strengthening - 257 -
        8.3.2.3 Work hardening - 257 -
8.4 References - 260 -

Chapter 9 Conclusions

9. Conclusions - 264 -
9.1 References - 268 -

1. Introduction

1.1 Objective

The materials design has shifted emphasis to achieve light weight, environment friendliness and low cost during the past 40 years [1]. Metal-matrix composites, especially Al alloy composites (AlMCs) have been attracting growing interest due to the low density of Al alloy matrix which is only 35% of steel [2]. The lightweight property, coupled with high Young’s modulus and strength and high wear resistance, has made Al alloy composites an ideal candidate to substitute heavier metals in automotive, aeronautic and aerospace applications due to the continuous demand for lower energy consumption [3].

The strength of the Al alloy composites is varied to a large extent depending on many conditions, such as processing techniques, reinforcement size, reinforcement volume fractions, etc. The main objective of the thesis is trying to understand the effect of the matrix, reinforcements and the fabrication process on the microstructure and mechanical properties of Al alloy based composites produced by powder metallurgy routes and to provide insight to the future development of new Al alloy based composites.

1.2 Outline of the thesis

Bearing the objective in mind, the present work focuses on the fabrication of Al alloy composites using three types of reinforcements of different size ranges by different secondary processing techniques, including extrusion and cold rolling. The effect of Al alloy matrix, reinforcement type, size and volume fraction, processing technique on the overall microstructural development and in turn, the mechanical properties has been studied systematically.

Current understanding of the particulate reinforced Al alloy composites has been given in Chapter 2. The review gives an overview of the key factors affecting the mechanical properties of micro-sized and nano-sized particulate reinforced Al alloys and the effect of severe plastic deformation on the microstructural development and mechanical properties.

Chapter 3 describes the fabrication of composite materials and the characterization techniques used. Nano-sized SiC particles (~500nm; density: 3.21g/cm^3 [4]), micro-sized quasicrystalline alloy particles (<25μm; density: 2.88g/cm^3 [5]) and micro-sized Nb particles (~130μm; density: 8.57g/cm^3 [6]) have been added into the pure Al or 6061Al alloy matrix by powder metallurgy routes followed by extrusion and/or cold rolling for high strength applications.

The as-extruded bars of 6061Al/SiC composites have been analysed in Chapter 4. The microstructural characterization shows that powder metallurgy routes including high energy ball milling, HIPing followed by extrusion are effective procedures to produce homogeneously distributed nano-sized particle reinforced Al alloy composites with superior mechanical properties compared to either monolithic Al alloys or composites reinforced with micro-sized particles due to the improved strengthening mechanisms related with nano-sized reinforcement.

Chapter 5 studies the 6061Al/SiC composites after extrusion into strips and cold rolling. Despite the increasing amount of SiC particle cracking during cold rolling, the cold rolling process improves homogeneity of the microstructure and increases the strength considerably in terms of microhardness and three-point bending strength without introducing matrix anisotropy.

Chapter 6 studies 6061Al alloy reinforced with quasicrystalline $Al_{93}Fe_3Cr_2Ti_2$ alloy particles after extrusion and cold rolling. Although cold rolling improves mechanical properties of the composites by some extent, however, the techniques are not successful since poor interfacial bonding and large cracks have been observed which seriously deteriorate the mechanical properties. Other fabrication techniques, such as high energy ball milling and hot rolling, should be further studied to improve the microstructure and in turn the overall mechanical properties.

Chapter 7 studies as-extruded and cold rolled Al/Nb or 6061Al/Nb composites which are in the catalogue of deformation processed metal-metal composites (DPMMCs). During cold rolling, Nb particles have gradually developed into flattened ribbon-like morphology aligned parallel to the rolling plane. The interparticle spacings and Nb ribbon thickness decrease with increasing rolling strains. The mechanical property tests show improved strength due to work hardening effect, however, the improvement is relatively limited at the current rolling strains since the Nb interparticle spacings are not close enough to act as effective barriers to mobile dislocations. Future work such as larger plastic deformation process needs to be carried out to study the effect of closely aligned Nb ribbons on the mechanical properties despite the work hardening effect.

Chapter 8 is a general discussion of the previous result chapters. The microstructural development related to the reinforcement, matrix and the interfacial areas during extrusion and cold rolling has been summarized and compared for the produced composites and the main strengthening mechanisms have been discussed.

Chapter 9 sums up the findings of the previous chapters. The present work comprises studies of the fabrication of Al alloy composites with different types of reinforcements (non-deformable/deformable; nano-size/micro-size) with two secondary processing techniques (extrusion/cold rolling). Strategies for future development of new Al alloy based composites have been given based on the findings in this thesis.

1.3 References

[1] J. Ejiofor and R. Reddy, "Developments in the processing and properties of particulate Al-Si composites," *Jom*, vol. 49, pp. 31-37, 1997.

[2] Ø. Ryen, "Work hardening and mechanical anisotropy of aluminium sheets and profiles," Norwegian University of Science and Technology, 2003.

[3] D. Poirier, R. A. L. Drew, M. L. Trudeau, and R. Gauvin, "Fabrication and properties of mechanically milled alumina/aluminum nanocomposites," *Materials Science and Engineering A*, vol. 527, pp. 7605-7614, 2010.

[4] (18-12-2013). Available: http://en.wikipedia.org/wiki/Silicon_carbide

[5] S. Pedrazzini, M. Galano, G. D. W. Smith, and F. Audebert, "Characterisation and mechanical properties of nanoquasicrystalline Al-Fe-Cr-Ti based composites," Part II, University of Oxford, 2010.

[6] (07-01-2014). Available: http://en.wikipedia.org/wiki/Niobium

2. Literature Review

During the past thirty years, the development of metal matrix composites (MMCs) has been one of the prime innovations in materials. Early studies on MMCs mainly focused on the development of continuous fibre reinforced materials [1]. However, high manufacturing costs coupled with high costs of the reinforcement fibres and complex fabrication routes have hindered their industrial applications and led to the development of particulate reinforced composites [1].

Particulate reinforced Al alloy composites are attractive materials for automotive and aerospace applications due to their lightweight, high modulus and strength and high wear resistance [2]. In aerospace applications where weight is the prime concern, for example, the substitution of an unreinforced wrought counterpart by a discontinuous SiC reinforced Al alloy composite resulted in a 10% reduction in weight and also a 50% increase in modulus [1]. Recently, Al alloy composites reinforced with nanoparticles have received increasing attention of researchers in view of their much better mechanical properties than either micro-sized particulate reinforced composites or monolithic materials [3]. It has been shown that a variety of factors including the reinforcement, fabrication routes and matrix compositions, could significantly affect the microstructure and mechanical properties of these composites [4]. Hence, it is quite important to understand these key factors to be able to achieve optimum properties.

This chapter reviews the current research into micro-sized and nano-sized particulate reinforced Al alloys composites, particularly the key factors affecting the mechanical properties of the composites and the effect of plastic deformation.

2.1 Particulate reinforced Al alloy composites

Al alloy composites can be divided into three categories according to the forms of the reinforcements: composites reinforced with continuous fibres, short fibres and particles [5]. In this literature review, only particulate reinforced Al alloy composites will be discussed in detail. Both micro-sized and nano-sized particulate reinforced Al alloy composites will be reviewed in this section.

2.1.1 Fabrication process

Over the last thirty years, a variety of processing techniques have been developed to produce particulate reinforced MMCs. The processing methods can be mainly divided into two categories: liquid phase and solid phase processing techniques according to the different temperature of the metallic matrix during processing [1]. The solid phase processing techniques will be reviewed here.

Powder metallurgy (PM) is a common solid state net shape process for producing MMCs and has been successfully applied to large numbers of metal/ceramic combinations [1]. It involves the mixing of matrix powders and ceramic particulates followed by secondary processes such as compaction, HIPing and/or extrusion to reduce porosity and consolidate the powder mixture [5]. One typical powder metallurgy manufacturing route developed by Alcoa (Pennsylvania, PA) is shown in Figure 2.1 [4]. Compared with liquid phase processing techniques, powder metallurgy has several major advantages [4]:

1. It allows essentially any alloy to be used as matrix and any type of particles to be used as reinforcements because interfacial reactions between matrix and reinforcement particles can be minimised by using solid state processing.
2. The matrix powders can be produced by rapid solidification, such as powder atomisation process. The high cooling rates achieved through the liquid to solid transition [6] can refine

the grain structure and lead to obtain stable and/or metastable phases with a nano-scale size [7]. This is quite important for high temperature applications since rapidly solidified alloys have much better mechanical properties at elevated temperature than conventional alloys.

3. High volume fractions of reinforcements can be used which can maximise the Young’s modulus and minimise the coefficient of thermal expansion of the composite.

One of the powder metallurgy (PM) approaches, high energy mechanical alloying (MA), which is a solid state powder processing technique that can produce homogeneous materials from blended elemental powder mixture by repeated welding, fracturing and rewelding of powder particles in a high energy ball mill, is so far the most effective method to fabricate nano-sized particulate reinforced MMCs with minimised clustering issues [8]. When producing nano-sized particulate reinforced MMCs by MA, a uniform distribution of the reinforcement, a significant grain size reduction and increased lattice strains can be achieved which are beneficial to strength properties [2]. However, powder contamination, which can be traced to the milling equipment, milling atmosphere and the process control agents added to the powders, is an inherent drawback of this technique and special precautions need to be taken to minimise it [8].

Figure removed due to copyright reasons

Figure 2.1: Powder metallurgy manufacturing route [4].

2.1.2 Reinforcement selection

2.1.2.1 Ceramic particles and intermetallics

Ceramic particles are the most widely used materials for reinforcing Al alloys [9]. Many ceramic particles, such as Al_2O_3, SiC, B_4C and TiB_2, have been examined [1, 4]. However, several factors have to be taken into consideration when choosing suitable ceramic particles, such as the application, methods of composite manufacture and the cost [4]. With these considerations in mind, the two reinforcements receiving the most attention are SiC and Al_2O_3 [2, 4]. Some of the properties of these two reinforcements compared with pure Al are listed in Table 2.1 [4].

Material	**Young's modulus, GN m^{-2}**	**Density, g cm^{-3}**	**Coefficient of thermal expansion, K^{-1}**	**Specific heat, J kg^{-1} K^{-1}**	**Poisson's ratio**
SiC	420-450	3.21	4.3×10^{-6}	840	0.17
Al_2O_3	380-450	3.96	7.0×10^{-6}	1050	0.25
Al	70	2.70	24.0×10^{-6}	910	0.35

Table 2.1: Properties of SiC, Al_2O_3 and Al [4, 10-12].

SiC is widely used due to its low density, low cost and high availability. Besides, it can greatly increase the Young's modulus, tensile strength and wear resistance of the composites [9]. Al_2O_3, the second most widely used reinforcement, is more stable and has better corrosion and high temperature behaviour compared with SiC [9]. Generally speaking, an increase in stiffness of up to 50% can be achieved with an addition of up to 30vol.% of SiC or Al_2O_3 [2, 13].

Another type of reinforcement that has been used with promising results is intermetallics [9, 14-17]. It has been reported that Al based composites reinforced with Ni (NiAl or Ni_3Al) or Fe based intermetallics generally offer an increase in wear resistance, overall good mechanical properties and good thermal stability at high temperature which makes them ideal candidates for high temperature applications [9, 18].

2.1.2.2 Nanoquasicrystals

In addition to ceramic particles and intermetallics, another type of reinforcement, nanoquasicrystals [19], has drawn the researchers' serious attention because of their promising mechanical properties.

Shechtman et al. [20] first found the icosahedral quasicrystalline phase in Al-Mn alloys produced by rapid cooling in 1984. After that, several types of nanoquasicrystal reinforced Al based alloys have been produced in binary, ternary and quaternary Al alloys, such as Al-Cr [21], Al-Fe-V [22], Al-Fe-Cr [23], Al-Fe-Nb [24] and Al-Fe-Cr-Ti [25] systems, by rapid quenching including melt spinning [26] and powder atomisation [25, 27, 28]. These alloys share similar microstructure with nano-sized quasicrystalline particles embedded in an α-Al matrix [26]. An example is shown in Figure 2.2 [29].

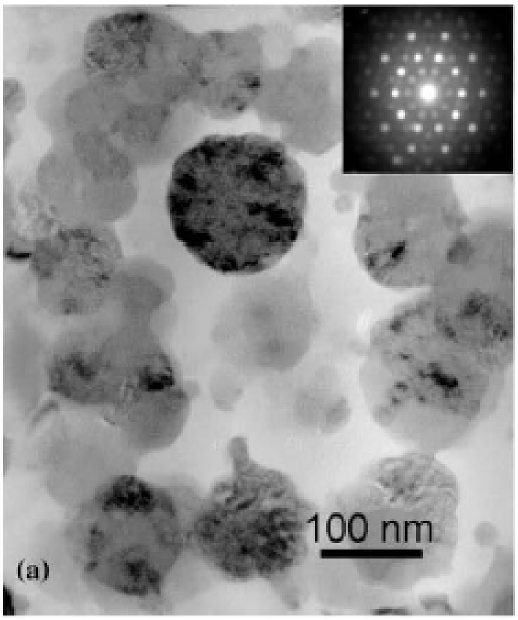

Figure 2.2: TEM image of the microstructure of the Al-Fe-Cr-Ti alloys in the as-spun state showing nanoquasicrystalline particles embedded in Al matrix [29] (with permission from Elsevier).

Among all the nanoquasicrystalline based Al alloys, nanoquasicrystalline alloys from Al-Fe-Cr-Ti system ($Al_{93}Fe_3Cr_2Ti_2$ (at.%)) show excellent mechanical properties coupled with reasonable ductility at both room temperature and elevated temperature with promising industrial applications [30]. Figure 2.3(a) shows the mechanical properties of icosahedral based $Al_{93}Fe_3Cr_2Ti_2$ alloys at different testing temperatures. The σ_{UTS}, $\sigma_{0.2}$ and ε_p for the bulk alloy produced from 26μm gas atomised powders are 650MPa, 530MPa and 4.4% at room temperature and 360MPa, 330MPa and 1.5% at 573K, which is much superior than the conventional Al alloys [25]. The high temperature performance and thermal stability of the alloy was further tested after a holding time of 100h by

Inoue and Kimura [31]. It can be seen from Figure 2.3(b) that the proof stress of the alloys shows much higher values than the conventional Al alloys in the whole temperature range up to 700K. It is believed that nanoquasicrystalline Al-Fe-Cr-Ti alloys are promising new Al alloys for high strength and high temperature applications. If the alloys can be incorporated in a ductile matrix, a compromise between strength and ductility may be achieved.

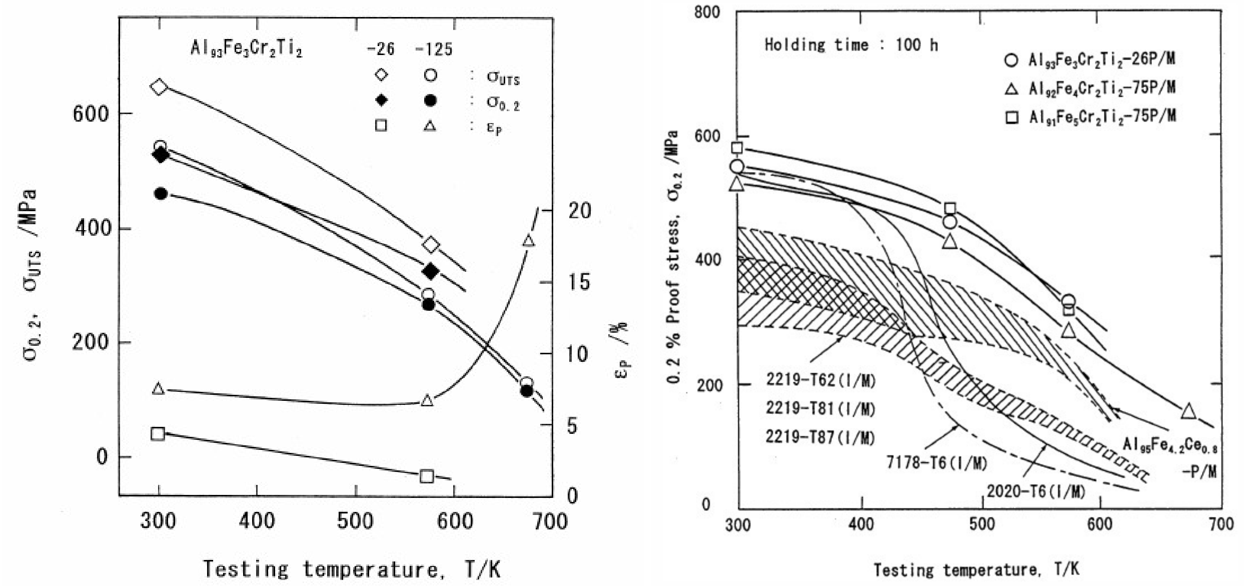

(a) (b)

Figure 2.3: (a) Tensile properties as a function of testing temperature for an icosahedral-based $Al_{93}Fe_3Cr_2Ti_2$ bulk alloy prepared from -26 and -125μm powders [25] (with permission from Elsevier) and (b) 0.2% proof stress as a function of testing temperature for the extruded Al_{91}-$_{93}Fe_{3-5}Cr_2Ti_2$ alloys produced by powder metallurgy after a holding time of 100h [31] (with permission from Elsevier).

2.1.3 Mechanical properties of particulate reinforced Al alloy composites

Mechanical properties of particulate reinforced Al alloy composites depend on many factors, such as matrix alloy composition, reinforcement material, reinforcement size, shape and volume fraction, reinforcement distribution, secondary processing conditions, heat treatment, etc. [32]. Some of the key factors are discussed below.

2.1.3.1 Effect of reinforcement size

It is commonly recognized that the reinforcement size has an obvious effect on the microstructure and mechanical properties of MMCs [33]. For a given reinforcement volume fraction, there is a close relationship between reinforcement size and the homogeneity of the reinforcement particle distribution [32]. A large reinforcement size can improve the homogeneous distribution of reinforcements among matrix. However, because of the higher damage accumulation rates due to particle cracking, increasing reinforcement size can also lead to poor mechanical properties [32].

Figure 2.4 summarizes the tensile or compression yield stress (YS) and UTS of commercial pure Al reinforced with SiC or Al_2O_3 particles in literature [2, 34-44]. A clear trend has been observed that the YS and UTS increase with decreasing reinforcement size. Especially when the particle sizes reduce to nanometres, a significant improvement in YS and UTS is observed.

Figure 2.5 [35] further shows the effect of nano-sized Al_2O_3 (25nm) and micro-sized SiC (10μm) on the tensile strength and elongation of the Al composites fabricated following the same route. It can be observed that the tensile strength (UTS) of the Al/Al_2O_3 composite with only 1vol.% Al_2O_3 nanoparticles is equivalent to that of the 10vol.% Al/SiC composite with a higher yield strength. This strongly suggests that the mechanical properties of nanoparticle reinforced metal matrix composites (NMMCs) would be improved considerably with a very low volume fraction of nanoreinforcements [45], which is reported to be mainly due to a combined effect of thermal mismatch and Orowan strengthening [46]. Thermal mismatch was first proposed by Arsenault and Fisher [47]. Because of the large difference between the coefficients of thermal expansions of the matrix and reinforcements, upon cooling from the processing temperature, misfit strains which are sufficient to generate dislocations occur because of differential thermal contraction at the interface [48], leading to the work hardening of the matrix. The presence of a high dislocation density in the

Al matrix in the vicinity of SiC particles has been experimentally observed from annealed and furnace cooled Al/SiC composites [48].

The above paper [35] didn't report any results on Young's modulus of the Al/Al_2O_3 and Al/SiC composites, which measures the materials' stiffness and is reported to be mainly depend on the load transfer from the soft matrix to the hard reinforcements [5]. Gains in Young's modulus are usually seen with increasing reinforcement volume fraction assuming effective load transfer [4], while the effect of reinforcement size on Young's modulus is not straightforward. A decrease in reinforcement size can decrease the interface stress delaying interface failure, which allows a higher maximum load transfer, increasing Young's modulus [5] while particle cluster associated with smaller reinforcement size can also generate porosity and decrease Young's modulus [49].

Despite of the increased yield strength and UTS of Al/Al_2O_3 nanocomposites, Figure 2.5 shows that the ductility gradually reduces from 27% for pure Al to 9% for Al/Al_2O_3 (7vol.%). The reduced ductility is reported to be a result of grain boundary embrittlement, which is due to grain boundary aggregated nanoparticles and clustered nanoparticles with increasing reinforcement amount, providing crack initiation sites [35].

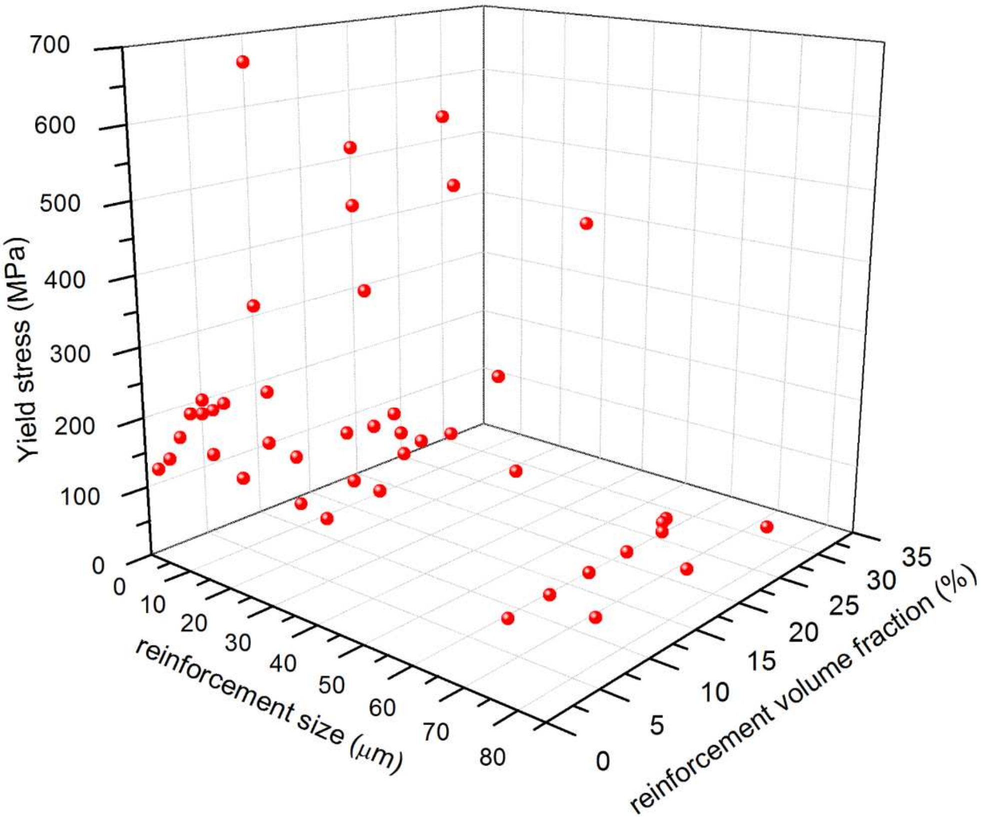

(a)

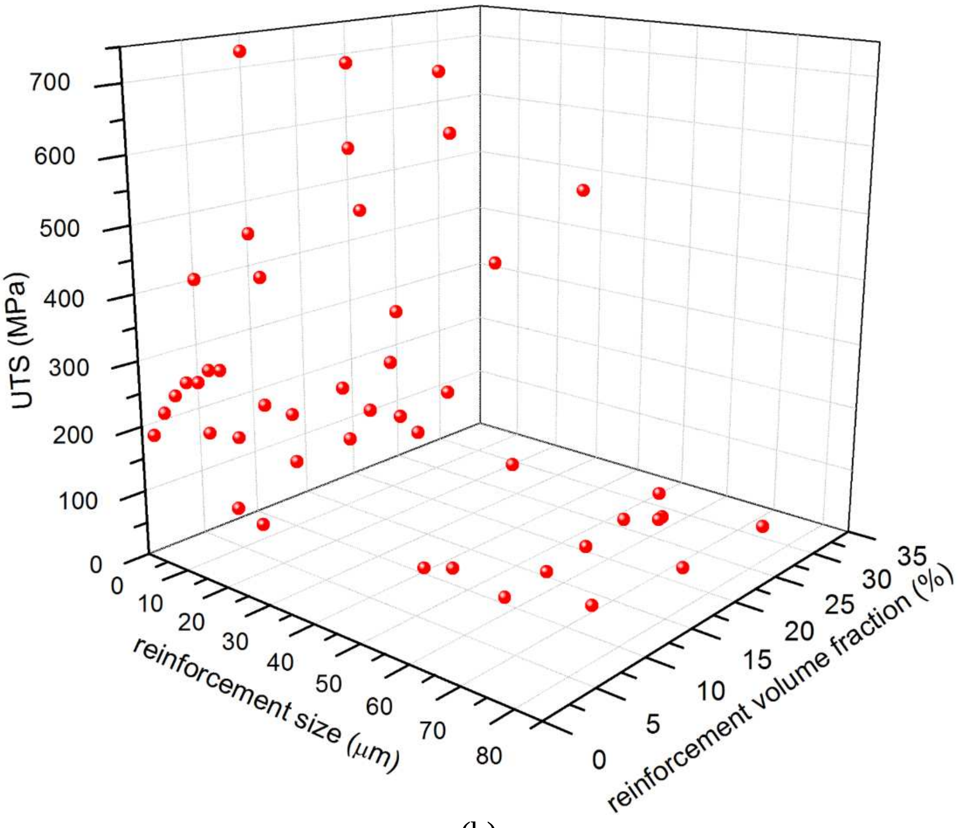

(b)

Figure 2.4: Summary of tensile or compression (a) yield stress and (b) UTS values of commercial pure Al reinforced with SiC or Al_2O_3 particles against reinforcement size and volume fractions from literature [2, 34-44].

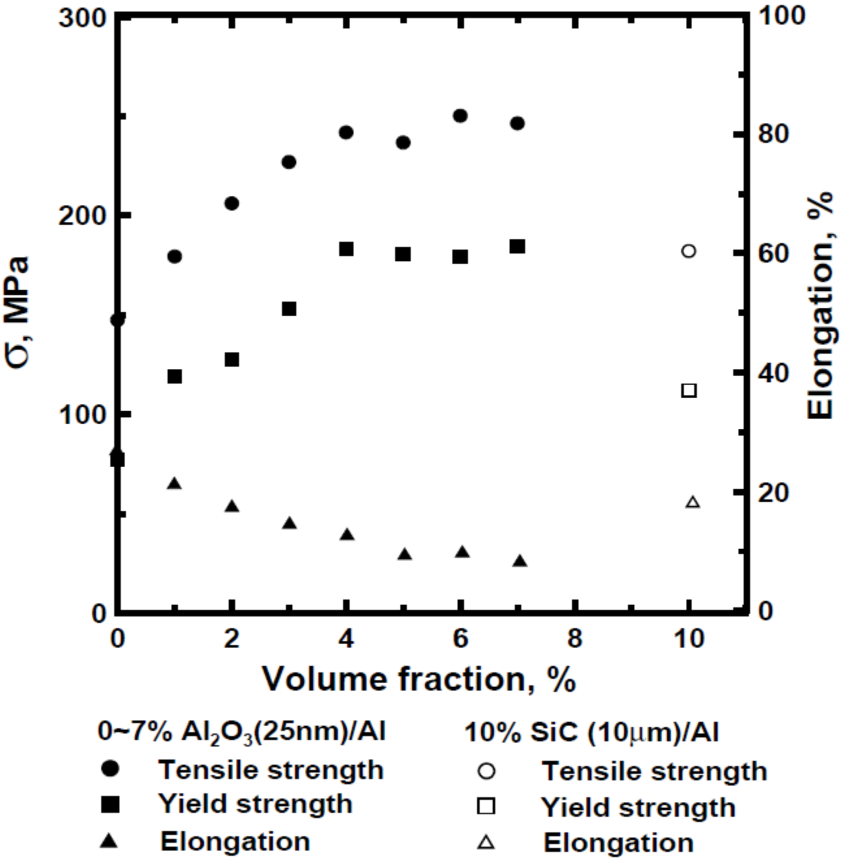

Figure 2.5: Tensile properties of Al/Al_2O_3 (25nm) and Al/SiC (10μm) composites [35] (with permission from Elsevier).

Besides its influence on tensile or compression strength, reinforcement size also has a prominent effect on ductility. Figure 2.6 summarizes the elongation to failure of commercial pure Al reinforced with SiC or Al_2O_3 particles from literature [34-37, 39, 41, 44]. An increased ductility with decreasing reinforcement size is observed. It is reported from literature that large particles (above 1.5μm) can act as microconcentrators of stress and give rise to particle fracture and early failure [35]; for medium sized particles (200nm~1.5μm), the particles are less likely to fracture due to the reduced stress within each particles as well as reduced flaw sizes [50], so the failure is generally associated with void formations at debonded particle/matrix interface; for smallest particles (usually below 200nm), retained ductility and toughness are normally achieved since the particles are usually well bonded to the matrix and do not initiate cavities [35]. However, nanoparticles have a tendency to agglomerate and form clusters, which have poor interparticle bonding and are known to fail prematurely [51].

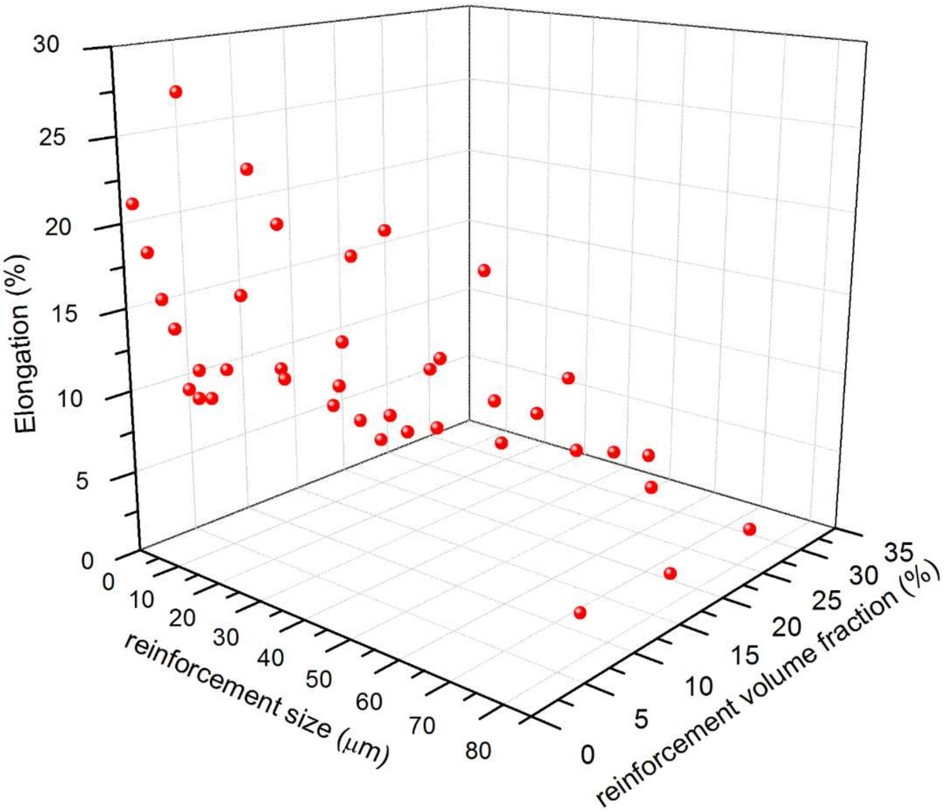

Figure 2.6: Summary of elongation to failure of commercial pure Al reinforced with SiC or Al_2O_3 particles against reinforcement size and volume fractions from literature [34-37, 39, 41, 44].

2.1.3.2 Effect of reinforcement volume fraction

Generally speaking, increasing the volume fraction of reinforcement particles will improve the strength of the composites, coupled with decreased ductility [50], as can be observed from Figures 2.4 and 2.6.

Chawla and Shen [52] investigated the tensile behaviour of an Al-Cu-Mg (2080)/SiC_p-T8 composite and found that with increased volume fractions of SiC (from 0vol.% to 30vol.%), higher Young's modulus, yield strength and UTS have been observed. Similar trends were also reported by Pal et al. [53], Poirier et al. [2] and Song [41] on Al/SiC_p or Al/$(Al_2O_3)_p$ systems. These trends were explained by multiple strengthening mechanisms, such as load transfer from the soft matrix to the stiffer reinforcements [50] and in situ strengthening of the matrix because of the additions of the reinforcements [2].

Other papers [35, 49] reported that the tensile strengths increased with the increasing amount of reinforcements up to some critical volume fractions. Figure 2.5 shows that the strengths of the Al/Al_2O_3 composites increase with increasing reinforcement volume fractions until 4%, beyond which the strengths of the composites are similar. Slipenyuk et al. [49] studied the mechanical properties of the Al-6Cu-0.4Mn (wt.%)/SiC_p composites (0-20vol.%) and found that the yield stress and UTS first increased with increasing amount of SiC, however, when the reinforcement concentration exceeded 10vol.%, these values decreased. The saturation or decrease of the tensile strengths was reported to be mainly due to the formation of reinforcement clusters in the composites which reduced the amount of effective reinforcement particles available [35].

2.1.3.3 Effect of secondary processing

Secondary processing techniques such as extrusion, rolling or forging are necessary for decreasing the porosity and consolidating the composites after the primary fabrication methods [54]. The effect of extrusion and cold rolling is discussed in detail.

Extrusion is a very effective step to improve the density, homogenize the microstructure and mechanical properties of MMCs. Cocen and Önel [55] studied as cast and extruded Al-5Si-0.2Mg (wt.%)/SiC_p composites and found that keeping the other parameters constant, the tensile strength values of the extruded composites were improved by ~40% compared with as cast composites. Similar experimental results were also reported by Rahmani Fard and Akhlaghi [54] on A356/SiC_p composites and Tham et al. [56] on Al/SiC_p composites. Multiple explanations are given for these effects of the extrusion process. First of all, the combination of high pressure and temperature during extrusion results in a high shear stress between particles, which will help break up the oxide layer on the surface of the powder particles and lead to a better adhesion of the matrix-particle interfacial areas [50, 57]. At the same time, extrusion can reduce porosity, break up particle clusters and lead to a more uniform distribution of secondary particles [57]. All these factors will result in a development of better microstructure with fewer defects after extrusion and therefore a significant improvement on the mechanical properties of the composites.

Rolling is another secondary processing technique which allows obtaining MMCs in flat shapes. Lee and Subramanian [58] studied the cold rolling of $Al/(Al_2O_3)_p$ composites up to a thickness reduction of 75% and found that rolling broke up $(Al_2O_3)_p$ clusters and improved particle distribution. Amirkhanlou et al. [59] compared $6061Al/SiC_p$ composite produced by compocasting followed by cold rolling to different reductions and found out that the rolled specimens exhibited reduced porosity and a more uniform distribution of SiC particles in the matrix, resulting in a much higher tensile strength and elongation. In general, during cold rolling, the strength of the composites can increase significantly due to work hardening effects [60]. In addition, porosity elimination and particle realignment can be achieved [5]. However, severe damages such as cavitations, particle cracking and crack growth can easily happen since rolling involves high local strains being imposed really quickly, especially at low temperature [5]. Despite the need for cold rolling as a secondary metal-working technique to produce sheet materials, the results on systematic studies of cold rolling with high rolling reductions are quite limited. It is necessary to carry out more experiments to further analyse the effect of cold rolling on the evolution of the microstructure and the mechanical properties of the composites.

2.1.4 Problems existing so far hindering mechanical behaviour

Although Al based composites have shown great potential with their unique mechanical properties, there are still unresolved issues, such as inhomogeneous distribution of reinforcements [35], undesirable reactions at interface [1] and interfacial debonding [5], which will significantly deteriorate their mechanical properties.

2.1.4.1 Inhomogeneous distribution of reinforcements

Because of the large surface-to-volume ratio, nanoreinforcements tend to agglomerate easily during fabrication process [45]. Many processing techniques have been tried to possibly eliminate clusters. Mula et al. [61] produced 2wt.% Al/Al_2O_3 (10nm) nanocomposites by ultrasonic casting and found that the nano-sized Al_2O_3 segregated near the Al grain boundaries, resulting in small-chain like structures. Kang and Chan [35] attempted to produce Al/Al_2O_3 (50nm) nanocomposites by traditional powder metallurgy routes and observed severe agglomerations when the nanoparticle content exceeded 4vol.% which eliminated the particle strengthening effects.

A possible solution to minimise the clustering issue is to use high energy mechanical milling/alloying (MA). For instance, Tang et al. [62] reported a homogeneous distribution of SiC nanoparticles (25nm) in a 5083Al matrix by milling process. Poirier et al. [2] also investigated mechanical milling as a possible way to disperse nanoparticles uniformly and found that the Al/Al_2O_3 nanocomposites had an uniform distribution of reinforcement particles with few agglomerates of around 1μm even when the size of Al_2O_3 was only 4nm. Other encouraging results showing that MA is a useful method for improving the reinforcement particle distribution in nanocomposites have also been reported on nanoscaled SiC or Al_2O_3 particle reinforced Al, Cu or Mg based composites [63-67]. Additional research on the parameters that affect the mechanical milling, including miller type, ball to powder weight ratio, characteristics of the balls and speed, milling atmosphere and process control agent should be carried out to study their effect on the morphology and the microstructure of Al based nanocomposites to be able to fully optimize the mechanical properties [68].

2.1.4.2 Undesirable reactions at interface

During the manufacturing process, chemical reactions will occur at interfacial areas. Some interfacial reactions can effectively improve the mechanical properties of MMCs due to the enhanced wettability between particles and matrix [69]. However, some reactions can produce undesirable brittle and unstable phases, such as Al_4C_3 and Si in Al/SiC composite systems [4]. These phases will degrade the mechanical properties [70] since the Al_4C_3-SiC interface is usually rough and can cause stress localization, which can act as preferred sites for crack initiation and propagation [1].

This problem can most likely be resolved or minimised by three methods [69]: (1) matrix composition modification, for example, the interfacial reactions to form Al_4C_3 phase can be suppressed by adding Si element into Al matrix alloy; (2) proper selection of processing parameters, such as fabrication temperature and holding time; (3) surface modification of reinforcement, such as coating or pre-oxidation of reinforcement particles. Coating can eliminate undesirable chemical reactions, encourage wetting and promote desirable mechanical properties at interface [5]. The pre-oxidation of reinforcement particles, for example, SiC, forms a coherent layer of SiO_2 on the particle surfaces, which can protect the particles from Al attack, inhibiting the formation of Al_4C_3 [71].

2.1.4.3 Weak interfacial bonding

The interfacial regions in composites are very important since the effects of stiffening and strengthening rely on load transfer across the interface [5]. However, due to the difficulty of fully consolidation, the bonding between the reinforcements and metal matrix is quite limited [2]. Figure 2.7 [2] shows a STEM image of 10vol.% Al/Al_2O_3 (80nm) interface. It is clearly observed that a large number of cavities have formed at the interface, which led to a mismatch between the experimental data and the predicted strengths [2]. As previously discussed, secondary processing techniques, such as extrusion and rolling, can help to better consolidate the composites and improve the composites densification and properties. Also, cold spray technique is being investigated as an alternative method to help consolidate the powders [2].

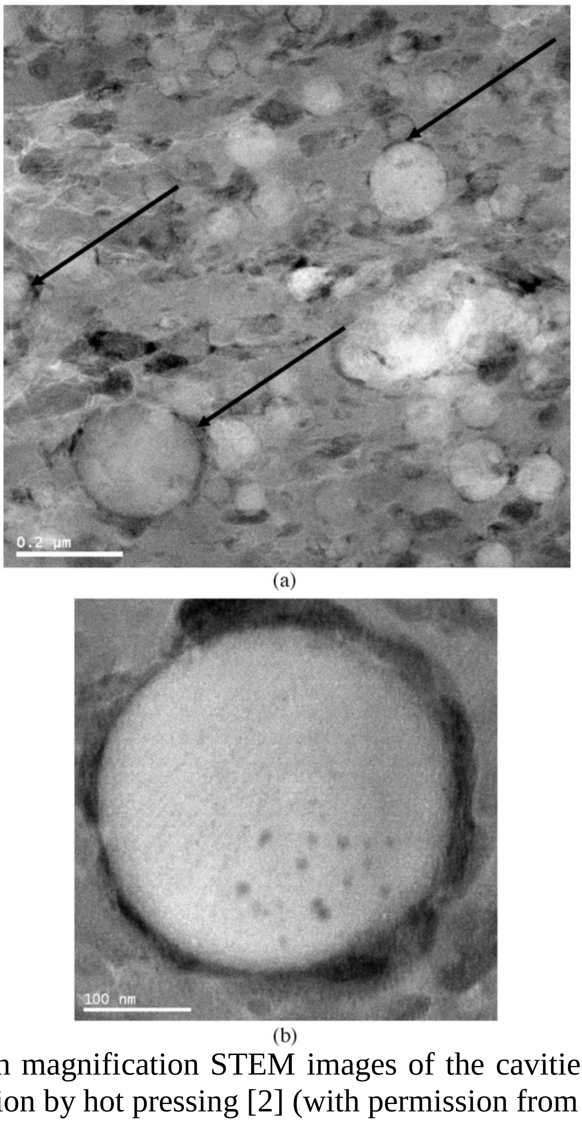

Figure 2.7: Low and high magnification STEM images of the cavities at the Al/Al_2O_3 (80nm) interfaces after consolidation by hot pressing [2] (with permission from Elsevier).

2.2 Plastic deformation of Al alloy composites

Plastic deformation process is a metal forming process in which a plastic strain is introduced to the bulk metals [60]. In conventional metal forming processes, extrusion, forging and rolling are commonly applied [72]. In recent years, many severe plastic deformation (SPD) processes (shown in Figure 2.8) have been developed in order to produce highly strained workpieces while remaining the same shape, such as equal channel angular pressing (ECAP), accumulative roll-bonding (ARB), high pressure torsion (HPT), accumulative back extrusion (ABE), etc. [72, 73]. The extreme straining during the plastic deformation processes has a great impact on the microstructure and the crystallographic texture of the materials. In this section, a brief overview of deformation microstructure, texture development and deformation processed metal-metal composites (DPMMCs) will be reviewed.

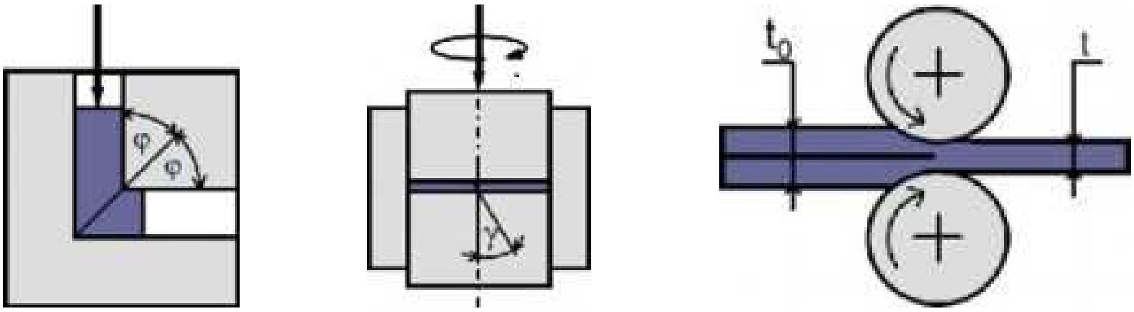

(a) (b) (c)

Figure 2.8: Summary of major SPD processes: (a) equal channel angular extrusion (ECAE); (b) high pressure torsion (HPT); (c) accumulative roll-bonding [72] (with permission from Elsevier).

2.2.1 Deformation microstructure

The development of deformation microstructure of fcc metals has been studied extensively. It is now generally accepted that during most deformation processes, most metals develop a cellular substructure [74]. New boundaries separating the substructures are introduced by a misorientation between neighbouring cells. With further deformation, the misorientation arises and the boundary spacings decrease [74].

The development of substructures of deformed high and medium stacking fault energy polycrystalline metals (such as Al) are summarized here. At low strains, dislocation tangles become progressively interconnected and form a rough cellular structure (order of 1μm) in some preferred regions. With further deformation, cell dimensions decrease rapidly with strains at a degressive rate [75]. Figure 2.9 shows the development of average cell size of deformed pure Al up to high strains reported in a review by Sevillano et al. [75]. It can be seen that regardless of the different deformation modes, the Al cell size decreases with increasing strains and attains a limit size of about 0.4μm after a strain of 3.

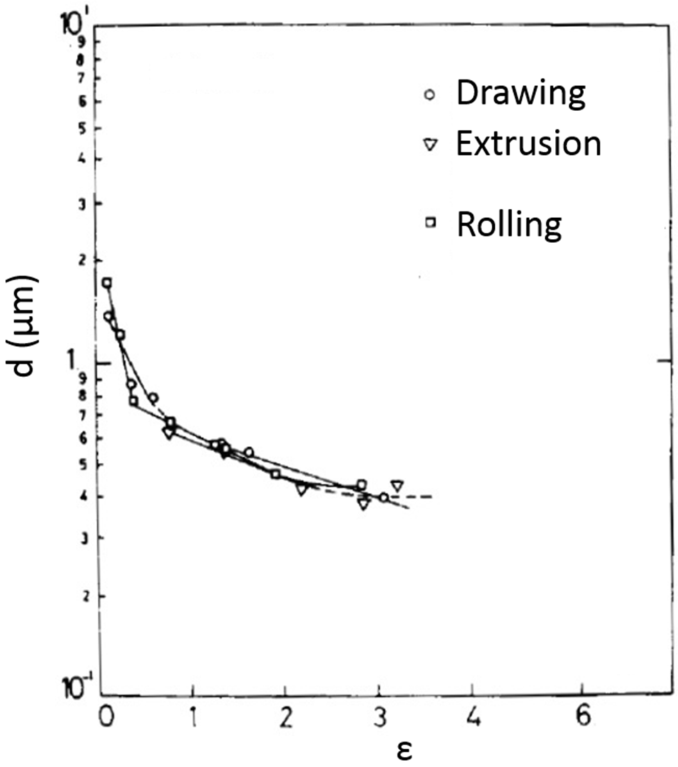

Figure 2.9: Average cell size of pure Al versus deformation strains [75] (with permission from Elsevier).

Despite of the development of cell size, the boundary misorientations also change significantly during deformation. Jazaeri and Humphreys [76] investigated the microstructure evolution in cold rolled Al-0.1Mg, AA1200 and AA8006 alloys. Some of the results are shown in Figures 2.10 and 2.11. It can be seen that the misorientation distribution widens as strain increases and the fractions of high angle grain boundaries (HAGB%) (>15°) first decrease due to the formation of low angle boundaries, then the HAGB% increases and tends to saturate at values of 60%-80% at the largest strains. Two effects have been ascribed to the increasing fractions of HAGB%. During deformation, the pre-existing high angle boundary areas are found to increase with increasing strains at a rate depending on the deformation mode. In addition, additional high angle boundaries are also formed due to the increase in the misorientations of the substructures at high strains [76].

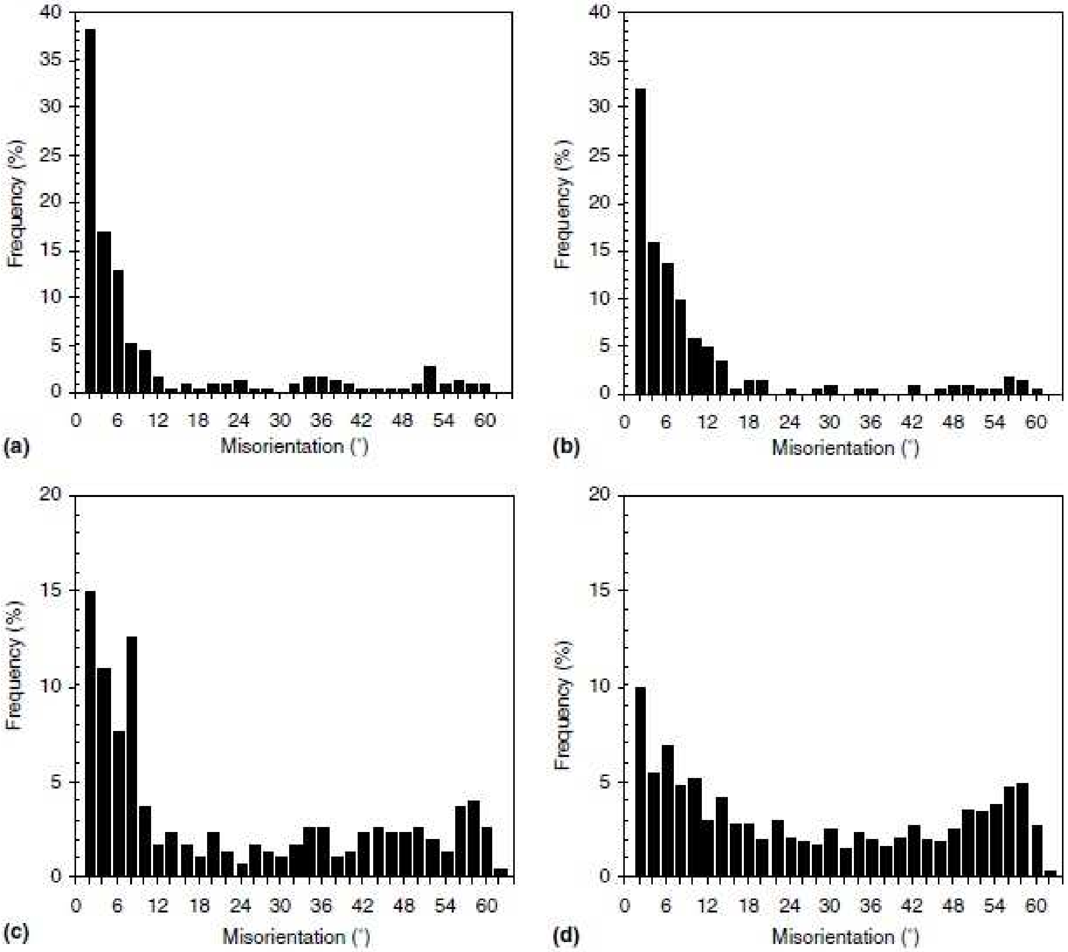

Figure 2.10: Grain boundary misorientation distribution of cold rolled Al-0.1Mg after deformation at strains: (a) 0.69, (b) 1.2, (c) 2.6 and (d) 3.9 [76] (with permission from Elsevier).

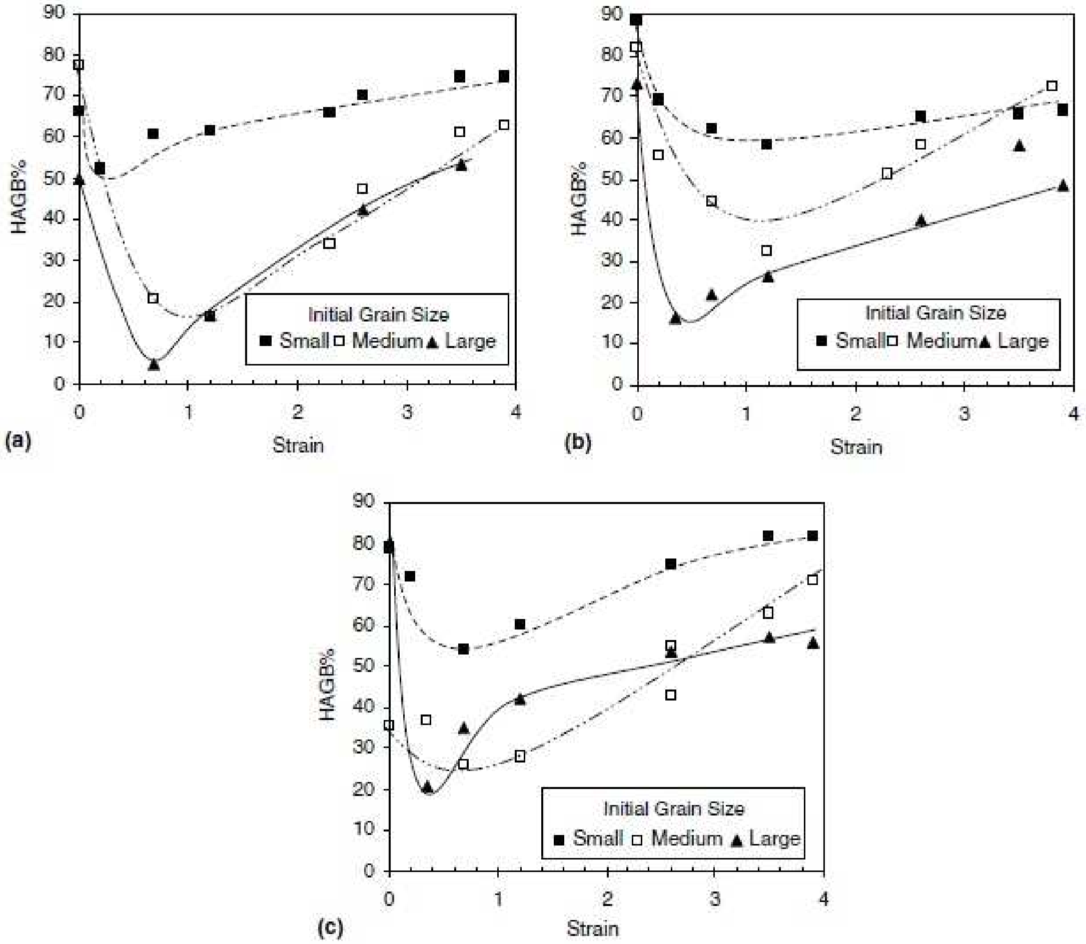

Figure 2.11: The development of high angle grain boundary (>15°) in the cold rolled (a) Al-0.1Mg, (b) AA1200 and (c) AA8006 alloys [76] (with permission from Elsevier).

2.2.2 Deformation texture

In a polycrystalline material, if the grains have a non-uniform distribution of crystallographic orientations, then the term "texture" is used to describe the preferred orientations [77]. Textures can arise during many manufacturing procedures, such as solidification, mechanical deformation and recrystallization [78]. The formation of textures can greatly influence the anisotropy of the overall materials, thus it is quite important to characterize them in order to understand how they are formed and how they affect materials' properties. In the past, optical methods and etching have been primarily used to determine grain orientations [78]. Nowadays, X-ray diffraction and Electron Backscatter Diffraction (EBSD) are two most widely used techniques for texture measurement [78].

There are mainly two ways to represent the crystallographic texture graphically, the pole figure and the Orientation Distribution Function (ODF) [78]. The pole figure plots the orientations of a given plane normal (pole) from all of the grains in the polycrystal with respect to the sample reference frame [79]. Typically, for rolled sample, the sample reference frame is usually defined by the normal direction (ND), the rolling direction (RD) and the transverse direction (TD). Figure 2.12 gives an example about the relationships between the orientation of the crystal and the stereographic projection obtained for a certain pole. The pole figures are constructed by the following steps [80]. First, a unit cell of the crystal (in this case, it is a cube) is placed in the centre of the unit sphere which is defined by the sample reference frame. Considering a specific set of crystal planes {h k l}, the intersection points of the normal vector of the {h k l} planes with the surface of the unit sphere are determined. Then the intersection points on the northern hemisphere are connected with the South pole. The points of the intersections of the lines with the equatorial plane represent the orientations of the {h k l} planes with respect to the sample reference frame. These points are called poles of the {h k l} planes. Pole figures are the superimposed plot of a set of poles for each individual grain for polycrystalline materials [78].

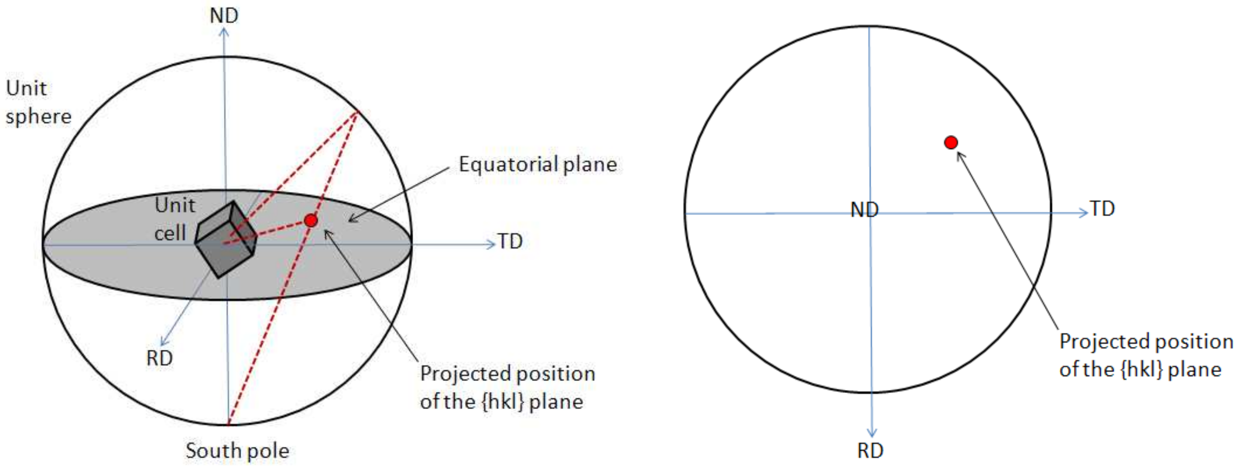

(a) (b)

Figure 2.12: Schematic diagrams showing the pole figure constructions.

Pole figure is a traditional way to represent crystallographic texture for the past years. However, pole figure is a two-dimensional plot and one pole on the pole figure only cannot represent the orientation of a grain in a three dimensional space. In order to represent the orientation unambiguously, several poles need to be determined. This is not a problem when comes to single crystals. However, for a large number of grains in a polycrystal, as more poles are plotted onto the pole figure, poles may overlap on the pole figure which makes it difficult to determine the true orientation density of specific orientations, making it almost impossible to perform any quantitative analysis [78, 79].

In order to study the texture quantitatively, Orientation Distribution Functions (ODFs) constructed from several pole figures are more and more used for complex texture analysis [79]. ODF is a 2D representation of Euler space defined by three Euler angles (φ_1, Φ, φ_2) and describes the orientation of each crystal with three Euler angles [77, 79]. The three Euler angles describe the three rotations to overlap the sample reference frame with crystal reference frame. There are multiple definitions of Euler angles, such as Bunge, Kocks and Roe [77, 79]. The Bunge definition is used through this thesis and the definition is shown in Figure 2.13. For example, in rolled sheets, the sample reference frame is defined by RD, TD and ND, and the cubic crystal reference frame is determined by three coordinates X_c, Y_c and Z_c. A sequence of three rotations needs to be performed in order to bring the sample reference frame in coincidence with crystal reference frame. The three rotations according to the Bunge definition are [79, 81]:

Rotation 1: rotate the sample system around ND with angle φ_1 so that the new RD’ is perpendicular with Z_c.

Rotation 2: rotate the sample system around the new RD’ with angle Φ so that the new orientation of ND’ is parallel to Z_c.

Rotation 3: rotate the sample system around the new ND’ with angle φ_2 to bring the two system overlap.

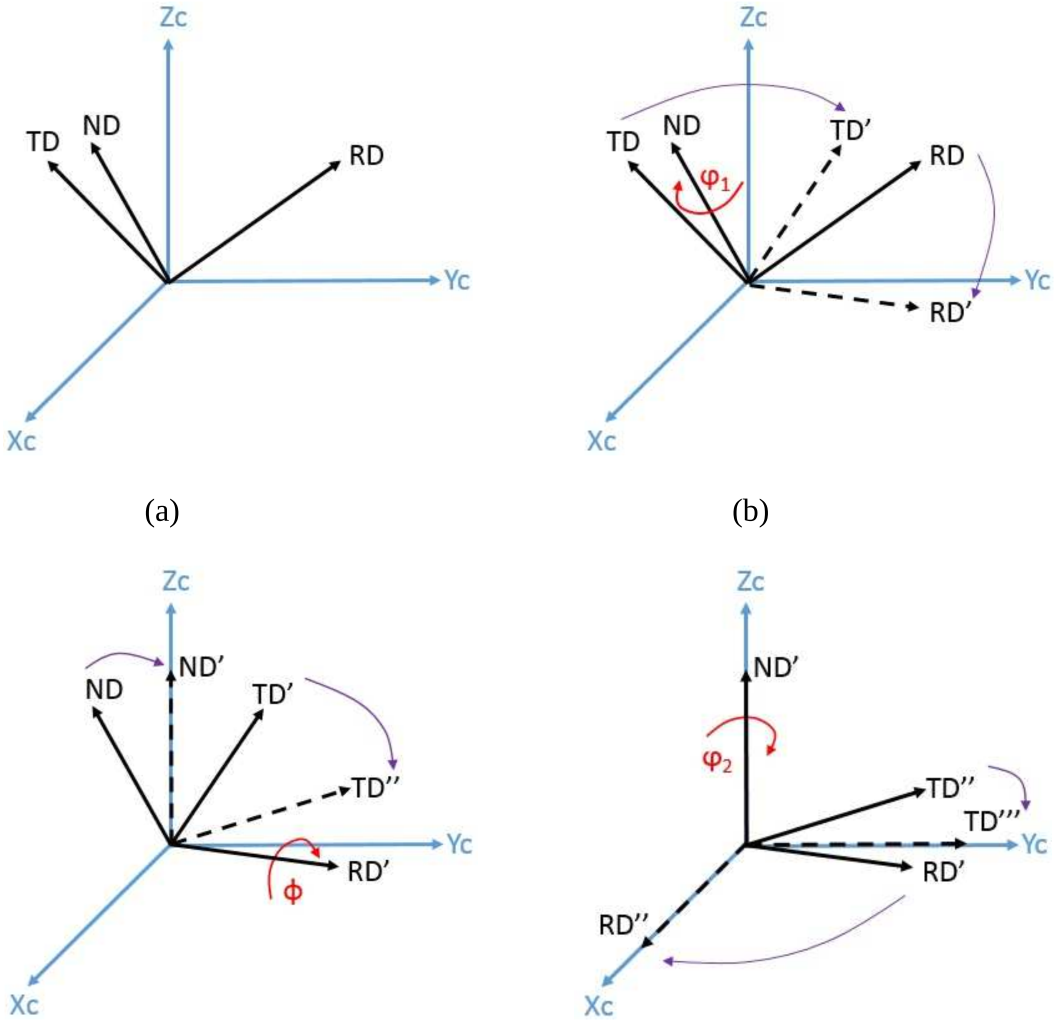

(a) (b)

(c) (d)

Figure 2.13: Operation of Euler angles. (a) Sample reference frame defined by RD, TD and ND, and cubic crystal reference frame defined by X_c, Y_c and Z_c; (b)-(d) three rotations according to the Bunge definition to bring the sample reference frame in coincidence with crystal reference frame [79].

The three Euler angles can construct a 3D Euler space in which each point is a presentation of a unique orientation. Since it is difficult to interpret a 3D graph, ODF, a 2D representation of Euler space is constructed by slicing the Euler space into constant φ_2 sections [82]. Compared with pole figures, ODF is a clearer and more straightforward method to interpret texture analysis and quantitative calculations, such as volume fractions of specific orientations, can be achieved through ODF analysis.

Cold rolling textures for fcc metals, like Al alloys, have been studied for many years. The main textures observed experimentally are Copper (C) component, S component, Goss (G) component, Brass (B) component, Dillamore (D) component and Cube component [77, 83]. Their detailed orientations and positions in Euler space and inverse pole figures are listed in Table 2.2 and Figure 2.14(c), respectively.

Texture component	{h k l}	<u v w>	φ_1 (°)	Φ(°)	φ_2 (°)
Copper, C	112	111	90	35	45
S	123	634	59	37	63
S1	124	211	59	29	63
S2	123	412	47	37	63
Goss, G	011	100	0	45	90
Brass, B	011	211	35	45	90
Dillamore, D	4,4,11	11,11,8	90	27	45
Cube	001	100	0	0	0

Table 2.2: Main texture component in rolled fcc metals (1st subspace): Indices and Euler angles [77, 83].

Instead of describing the textures using ideal orientations, another way to represent the textures is to use continuous tubes or fibres of orientations limited to a single degree of rotational freedom about a fixed axis in three dimensional Euler space [77]. Cold rolling of fcc metals will generally lead to the formation of two main fibres in Euler space, see Figure 2.14:

(1) The α fibre: the α fibre goes from Goss component to Brass component.

(2) The β fibre: the β fibre goes from Brass component to Copper component through S component [74].

The orientation density values along the α and β fibres have been commonly used to describe the texture evolution during plastic deformation. Previous researchers [83-87] have found that at low degrees of rolling, the orientation densities along the two fibres distributed homogeneously. With further rolling reductions, the deterioration of α and β fibres began and pronounced peaks at Copper, Brass and S components developed. In order to quantify the formation of textures during rolling and relate the texture components to mechanical properties, the volume fractions of each selected texture component are usually calculated by integration of the intensities of the ODF f(**g**) (**g** is the general representation of an orientation in Euler space while f(**g**) stands for the orientation density as a function of different orientations [77]) within 10~15 degree of the ideal positions in the subset of Euler space [83].

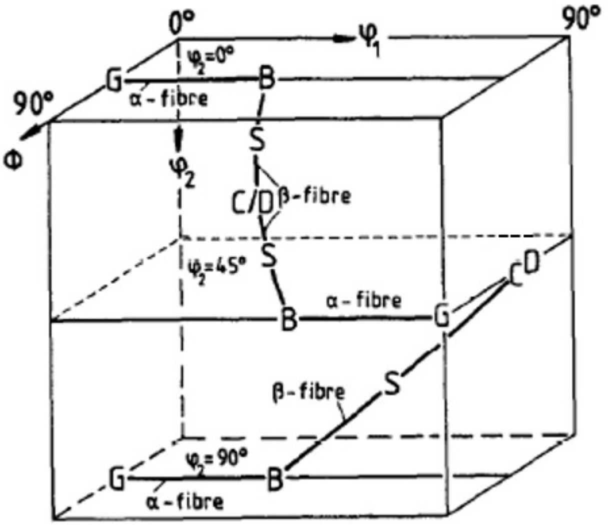

(a)

Figure removed due to copyright reasons

(b)

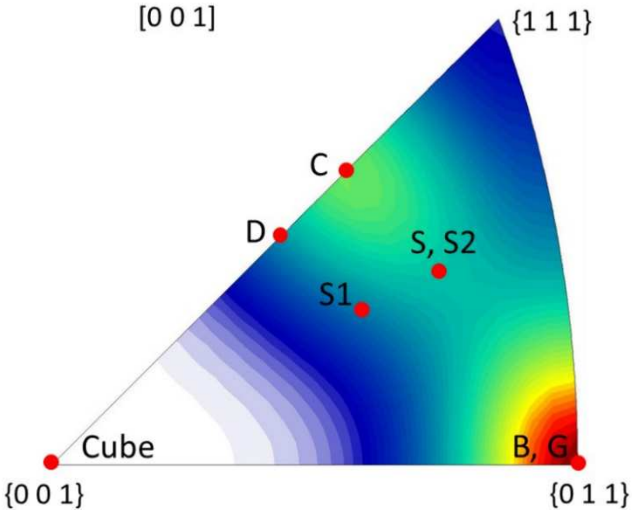

(c)

Figure 2.14: (a) Schematic representation of the fcc rolling texture in three dimensional Euler space [85] (with permission from Elsevier), it should be noted that there are generally three equivalent points for each orientation in Euler space due to the sample and crystal symmetries [79]; (b) The Euler space represented by constant φ_2 sections, the ideal texture components (B, G, S and C) are listed [88] and (c) The β fibre texture running from Brass to Copper through S as well as the ideal texture components listed in Table 2.2 in an inverse pole figure [77].

2.2.3 Deformation processed metal-metal composites (DPMMCs)

Deformation processed metal-metal composites (DPMMCs) have long been the interest of many researchers due to their high strength at room temperature or elevated temperatures and excellent thermal and electrical conductivities [89-100]. A DPMMC is composed of two immiscible metals with different lattice structures or those having limited mutual solubility [101]. For example, a fcc matrix materials, such as Cu and Al, and a bcc second phase metal, e.g. Nb, Fe, Cr or Ta, are usually utilized to produce this kind of composites (fcc/bcc type) [95, 96, 98, 100, 102-105]. In addition, an hcp metal, such as Ti, or a body-centered tetragonal (bct) metal, such as Sn, has been also used as reinforcement (fcc/hcp and fcc/bct types) [99, 106-108]. There are also some remarkable reports on the DPMMCs containing two fcc metals (fcc/fcc type), such as Cu/Ag, Ag/Ni [94, 109-113].

Anomalous increase in strength is usually observed for DPMMCs, with tensile strengths greater than those predicted by rule of mixtures (ROM) [114]. For example, deformation processed Cu-Nb alloys have been shown to be able to achieve tensile strengths above 2000MPa [90, 92, 115]. In these studies, solidified Cu-Nb billets were mechanically deformed to wire at room temperature to very large strains without annealing and strains larger than 10 were required to achieve tensile strengths of 2000MPa. Figure 2.15 [115] shows the effect of drawing ratio on the UTS of Cu, Nb and Cu-Nb composites with initial Nb dendrite sizes of 6.2μm and 3.8μm, respectively. It can be seen that the strengths of the Cu-Nb composites increase with increasing drawing ratios up to a UTS of 2200MPa with no signs of levelling off. In addition, the strengths of the composites are always greater than that predicted by ROM suggesting additional strengthening mechanisms. Other severe plastic deformation techniques, such as accumulative roll-bonding and high pressure torsion, have also been utilised to fabricate Cu-Nb composites recently and layer thicknesses below 20nm were achieved leading to exceptional hardness and strength [116, 117]. For example, Beyerlein et al. [116] studied microstructure development and mechanical properties of Cu-Nb composites fabricated via accumulative roll-bonding. As the rolling strain increased to 12.21, the Cu-Nb layer thickness decreased from 97μm to 10nm, leading to a hardness of ~4.5GPa and a compression strength of ~2GPa.

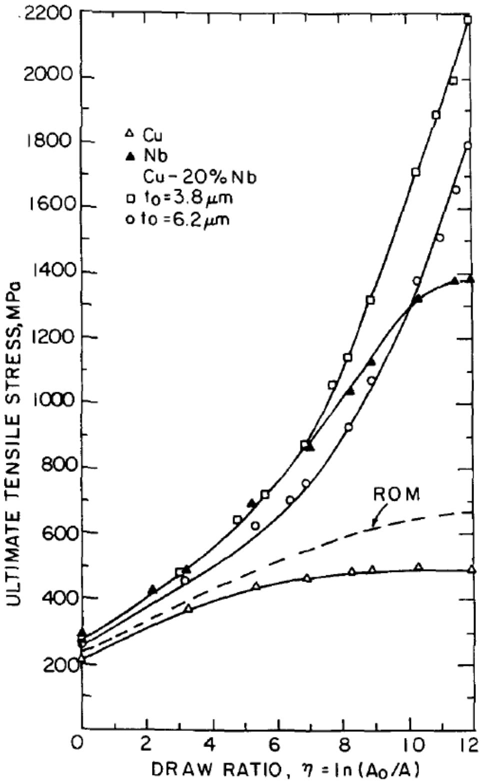

Figure 2.15: Effect of drawing ratio on the UTS of Cu, Nb, and Cu-20.vol%Nb composites [115] (with permission from Elsevier).

DPMMCs are usually made by preparing initial billets by ingot casting or powder metallurgy routes followed by extrusion, swaging, wire drawing or rolling techniques [118]. Compared with ingot casting, powder metallurgy process is a more attractive way since it can effectively avoid the interfacial reactions between matrix and reinforcement. In addition, most of the DPMMCs studied so far were prepared by hot extrusion followed by cold swaging or drawing [101] while very rare studies have focused on sheet DPMMCs associated with rolling technology. Considering the potential applications of Al sheet composites, investigations of Al sheet DPMMCs fabricated by hot extrusion followed by cold rolling are needed.

2.3 Summary

Particulates reinforced Al alloy composites are promising materials for industrial applications including aerospace and automotive due to their improved mechanical and physical properties coupled with favourable metalworking characteristics [49].

The mechanical properties of MMCs depend on many factors, such as reinforcement volume fraction, reinforcement size, secondary processing techniques, etc. Compared with micro-sized MMCs, Al based nano-sized metal matrix composites (NMMCs) have shown great potential. A small amount of additions of nanoparticles can significantly enhance the mechanical properties of nanocomposites with retained ductility. However, the fabrication of NMMCs is still an issue since the nanoparticles tend to agglomerate easily which greatly degrade the overall properties. High energy mechanical alloying is so far the most effective way to eliminate the clusters; however, proper parameters need to be found for specific NMMCs.

Plastic deformation, such as rolling, have a significant effect on the substructure development and texture evolution. Most metals develop a cellular substructure and the cell size decreases with increasing strains up to a minimum size. With increasing deformation strains, the misorientations between neighbouring cells increase and increased fractions of high angle grain boundaries will be developed. Preferred orientations tend to form during manufacturing process, cold rolling of Al alloys usually lead to the formation of α and β fibre texture and the intensities increase with increasing rolling strains.

Considering all the factors affecting the microstructure and mechanical properties of MMCs, a systematic study on different MMCs and NMMCs with or without plastic deformation is needed. The present work focuses on the fabrication and characterization of Al alloy composites reinforced with different types of reinforcement (nano-size/micro-size; non-deformable/deformable) followed by extrusion and/or cold rolling in order to fully understand the key factors. Only on the base of this knowledge can it be possible to develop new MMCs or NMMCs with best combination of properties for a specific industrial application.

2.4 References

[1] I. A. Ibrahim, F. A. Mohamed, and E. J. Lavernia, "Particulate reinforced metal matrix composites - a review," *Journal of Materials Science,* vol. 26, pp. 1137-1156, 1991.

[2] D. Poirier, R. A. L. Drew, M. L. Trudeau, and R. Gauvin, "Fabrication and properties of mechanically milled alumina/aluminum nanocomposites," *Materials Science and Engineering A,* vol. 527, pp. 7605-7614, 2010.

[3] C. Suryanarayana, "Synthesis of nanocomposites by mechanical alloying," *Journal of Alloys and Compounds,* vol. 509, pp. S229-S234, 2011.

[4] D. J. Lloyd, "Particle-reinforced aluminum and magnesium matrix composites," *International Materials Reviews,* vol. 39, pp. 1-23, 1994.

[5] T. W. Clyne and P. J. Withers, *An introduction to metal matrix composites*, First paperback edition 1995. ed. Cambridge: Cambridge University Press, 1993.

[6] H. Jones, "A perspective on the development of rapid solidification and nonequilibrium processing and its future," *Materials Science and Engineering A*, vol. 304, pp. 11-19, 2001.

[7] F. Audebert, M. Galano, C. T. Rios, H. Kasama, M. Peres, C. Kiminami, *et al.*, "Nanoquasicrystalline Al-Fe-Cr-Nb alloys produced by powder metallurgy," *Journal of Alloys and Compounds,* vol. 577, pp. 650-657, 2013.

[8] C. Suryanarayana, "Mechanical alloying and milling," *Progress in Materials Science,* vol. 46, pp. 1-184, 2001.

[9] J. M. Torralba, C. E. da Costa, and F. Velasco, "P/M aluminum matrix composites: an overview," *Journal of Materials Processing Technology,* vol. 133, pp. 203-206, 2003.

[10] (07-10-2013). Available: http://en.wikipedia.org/wiki/Aluminium

[11] M. Wang, D. Chen, Z. Chen, Y. Wu, F. Wang, N. Ma, *et al.*, "Mechanical properties of in-situ TiB_2/A356 composites," *Materials Science and Engineering A,* vol. 590, pp. 246-254, 2014.

[12] H. Sekine and R. Chen, "A combined microstructure strengthening analysis of SiCp/Al metal-matrix composites," *Composites,* vol. 26, pp. 183-188, 1995.

[13] I. Sinclair and P. J. Gregson, "Structural performance of discontinuous metal matrix composites," *Materials Science and Technology,* vol. 13, pp. 709-726, 1997.

[14] R. A. Varin, M. Metelnick, and Z. Wronski, "Structure of as-cast aluminum matrix composite containing Ni_3Al-type intermetallic ribbons," *Metallurgical transactions. A, Physical metallurgy and materials science,* vol. 20 A, pp. 1153-1161, 1989.

[15] R. A. Varin, Z. Wronski, and M. P. Metelnick, "Metal matrix composites reinforced with intermetallic ribbons," *Materials and Manufacturing Processes,* vol. 5, pp. 197-213, 1990.

[16] B. Torres, M. Campo, M. Lieblich, and J. Rams, "Oxy-acetylene flame thermal sprayed coatings of aluminium matrix composites reinforced with $MoSi_2$ intermetallic particles," *Surface and Coatings Technology,* vol. 236, pp. 274-283, 2013.

[17] K. R. Cardoso, M. A. Muñoz-Morris, M. Lieblich, and D. Morris, "Effect of equal channel angular pressing (ECAP) on microstructure and properties of Al-FeAlCr intermetallic phase composites," *Materials Research,* vol. 17, pp. 775-780, 2014.

[18] M. Lieblich, J. L. GonzalezCarrasco, and G. Caruana, "Thermal stability of an Al/Ni_3Al composite processed by powder metallurgy," *Intermetallics,* vol. 5, pp. 515-524, 1997.

[19] A. Inoue, "Amorphous, nanoquasicrystalline and nanocrystalline alloys in Al-based systems," *Progress in Materials Science,* vol. 43, pp. 365-520, 1998.

[20] D. Shechtman, I. Blech, D. Gratias, and J. W. Cahn, "Metallic phase with long-range orientational order and no translational symmetry," *Physical Review Letters,* vol. 53, pp. 1951-1953, 1984.

[21] A. Inoue, H. Kimura, and T. Masumoto, "Formation, thermal-stability and electrical-resistivity of quasi-crystalline phase in rapidly quenched Al-Cr alloys," *Journal of Materials Science,* vol. 22, pp. 1758-1768, 1987.

[22] D. J. Skinner, V. R. V. Ramanan, M. S. Zedalis, and N. J. Kim, "Stability of quasicrystalline phases in Al-Fe-V alloys," *Materials Science and Engineering,* vol. 99, pp. 407-411, 1988.

[23] R. A. Dunlap, G. Stroink, K. Dini, and D. F. Jones, "Structural, electrical and magnetic-properties of icosahedral Al-Co alloys," *Journal of Physics F-Metal Physics,* vol. 16, pp. 1247-1254, 1986.

[24] F. Audebert, H. Sirkin, and A. G. Escorial, "Approach to the atomic structure of amorphous Al-Fe-Nb," *Philosophical Magazine B-Physics of Condensed Matter Statistical Mechanics Electronic Optical and Magnetic Properties,* vol. 76, pp. 483-487, 1997.

[25] A. Inoue and H. Kimura, "High elevated-temperature strength of Al-based nanoquasicrystalline alloys," *Nanostructured Materials,* vol. 11, pp. 221-231, 1999.

[26] M. Galano, F. Audebert, B. Cantor, and I. Stone, "Structural characterisation and stability of new nanoquasicrystalline Al-based alloys," *Materials Science and Engineering A,* vol. 375, pp. 1206-1211, 2004.

[27] I. Todd, Z. Chlup, J. G. O'Dwyer, M. Lieblich, and A. Garcia-Escorial, "The influence of processing variables on the structure and mechanical properties of nano-quasicrystalline

reinforced aluminium alloys," *Materials Science and Engineering A,* vol. 375, pp. 1235-1238, 2004.

[28] M. Yamasaki, Y. Nagaishi, and Y. Kawamura, "Inhibition of Al grain coarsening by quasicrystalline icosahedral phase in the rapidly solidified powder metallurgy Al-Fe-Ti-Cr alloy," *Scripta Materialia,* vol. 56, pp. 785-788, 2007.

[29] M. Galano, F. Audebert, I. C. Stone, and B. Cantor, "Nanoquasicrystalline Al-Fe-Cr-based alloys. Part I: Phase transformations," *Acta Materialia,* vol. 57, pp. 5107-5119, 2009.

[30] M. Galano, F. Audebert, A. G. Escorial, I. C. Stone, and B. Cantor, "Nanoquasicrystalline Al-Fe-Cr-based alloys. Part II. Mechanical properties," *Acta Materialia,* vol. 57, pp. 5120-5130, 2009.

[31] A. Inoue and H. Kimura, "High-strength aluminum alloys containing nanoquasicrystalline particles," *Materials Science and Engineering A,* vol. 286, pp. 1-10, 2000.

[32] A. Slipenyuk, V. Kuprin, Y. Milman, J. E. Spowart, and D. B. Miracle, "The effect of matrix to reinforcement particle size ratio (PSR) on the microstructure and mechanical properties of a P/M processed AlCuMn/SiCp MMC," *Materials Science and Engineering A,* vol. 381, pp. 165-170, 2004.

[33] Z. W. Wang, M. Song, C. Sun, and Y. H. He, "Effects of particle size and distribution on the mechanical properties of SiC reinforced Al-Cu alloy composites," *Materials Science and Engineering A,* vol. 528, pp. 1131-1137, 2011.

[34] M. Zakeri and A. V. A. Rudi, "Effect of shaping methods on the mechanical properties of Al-SiC composite," *Materials Research-Ibero-American Journal of Materials*, vol. 16, pp. 1169-1174, 2013.

[35] Y. C. Kang and S. L. I. Chan, "Tensile properties of nanometric Al_2O_3 particulate-reinforced aluminum matrix composites," *Materials Chemistry and Physics,* vol. 85, pp. 438-443, 2004.

[36] S. J. Hong and P. W. Kao, "Mechanical properties of Al-SiC composites made by resistance sintering of mechanically alloyed powders," *Materials Science and Engineering A,* vol. 148, pp. 189-195, 1991.

[37] C. P. Ling, M. B. Bush, and D. S. Perera, "The effect of fabrication techniques on the properties of Al-SiC composites," *Journal of Materials Processing Technology,* vol. 48, pp. 325-331, 1995.

[38] P. Katiyar, "Processing, microstructural and mechanical characterization of mechanically alloyed Al-Al_2O_3 nanocomposites," University of Central Florida Orlando, Florida, 2004.

[39] M. Jahedi, B. Mani, S. Shakoorian, E. Pourkhorshid, and M. H. Paydar, "Deformation rate effect on the microstructure and mechanical properties of Al-SiCp composites consolidated by hot extrusion," *Materials Science and Engineering A*, vol. 556, pp. 23-30, 2012.

[40] B. S. Unlu, "Investigation of tribological and mechanical properties Al_2O_3-SiC reinforced Al composites manufactured by casting or P/M method," *Materials & Design*, vol. 29, pp. 2002-2008, 2008.

[41] M. Song, "Effects of volume fraction of SiC particles on mechanical properties of SiC/Al composites," *Transactions of Nonferrous Metals Society of China*, vol. 19, pp. 1400-1404, 2009.

[42] G. Ramu and R. Bauri, "Effect of equal channel angular pressing (ECAP) on microstructure and properties of Al-SiCp composites," *Materials & Design*, vol. 30, pp. 3554-3559, 2009.

[43] M. Song and Y. H. He, "Effects of die-pressing pressure and extrusion on the microstructures and mechanical properties of SiC reinforced pure aluminum composites," *Materials & Design*, vol. 31, pp. 985-989, 2010.

[44] C. Sun, M. Song, Z. W. Wang, and Y. H. He, "Effect of particle size on the microstructures and mechanical properties of SiC-reinforced pure aluminum composites," *Journal of Materials Engineering and Performance*, vol. 20, pp. 1606-1612, 2011.

[45] Y. Yang, J. Lan, and X. C. Li, "Study on bulk aluminum matrix nano-composite fabricated by ultrasonic dispersion of nano-sized SiC particles in molten aluminum alloy," *Materials Science and Engineering A*, vol. 380, pp. 378-383, 2004.

[46] Y. Wu and E. J. Lavernia, "Strengthening behavior of particulate reinforced MMCs," *Scripta Metallurgica Et Materialia*, vol. 27, pp. 173-178, 1992.

[47] R. J. Arsenault and R. M. Fisher, "Microstructure of fiber and particulate SiC in 6061Al composites," *Scripta Metallurgica*, vol. 17, pp. 67-71, 1983.

[48] R. J. Arsenault and N. Shi, "Dislocation generation due to differences between the coefficients of thermal expansion," *Materials Science and Engineering*, vol. 81, pp. 175-187, 1986.

[49] A. Slipenyuk, V. Kuprin, Y. Milman, V. Goncharuk, and J. Eckert, "Properties of P/M processed particle reinforced metal matrix composites specified by reinforcement concentration and matrix-to-reinforcement particle size ratio," *Acta Materialia*, vol. 54, pp. 157-166, 2006.

[50] Z. W. Wang, M. Song, C. Sun, D. H. Xiao, and Y. H. He, "Effect of extrusion and particle volume fraction on the mechanical properties of SiC reinforced Al-Cu alloy composites," *Materials Science and Engineering A*, vol. 527, pp. 6537-6542, 2010.

[51] Z. Y. Liu, Q. Z. Wang, B. L. Xiao, and Z. Y. Ma, "Clustering model on the tensile strength of PM processed SiCp/Al composites," *Composites Part a-Applied Science and Manufacturing,* vol. 41, pp. 1686-1692, 2010.

[52] N. Chawla and Y. L. Shen, "Mechanical behavior of particle reinforced metal matrix composites," *Advanced Engineering Materials,* vol. 3, pp. 357-370, 2001.

[53] S. Pal, K. K. Ray, and R. Mitra, "Room temperature mechanical properties and tensile creep behavior of powder metallurgy processed and hot rolled Al and Al-SiCp composites," *Materials Science and Engineering A,* vol. 527, pp. 6831-6837, 2010.

[54] R. Rahmani Fard and F. Akhlaghi, "Effect of extrusion temperature on the microstructure and porosity of A356-SiCp composites," *Journal of Materials Processing Technology,* vol. 187-188, pp. 433-436, 2007.

[55] U. Cocen and K. Onel, "Ductility and strength of extruded SiCp/aluminium-alloy composites," *Composites Science and Technology,* vol. 62, pp. 275-282, 2002.

[56] L. M. Tham, M. Gupta, and L. Cheng, "Effect of reinforcement volume fraction on the evolution of reinforcement size during the extrusion of Al-SiC composites," *Materials Science and Engineering A,* vol. 326, pp. 355-363, 2002.

[57] C. Sun, R. J. Shen, and M. Song, "Effects of sintering and extrusion on the microstructures and mechanical properties of a SiC/Al-Cu composite," *Journal of Materials Engineering and Performance,* vol. 21, pp. 373-381, 2012.

[58] J. C. Lee and K. N. Subramanian, "Effect of cold-rolling on the tensile properties of $(Al_2O_3)_P$/Al composites," *Materials Science and Engineering A,* vol. 159, pp. 43-50, 1992.

[59] S. Amirkhanlou, M. R. Rezaei, B. Niroumand, and M. R. Toroghinejad, "High-strength and highly-uniform composites produced by compocasting and cold rolling processes," *Materials & Design,* vol. 32, pp. 2085-2090, 2011.

[60] W. F. Hosford, *Mechanical behavior of materials*. Cambridge: Cambridge University Press, 2005.

[61] S. Mula, P. Padhi, S. C. Panigrahi, S. K. Pabi, and S. Ghosh, "On structure and mechanical properties of ultrasonically cast Al-2%Al_2O_3 nanocomposite," *Materials Research Bulletin,* vol. 44, pp. 1154-1160, 2009.

[62] F. Tang, A. Hagiwara, and J. A. Schoenung, "Microstructure and tensile properties of bulk nanostructured Al-5083/SiCp composites prepared by cryomilling," *Materials Science and Engineering A,* vol. 407, pp. 306-314, 2005.

[63] H. Ferkel and B. L. Mordike, "Magnesium strengthened by SiC nanoparticles," *Materials Science and Engineering A,* vol. 298, pp. 193-199, 2001.

[64] D. Y. Ying and D. L. Zhang, "Processing of Cu-Al_2O_3 metal matrix nanocomposite materials by using high energy ball milling," *Materials Science and Engineering A*, vol. 286, pp. 152-156, 2000.

[65] H. Ferkel, "Properties of copper reinforced by laser-generated Al_2O_3-nanoparticles," *Nanostructured Materials*, vol. 11, pp. 595-602, 1999.

[66] F. Tang, M. Hagiwara, and J. M. Schoenung, "Formation of coarse-grained inter-particle regions during hot isostatic pressing of nanocrystalline powder," *Scripta Materialia*, vol. 53, pp. 619-624, 2005.

[67] J. Naser, W. Riehemann, and H. Ferkel, "Dispersion hardening of metals by nanoscaled ceramic powders," *Materials Science and Engineering A*, vol. 234, pp. 467-469, 1997.

[68] Z. R. Hesabi, A. Simchi, and S. M. S. Reihani, "Structural evolution during mechanical milling of nanometric and micrometric $A1_2O_3$ reinforced A1 matrix composites," *Materials Science and Engineering A*, vol. 428, pp. 159-168, 2006.

[69] B. Xiong, Z. Xu, Q. Yan, B. Lu, and C. Cai, "Effects of SiC volume fraction and aluminum particulate size on interfacial reactions in SiC nanoparticulate reinforced aluminum matrix composites," *Journal of Alloys and Compounds*, vol. 509, pp. 1187-1191, 2011.

[70] B. W. Xiong, Z. F. Xu, Q. S. Yan, C. C. Cai, Y. H. Zheng, and B. P. Lu, "Fabrication of SiC nanoparticulates reinforced Al matrix composites by combining pressureless infiltration with ball-milling and cold-pressing technology," *Journal of Alloys and Compounds*, vol. 497, pp. L1-L4, 2010.

[71] Z. L. Shi, J. M. Yang, J. C. Lee, D. Zhang, H. I. Lee, and R. J. Wu, "The interfacial characterization of oxidized SiC(p)/2014 Al composites," *Materials Science and Engineering A*, vol. 303, pp. 46-53, 2001.

[72] A. Azushima, R. Kopp, A. Korhonen, D. Y. Yang, F. Micari, G. D. Lahoti, *et al.*, "Severe plastic deformation (SPD) processes for metals," *Cirp Annals-Manufacturing Technology*, vol. 57, pp. 716-735, 2008.

[73] N. Haghdadi, A. Zarei-Hanzaki, and D. Abou-Ras, "Microstructure and mechanical properties of commercially pure aluminum processed by accumulative back extrusion," *Materials Science and Engineering A*, vol. 584, pp. 73-81, 2013.

[74] Ø. Ryen, "Work hardening and mechanical anisotropy of aluminium sheets and profiles," Norwegian University of Science and Technology, 2003.

[75] J. G. Sevillano, P. Vanhoutte, and E. Aernoudt, "Large strain work-hardening and textures," *Progress in Materials Science*, vol. 25, pp. 69-412, 1980.

[76] H. Jazaeri and F. J. Humphreys, "The transition from discontinuous to continuous recrystallization in some aluminium alloys I - the deformed state," *Acta Materialia*, vol. 52, pp. 3239-3250, 2004.

[77] U. F. Kocks, C. N. Tomé, and H.-R. Wenk, *Texture and anisotropy : preferred orientations in polycrystals and their effect on materials properties*. New York ; Cambridge: Cambridge University Press, 1998.

[78] (15-08-2013). Available: http://www.doitpoms.ac.uk/tlplib/crystallographic_texture/texture_representation.php

[79] V. Randle and O. Engler, *Introduction to texture analysis : macrotexture, microtexture and orientation mapping*. Amsterdam: Gordon & Breach;, 2000.

[80] (17-08-2013). Available: http://aluminium.matter.org.uk/content/html/eng/default.asp?catid=100&pageid=10740872

[81] H. J. Bunge, *Texture analysis in materials science : mathematical methods,* English ed. London ; Boston: Butterworths, 1982.

[82] (10-05-2014). Available: http://aluminium.matter.org.uk/content/html/eng/default.asp?catid=100&pageid=1050588871

[83] F. J. Humphreys and M. Hatherly, *Recrystallization and related annealing phenomena*. Oxford: Pergamon, 1995.

[84] J. Hirsch and K. Lucke, "Mechanism of deformation and development of rolling textures in polycrystalline fcc metals .1. Description of rolling texture development in homogeneous CuZn alloys," *Acta Metallurgica*, vol. 36, pp. 2863-2882, 1988.

[85] J. Hirsch and K. Lucke, "Mechanism of deformation and development of rolling textures in polycrystalline fcc metals .2. Simulation and interpretation of experiments on the basis of taylor-type theories," *Acta Metallurgica,* vol. 36, pp. 2883-2904, 1988.

[86] J. Hirsch, K. Lucke, and M. Hatherly, "Mechanism of deformation and development of rolling textures in polycrystalline fcc metals .3. The influence of slip inhomogeneities and twinning," *Acta Metallurgica,* vol. 36, pp. 2905-2927, 1988.

[87] Y. Zhou, L. S. Toth, and K. W. Neale, "On the stability of the ideal orientations of rolling textures for fcc polycrystals," *Acta Metallurgica Et Materialia,* vol. 40, pp. 3179-3193, 1992.

[88] J. R. Hirsch, "Correlation of deformation texture and microstructure," *Materials Science and Technology,* vol. 6, pp. 1048-1057, 1990.

[89] G. Wasserma, "Deformation mechanism and properties of 2 phase composite wires," *Zeitschrift Fur Metallkunde,* vol. 64, pp. 844-848, 1973.

[90] J. Bevk, J. P. Harbison, and J. L. Bell, "Anomalous increase in strength of in situ formed Cu-Nb multifilamentary composites," *Journal of Applied Physics,* vol. 49, pp. 6031-6038, 1978.

[91] J. J. Petrovic and A. K. Vasudevan, "Rolling deformation of 2-ductile-phase Ag-Ni alloys," *Materials Science and Engineering,* vol. 34, pp. 39-51, 1978.

[92] W. A. Spitzig, A. R. Pelton, and F. C. Laabs, "Characterization of the strength and microstructure of heavily cold-worked Cu-Nb composites," *Acta Metallurgica,* vol. 35, pp. 2427-2442, 1987.

[93] W. A. Spitzig, C. L. Trybus, and F. C. Laabs, "Structure properties of heavily cold-drawn niobium," *Materials Science and Engineering A,* vol. 145, pp. 179-187, 1991.

[94] P. D. Funkenbusch, T. H. Courtney, and D. G. Kubisch, "Fabricability of an microstructural development in cold-worked metal matrix composites," *Scripta Metallurgica,* vol. 18, pp. 1099-1104, 1984.

[95] S. I. Hong, M. A. Hill, Y. Sakai, J. T. Wood, and J. D. Embury, "On the stability of cold drawn, 2-phase wires," *Acta Metallurgica Et Materialia,* vol. 43, pp. 3313-3323, 1995.

[96] S. I. Hong and M. A. Hill, "Microstructural stability of Cu-Nb microcomposite wires fabricated by the bundling and drawing process," *Materials Science and Engineering A,* vol. 281, pp. 189-197, 2000.

[97] D. G. Morris and M. A. Muñoz-Morris, "New model for strengthening by dislocation nucleation in nanoscale in situ composite microwires," *Scripta Materialia,* vol. 59, pp. 838-841, 2008.

[98] D. G. Morris and M. A. Muñoz-Morris, "The effectiveness of Equal Channel Angular Pressing and rod rolling for refining microstructures and obtaining high strength in a Cu-Fe composite," *Materials Science and Engineering A,* vol. 528, pp. 6293-6302, 2011.

[99] A. Kelly, "Processing of bulk hierarchical metal-metal composites," Doctor of Philosophy, University of Oxford, 2011.

[100] W. J. Głuchowski, Z. M. Rdzawski, J. P. Stobrawa, and K. J. Marszowski, "Microstructure and properties of Cu-Nb wire composites," *Archives of Metallurgy and Materials,* vol. 59, pp. 35-40, 2014.

[101] L. Q. Chen and N. Kanetake, "Fabrication and mechanical behavior of powder metallurgy processed in situ Nb/Al sheet metal-metal composites," *Materials Science and Engineering A,* vol. 367, pp. 295-300, 2004.

[102] J. D. Verhoeven, F. A. Schmidt, E. D. Gibson, and W. A. Spitzig, "Copper-refractory metal-alloys," *Journal of Metals,* vol. 38, pp. 20-24, 1986.

[103] Y. Jin, K. Adachi, T. Takeuchi, and H. G. Suzuki, "Microstructural evolution of a heavily cold-rolled Cu-Cr in situ metal matrix composite," *Materials Science and Engineering A,* vol. 212, pp. 149-156, 1996.

[104] J. Q. Deng, X. Q. Zhang, S. Z. Shang, Z. X. Zhao, and Y. F. Ye, "Structural evolution characteristics of Cu-10Cr-0.4Zr in-situ composites," *Cailiao Gongcheng/Journal of Materials Engineering,* pp. 59-62+68, 2010.

[105] J. Deng, X. Zhang, S. Shuzhen, Z. Zhao, and Y. Ye, "Microstructural evolution and mechanical properties of Cu-10Cr-0.4Zr filamentary in-situ composites," *International Journal of Materials Research,* vol. 102, pp. 54-58, 2011.

[106] K. Xu, A. M. Russell, L. S. Chumbley, and F. C. Laabs, "A deformation processed Al-20%Sn in-situ composite," *Scripta Materialia,* vol. 44, pp. 935-940, 2001.

[107] A. M. Russell, T. Lund, L. S. Chumbley, F. A. Laabs, L. L. Keehner, and J. L. Harringa, "A high-strength, high-conductivity Al-Ti deformation processed metal metal matrix composite," *Composites Part a-Applied Science and Manufacturing,* vol. 30, pp. 239-247, 1999.

[108] A. J. Kelly, J. Mi, G. V. Sinha, P. Krug, F. Crosa, F. Audebert, *et al.*, "An Al-Si-Ti hierarchical metal-metal composite manufactured by co-spray forming," *Journal of Materials Processing Technology,* vol. 211, pp. 2045-2049, 2011.

[109] K. Han, J. D. Embury, J. R. Sims, L. J. Campbell, H. J. Schneider-Muntau, V. I. Pantsyrnyi, *et al.*, "The fabrication, properties and microstructure of Cu-Ag and Cu-Nb composite conductors," *Materials Science and Engineering A,* vol. 267, pp. 99-114, 1999.

[110] J. J. Petrovic and A. K. Vasudevan, "Softening behavior of 2-ductile-phase Ag-Ni Alloys after cold rolling," *Materials Science and Engineering,* vol. 34, pp. 53-59, 1978.

[111] G. Frommeyer and G. Wassermann, "Microstructure and anomalous mechanical-properties of in situ-produced silver-copper composite wires," *Acta Metallurgica,* vol. 23, pp. 1353-1360, 1975.

[112] G. L. Xie, Q. S. Wang, Q. M. Guo, X. J. Mi, and B. Q. Xiong, "The characteristic of microstructures and mechanical properties of a Cu-Ag in-situ composite material," *Advanced Materials Research,* vol. 915-916, ed, 2014, pp. 654-659.

[113] J. B. Liu, L. Zhang, D. W. Yao, and L. Meng, "Microstructure evolution of Cu/Ag interface in the Cu-6 wt.% Ag filamentary nanocomposite," *Acta Materialia,* vol. 59, pp. 1191-1197, 2011.

[114] (14-05-2014). Available: http://en.wikipedia.org/wiki/Rule_of_mixtures

[115] W. A. Spitzig and P. D. Krotz, "A comparison of the strength and microstructure of heavily cold-worked Cu-20-percent Nb composites formed by different melting procedures," *Scripta Metallurgica*, vol. 21, pp. 1143-1146, 1987.

[116] I. J. Beyerlein, N. A. Mara, J. S. Carpenter, T. Nizolek, W. M. Mook, T. A. Wynn, *et al.*, "Interface-driven microstructure development and ultra high strength of bulk nanostructured Cu-Nb multilayers fabricated by severe plastic deformation," *Journal of Materials Research*, vol. 28, pp. 1799-1812, 2013.

[117] E. H. Ekiz, T. G. Lach, R. S. Averback, N. A. Mara, I. J. Beyerlein, M. Pouryazdan, *et al.*, "Microstructural evolution of nanolayered Cu–Nb composites subjected to high-pressure torsion," *Acta Materialia*, vol. 72, pp. 178-191, 2014.

[118] K. Xu and A. M. Russell, "Texture-strength relationships in a deformation processed Al-Sn metal-metal composite," *Materials Science and Engineering A*, vol. 373, pp. 99-106, 2004.

3. Experimental Details

This chapter describes the fabrication procedures of the composite materials, the characterization techniques and the mechanical property tests used to investigate the produced samples.

Three different types of reinforcements, nano-sized SiC particles, micro-sized $Al_{93}Fe_3Cr_2Ti_2$ quasicrystalline alloy particles and micro-sized Nb particles were added into the pure Al or 6061Al alloy matrix by powder metallurgy routes followed by different secondary processing procedures including extrusion and cold rolling.

The effect of the reinforcement type, size, volume fraction, heat treatment conditions and secondary processing techniques on the microstructure of the Al alloy based composites was investigated by different characterization techniques and their mechanical properties were also tested.

3.1 Billet production

3.1.1 Production of 6061Al/SiC billets

6061Al alloy matrix composites reinforced with 10wt.% and 15wt.% of SiC nanoparticles with an average diameter of ~500nm were received from the former Aerospace Metal Composites Ltd (AMC) in the form of billets. The billets were fabricated by high energy ball milling followed by solid state compaction and HIPing. According to the density of 6061Al alloy [1] and SiC particles [2], 10wt.% and 15wt.% of SiC nanoparticles equal to reinforcement volume fractions of 8.5vol.% and 12.9vol.%, respectively.

3.1.2 Production of 6061Al/$Al_{93}Fe_3Cr_2Ti_2$ billets

3.1.2.1 Sieving of $Al_{93}Fe_3Cr_2Ti_2$ powders

The gas atomised $Al_{93}Fe_3Cr_2Ti_2$ powders were received from industrial collaborator, Alpoco. Most of the atomised powders were in the range of 0-100μm in diameter. A stack of Retsch sieves was placed onto a Retsch AS200 automatic sieve shaker (Figure 3.1) to divide the powder particles into size fractions of >75μm, 75-50μm, 50-25μm and <25μm. Approximately 30ml atomised powders were sieved at a time for 7min. Only the $Al_{93}Fe_3Cr_2Ti_2$ powders with a size of <25μm were used to produce the composite billets.

Figure 3.1: Retsch AS200 automatic sieve shaker.

3.1.2.2 Mixing

Gas atomised 6061Al alloy powders with an average diameter of 10μm were received from industrial collaborator, Alpoco. The as-received 6061Al alloy powders were mixed with 8.5vol.% and 12.9vol.% sieved $Al_{93}Fe_3Cr_2Ti_2$ powders (<25μm) in a Turbula type T2F automatic mixer (Figure 3.2) for 2 hours.

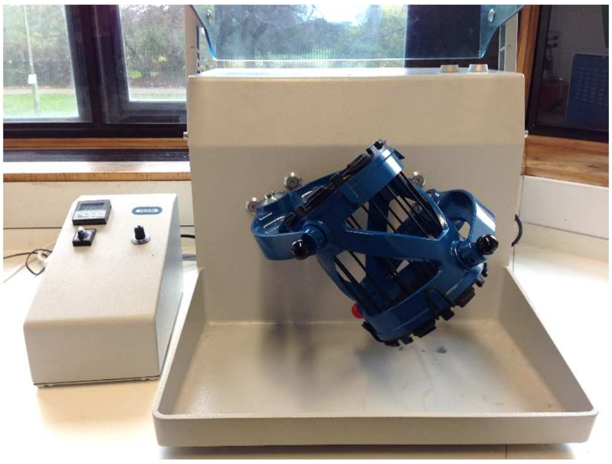

Figure 3.2: Turbula type T2F automatic mixer.

3.1.2.3 Compaction

Cold compaction of the mixed 6061Al/$Al_{93}Fe_3Cr_2Ti_2$ powders was carried out before extrusion for preliminary consolidation. About 60g of the mixed powders were loaded into a 23S steel die followed with a silver steel ram lubricated with boron nitride or molybdenum disulfide (MoS_2) and then compacted using a 100 tonne ‘Stenhoj Flex 100’ press at Oxford. A load of 50 tonne was applied onto the ram for ~2min to produce consolidated billets with a diameter of 30mm and a length of 30mm.

3.1.3 Production of Al/Nb and 6061Al/Nb billets

3.1.3.1 Mixing and Compaction

Gas atomised pure Al powders (99.7% purity) with an average diameter of 4μm and 6061Al alloy powders with an average diameter of 10μm were received from industrial collaborator, Alpoco. Pure Nb powders were received from Companhia Brasileira de Metalurgia e Mineração (CBMM) Company. Pure Al and 6061Al alloy powders were mixed with 12.9vol.% Nb powders in a Turbula type T2F automatic mixer for 2 hours. The same compaction procedures described in session 3.1.2.3 were carried out on the mixed Al/Nb and 6061Al/Nb powders. For comparison purposes, pure Al billets and 6061Al alloy billets were also compacted in the same way with a load of 35 tonne. The detailed information on both the as-received and compacted billets is listed in Table 3.1.

Sample billet	**Matrix**	**Reinforcement**	**Reinforcement size**	**Reinforcement volume fraction (%)**
6061Al/SiC	6061Al	SiC	~500nm	8.5
	6061Al	SiC	~500nm	12.9
6061Al/ $Al_{93}Fe_3Cr_2Ti_2$	6061Al	$Al_{93}Fe_3Cr_2Ti_2$	<25μm	8.5
	6061Al	$Al_{93}Fe_3Cr_2Ti_2$	<25μm	12.9
Al/Nb or 6061Al/Nb	Pure Al	Nb	130±57μm	12.9
	6061Al	Nb	130±57μm	12.9
Pure Al	Pure Al	-	-	-
6061Al alloy	6061Al	-	-	-

Table 3.1: Detailed information on as-received and compacted billets.

3.2 Secondary processing

3.2.1 Extrusion into bars

Extrusion is a very effective secondary processing technique to improve the density and mechanical properties of MMCs. The as-received and compacted billets were extruded into bars with a diameter of 7.5mm by a Fogg and Young extruder at Oxford (Figure 3.3). Before extrusion, a thermocouple was inserted into the small hole that was drilled in one end of the billets to measure the extrusion temperature. The billets were heated to 375°C or 450°C in about 15min and then soaked for another 20min. Extrusions were performed at a speed of 8mm/s with an extrusion ratio of 16:1 which gave a true strain of 2.8 ($\varepsilon = \ln(\frac{A_{initial}}{A_{final}})$). The detailed extrusion conditions are summarized in Table 3.2.

Figure 3.3: Fogg and Young extruder at Oxford.

Materials	Extrusion Temperature	Extrusion ratio	Extrusion dimension
6061Al/SiC	450°C	16:1	Bars with a diameter of 7.5mm
6061Al/$Al_{93}Fe_3Cr_2Ti_2$	375°C	16:1	
6061Al/Nb	375°C	16:1	
6061Al alloy	450°C	16:1	

Table 3.2: Extrusion conditions for bars.

3.2.2 Extrusion into strips

Some of the as-received and compacted billets were extruded into strips for the sake of cold rolling purposes by the same extruder. The billets were heated to 375°C in about 15min and then soaked for another 20min. Extrusions were performed at a speed of 8mm/s with an extrusion ratio of 6:1 which gave a true strain of 1.8. Table 3.3 summarizes the extrusion conditions for strips.

Materials	**Extrusion temperature**	**Extrusion ratio**	**Extrusion dimension**
6061Al/SiC	375°C	6:1	Strips with a thickness of 6mm and a width of 20mm
6061Al/$Al_{93}Fe_3Cr_2Ti_2$	375°C	6:1	
Al/Nb	375°C	6:1	
6061Al/Nb	375°C	6:1	
Pure Al	375°C	6:1	
6061Al alloy	375°C	6:1	

Table 3.3: Extrusion conditions for strips.

3.2.3 Heat treatment

Heat treatment was applied to the as-extruded samples to achieve improved mechanical properties. For as-extruded bars, the 6061Al alloy and 6061Al/SiC composite samples were solution heat treated at 525°C for 1h followed by water quenching and then artificial aged at 165°C for 8h followed by air cool. A thermocouple was put in the furnace to make sure of the correct temperature. Composites normally have different aging behaviors compared with monolithic alloys. It is generally reported that the composites have accelerated aging kinetics in the matrix due to the increased dislocation density as a result of the additions of the reinforcement particles providing suitable sites for heterogeneous nucleation of precipitates and acting as diffusion paths of the alloying elements [3, 4]. However, for 6061Al alloy based composites, alloying elements, such as Mg, have a tendency to segregate at the interfacial areas and the composites can lose age hardenability due to a depletion of Mg or Si in the matrix [5]. The above aging conditions (165°C for 8h) were chosen as similar conditions were used in the literature for 6061Al/SiC_p or

6061Al/$(Al_2O_3)_p$ composites [6-9]. Since the thesis is only focusing on the effect of aging heat treatment on the mechanical properties of 6061Al alloy and 6061Al/SiC composites, rather than the effect of SiC additions on the aging response, same aging heat treatment conditions were carried out for both the 6061Al alloy and 6061Al/SiC composites. In the following text, an “aged” will be added after the sample code if the sample has been artificially aged using the above heat treatment conditions.

For as-extruded strips, 6061Al alloy, 6061Al/SiC composites and 6061Al/Nb composites were solution heat treated at 525°C for 1h followed by water quenching. The heat treated strips were then subjected to cold rolling. In the following text, a “(SH)” will be added after the sample code if the sample has been solution heat treated after extrusion.

3.2.4 Cold rolling

Pure Al, 6061Al alloy, 6061Al/SiC, 6061Al/$Al_{93}Fe_3Cr_2Ti_2$, Al/Nb and 6061Al/Nb strips were cold rolled directly from as-extruded or solution heat treated conditions in a laboratory mill at University of Buenos Aires with a roller speed of 18HZ. Multiple cold rolling passes were carried out until a final thickness of ~1mm was achieved. A sketch of cold rolling process with sample directions is shown in Figure 3.4.

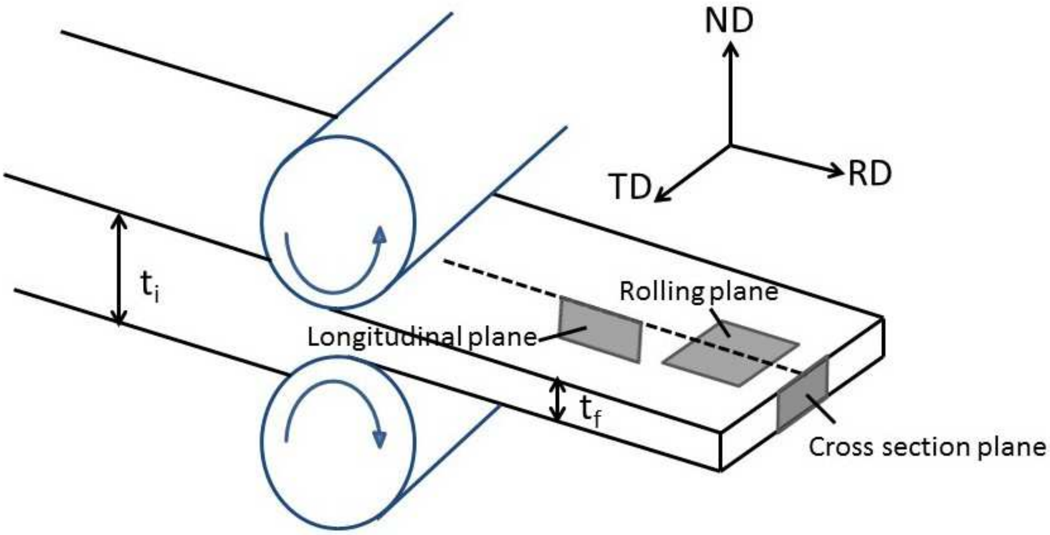

Figure 3.4: A schematic illustration of cold rolling process, t_i: initial thickness, t_f: final thickness, RD: rolling direction, ND: normal direction, TD: transverse direction. The cross section plane (ND-TD), longitudinal plane (ND-RD) and rolling plane (TD-RD) for microscopy and texture measurements are also shown.

Table 3.4 lists all the sample information, detailed thickness reductions and true strain values for every rolling pass. Thickness reductions and cold rolling strains are calculated as follows.

Thickness reductions:

$$\%reductions = \frac{t_i - t_f}{t_i} \times 100\% \tag{3.1}$$

True strain:

$$\varepsilon = ln(\frac{A_i}{Af}) \tag{3.2}$$

where t_f, t_i, A_f, A_i represents final thickness, initial thickness, final areas and initial areas, respectively [10].

Sample codes have been designated for different materials in the following text for convenience purposes and are also included in Table 3.4. In addition, to distinguish rolled samples, a true strain value will be added as a subscript after the sample code. For example, "6061Al/8.5SiC(SH)$_{2.7}$" means that the sample is 6061Al alloy reinforced with 8.5vol.% of SiC particles, the sample billets were extruded into strips, solution heat treated and then cold rolled until a true strain of 2.7, which corresponds to rolling pass 3 and a thickness reduction of 60% according to Table 3.4. “NQX” has been used as an acronym for $Al_{93}Fe_3Cr_2Ti_2$ particles. For example, “6061Al/12.9NQX$_{3.6}$” means that the sample is 6061Al alloy reinforced with 12.9vol.% of $Al_{93}Fe_3Cr_2Ti_2$ nanoquasicrystalline alloy particles and the composite is cold rolled until a true strain of 3.6, which corresponds to rolling pass 8 and a thickness reduction of 83% according to Table 3.4.

Sample code	**Materials**	**Heat treat-ment**	**Reduction info**	**As-extruded strips**	**Pass 1**	**Pass 2**	**Pass 3**	**Pass 4**	**Pass 5**	**Pass 6**	**Pass 7**	**Pass 8**	**Pass 9**
Al	Pure Al	-	Thickness reductions (%)	-	40	53	62	71	75	79	-	-	-
			True strains (ε)	1.8	2.3	2.5	2.7	3.0	3.2	3.4	-	-	-
6061Al (SH)	6061Al alloy	√	Thickness reductions (%)	-	41	50	60	70	77	82	84	-	-
			True strains (ε)	1.8	2.3	2.5	2.7	3.0	3.3	3.5	3.6	-	-
6061Al/ 8.5SiC(SH)	6061Al/ 8.5vol.%SiC	√	Thickness reductions (%)	-	40	50	60	67	71	77	-	-	-
			True strains (ε)	1.8	2.3	2.5	2.7	2.9	3.0	3.3	-	-	-
6061Al/ 12.9SiC(SH)	6061Al/ 12.9vol.%SiC	√	Thickness reductions (%)	-	16	33	45	55	65	69	72	76	78
			True strains (ε)	1.8	2.0	2.2	2.4	2.6	2.8	2.9	3.1	3.2	3.3
6061Al/ 8.5NQX	6061Al/8.5vol.% $Al_{93}Fe_3Cr_2Ti_2$	-	Thickness reductions (%)	-	43	53	64	72	78	83	-	-	-
			True strains (ε)	1.8	2.4	2.6	2.8	3.1	3.3	3.6	-	-	-
6061Al/ 12.9NQX	6061Al/12.9vol.% $Al_{93}Fe_3Cr_2Ti_2$	-	Thickness reductions (%)	-	19	35	48	59	67	74	78	83	-
			True strains (ε)	1.8	2.0	2.2	2.5	2.7	2.9	3.2	3.3	3.6	-
Al/Nb	Al/12.9vol.%Nb	-	Thickness reductions (%)	-	45	70	78	83	88	-	-	-	-
			True strains (ε)	1.8	2.4	3.0	3.3	3.6	3.8	-	-	-	-
6061Al/Nb	6061Al/ 12.9vol.%Nb	-	Thickness reductions (%)	-	43	55	64	72	78	83	-	-	-
			True strains (ε)	1.8	2.4	2.6	2.8	3.1	3.3	3.6	-	-	-
6061Al/Nb (SH)	6061Al/ 12.9vol.%Nb	√	Thickness reductions (%)	-	17	35	48	59	67	74	78	83	-
			True strains (ε)	1.8	2.0	2.2	2.5	2.7	2.9	3.2	3.3	3.6	-

Table 3.4: Sample information and detailed rolling reductions and rolling strains after every rolling pass.

3.3 Characterization techniques

Different characterization techniques including Optical Emission Spectroscopy (OES), density measurement, X-ray diffraction (XRD), Optical microscope (OM), Scanning electron microscope (SEM) and Energy dispersive X-ray (EDX), Transmission electron microscope (TEM), Texture X-ray diffraction and Electron backscatter diffraction (EBSD) were used to investigate the microstructure of the samples under different sample preparation stages.

3.3.1 Optical Emission Spectroscopy (OES)

A Spectrolab LAVFA05A spark analyzer was used to measure the chemical composition of the as-received 6061Al/SiC billets. The samples were polished with 1200 grit silicon carbide paper and eight measurements were made for each sample, the average element concentrations were subsequently calculated.

3.3.2 Density measurement

Archimedes' principle was used to measure the density of the samples with known liquids. The mass of the sample was first weighed in air as M_{sample}. Then the sample was completely submerged in the known liquid. Due to the upward buoyant force (F_b) which is in the opposite direction of the gravitational force, the mass of the sample when it was fully submerged in water was different from the mass of the sample weighed in air and was measured as M'. Thus, the density of the sample is calculated by

$$M_{sample}g = M'g + F_b \tag{3.3}$$

$$\left(M_{sample} - M'\right)g = F_b = \rho_{liquid} g V_{sample} \tag{3.4}$$

$$\rho_{sample} = \frac{M_{sample}}{V_{sample}} = \frac{M_{sample} \cdot \rho_{liquid}}{M_{sample} - M'} \tag{3.5}$$

where ρ_{sample} is the density of the sample; g is the acceleration of free fall; ρ_{liquid} is the density of known liquid, which is 1g/mL for distilled water used in present work. For sample preparation, samples were polished with 1200 grit silicon carbide paper to remove the surface layers. More than 10 measurements were carried out on each sample to ensure reproducibility.

3.3.3 Grain size estimation

The mean linear intercept method [11] was used to estimate the grain size based on the micrographs taken. For each selected micrograph, more than 10 straight lines of random orientations were drawn. The mean linear intercept grain size for each line was given by the length of each line divided by the number of whole grains intercepted. 5-10 representative micrographs were used for each sample to improve accuracy.

3.3.4 X-ray diffraction (XRD)

XRD was used to identify the phases present in the samples. It was performed using a Philips 1810 θ-2θ diffractometer with Cu-Kα radiation. The scans were all performed at a voltage of 35kV, a current of 50mA with a scanning angle 2θ between 10-100° with a step size of 0.02°. For sample preparation, bulk samples were cut into the appropriate sizes and ground using 1200 grit silicon carbide paper to ensure flat surfaces. Powder samples were mounted on glass slides with a layer of vacuum grease.

3.3.5 Optical Microscope (OM)

Optical Microscope was used to examine the general microstructure of the samples at really low magnifications. The work was carried out on a Zeiss Axiophot2 microscope with an eyepiece magnification of x10 and objective lenses of x5 and x10. The sample preparation procedure for Optical Microscope imaging is similar to the SEM sample preparation described in section 3.3.6.

3.3.6 Scanning electron microscope (SEM) and Energy dispersive X-ray (EDX)

SEM analysis was used to study the microstructure of the alloys and the composites. SEM work was carried out on a JEOL 6300 or JSM 840A microscope with tungsten filament. 20kV and 15mm were typically used for the accelerating voltage and the working distance. For higher magnification images (usually greater than x5000), a JSM 840F microscope with a field emission gun was used with an accelerating voltage of 5kV and a working distance of 15mm. EDX was carried out on a JEOL 6300 or JSM 840A microscope with an EDX detector. A working distance of 15mm and a voltage of 20kV were always used for maximum signals. For sample preparation, bulk samples were mounted in conductive Bakelite using a Kemet Metkon MetaPress. The mounted samples were first ground with 600-4000 grit silicon carbide paper. Then they were polished with 6μm, 3μm and 1μm grade diamond paste on Kemet NLH cloths (code: 341247). Finally, the samples were polished with colloidal silica with 10% hydrogen peroxide on a Kemet Chem H cloth (code: 341783). For powder samples, the powders were mounted on Al stubs with carbon adhesive tabs which can be fit into the SEM holders directly.

3.3.7 Transmission electron microscope (TEM)

TEM work was performed on a Philips CM20 or JEOL 2000FX tungsten filament microscope operating at 200kV. To prepare samples for TEM studies, thin slices of samples (~500μm) were cut using an Isomet diamond slow saw. The slices were then ground with 800-2500 grit silicon carbide paper down to a thickness of ~120μm. After that, 3mm disks were punched out of the thin slices. The disks were then polished with diamond lapping films from 9μm down to 3μm grade until the disks reached a thickness of ~80μm. Next, the disks were double-side dimpled down to a thickness of ~20μm in the centre with diamond paste from 3μm to 0.25μm grade on a Gatan Dimpler. For final thinning of the TEM samples, a Precision Ion Polishing System (PIPS) Gatan Model 691 was used. Ar+ ions polished the surface of a rotating sample at angles between 4° to 6°

at a voltage of 5kV for 1-6h until a hole appeared in the center of the sample.

3.3.8 Texture X-ray diffraction

Texture XRD was used to analyze the global crystallographic texture of the Al matrix of as-extruded and cold rolled samples in the normal plane (TD-ED/RD). The Al texture was measured on a Philips X'pert MRD system with Cu Kα radiation generated at 40kV and 40mA shown in Figure 3.5. The system consists of a four-axis goniometer which allows rotations about the θ, ω, ϕ and ψ axes. The ω, ϕ and ψ axes are shown in Figure 3.6. Texture is measured by changing the angular orientations of the sample systematically and measuring the diffraction peaks using x-ray diffraction. When measuring texture, a 2θ angle between the source and the detector is selected to satisfy the Bragg's law for a certain diffracting {h k l} plane and is kept constant during the measurement. The pole figure is then measured by rotating the specimens around ϕ axis and tilting around ψ axis during which the distribution of the normal of the {h k l} planes are recorded [10]. For a given ψ, intensity data is collected for all ϕ values from 0° to 360° with a step size of 5°. The ψ value is then increased by 5° and the process is repeated until ψ reaches its maximum, 85°.

For the pure Al, 6061Al and 6061Al reinforced with SiC and $Al_{93}Fe_3Cr_2Ti_2$ composites, four incomplete pole figures {1 1 1}, {2 0 0}, {2 2 0} and {3 1 1} [12] were measured up to a maximum tilt angle of 85^o. For the Al alloy reinforced with Nb composites, only three incomplete pole figures {2 0 0}, {2 2 0} and {3 1 1} were measured since the {1 1 1} Al peak overlaps with {1 1 0} Nb peak. Orientation distribution functions (ODFs) were then calculated from the pole figures after background and defocusing corrections by means of Mtex. Mtex is originally developed by Hielscher [13] as part of his Ph.D. thesis and is now a MATLAB toolbox that allows to solve a wide range of problems in quantitative texture analysis. It offers a novel algorithm to compute an ODF from pole figure measurements based on a discretization of the ODF space by radially symmetric functions and on the fast Fourier transform [14]. The detailed algorithms can be found in his paper [15]. ODFs were presented in plots in constant φ_2 sections with iso-intensity contours in Euler space. The volume fraction of individual texture component was calculated using the same software within a tolerance of 15º.

For sample preparation, all samples used for texture analysis were cut and polished down to the intermediate layer of the strips. The polishing procedure is similar to the SEM sample preparation described in session 3.3.6. A final polishing with colloidal silica was used to minimize the surface deformation layer due to polishing.

Figure 3.5: Philips X'Pert MRD system for texture measurement.

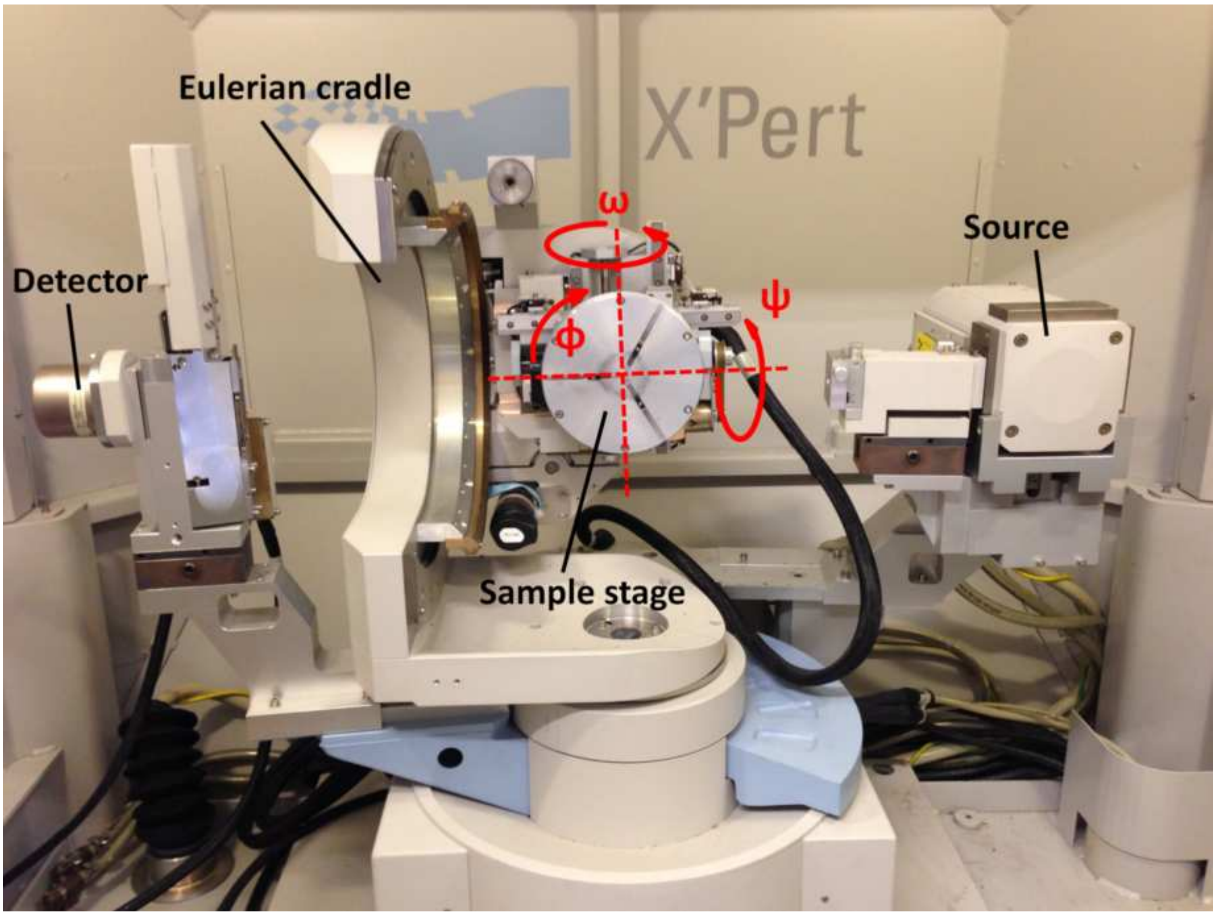

Figure 3.6: Philips X’Pert MRD system, indicating the ω, ϕ and ψ axes.

3.3.9 Electron backscatter diffraction (EBSD)

Electron Backscatter Diffraction (EBSD) technique was used to investigate the microscopic texture of as-extruded and cold rolled samples. EBSD scans were conducted at the normal plane (TD-ED/RD) of the samples by means of automated acquisition and indexing of Kikuchi patterns in a TSL system interfaced to a JEOL-6300 or JSM-840A SEM, with the samples tilted at 70º to the incident electron beam and with a scan step of 0.1-0.3μm. An accelerating voltage of 20kV and a working distance of 15~20mm were usually used for the microscope settings and a camera binning of 4 x 4 pixels was normally used.

The post-processing of the EBSD data was performed by an OIM analysis software. Inverse pole figure (IPF) maps with highlighted grain boundaries, misorientation angle distribution plots, scattered IPFs, Taylor Factor plots have been generated based on EBSD data. Since some data points were measured incorrectly, several steps have been taken to remove incorrectly indexed points and include only correctly defined grains in the analysis when processing the EBSD data. Dilation cleanup method which involves a grain tolerance angle of 5° and a minimum grain size of 3-5 data points was used to modify incorrectly indexed points at grain boundaries. For several EBSD maps, Confidence Index (CI) which is a parameter showing confidence of indexing was set with a minimum number of 0.01 so that any indexed points with a CI less than 0.01 were removed. When plotting EBSD maps with highlighted grain boundaries, boundaries with misorientation less than 2° have not been taken into consideration to remove inaccuracy [16].

EBSD sample preparation for samples with multiple phases with different mechanical and chemical properties is always quite difficult, especially for areas in the vicinity of secondary particles. Two polishing methods have been used for the EBSD analysis:

1. The samples were polished in the same way as for SEM analysis.
2. The samples were inserted in a Precision Ion Polishing System (PIPS) Gatan Model 691 after standard mechanical grinding and polishing. Ar^+ ions polished the surface of a rotating sample at very low bombardment angle (1°) at a voltage of 4kV, lowering the height difference between the matrix and secondary particles and greatly reducing the surface roughness in the matrix reinforcement interfaces [17].

One of the cold rolled $Al/Nb_{3.8}$ sample was sent to Oxford Instrument for large area EBSD analysis. EBSD measurements were carried out on a TESCAN MIRA field emission scanning electron microscope with NordlysNano EBSD detector at an acceleration voltage of 20kV by Dr. Singh Ubhi. The sample was prepared by mechanical polishing followed by ion electro-chemical polishing.

3.4 Mechanical testing

Different mechanical testing methods including microhardness, compression tests, tensile tests, load-controlled fatigue tests and three-point bending tests were conducted at room temperature to analyze the mechanical properties of the as-received, as-extruded and cold rolled samples

3.4.1 Microhardness

Microhardness is a useful method for quickly judgment of a material’s performance as it is closely related to the yield strength. The samples were prepared in the same way as for OM analysis. Microhardness tests were all carried out on a Wilson Instruments 402MVD Vickers Microhardness tester with a load of 500g or 200g with an indentation time of 20s. Measurements were carefully done on the sample so that the distance of every two indents and the distance of the indent to the edge of the sample were at least three times of the diagonal length of the indent. The two diagonal lengths of indents were measured by MinuteMan software and the software calculates the Vickers microhardness values automatically. More than 20 measurements were done for each sample to ensure reproducibility.

3.4.2 Compression tests

Compression tests were carried out in an Instron 4204 tensile testing frame with a load cell of 50kN at room temperature. Samples for compression tests were machined from the as-extruded bars down to a cylinder of a diameter of 6mm and a length of 12mm by lathe. Both ends of the lathed cylinder were polished with 4000 grit silicon carbide paper to ensure smooth and parallel surfaces. The samples were lubricated with MoS_2 grease before inserting in the compression platen to reduce friction and the likelihood of barreling. The tests were conducted at a constant strain rate of $10^{-4}s^{-1}$. Two tests were done for each sample.

3.4.3 Tensile tests

Room temperature tensile tests were carried out on an Instron 5582 tensile testing machine with a load cell of 50kN. For as-extruded bars, standard sized samples with a gauge length of 20mm and a gauge diameter of 4mm were machined according to ASTM E8M-08. For cold rolled samples, dog-bone shaped samples with a gauge length of 10mm and a gauge width of 3mm were made. The surface of the gauge sections was polished with 4000 grit silicon carbide paper to remove machine cracks and ensure a smooth surface. The tests were carried out at a constant strain rate of $10^{-4}s^{-1}$. For round bar tensile samples, an extensometer with a 10mm strain gauge was carefully attached to the sample to record the strain values. Two tests were done for each sample.

3.4.4 Load-controlled fatigue tests

Load-controlled fatigue tests were carried out on an ESH servo-hydraulic testing system controlled by $CaTs^3$ software programs at room temperatures with a load cell of 100kN. The fatigue samples were machined according to ASTM E606 with a gauge length of 12mm and a gauge diameter of 4mm. The surface of the gauge sections was carefully polished with 4000 grit silicon carbide paper to remove scratches and machining marks. All the tests were carried out at a constant cyclic frequency of 40Hz with a sinusoidal waveform. A positive mean stress was applied and the load ratio was $R=\sigma_{min}/\sigma_{max}=0.1$ (i.e. tension-tension loading).

3.4.5 Three-point bending tests

Bending test is normally required at industry to evaluate sheet formability and anisotropy of produced sheet [18]. Three-point bending tests were carried out on an Instron 3366 testing machine at a constant strain rate of $10^{-4}s^{-1}$ to compare the bending strength of as-extruded and cold rolled samples. For sample preparations, the flat bending samples were cut along the extrusion (ED) or rolling direction (RD) with a dimension of 12mm (length) × 1mm (width) × 1mm (height) and then mechanically polished on every side down to 4000 grit silicon carbide paper.

The schematic illustrations for the three-point bending tests with sample orientations are shown in Figure 3.7. Based on the Force-Displacement curves from the tests, flexural stress (σ) and flexural strain (ε) are calculated by Equations 3.6 and 3.7:

$$\sigma = (3 \cdot P \cdot L)/(2 \cdot w \cdot t^2) \tag{3.6}$$

$$\varepsilon = (6 \cdot t \cdot D)/L^2 \tag{3.7}$$

where P is the applied load at the center of the beam, L is the span length which is 10mm in the present work, w is the width of the specimen, t is the thickness of the specimen and D is the displacement of the beam at the center, respectively [18]. It should be noted that none of the specimens have fractured during the tests since the equipment limitation was reached. At least two tests were done for each sample to ensure reproducibility.

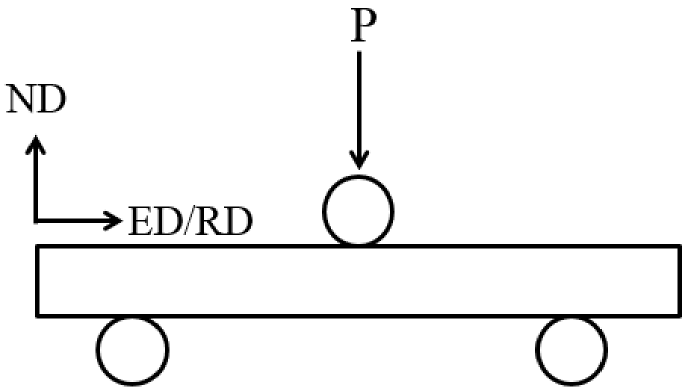

Figure 3.7: Schematic illustration for the three-point bending tests (ED: Extrusion direction; RD: Rolling direction; ND: Normal direction).

3.5 References

[1] (10-10-2013). Available: http://en.wikipedia.org/wiki/6061_aluminium_alloy

[2] (18-12-2013). Available: http://en.wikipedia.org/wiki/Silicon_carbide

[3] M. Wang, D. Chen, Z. Chen, Y. Wu, F. Wang, N. Ma, *et al.*, "Mechanical properties of in-situ TiB_2/A356 composites," *Materials Science and Engineering A*, vol. 590, pp. 246-254, 2014.

[4] S. M. R. M. Abarghouie and S. M. S. Reihani, "Aging behavior of a 2024 Al alloy-SiCp composite," *Materials & Design*, vol. 31, pp. 2368-2374, 2010.

[5] R. M. Wang, M. K. Surappa, C. H. Tao, C. Z. Li, and M. G. Yan, "Microstructure and interface structure studies of SiCp-reinforced Al (6061) metal-matrix composites," *Materials Science and Engineering A*, vol. 254, pp. 219-226, 1998.

[6] T. S. Srivatsan, M. Al-Hajri, M. Petraroli, B. Hotton, and P. C. Lam, "Influence of silicon carbide particulate reinforcement on quasi static and cyclic fatigue fracture behavior of 6061 aluminum alloy composites," *Materials Science and Engineering A*, vol. 325, pp. 202-214, 2002.

[7] B. F. Luan, N. Hansen, A. Godfrey, G. H. Wu, and Q. Liu, "High strength Al-Al_2O_{3p} composites: Optimization of extrusion parameters," *Materials & Design*, vol. 32, pp. 3810-3817, 2011.

[8] A. M. El-Sabbagh, M. Soliman, M. A. Taha, and H. Palkowski, "Effect of rolling and heat treatment on tensile behaviour of wrought Al-SiCp composites prepared by stir-casting," *Journal of Materials Processing Technology*, vol. 213, pp. 1669-1681, 2013.

[9] C. S. Shin and J. C. Huang, "Effect of temper, specimen orientation and test temperature on the tensile and fatigue properties of SiC particles reinforced PM 6061 Al alloy," *International Journal of Fatigue*, vol. 32, pp. 1573-1581, 2010.

[10] Ø. Ryen, "Work hardening and mechanical anisotropy of aluminium sheets and profiles," Norwegian University of Science and Technology, 2003.

[11] A. Lui and K. O'Reilly, "The role of grain refiner and poisoning on intermetallics selection during casting," D.Phil., University of Oxford, 2009.

[12] U. F. Kocks, C. N. Tomé, and H.-R. Wenk, *Texture and anisotropy : preferred orientations in polycrystals and their effect on materials properties*. New York ; Cambridge: Cambridge University Press, 1998.

[13] R. Hielscher, "The Radon transform on the rotation group - inversion and application in texture analysis," PhD, Geoscience Mathematics and Informatics, Freiberg University of

Mining and Technology, 2006.

[14] (08-10-2013). Available: https://code.google.com/p/mtex/

[15] R. Hielscher and H. Schaeben, "A novel pole figure inversion method: specification of the MTEX algorithm," *Journal of Applied Crystallography,* vol. 41, pp. 1024-1037, 2008.

[16] M. Alizadeh, M. H. Paydar, D. Terada, and N. Tsuji, "Effect of SiC particles on the microstructure evolution and mechanical properties of aluminum during ARB process," *Materials Science and Engineering A,* vol. 540, pp. 13-23, 2012.

[17] V. Ocelik, J. A. Vreeling, and J. T. M. De Hosson, "EBSP study of reaction zone in SiC/Al metal matrix composite prepared by laser melt injection," *Journal of Materials Science,* vol. 36, pp. 4845-4849, 2001.

[18] M. Tajally, Z. Huda, and H. H. Masjuki, "Effect of cold rolling on bending and tensile behavior of 7075 aluminum alloy," *Journal of Applied Sciences,* vol. 9, pp. 3888-3893, 2009.

4. Extruded bars of 6061Al/SiC composites

Chapter 4 studies the microstructure and mechanical properties of as-received and as-extruded 6061Al/SiC composites. For comparison purposes, as-extruded 6061Al alloy was also produced and examined. The details of the production of the bars can be found in Chapter 3.

Microstructural characterization (Section 4.1) including OES, density measurement, XRD, SEM, EDX and TEM analysis was carried out to examine the as-received, as-extruded and aging heat treated 6061Al, 6061Al/SiC samples.

Mechanical property tests (Section 4.2) including microhardness, room temperature compression and tensile tests and load-controlled fatigue tests were performed to examine the overall mechanical properties. Fractography analysis was carried out to study the fracture behaviour.

The effect of the extrusion process, aging heat treatment, additions of nano-sized SiC particles and SiC volume fractions on the microstructure and mechanical properties is discussed in Section 4.3

4.1 Microstructural characterization of 6061Al alloy and 6061Al/SiC composites

4.1.1 Chemical analysis

Optical Emission Spectroscopy (OES) was used to analyse the chemical composition of as-received 6061Al/SiC billets. EDX was carried out on as-extruded 6061Al alloy. The averaged results are listed in Table 4.1 as well as the typical composition for 6061Al alloy [1] for comparison. Other alloying elements less than 0.005wt.% and the remainder Al are not shown. It can be seen that the measured Si compositions are close to the claimed weight fractions of the as-received composite billets and the rest alloying elements are mostly within the range of the typical values for the 6061Al alloy [1].

Sample	Method	Si	Fe	Cu	Mn	Mg	Zn	Cr	Ti
6061Al/8.5SiC	OES	8.057	0.094	0.384	0.005	0.759	0.018	0.200	0.020
6061Al/12.9SiC	OES	11.667	0.092	0.374	0.005	0.707	0.018	0.187	0.021
6061Al	EDX	0.65	0.25	0.35	-	0.72	-	-	-
6061 [1]	-	0.4-0.8	Max. 0.7	0.15-0.40	Max. 0.15	0.8-1.2	Max. 0.25	0.04-0.35	Max. 0.15

Table 4.1: Average compositions (wt.%) of as-received 6061Al/8.5SiC and 6061Al/12.9SiC billets measured by OES and as-extruded 6061Al sample measured by EDX as well as the typical compositions for 6061Al alloy [1].

4.1.2 Density measurements

The bulk densities of the as-received and as-extruded samples were measured by standard Archimedes method (see section 3.3.2) and the porosity values of the samples were calculated. Table 4.2 shows the density and porosity evolution of the materials before and after extrusion. It can be seen that densities of the materials have been substantially improved after extrusion and the porosity level has reduced by ~50% for the composites.

Materials	As-received Density ($g\cdot cm^{-3}$)	As-extruded Density ($g\cdot cm^{-3}$)	Theoretical Density ($g\cdot cm^{-3}$)	Porosity (%)	
				As-received	As-extruded
6061Al	-	2.692±0.005	2.700	-	0.30±0.19
6061Al/8.5SiC	2.728±0.005	2.735±0.004	2.744	0.58±0.18	0.33±0.15
6061Al/12.9SiC	2.735±0.009	2.750±0.004	2.766	1.12±0.33	0.58±0.14

Table 4.2: Measured densities, calculated theoretical densities and porosity content of as-received and as-extruded 6061Al, 6061Al/SiC samples. Theoretical density is calculated using $2.7 g\cdot cm^{-3}$ as theoretical density for 6061Al matrix and $3.21\ g\cdot cm^{-3}$ as theoretical density for SiC reinforcements [1, 2]. Porosity content is calculated by $(\rho_{theoretical} - \rho_{measured})/\rho_{theoretical}$.

4.1.3 X-ray diffraction analysis

The diffractograms of the cross sectional planes of the as-received, as-extruded and aging heat treated samples are shown in Figure 4.1 where it can be observed the presence of the fcc-Al phase (2θ=38.2°, 44.4°,64.8°, 77.9° and 82.2° corresponding to reflections from (1 1 1), (2 0 0), (2 2 0), (3 1 1) and (2 2 2) planes, respectively), the 6H-SiC (2θ=33.8°, 35.4°, 41.2°, 54.4°, 59.7°, 65.4° and 71.5°) and the α-AlFeSi (2θ=36.6° and 42.8°) [3-5] and Mg_2Si (2θ=39.9°) intermetallics in both composite samples, with higher peak intensities for the 6H-SiC phase for the 6061Al/12.9SiC sample. No peaks of Al_4C_3 (this phase is known to embrittle the composites when present [6]) are observed suggesting that no interfacial reaction has occurred or the interfacial reaction product is below the XRD detection limit, which is about 5vol.%.

Also, it is noticeable that there are no Mg_2Si phase peaks visible that are expected after the aging heat treatment. The phase peaks might still be present but are overlapping with the broadened Al (1 1 1) peaks due to extrusion or the phase reflection is below the XRD detection limit.

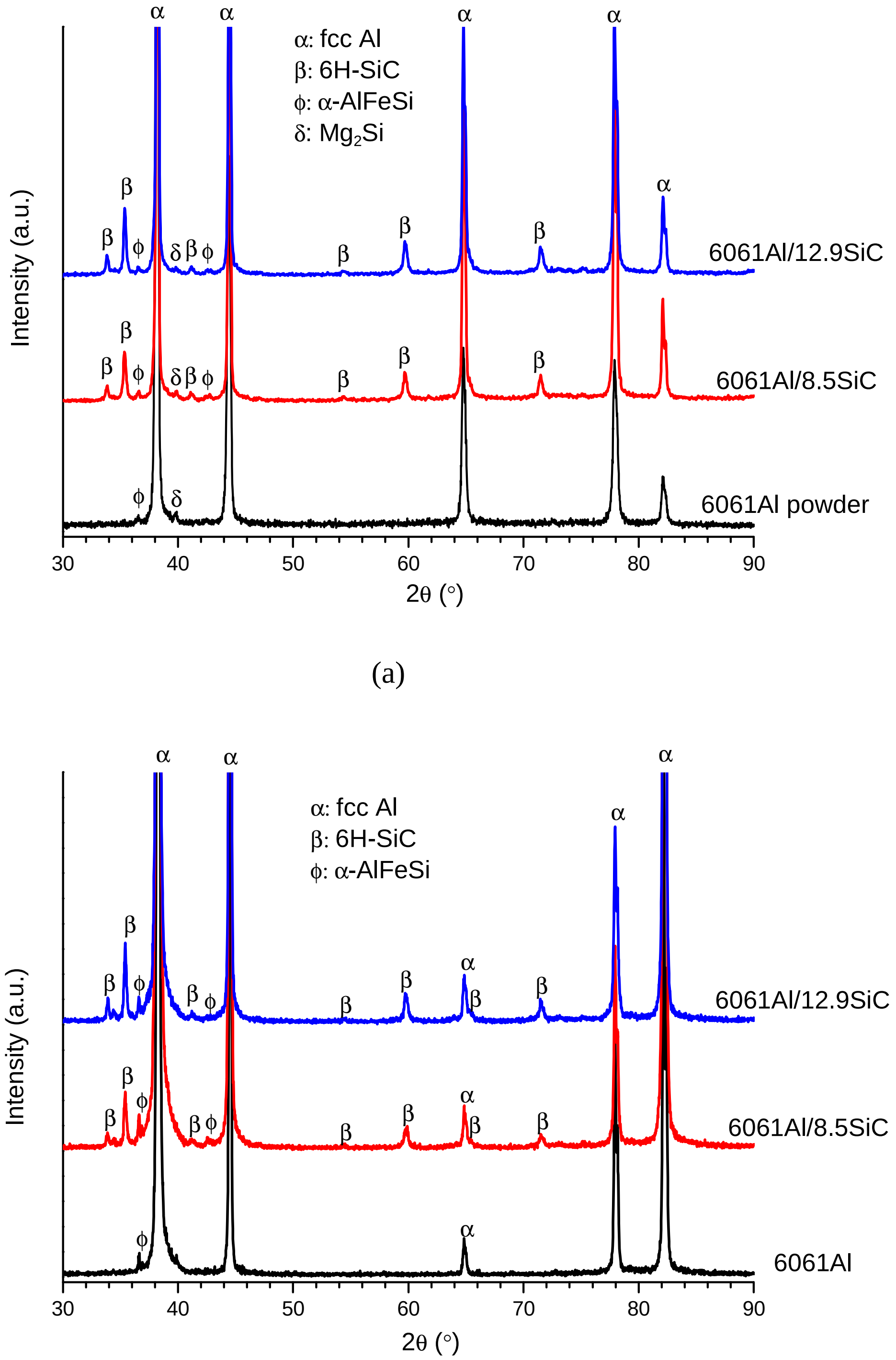

(a)

(b)

Figure 4.1: X-ray diffractograms of the cross sectional planes of 6061Al alloy, 6061Al/8.5SiC and 6061Al/12.9SiC sample in (a) as-received condition; (b) as-extruded condition and (c) aging heat treated condition.

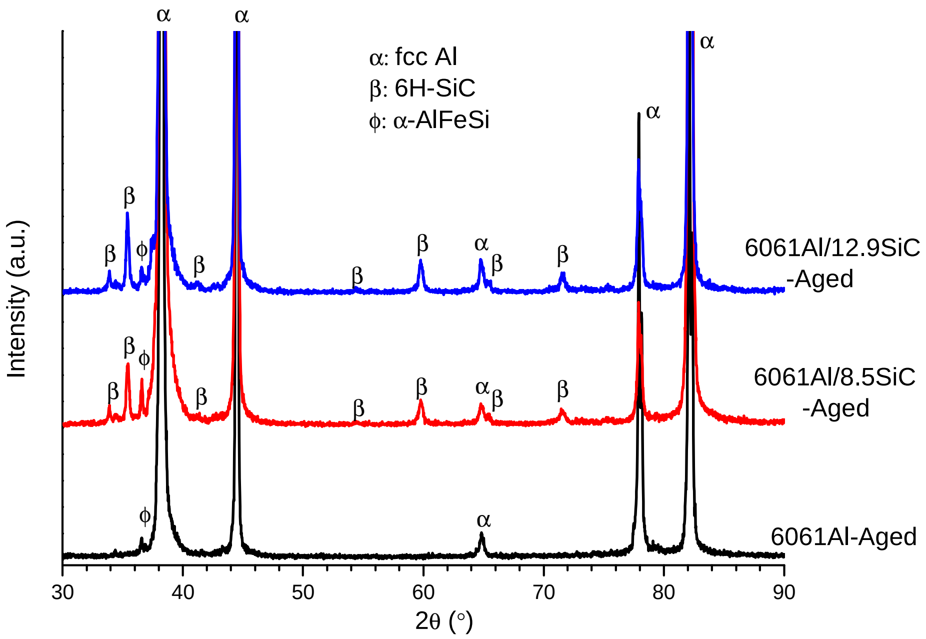

(c)

Figure 4.1: X-ray diffractograms of the cross sectional planes of 6061Al alloy, 6061Al/8.5SiC and 6061Al/12.9SiC sample in (a) as-received condition; (b) as-extruded condition and (c) aging heat treated condition.

4.1.4 Scanning electron microscopy analysis

To investigate the homogeneity of the microstructure over the as-received billets, SEM analysis was carried out on cross sectional planes and longitudinal planes of the as-received billets and the representative SEM images are displayed in Figure 4.2. It can be seen that the SiC particles are not homogeneously distributed in the as-received billets. There are some areas free of SiC particles (see black arrows). Also, a significant amount of porosity is observed (see white arrows). The porosity level has been estimated to be 0.58±0.18% for the as-received 6061Al/8.5SiC and 1.12±0.33% for the as-received 6061Al/12.9SiC sample according to Table 4.2.

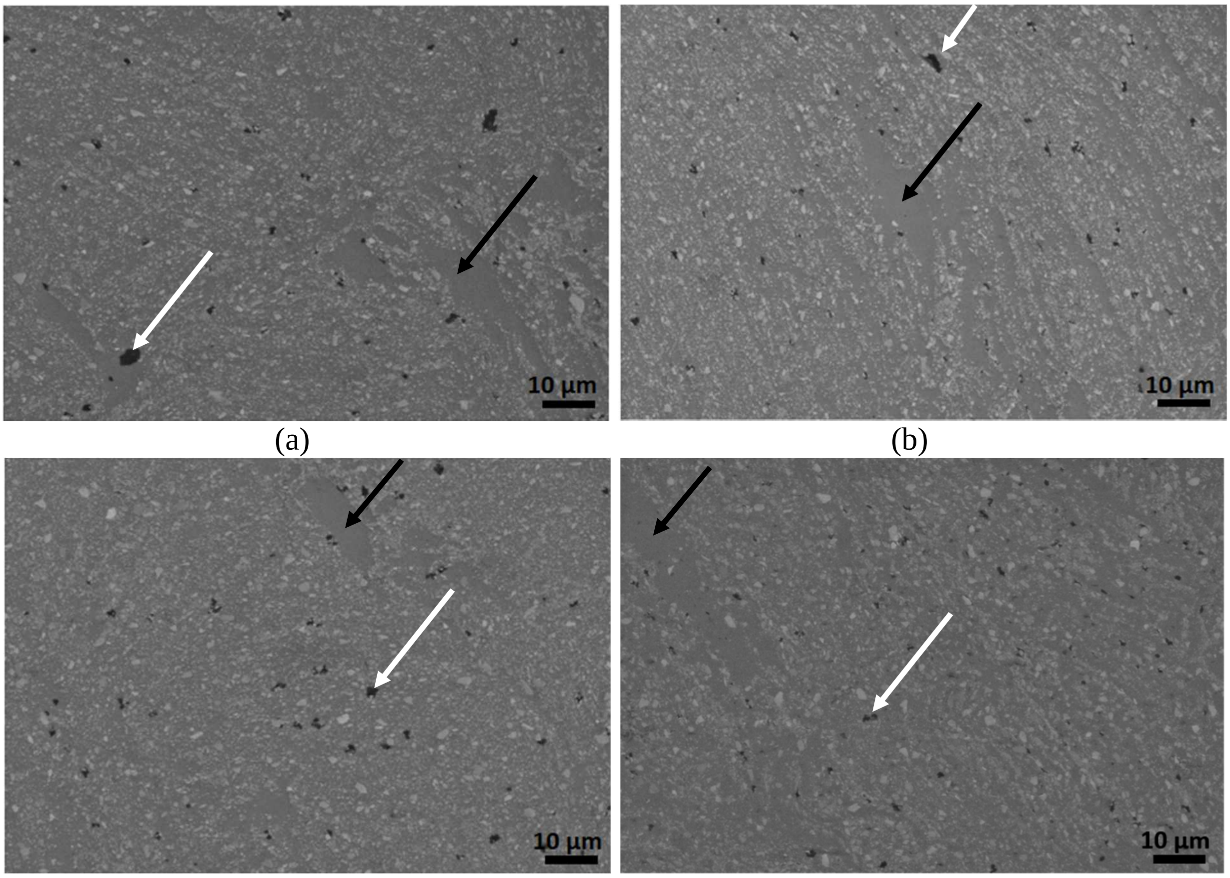

(a) (b)

(c) (d)

Figure 4.2: Secondary electron images of as-received 6061Al/8.5SiC in (a) cross sectional plane; (b) longitudinal plane and as-received 6061Al/12.9SiC in (c) cross sectional plane; (d) longitudinal plane (black arrows indicate SiC free areas; white arrows indicate porosity).

The SEM images of the as-extruded 6061Al/8.5SiC and 6061Al/12.9SiC samples in longitudinal sections are shown in Figure 4.3. Compared with as-received 6061Al/SiC samples, Figure 4.3 shows a homogeneous distribution of SiC particles. The insets are high magnification SEM images showing the uniform distribution of ~500nm sized SiC particles with no agglomerations. Careful observation of Figure 4.3 also shows that the amount of porosity in the composites has largely decreased compared with the as-received samples. According to Table 4.2, the porosity level has decreased to be 0.33±0.15% for the as-extruded 6061Al/8.5SiC and 0.58±0.14% for the as-extruded 6061Al/12.9SiC sample.

Figure 4.4 shows the SEM images of aging heat treated 6061Al/8.5SiC and 6061Al/12.9SiC samples in longitudinal sections. No obvious precipitates have been seen in the SEM images and no major difference in the microstructure has been observed.

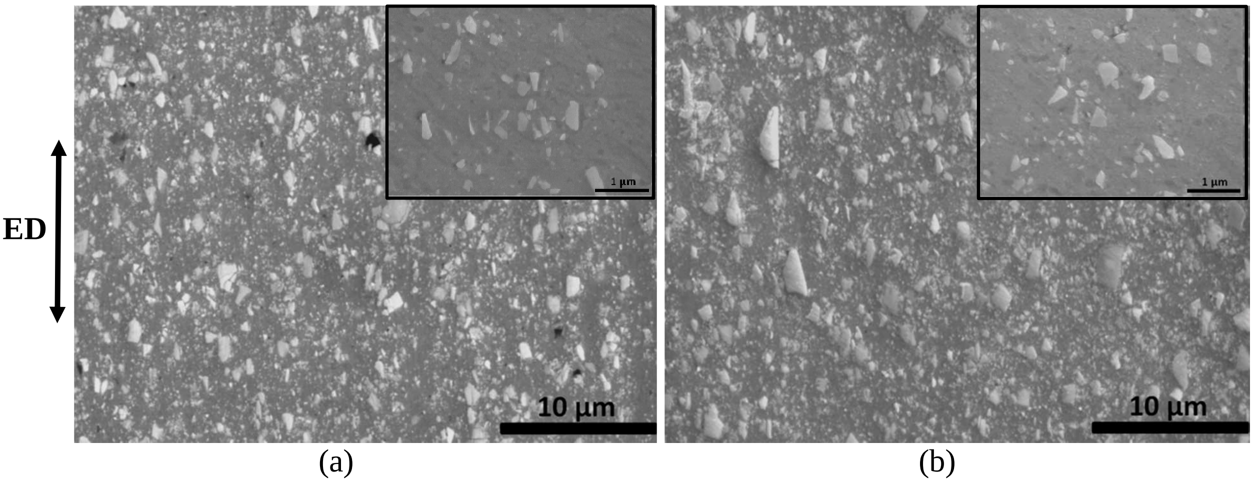

Figure 4.3: Secondary electron images of (a) as-extruded 6061Al/8.5SiC longitudinal sample and (b) as-extruded 6061Al/12.9SiC longitudinal sample. Insets are high magnification secondary electron images showing SiC particle distribution.

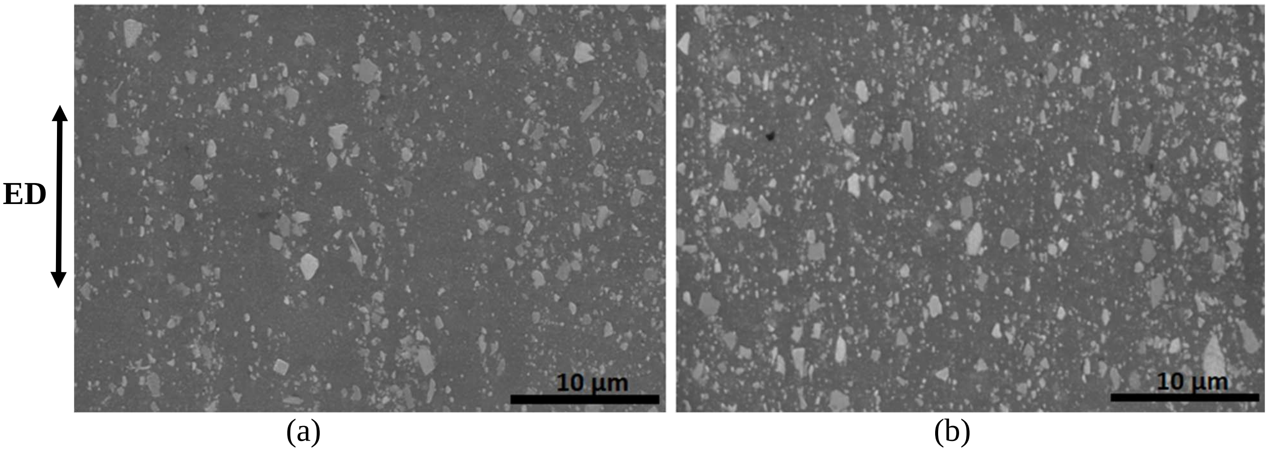

Figure 4.4: Secondary electron images of aging heat treated (a) 6061Al/8.5SiC longitudinal sample and (b) 6061Al/12.9SiC longitudinal sample.

4.1.5 Transmission electron microscopy analysis

To further investigate the microstructure of the as-extruded samples, bright field TEM images of as-extruded 6061Al alloy, 6061Al/8.5SiC and 6061Al/12.9SiC samples are shown in Figures 4.5, 4.6 and 4.7, respectively.

Figure 4.5 shows the general microstructure of 6061Al alloy. An average Al grain size of 1.2±0.2μm is estimated using the mean linear intercept method (see section 3.3.3) based on micrographs similar to Figure 4.5(a). In addition, it can be observed from Figures 4.5(b) and (c) that the 6061Al alloy in the as-extruded condition has ~100nm and 300-500nm sized precipitates within the Al grains. EDX analysis on some of the precipitates and the matrix was carried out and the results are shown in Figure 4.5(d). Compared to the matrix, the 300-500nm sized particles (particles A and B) are rich in Mg and Si and have an atomic ratio (Mg:Si) of 1.9 and 2.0, respectively, while the ~100nm sized particles (particles C and D) are likely to be AlMnFeCuSi phase, as it is shown in the EDX spectra. This phase was also reported by Wang et al. [7] in as-extruded 6061Al/SiC$_p$ composites and Shahzad et al. in 2214Al alloy [8].

The general microstructure of the composites (Figures 4.6 and 4.7) is found to be a 6061Al alloy matrix which contains an even dispersion of sub-micron particles as well as smaller precipitates. EDX analysis was carried out on the sub-micron particle E (Figure 4.6(b)) and particle F (Figure 4.7(b)) and the results are displayed in Figure 4.8 and Table 4.3, strongly suggesting that the sub-micron particles are SiC particles. It should be noted that the atomic ratio of Si:C is greater than 1 since the Carbon X-ray K line is of low energy and can be easily absorbed by the specimen [9].

During TEM analysis, most of the Al and SiC interface shows a clean interface, good bonding and no clear aluminium carbides or intermetallics have been observed at the Al matrix-SiC particle interface, agreeing with the XRD findings.

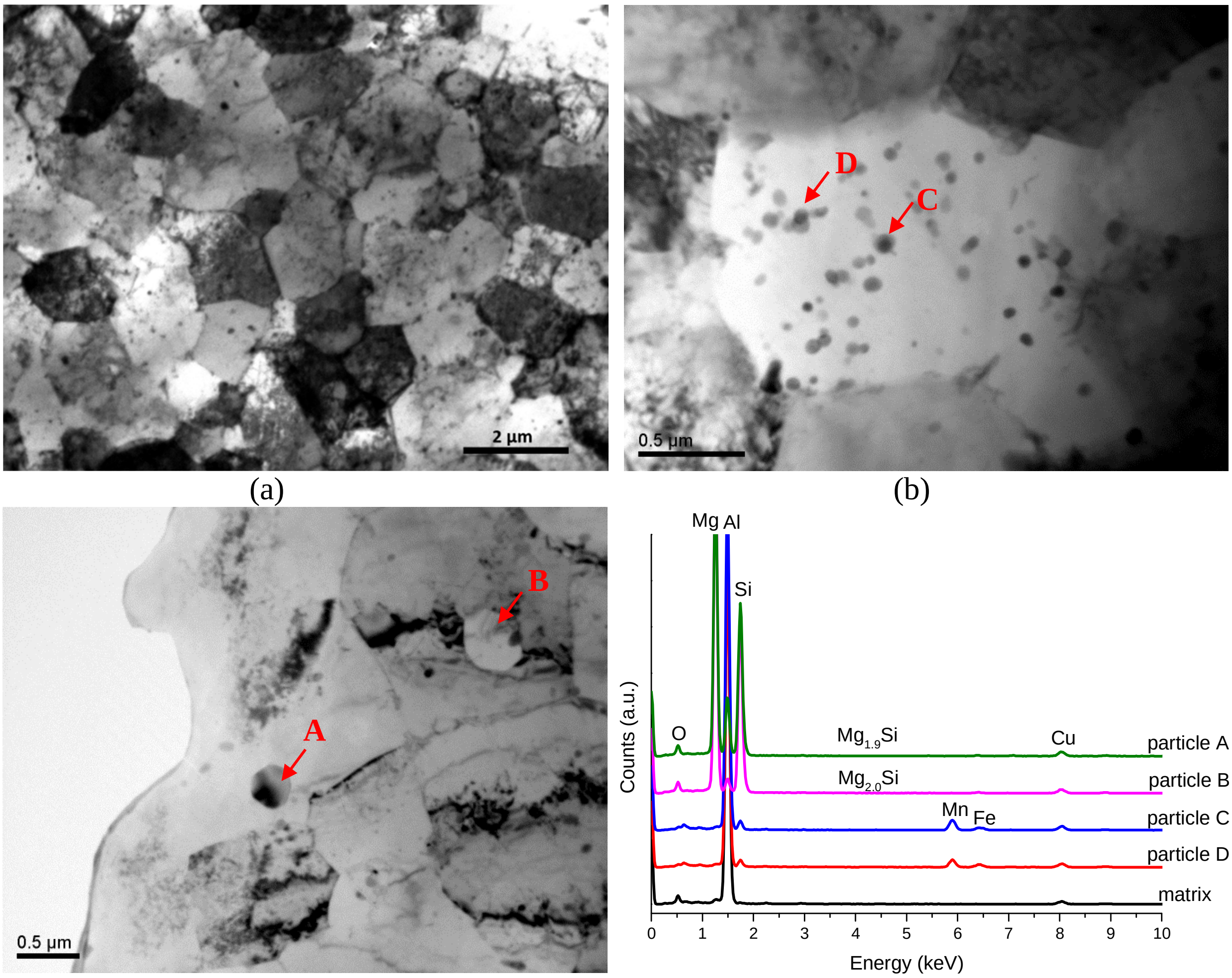

(a) (b)

(c) (d)

Figure 4.5: TEM bright field micrographs of as-extruded 6061Al alloy showing (a) general microstructure; (b), (c) precipitates within the Al grains and (d) EDX spectra for particles A, B, C and D.

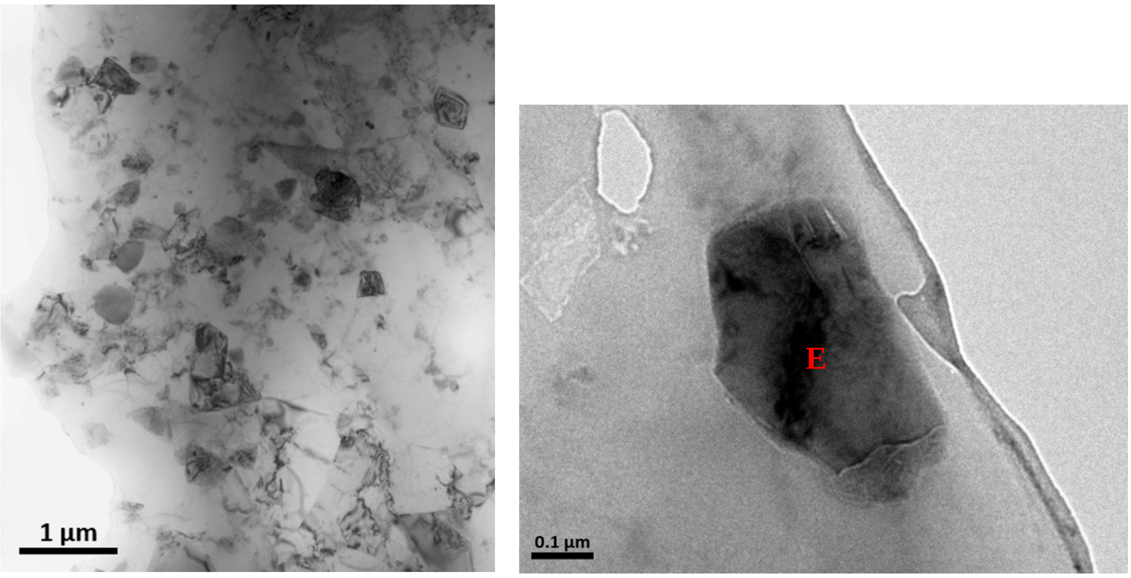

(a) (b)

Figure 4.6: TEM bright field micrographs of as-extruded 6061Al/8.5SiC sample showing (a) general microstructure and (b) SiC particle E.

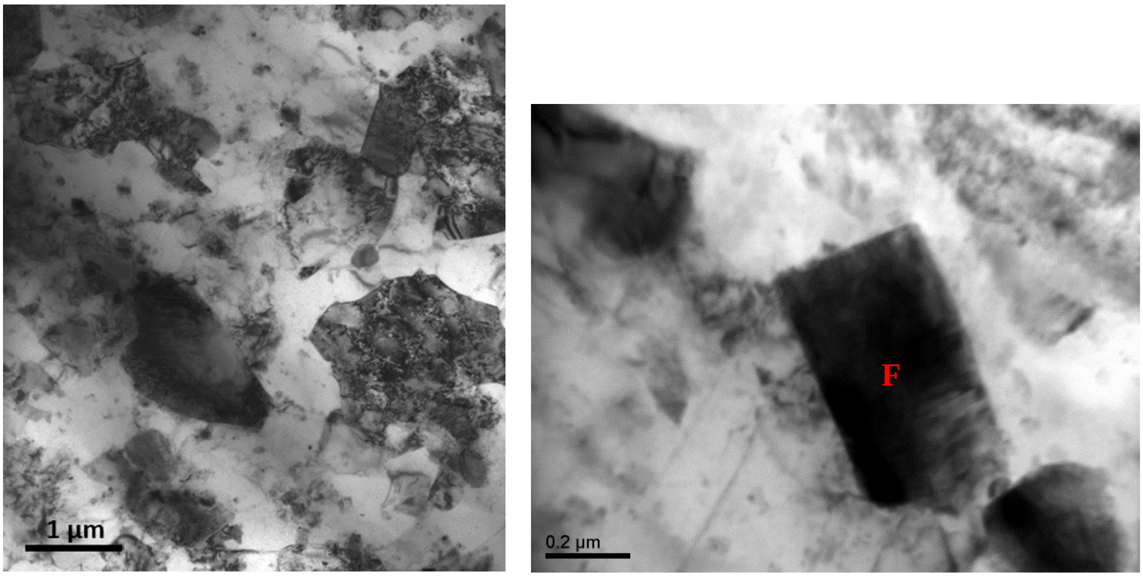

(a) (b)

Figure 4.7: TEM bright field micrographs of as-extruded 6061Al/12.9SiC sample showing (a) general microstructure and (b) SiC particle F.

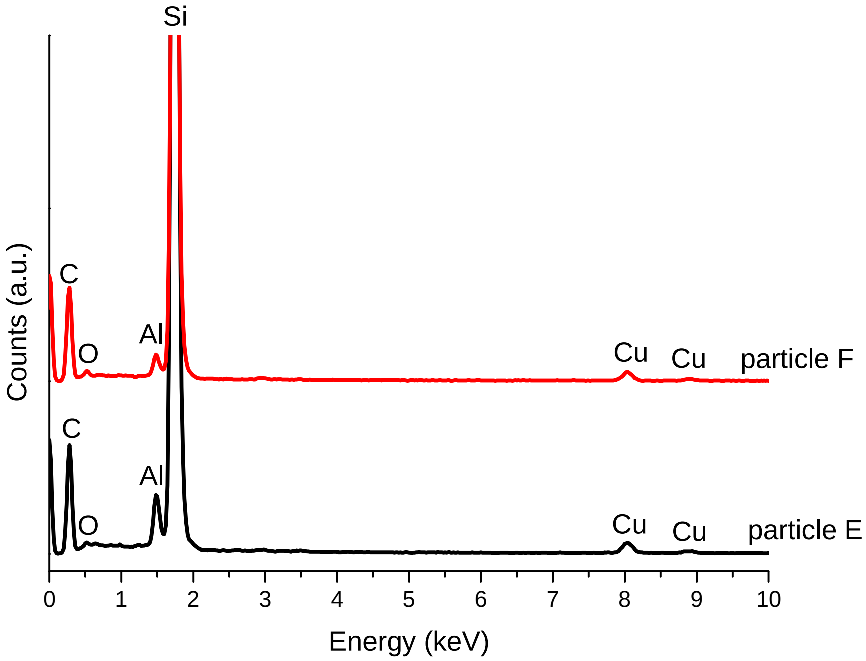

Figure 4.8: EDX spectra from particles E and F.

EDX points	C	O	Al	Si	Cu
particle E	23.36	0.63	2.21	73.31	0.49
particle F	31.45	0.57	1.32	66.08	0.58

Table 4.3: Numerical EDX results (atomic %) of particles E and F labelled in Figures 4.6 and 4.7.

The aging heat treated samples were also examined by TEM and the results are displayed in Figures 4.9 and 4.10. Figure 4.9 shows the general microstructure of aging heat treated 6061Al alloy. The Al grain size is estimated as 1.7±0.2μm using the mean linear intercept method (see section 3.3.3) based on micrographs similar to Figure 4.9(a). Precipitates are also observed both inside the Al grains and at the grain boundaries after heat treatment (Figures 4.9(b) and (c)). EDX spectra on some of the precipitates suggest that they are likely to be AlFeSi or AlFeCrSi particles. Faceted precipitates (Figure 4.9(e)) less than 100nm have been observed inside the Al grains after 8h of aging. The EDX spectrum (Figure 4.9(f)) on one of the faceted precipitates shows the presence of Mg and Si with an atomic ratio of 2.2, which is believed to be β' or β-Mg_2Si phase.

Figure 4.10 shows the microstructure of aging heat treated 6061Al/8.5SiC composite. Similar with as-extruded composite samples, it also contains an even dispersion of sub-micron particles as well as smaller precipitates. A closer look of Al and SiC interface in Figure 4.10(b) shows some cluster-like features at or near the interfacial areas. EDX analysis on region 1-4 was carried out and the results are displayed in Figure 4.10(c) and Table 4.4. Compared to matrix, region 1 is rich in C and Si, which suggests that the sub-micron particle is a SiC particle. Region 2-4 shows the existence of Mg and O at or near the interfacial areas. It seems that Mg and O have a tendency to segregate at the interface and possibly form MgO or $MgAl_2O_4$ spinel at the interface according to the reactions [7]:

$$3Mg + Al_2O_3 = 2Al + 3MgO$$

$$3Mg + 4Al_2O_3 = 2Al + 3MgAl_2O_4$$

The formation of MgO or $MgAl_2O_4$ spinel can act as diffusion barrier, further restricting reactions between Al and SiC to form Al_4C_3 [10]. Similar interfacial reaction products at Al alloy matrix and SiC interfaces were also reported by Wang et al. [7] and Fan et al. [11] on 6061Al/SiC_p and 7075Al/SiC_p composite systems. Since some of the Mg in the matrix is consumed during the above reactions, less Mg_2Si precipitates are going to be formed after aging heat treatment, reducing the precipitation hardening capacity of the composites. Similar TEM results are also found for aging heat treated 6061Al/12.9SiC composite sample.

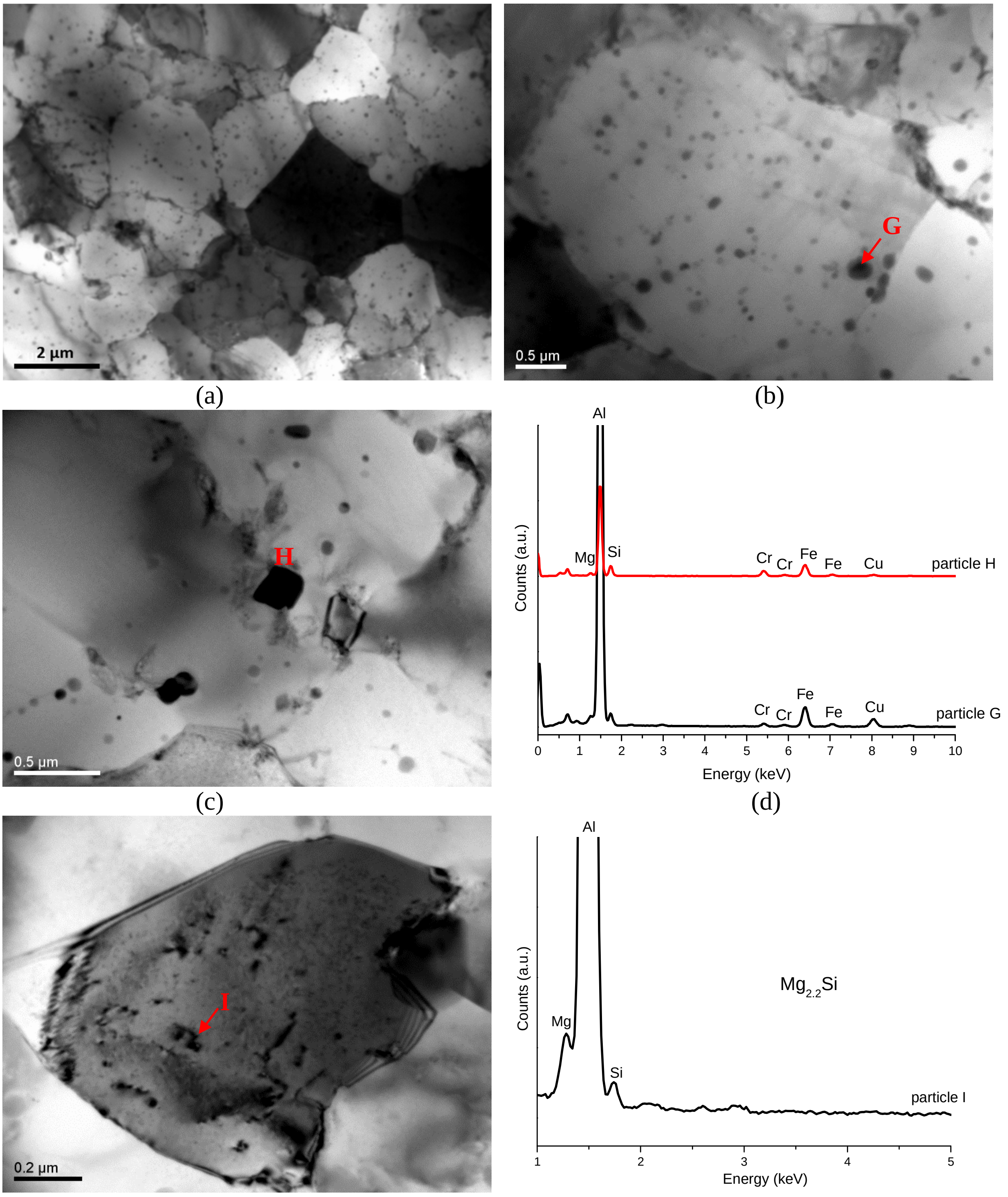

(a) (b)

(c) (d)

(e) (f)

Figure 4.9: TEM bright field micrographs of aging heat treated 6061Al alloy showing (a) general microstructure; (b), (c) precipitates within or at the Al grains and (d) EDX spectra of particles H and G; (e) faceted precipitate within the Al grains and (f) EDX spectrum of particle I.

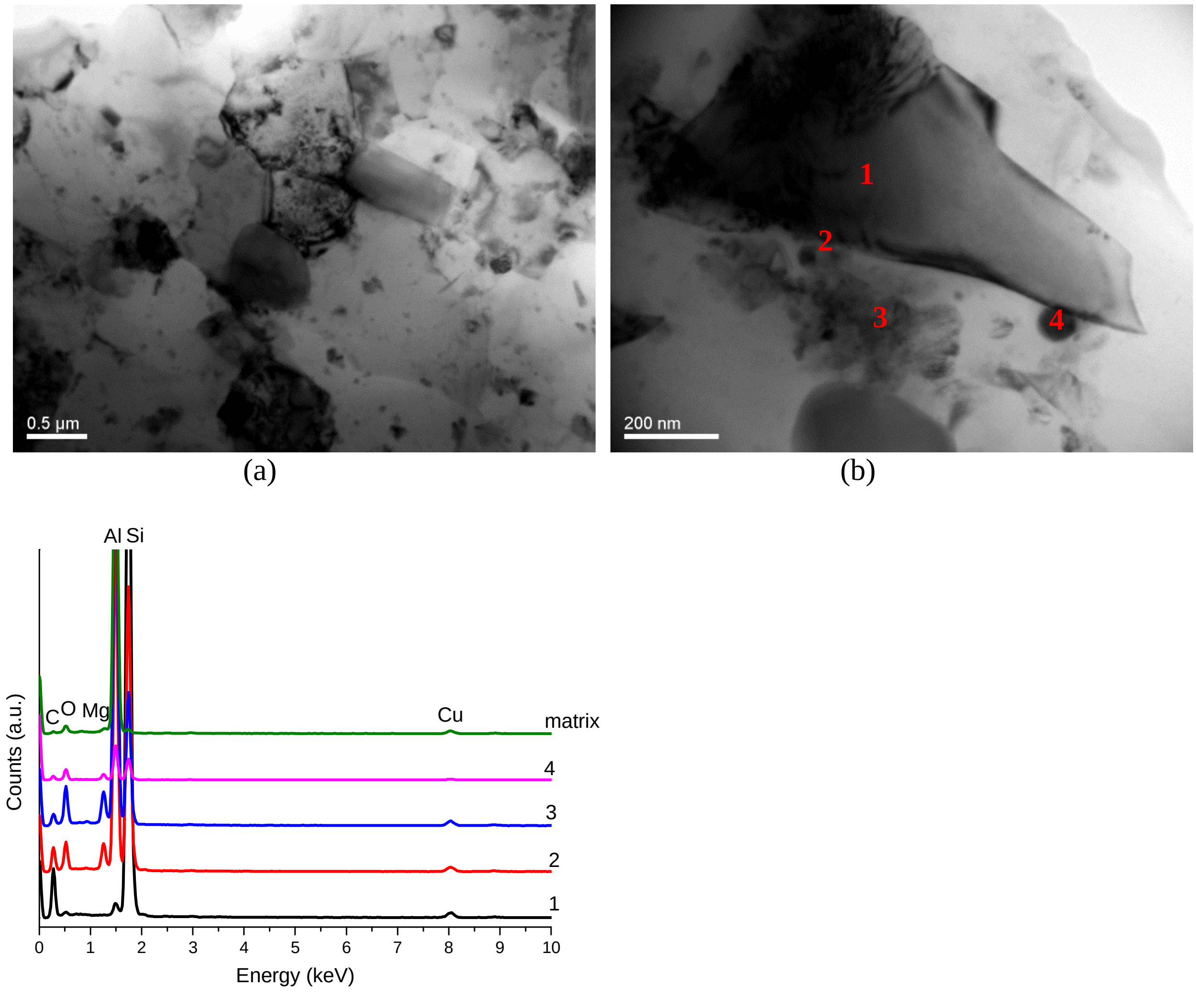

(a) (b)

(c)

Figure 4.10: TEM bright field micrographs of aging heat treated 6061Al/8.5SiC sample showing (a) general microstructure; (b) SiC particle and (c) EDX spectra on region 1-4 and the matrix.

EDX points	C	O	Mg	Al	Si	Cu
1	27.76	1.23	-	1.27	69.18	0.56
2	13.92	9.07	3.41	39.80	33.26	0.54
3	6.96	12.75	4.47	58.35	16.88	0.59
4	15.07	26.50	5.73	32.91	19.22	0.56
matrix	1.95	3.97	0.71	91.93	0.77	0.68

Table 4.4: Numerical EDX results (atomic %) of region 1-4 labelled in Figure 4.10(b) and the matrix.

4.2 Mechanical properties of 6061Al alloy and 6061Al/SiC composites

4.2.1 Microhardness analysis

Table 4.5 displays the average microhardness results of cross sectional 6061Al, 6061Al/8.5SiC and 6061Al/12.9SiC samples in as-received, as-extruded, solution heat treated and aging heat treated conditions with standard deviations.

The data shows similar microhardness results for as-received billets and as-extruded bars. After solution heat treatment, the microhardness result for 6061Al sample has increased slightly (~5%), while the results for solution heat treated 6061Al/8.5SiC and 6061Al/12.9SiC composites show a significant increase (~23%). This could be the result of the large different coefficients of thermal expansions (6:1) between 6061Al matrix and SiC particles [12]. When the composites were quenched after solution heat treatment, a high density of dislocations can be generated near the matrix-reinforcement interfaces due to the misfit strains caused by differential thermal contractions at 6061Al-SiC interfaces [13, 14], accounting for the significant increase in microhardness for the composites. After aging heat treatment, all three samples show a large increase in microhardness because of precipitation hardening. Compared with 6061Al sample, 6061Al/SiC composite samples show increasing microhardness results with increasing volume fraction of SiC particles in all processing conditions, suggesting effective strengthening from SiC particles.

Materials	**As-received**	**As-extruded**	**Solution heat treated**	**aging heat treated**
6061Al	-	57±2	60±1	106±1
6061Al/8.5SiC	87±6	88±2	109±3	138±2
6061Al/12.9SiC	103±7	102±2	125±2	146±3

Table 4.5: Microhardness (μHV_{500}) values of 6061Al, 6061Al/8.5SiC and 6061Al/12.9SiC samples in as-received, as-extruded, solution heat treated and aging heat treated conditions.

4.2.2 Room temperature compression tests

Room temperature compression tests for as-extruded samples were carried out to study their mechanical properties up to large strains. The compression test curves in engineering values are presented in Figure 4.11 and the compressive proof stress values are summarized in Table 4.6.

It can be observed that the compression test curves of the as-extruded 6061Al/SiC composites show similar features and as expected, the composites develop higher compressive proof stress when comparing to unreinforced 6061Al alloy and the proof stress increases with increasing volume fraction of SiC reinforcement.

In addition, when comparing the compression test curves, it can be seen that the composites have higher work hardening rate ($^{d\sigma}/_{d\varepsilon}$) than the unreinforced 6061Al alloy over the whole test range. The enhanced work hardening rates of materials containing non-deformable particles have been reported in books and papers [15-17]. During deformation, the matrix around the non-deformable particles develops much higher dislocation density than that of the unreinforced materials. The increased dislocation density regions restrict plastic flow and contribute to higher work hardening rates [18].

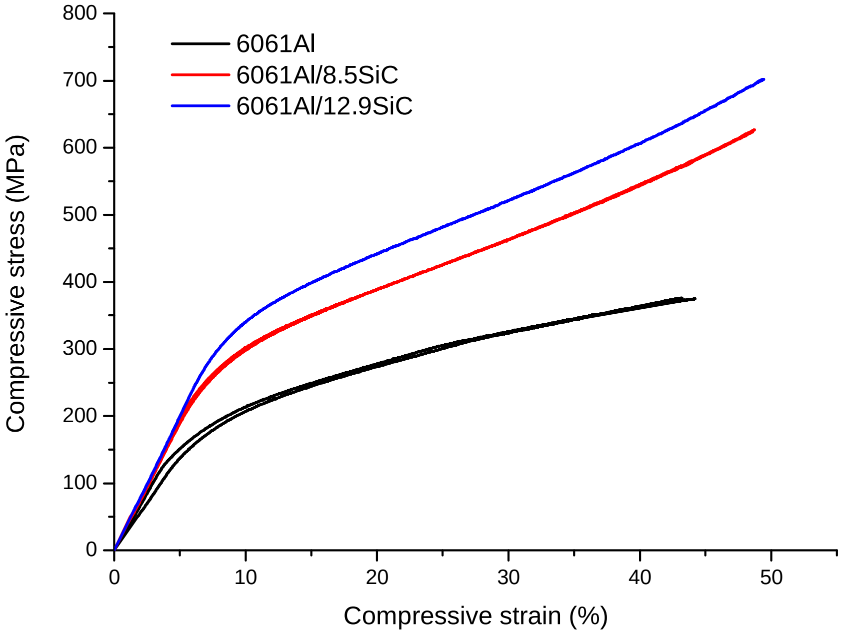

Figure 4.11: Room temperature compression test curves in engineering values for as-extruded 6061Al, 6061Al/8.5SiC and 6061Al/12.9SiC composites.

Materials	**Compressive σ_y (MPa)**
6061Al	130±3
6061Al/8.5SiC	212±1
6061Al/12.9SiC	264±1

Table 4.6: Compressive σ_y of as-extruded 6061Al, 6061Al/8.5SiC and 6061Al/12.9SiC composites extracted from room temperature compression tests (Figure 4.11).

4.2.3 Room temperature tensile tests

Room temperature tensile tests for as-extruded and aging heat treated samples were also carried out. The engineering stress-strain curves are plotted in Figures 4.12 and 4.13 and the results are summarized in Table 4.7.

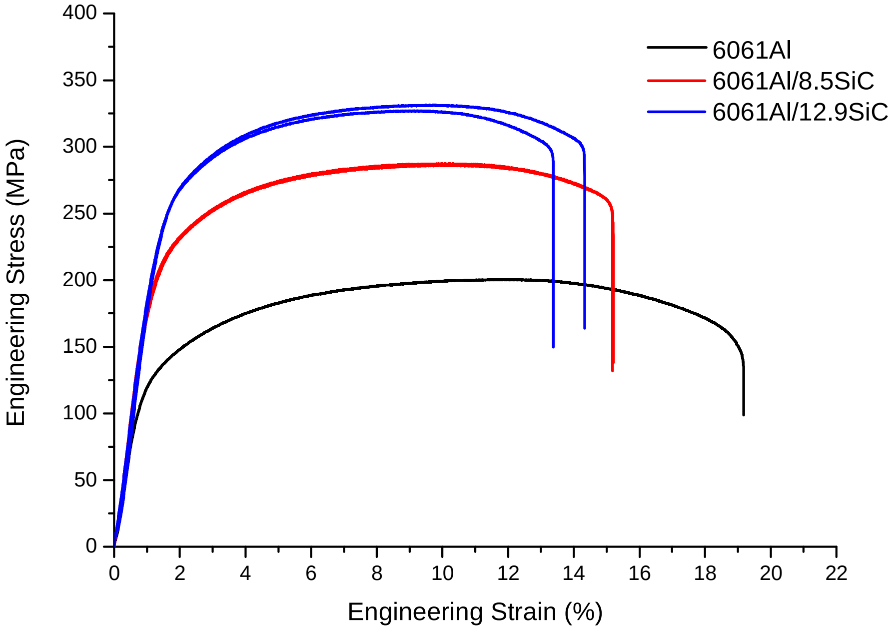

Figure 4.12: Room temperature tensile test curves in engineering values for as-extruded 6061Al, 6061Al/8.5SiC and 6061Al/12.9SiC composites.

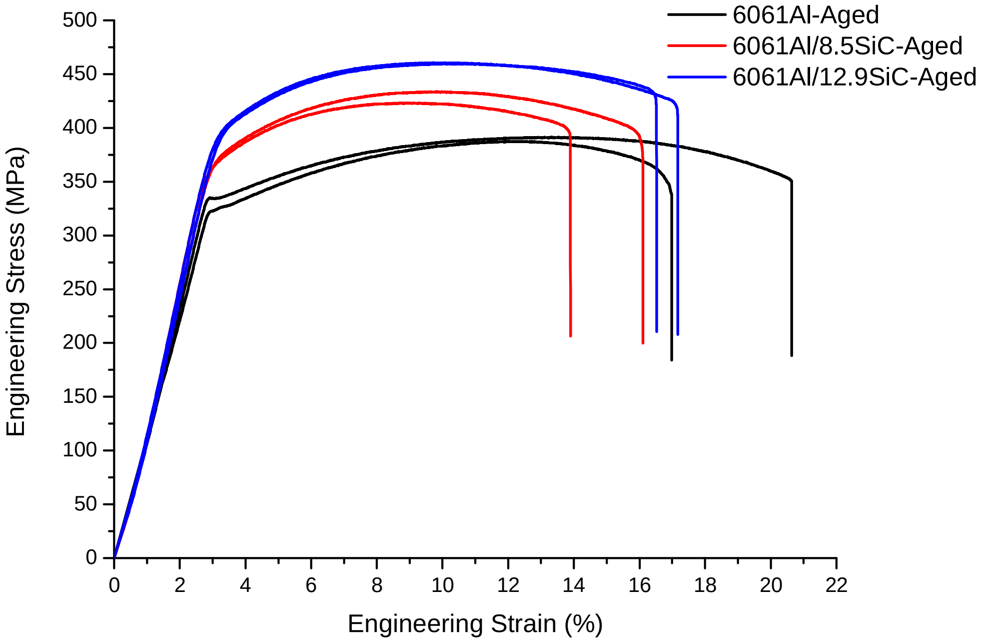

Figure 4.13: Room temperature tensile test curves in engineering values for aging heat treated 6061Al, 6061Al/8.5SiC and 6061Al/12.9SiC composites.

Materials	Predicted E (ROM)	E (GPa)	σ_y (MPa)	UTS (MPa)	ε_f (%)	Fracture toughness (MJ/m^3)
6061Al	69.0 [1]	69±2	131±5	205±5	19±1	34±4
6061Al/8.5SiC	98.1	87±1	192±1	287±1	15±1	39±1
6061Al/12.9SiC	113.1	103±1	229±6	329±2	14±1	41±2
6061Al-Aged	69.0 [1]	72±3	329±9	389±3	19±3	64±10
6061Al/8.5SiC-Aged	98.1	88±5	361±8	429±7	15±2	55±7
6061Al/12.9SiC-Aged	113.1	101±5	392±3	460±1	17±1	67±2

Table 4.7: Mechanical properties of as-extruded and aging heat treated 6061Al, 6061Al/8.5SiC and 6061Al/12.9SiC composites extracted from room temperature tensile tests (Figures 4.12 and 4.13) as well as predicted Young's modulus based on Rule of Mixtures (ROM) [19].

It can be seen from Table 4.7 that the values of E, σ_y and UTS all increase with increasing volume fractions of SiC particles in both as-extruded and aging heat treated conditions. The enhancement of E indicates a uniform distribution of SiC particles with good interfacial integrity as observed in Figure 4.6(b) which leads to effective load transfer between reinforcement and matrix. Compared with the predicted E values calculated from Rule of Mixtures [19], the experimental E values show a slight decrease (~10%) which also could indicate effective load transfer with a small number of debonded SiC particles from the matrix. Despite of the effect of load transfer, the significant increase of σ_y and UTS of 6061Al/SiC composites compared to 6061Al alloy can also be attributed to the coupled effect of Orowan strengthening, thermal mismatch, grain size refinement, etc. [20, 21]. σ_y and UTS values of aging heat treated tensile samples show a significant increase compared with as-extruded properties due to precipitation hardening.

Despite the improved tensile strength for 6061Al/SiC composites, surprisingly there is little change in ductility with the additions of SiC particles. Also, it should be noted that because of the increase in strength and the small reduction in strain, the area under the stress-strain tensile curves (energy to fracture), which is an indication of "static toughness", is maintained for the 6061Al/SiC composites. This result of retained ductility and toughness is consistent with the findings of Yang et al. [22] for A356/SiC$_p$ (30nm) composites, Xiong et al. [23] for Al-3wt.%Mg/SiC$_p$ (40nm) and Mazahery and Ostadshabani [24] for A356/(Al$_2$O$_3$)$_p$ (50nm) composites.

4.2.4 Fracture surface analysis of tensile samples

The fracture surfaces of as-extruded 6061Al, 6061Al/8.5SiC and 6061Al/12.9SiC tensile samples are shown in Figures 4.14-4.16, respectively. For as-extruded 6061Al tensile sample, dimples can be observed in Figure 4.14(b). The fracture of 6061Al sample was associated with the formation and growth of voids which were probably initiated at some precipitates, inclusions or impurities in the matrix. With the addition of SiC particles, ~45° fracture surfaces can be observed (Figures 4.15(a) and 4.16(a)). Dimples are still present in 6061Al/SiC tensile samples indicating ductile fracture (Figures 4.15(b) and 4.16(b)). A close look of the dimples reveals agglomerations of particles (Figure 4.15(c)) and debonded particles inside some of the dimples (Figure 4.16(c)).

According to Clyne and Withers [25], there are mainly two types of failure initiations in MMCs: (1) reinforcement cracking which happens when the reinforcement particles are relatively large and are highly possible to have a sufficiently large flaw; (2) Matrix cavitations and interfacial debonding which means that voids will originate solely within the matrix for highly bonded materials or at interfacial regions for weakly bonded materials. In the present work, a large number of dimples are present without particles inside. However, it is not clear whether the dimples are systematically absent of SiC particles since the particles are likely to be lost when fractured. A small number of dimples have agglomerated particles inside (Figure 4.15(c)), showing that agglomeration provides sites for crack initiations which will greatly reduce ductility. After crack nucleation, the voids will grow larger and larger and their coalescence will give the final failure of the materials. The aging heat treated samples have similar failure behaviour to that of the as-extruded samples.

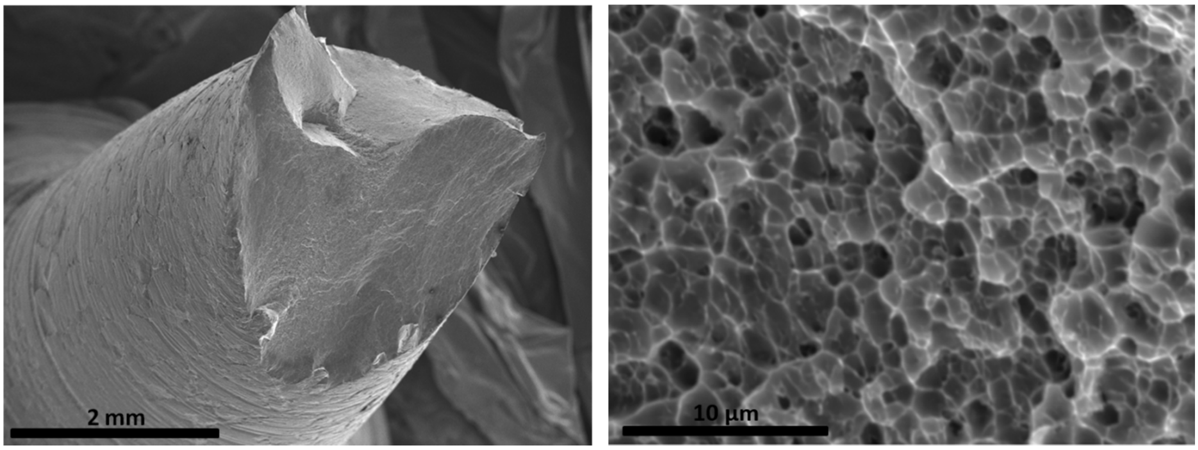

(a) (b)

Figure 4.14: Secondary electron images of the fracture surface of as-extruded 6061Al tensile sample showing (a) overview and (b) dimples.

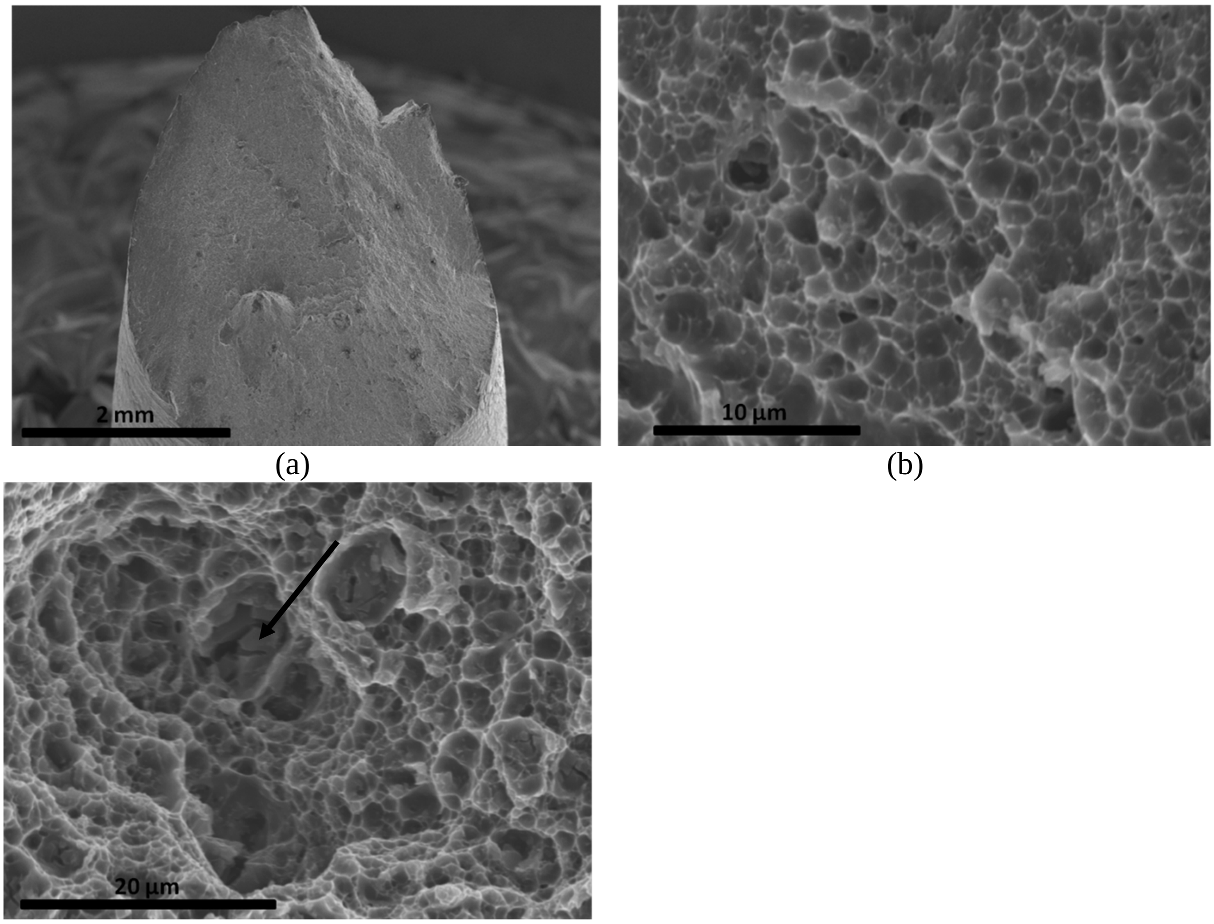

(a) (b)

(c)

Figure 4.15: Secondary electron images of the fracture surface of as-extruded 6061Al/8.5SiC tensile sample showing (a) overview, (b) dimples and (c) particles in dimples (arrow indicates SiC particles).

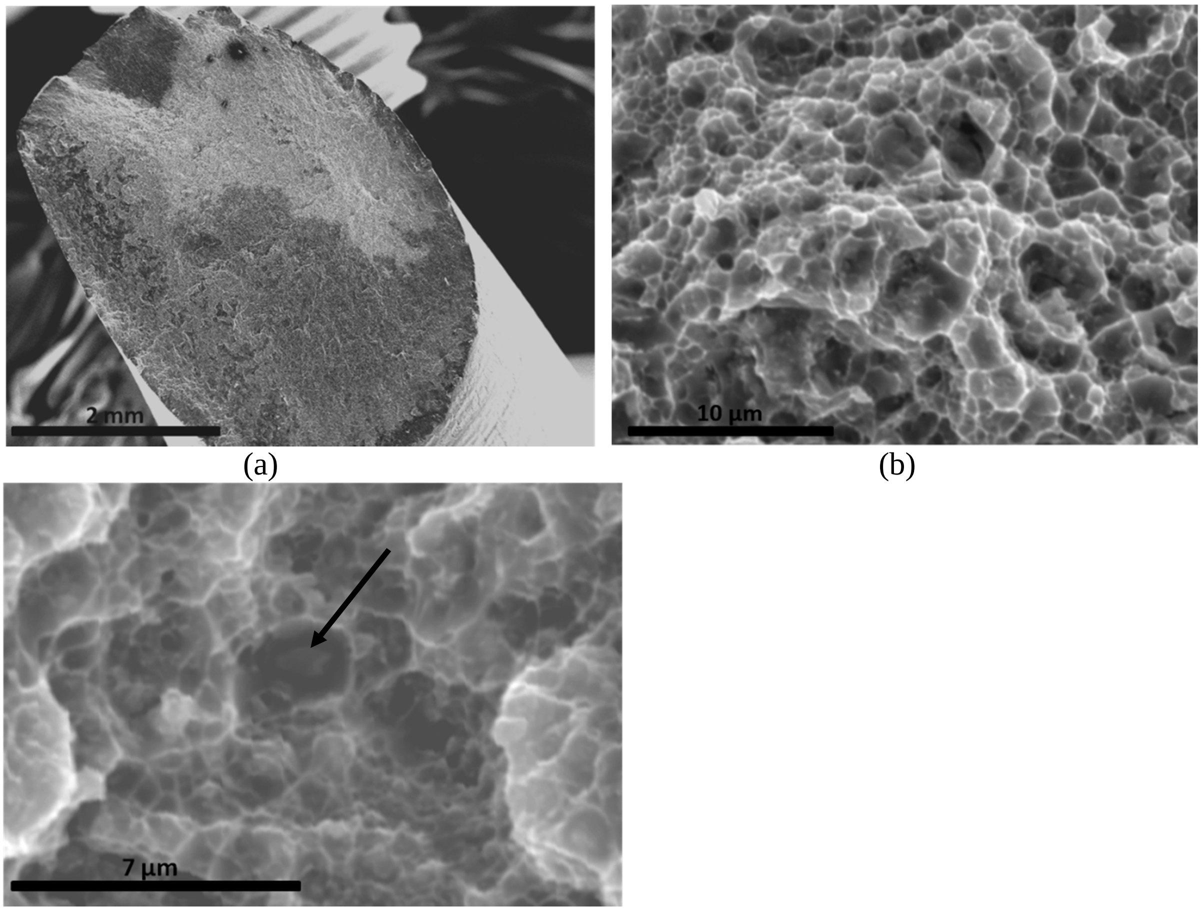

(a) (b)

(c)

Figure 4.16: Secondary electron images of the fracture surface of as-extruded 6061Al/12.9SiC tensile sample showing (a) overview, (b) dimples and (c) particles in dimples (arrow indicates SiC particles).

4.2.5 Load-controlled fatigue tests

The fatigue properties of aging heat treated 6061Al alloy, 6061Al/8.5SiC and 6061Al/12.9SiC samples were also tested since fatigue fracture is the most common source of failures of engineered materials and accounts for more than 80% of damage in practical applications [26].

Figure 4.17 shows the maximum stress versus the number of cycles to failure for 6061Al, 6061Al/8.5SiC and 6061Al/12.9SiC samples. It can be observed that the fatigue properties of the composites are superior than unreinforced 6061Al alloy, and improve with increasing volume fractions of SiC particles, especially in high cycle fatigue regimes. For example, at a maximum stress level of 310MPa, the 6061Al alloy fails at 4.7×10^4 cycles, the 6061Al/8.5SiC sample fails at 1.4×10^6 cycles while the 6061Al/12.9SiC sample has the longest fatigue life with a fatigue cycle of 2.2×10^6. Similar results that an improved stress-controlled high cycle fatigue properties with increasing reinforcement volume fractions have been also reported by Srivatsan el al. [27] on 6061Al/SiC$_p$, Hall et al. [28] on 2124Al/SiC$_p$ and Chawla et al. [29] on 2080Al/SiC$_p$. A variety of mechanisms are accounted for the improved performance including load transfer to the high modulus reinforcement, lowering total strain [30], reduced effective stress concentrations on intermetallic inclusions in the matrix [29] and higher tensile strength [27].

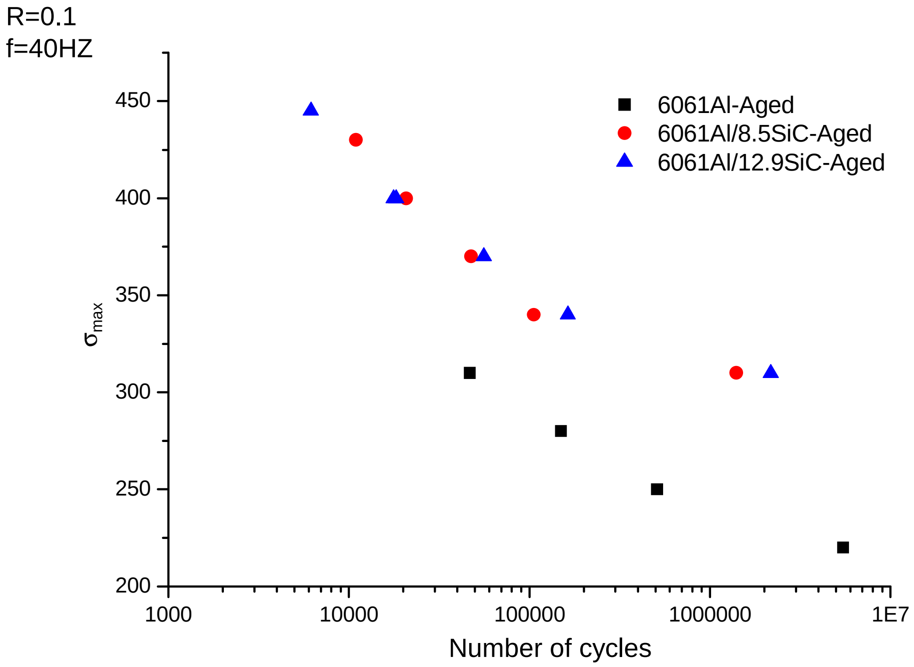

Figure 4.17: Maximum applied stress versus the number of cycles to failure for aging heat treated 6061Al, 6061Al/8.5SiC and 6061Al/12.9SiC samples under tension-tension loading with R=0.1 and a frequency of 40HZ.

4.2.6 Fracture surface analysis of fatigue samples

Figure 4.18 shows the fracture surface of aging heat treated 6061Al alloy tested at a maximum load level of 220MPa. Figure 4.18(a) is the overview of the fracture surface showing limited flat regions corresponding to fatigue crack initiation and stable growth (region A) and tortuous ridges associated with rapid dimpled fracture (region B). Typical fatigue fracture surfaces at region A are shown in Figure 4.18(b) with crack initiation regions near sample surfaces followed by subsequent crack growth areas. Most areas in region A are fatigue crack growth regions having typical features shown in Figure 4.18(c). Fatigue voids and river patterns in the direction of crack growth are observed. Fatigue voids are frequently observed on fatigue fractures of Al alloys [31-33]. They are formed due to the separation of secondary non-coherent precipitates from the matrix during fatigue. According to TEM analysis in section 4.1.5, aging heat treated 6061Al alloy has a large number of secondary precipitates which are preferable sites for fatigue voids. Their formation is through the initiation, growth and coalescence of multiple interfacial cracks around the particles and they become visible on the fatigue fracture surfaces when the crack front advances through them [31].

The fast fracture surfaces characterized by dimpled rupture in region B are shown in Figure 4.18(d) with rough, void rich fracture surfaces. A high magnification of voids consisting of twin fatigue voids of a size around 6-8μm are shown in Figure 4.18(e). EDX spectrum (Figure 4.18(g)) on particle 1 confirms the presence of Mg and Si. It is likely that the Mg_2Si precipitates initiated the fatigue voids in the present area. Compared to Figure 4.18(c), it seems that Figure 4.18(d) has a higher density of fatigue voids. Similar features were also reported by Sunder et al. [31] on 2014Al and 2024Al alloys that fatigue voids density increases dramatically with increasing crack growth rate. It has been reported that at high crack growth rates involving considerable crack tip shear, slip planes with particulate concentrations offer the path of least resistance and as cracks grow along this path of least resistance, clusters of particulate voids get interconnected and show an increasing density [31]. Despite the presence of fatigue voids, region B also shows ductile dimples as a sign of limited plastic deformation, as is shown in Figure 4.18(f).

To conclude, the fatigue failure initiates at foreign particles or inclusions near sample surfaces and continues with the formation, growth and coalescence of fatigue voids and ends with propagation of macro-cracks interconnecting the voids.

To study the effect of fatigue load level on the fracture surfaces, fracture surface analysis of aging heat treated 6061Al alloy tested at a maximum load level of 310MPa was carried out and the results are shown in Figure 4.19. Similar features consisting of flat regions corresponding to fatigue crack initiation and growth (region A) and final dimpled rupture (region B) are observed in Figure 4.19(a). Region A consists of fatigue voids and river patterns (Figures 4.19(b)), and region B consists of rough, fatigue voids surfaces (Figures 4.19(c) and (d)). Compared to Figures 4.18(c) and (d), it can be seen that the number of fatigue voids has been greatly reduced in the present sample tested at a maximum load level of 310MPa. It is likely that under a higher load level, the fatigue crack growth rate is faster than the formation of fatigue voids, hence reducing the number of fatigue voids on the fracture surfaces.

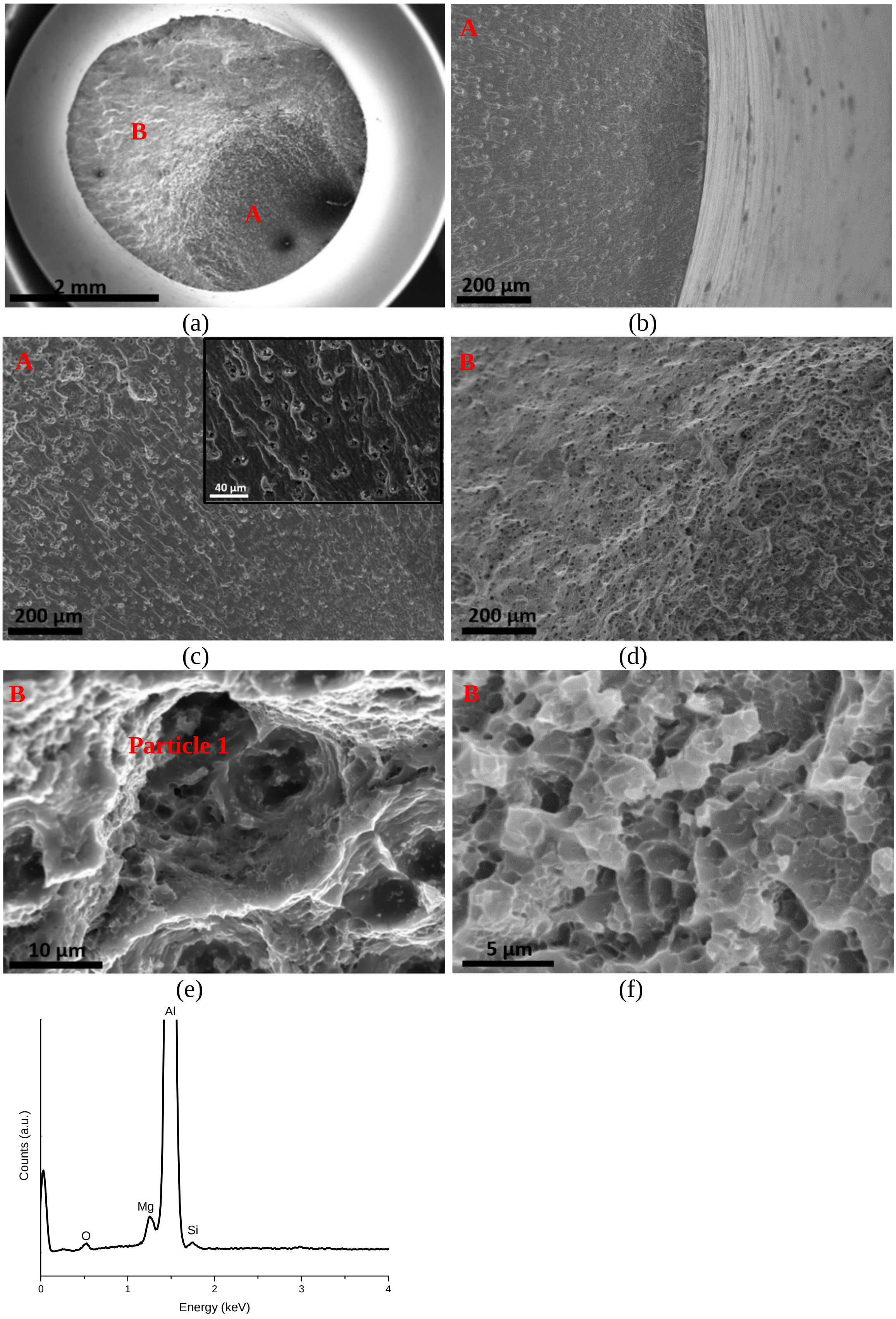

(a) (b) (c) (d) (e) (f) (g)

Figure 4.18: Fracture surface analysis of aging heat treated 6061Al alloy tested at a maximum load level of 220MPa showing (a) overview; (b) initiation region A; (c), (d), (e) fatigue voids; (f) microvoids and (g) EDX spectrum on particle 1.

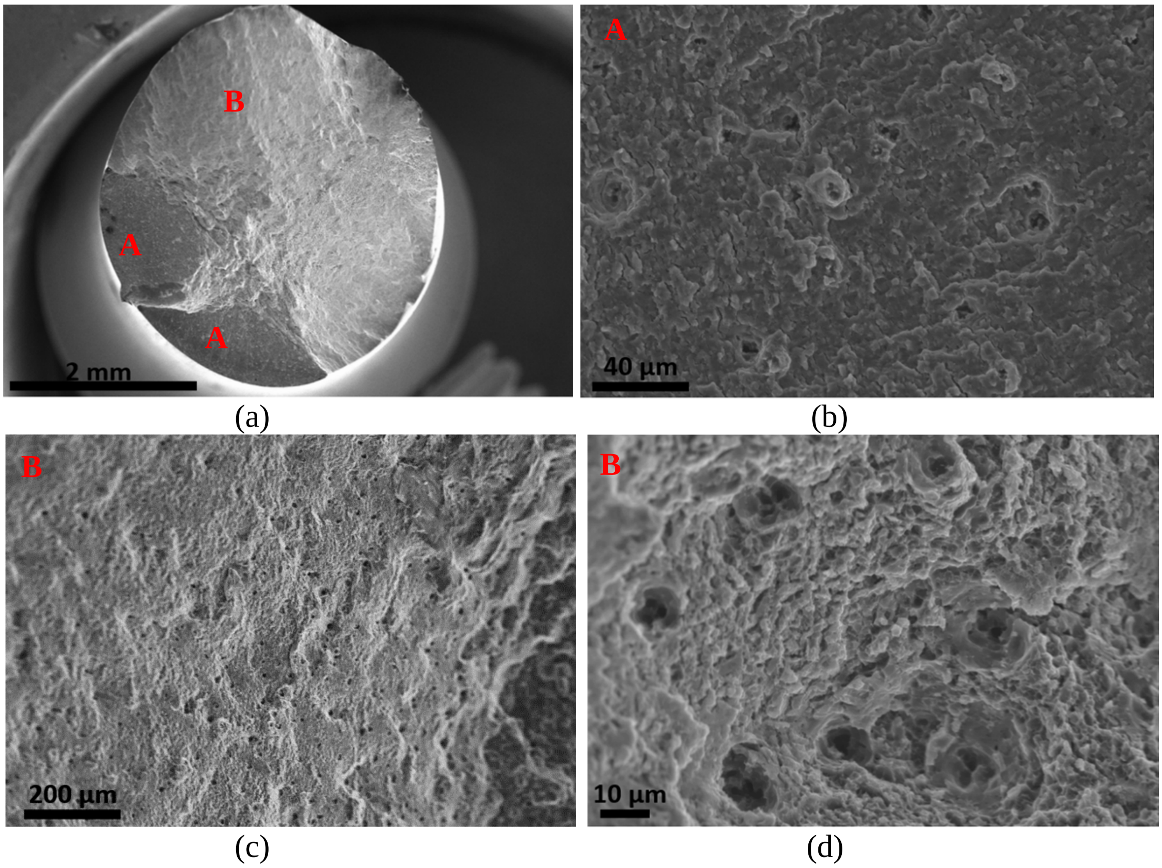

(a) (b)

(c) (d)

Figure 4.19: Fracture surface analysis of aging heat treated 6061Al alloy tested at a maximum load level of 310MPa showing (a) overview; (b), (c), (d) fatigue voids.

The fatigue fracture behaviour of 6061Al/8.5SiC and 6061Al/12.9SiC samples is similar to each other, hence only the fracture surface analysis on 6061Al/12.9SiC sample will be discussed. Figure 4.20 shows the fracture surface of aging heat treated 6061Al/12.9SiC sample tested at a maximum load level of 310MPa. It can be seen from Figure 4.20(a) that the fracture surface of 6061Al/12.9SiC sample also has two distinct fracture morphologies corresponding to fatigue initiation and growth (region A) and final fast fracture surfaces (region B). Figure 4.20(b) shows the crack initiation point near sample surface in region A. It seems that crack initiated from a foreign particle or inclusion (particle 1), EDX spectrum suggests that the particle might be AlFeSi precipitates. Most of region A is covered with crack propagation region where equi-spaced striation marks perpendicular to the direction of crack propagation are observed, as shown in Figure 4.20(c). The fast fracture surfaces are relatively rough and characterized by dimpled morphologies shown in Figure 4.20(d). The failure mode is the typical microvoid growth and coalescence. EDX spectra have confirmed the presence of SiC particles in some of the dimpled voids.

The fracture surfaces of aging heat treated 6061Al/12.9SiC sample tested at a maximum load level of 445MPa were also examined and the results are shown in Figure 4.21. Similar to other samples, the fracture surfaces consist of region A perpendicular to the loading direction corresponding to stable fatigue crack growth and relatively rough region B. Equi-spaced striation marks perpendicular to crack growth direction are also observed (Figure 4.21(b)). A closer look of the striations (Figure 4.21(c)) shows that they are made up of sub-micron dimples with SiC particles present in some of the dimpled voids confirmed by EDX. Region B is final fast fracture region and characterized by dimpled morphologies as shown in Figure 4.21(d).

To conclude, for 6061Al/SiC samples, no clear difference has been found in fatigue fracture surfaces between low and high stress levels. It appears that the fatigue cracks are initiated at the surface defects or inclusions and propagate in a ductile mode with some evidence of matrix/particle interfacial debonding. In the final fractured region, dimpled morphologies with sub-micron voids with or without the presence of SiC particles are observed. It seems that the crack growth mechanism occurs primarily through the matrix and also some of the SiC particles serve as sites for microvoid nucleation due to debonding. No fractured SiC particles have been observed in the fracture surfaces probably due to the small size of the particles.

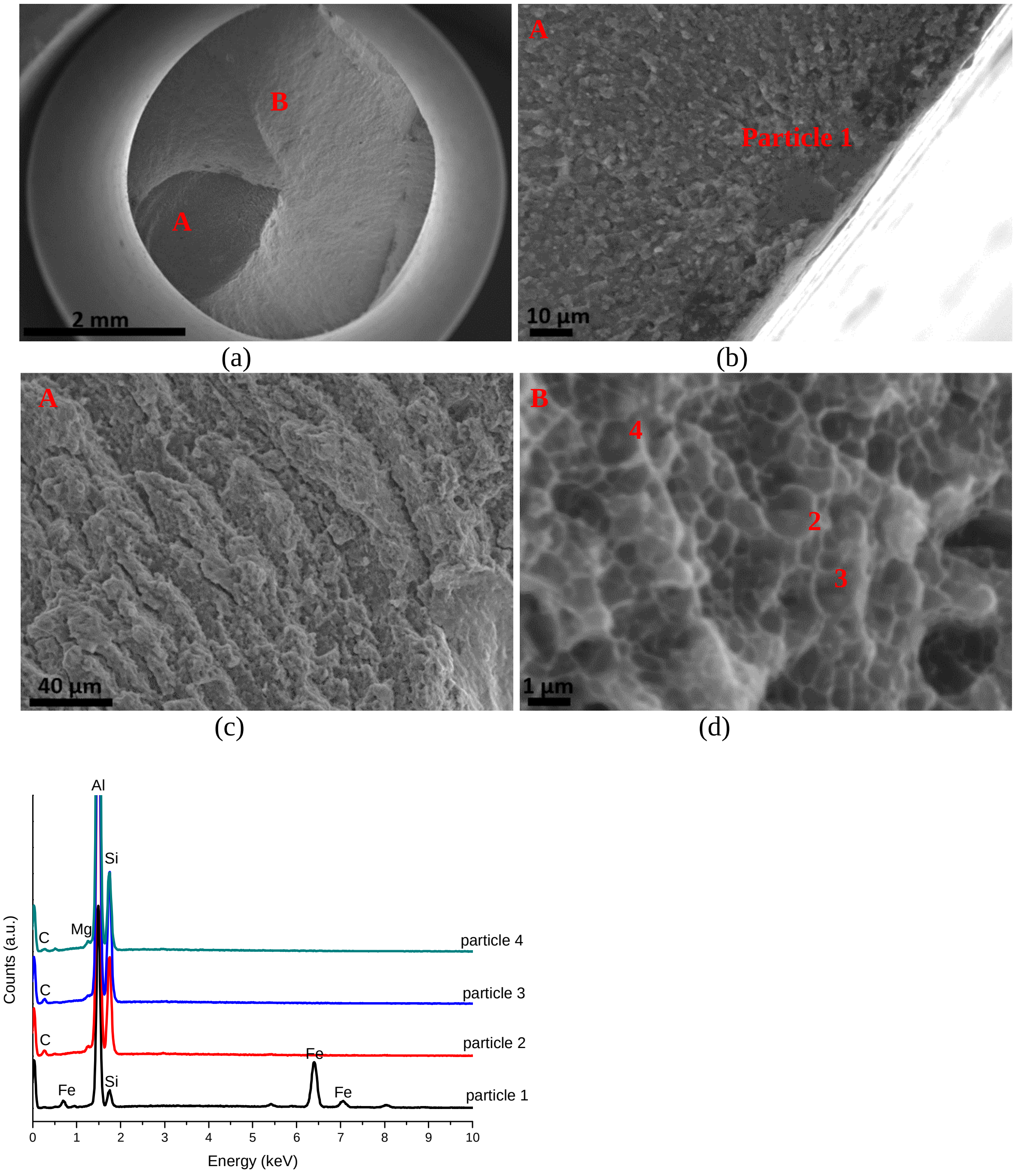

(a) (b)

(c) (d)

(e)

Figure 4.20: Fracture surface analysis of aging heat treated 6061Al/12.9SiC sample tested at a maximum load level of 310MPa showing (a) overview; (b) crack initiation region; (c) crack propagation region; (d) dimpled rupture and (e) EDX spectra on particle 1-4.

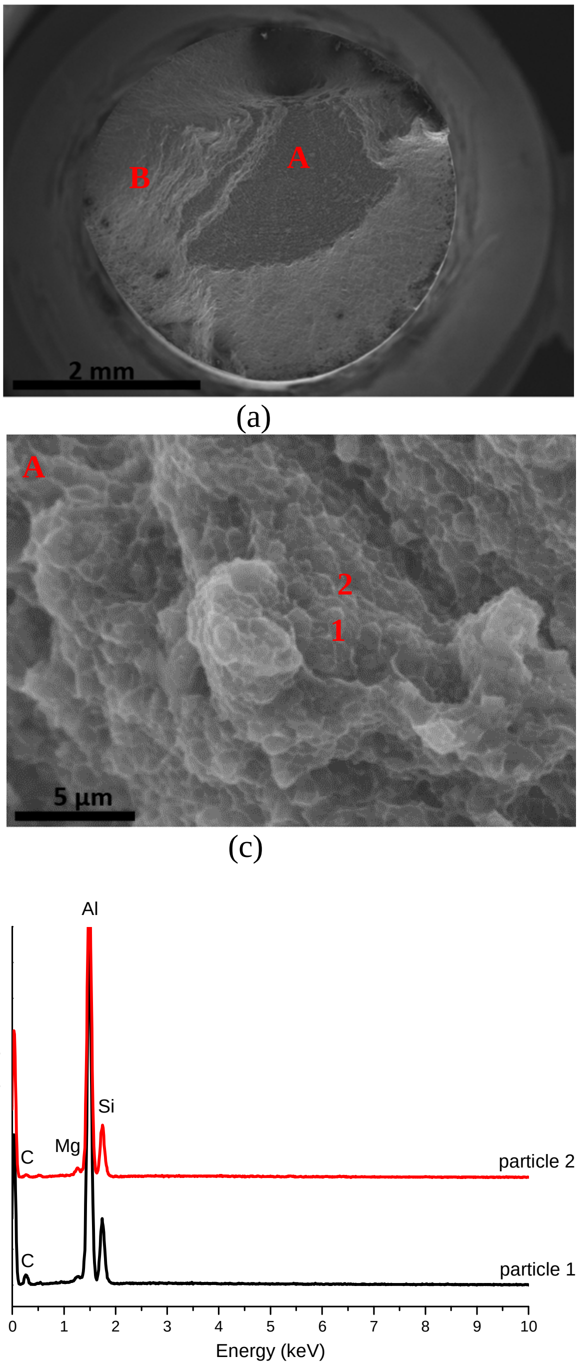

(a)

(b)

(c)

(d)

(e)

Figure 4.21: Fracture surface analysis of aging heat treated 6061Al/12.9SiC sample tested at a maximum load level of 445MPa showing (a) overview; (b), (c) crack propagation region; (d) dimpled rupture and (e) EDX spectra on particle 1-2.

4.3 Discussion

4.3.1 Effect of extrusion process

Extrusion is known to further consolidate the materials. Table 4.2 calculates the density and porosity content of the samples before and after extrusion. The effect of the extrusion procedure on the porosity content of the samples based on Table 4.2 is plotted in Figure 4.22 as a function of the reinforcement volume fractions. It can be seen that the as-received samples have higher porosity levels than the as-extruded ones and the application of hot extrusion results in a ~50% porosity reduction for both composites. In addition, the porosity level increases with increasing volume fraction of SiC particles for both as-received and as-extruded samples.

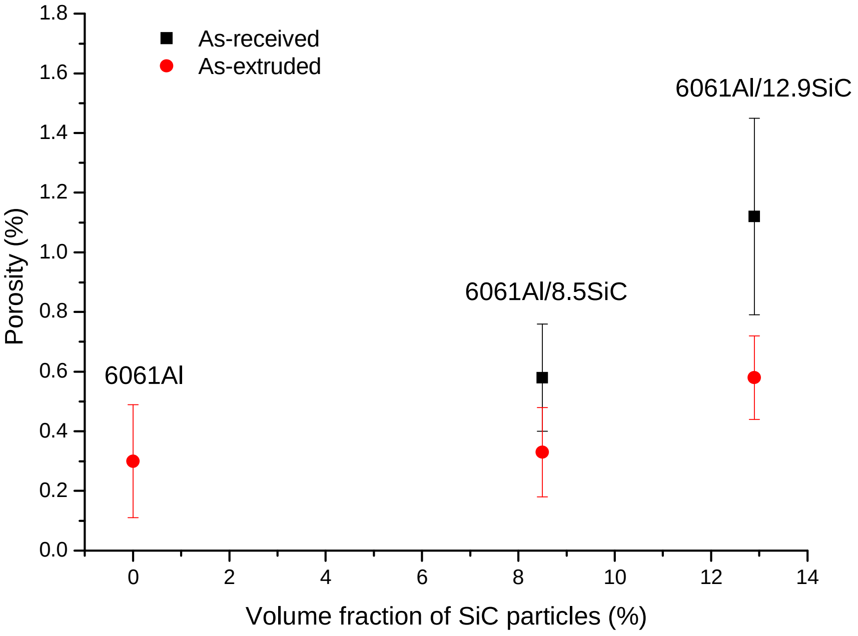

Figure 4.22: The change of porosity content in as-received and as-extruded 6061Al, 6061Al/8.5SiC and 6061Al/12.9SiC samples as a function of the volume fraction of SiC particles.

Extrusion can also help homogenize the microstructure. The as-received 6061Al/SiC samples have SiC particle free areas (Figure 4.2), after extrusion, the particle free areas have disappeared (Figure

4.3) and a quasi-uniform distribution of SiC particles has been achieved for both 6061Al/8.5SiC and 6061Al/12.9SiC samples. It is believed that the high extrusion ratio (16:1) and the appropriate extrusion temperature (450ºC) have led to a sufficient flow of the matrix alloy, resulting in a uniform distribution of SiC particles among the Al alloy matrix [34, 35].

The different microstructure before and after extrusion and porosity reduction indicate that extrusion is a very effective secondary processing step to further consolidate the materials, improve the density, homogenize the microstructure and thereby enhancing the overall mechanical properties. All these effects have been reported by other researchers as well [36-40] and the explanations have been reviewed in section 2.1.3.3.

Extrusion is also known to influence the crystallographic texture in Al alloys [41]. To investigate the effect of extrusion on the anisotropic properties, texture analysis calculated by the intensity ratios between the (1 1 1) α-Al peak and the (2 0 0), (2 2 0), (3 1 1) and (2 2 2) peaks was performed based on the XRD data of the cross sectional planes of 6061Al alloy, 6061Al/8.5SiC and 6061Al/12.9SiC samples in as-received and as-extruded conditions in Figures 4.1(a) and (b). The calculated relative intensities of the peaks are shown in Figure 4.23. It can be seen that extrusion has led to a reduction in relative intensities from (2 0 0), (2 2 0) and (3 1 1) reflections, suggesting that extrusion has developed a sharp <1 1 1> fibre along the extrusion direction for 6061Al matrix of all materials. The produced extrusion texture has also been seen by Poudens et al. [42] on 6061Al/SiC_p and 2124Al/SiC_p composites after extrusion into bars.

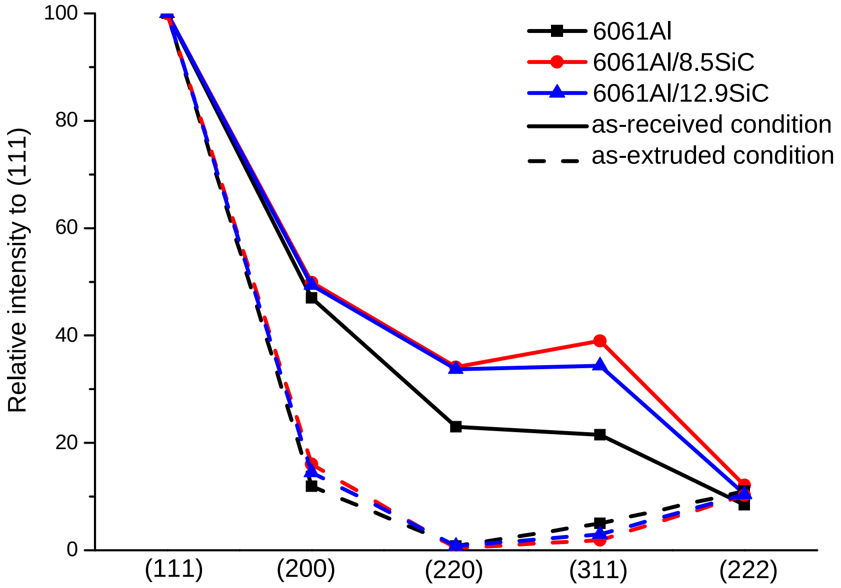

Figure 4.23: Texture analysis of the cross sectional planes of 6061Al alloy, 6061Al/8.5SiC and 6061Al/12.9SiC samples in as-received and as-extruded conditions.

4.3.2 Effect of aging heat treatment

It is well known that heat treatment has profound influence to the microstructure and mechanical properties of heat-treatable Al alloys [43].

According to Figure 4.9, faceted Mg_2Si precipitates have appeared inside the Al grains after aging heat treatment for 6061Al alloy. According to literature [44-47], during aging heat treatment, the following precipitation sequence has been proposed for Al-Mg-Si alloys: supersaturated solid solution (SSS) → Guinier-Preston (GP) zones → β″ needle shaped precipitates → β′ lath or rod-shaped precipitates → β (Mg_2Si) plates. The presence of β′ or β phase observed during aging heat treatment is consistent with the reported precipitation behaviour of Al-Mg-Si alloys.

For the composites, it is reported that the reinforcement particles can accelerate the aging precipitates in the matrix due to the increased dislocation density as a result of the additions of the reinforcement particles [48]. The increased density of dislocations provides suitable sites for heterogeneous nucleation of precipitates and also acts as diffusion paths of the alloying elements [48, 49]. As a result, the aging kinetics will be promoted for composite materials. However, in the present work, the additions of SiC particles are likely to cause a reduced precipitation hardening capacity for the 6061Al/SiC composites. According to the TEM analysis in section 4.1.5, it has been observed that Mg and O have a tendency to segregate at the 6061Al/SiC interfacial areas and possibly form MgO or $MgAl_2O_4$ spinel. The reduced Mg concentration in the 6061Al matrix is likely to slow and reduce the Mg_2Si precipitation during aging heat treatment, especially considering the increased interfacial areas associated with nano-sized reinforcement, leading to less precipitation hardening.

The formation of aging precipitates during aging heat treatment has led to improved mechanical properties for all the materials in terms of microhardness, σ_y, UTS and fracture toughness. For instance, the microhardness and σ_y of aging heat treated 6061Al alloy have increased by ~84% and ~150% when compared to that of the as-extruded 6061Al alloy, respectively. The enhanced mechanical properties due to precipitation hardening after aging heat treatment are also reported elsewhere [48, 50-52].

4.3.3 Effect of the additions of nano-sized SiC particles

To investigate the effect of the additions of nano-sized SiC particles, the tensile properties and fatigue properties of similar composites reinforced with micron-sized SiC particles from literature are summarized and shown in Table 4.8 and Figure 4.24, respectively.

Table 4.8 shows that the produced 6061Al/SiC composites in the present work have improved tensile properties when compared with similar composites reinforced with micron-sized SiC particles. At a given volume fraction of reinforcement, a reduction of particle size from micron to nano-size will lead to a significant improvement of mechanical properties especially due to the effect of Orowan strengthening and thermal mismatch [53]. Orowan strengthening is usually negligible for micro-sized particulate reinforced MMCs since the particles are coarse and the interparticle spacing is too large to impede dislocation motion. For nanocomposites, however, smaller particles decrease interparticle spacing and therefore increase the second phase resistance to dislocations [21]. For the mechanism of thermal mismatch, with a given volume fraction of reinforcement, more particles will be present in the composites if the particle size is smaller, hence generating more dislocations around the particles due to the effect of the difference of the coefficients of thermal expansions between the matrix and reinforcements upon cooling from processing temperature [21]. Mathematical models of incremental yield strength as a function of reinforcement size due to Orowan strengthening and thermal mismatch have been proposed by many researchers [14, 21, 53, 54]. These models show a significant increase in yield strength with decreasing reinforcement size, especially when the particle size is less than 100nm. It is believed that these two strengthening mechanisms increase with decreasing particle size and result in enhanced tensile properties when compared to micron-sized particulate reinforced MMCs.

In addition to the improved tensile strength, the obtained elongations for the produced composites decrease with the addition of SiC particles. However, the decrease is not as severe as is often seen with micron-sized reinforcements, such as those shown in Table 4.8. The maintenance of ductility and fracture toughness can be in part attributed to the particles being sufficiently small that there is no chance of fracture occurring within the particles [5]. It is believed that for relatively smaller particles, due to (i) homogeneous distribution of SiC particles with no clustering since clusters are known to fail prematurely and are less effective at transferring loads [55], and (ii) the reduced stress within each particles as well as the reduction in flaw size [56], the particles are less likely to fracture, leading to the retaining of ductility and toughness.

Materials	σ_y (MPa)	UTS (MPa)	ε_f (%)	Ref
6061Al/10vol.%SiC-T6 (10-20μm)	278	332	16.3	[27]
6061Al/10vol.%SiC-T6 (23μm)	-	310	6.0	[57]
6061Al/10vol.%SiC-T6 (37μm)	-	355	6.0	[58]
6061Al/15vol.%SiC-T6 (10-20μm)	343	372	7.0	[27]
6061Al/15vol.%SiC-T6 (23μm)	-	346	5.0	[57]
6061Al/8.5SiC-Aged	361±8	429±7	15±2	Present work
6061Al/12.9SiC-Aged	392±3	460±1	17±1	

Table 4.8: Comparisons of mechanical properties of T6 heat treated 6061Al alloy reinforced with micron-sized SiC particles taken from [27, 57, 58] and aging heat treated 6061Al/SiC samples used in the present work.

Figure 4.24 shows the fatigue data on similar composites reinforced with micron-sized SiC particles reported by Srivatsan et al. [27]. Compared with Figure 4.24, the produced composites (Figure 4.17) show a significant improvement in fatigue lives, especially in high cycle fatigue regimes. For example, a maximum stress level of ~300MPa gives a fatigue life of ~10^5 cycles for 6061Al/SiC$_p$ (10-20μm) composites based on Figure 4.24 while both the produced composites fail at ~10^6 cycles at a maximum stress level of 310MPa. Similar results showing an improved stress-controlled high cycle fatigue properties of Al alloy based composites with decreasing reinforcement size or interparticle spacings have also been reported and are attributed to lower frequency of particle fracture [28, 29].

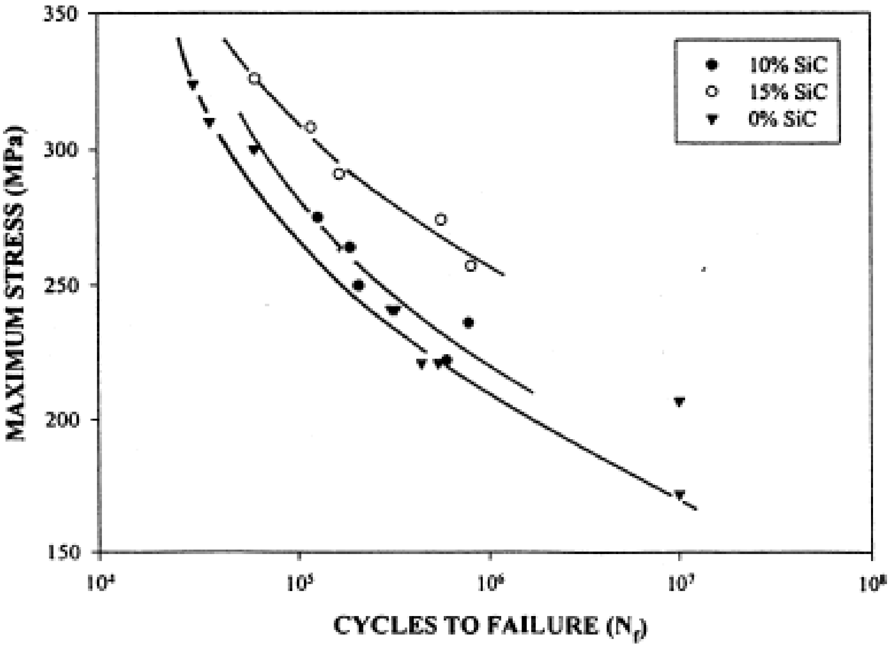

Figure 4.24: Fatigue results of T6 heat treated 6061Al, 6061Al/10vol.%SiC and 6061Al/15vol.%SiC with an average reinforcement size of 10-20µm tested at a constant cyclic frequency of 5Hz and at a stress ratio of 0.1 [27] (with permission from Elsevier).

4.3.4 Effect of SiC volume fractions

To study the effect of SiC volume fractions, the mechanical property results of as-extruded and aging heat treated samples including microhardness, Young’s modulus, proof stress, compressive proof stress and UTS obtained in Tables 4.5, 4.6 and 4.7 are plotted in Figure 4.25 as a function of volume fractions of SiC particles.

Figure 4.25 shows that all the mechanical properties increase with increasing volume fractions of SiC particles with no sign of levelling off. There is some literature reporting that the microhardness and tensile strength increase with increasing volume fraction of reinforcement particles up to a critical volume fraction and then level off or decrease with further additions of reinforcement due to the formation of reinforcement clusters which leads to a reduction in effective particle content [53, 59-61]. In the present work, all the mechanical properties of the composites improve with the additions of SiC particles with no sign of saturation, indicating a homogeneous distribution of SiC particles with no clusters when the particle volume fraction reaches 12.9%. The uniform distribution of SiC particles is also confirmed by microstructural analysis shown in Figure 4.3.

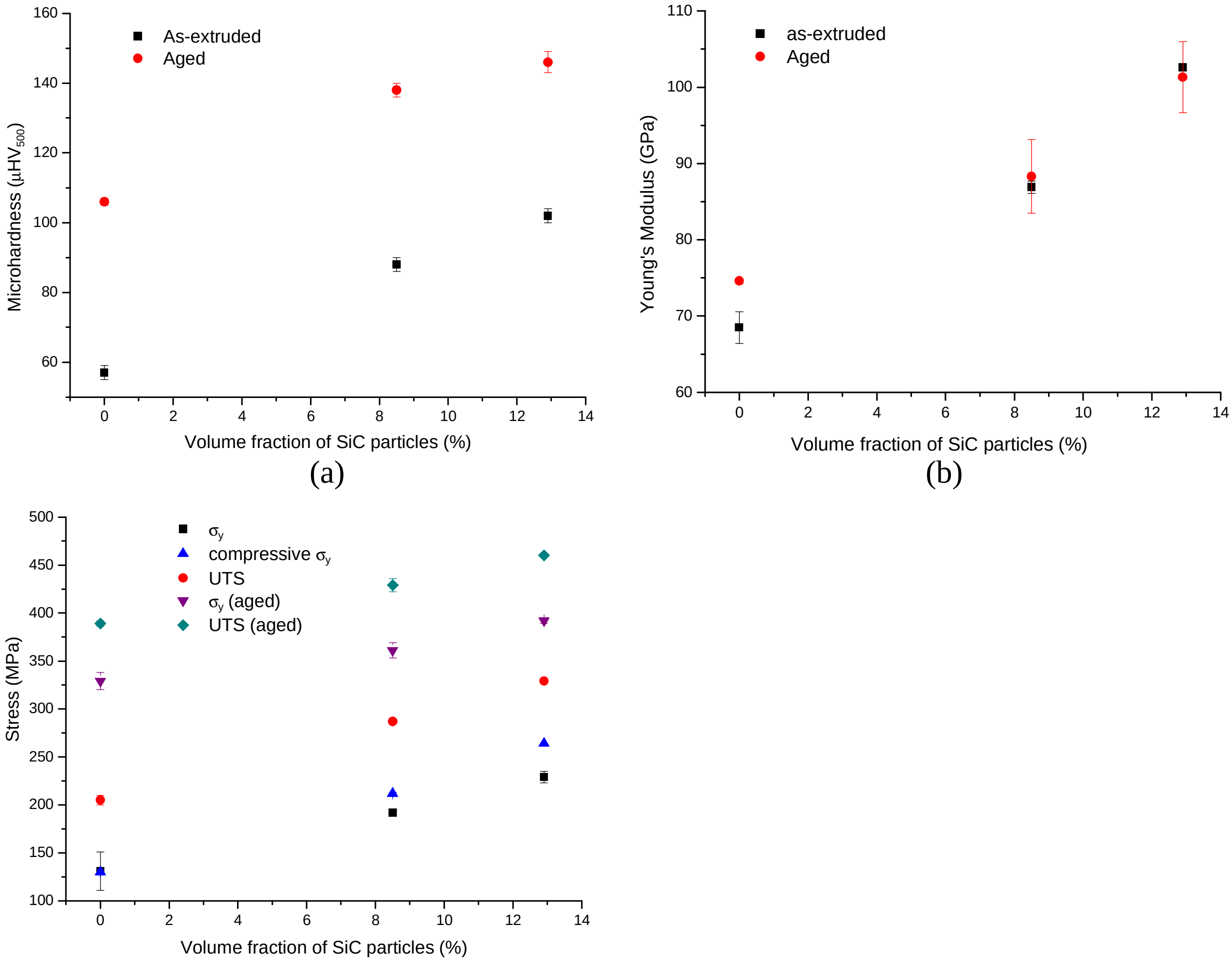

(a)

(b)

(c)

Figure 4.25: (a) Microhardness; (b) Young's modulus and (c) Proof stress, compressive proof stress and UTS of as-extruded and aging heat treated 6061Al, 6061Al/8.5SiC and 6061Al/12.9SiC samples as a function of volume fractions of SiC particles.

4.4 Summary

6061Al alloy composites reinforced with 8.5vol.% and 12.9vol.% of SiC particles with an average diameter of ~500nm have been successfully produced by powder metallurgy routes followed by extrusion. Despite of the inhomogeneous microstructure in the as-received billets, a homogeneous distribution of SiC particles among 6061Al alloy matrix has been obtained for both composites showing that extrusion is a very useful technique to further consolidate the materials, increase the density and homogenize the overall microstructure.

The mechanical properties of the produced composites show high tensile and compression strength and hardness whilst maintaining remarkable ductility at the same time. These superior mechanical properties are due to the improved strengthening mechanisms related with nano-sized reinforcement. In addition, the mechanical properties improve with increasing volume fraction of SiC particles and the application of aging heat treatment results in enhanced mechanical properties due to precipitation hardening.

The produced composites show superior fatigue properties than unreinforced 6061Al alloy and the similar composites reinforced with micron-sized SiC particles reported in literature, especially in high cycle fatigue regimes. The fracture surfaces of 6061Al alloy show the fatigue fracture mechanism of formation, growth and coalescence of fatigue voids and end with propagation of macro-cracks interconnecting the voids while the composite samples show a different mode of crack growth propagating primarily through the matrix and also some of the SiC particles serve as sites for microvoid nucleation due to debonding.

It can be concluded that powder metallurgy routes including high energy ball milling, HIPing followed by extrusion are effective procedures to produce homogeneously distributed nanoparticle reinforced Al alloy composites. And the nanocomposites have superior mechanical properties compared to either monolithic Al alloys or composites reinforced with micron-sized particles.

4.5 References

[1] (10-10-2013). Available: http://en.wikipedia.org/wiki/6061_aluminium_alloy

[2] (18-12-2013). Available: http://en.wikipedia.org/wiki/Silicon_carbide

[3] A. Korchef and A. Kahoul, "Corrosion behavior of commercial aluminum alloy processed by equal channel angular pressing," *International Journal of Corrosion,* vol. 2013, 2013.

[4] R. Thomas, "Microstructure development in multicomponent alloys," D Phil, University of Oxford, 1998.

[5] A. J. Knowles, X. Jiang, M. Galano, and F. Audebert, "Microstructure and mechanical properties of 6061 Al alloy based composites with SiC nanoparticles," *Journal of Alloys and Compounds*, 2014.

[6] J. A. Bannantine, J. J. Comer, and J. L. Handrock, *Fundamentals of metal fatigue analysis* vol. 90: Prentice hall Upper Saddle River, NJ, 1990.

[7] R. M. Wang, M. K. Surappa, C. H. Tao, C. Z. Li, and M. G. Yan, "Microstructure and interface structure studies of SiCp-reinforced Al (6061) metal-matrix composites," *Materials Science and Engineering A*, vol. 254, pp. 219-226, 1998.

[8] M. Shahzad, M. Chaussumier, R. Chieragatti, C. Mabru, and F. Rezai-Aria, "Effect of sealed anodic film on fatigue performance of 2214-T6 aluminum alloy," *Surface & Coatings Technology*, vol. 206, pp. 2733-2739, 2012.

[9] P. Rolland, V. Carlino, and R. Vane, "Improved carbon analysis with Evactron plasma cleaning," *Microscopy and Microanalysis,* vol. 10, pp. 964-965, 2004.

[10] R. Mitra, V. S. C. Rao, R. Maiti, and M. Chakraborty, "Stability and response to rolling of the interfaces in cast Al-SiCp and Al-Mg alloy-SiCp composites," *Materials Science and Engineering A*, vol. 379, pp. 391-400, 2004.

[11] J. Z. Fan, K. Zhang, L. K. Shi, and S. M. Zhang, "Interface characterization of the SiCp/Al composites made by powder metallurgy," *Journal of Materials Science & Technology,* vol. 15, pp. 147-150, 1999.

[12] D. J. Lloyd, "Particle-reinforced aluminum and magnesium matrix composites," *International Materials Reviews*, vol. 39, pp. 1-23, 1994.

[13] R. J. Arsenault and N. Shi, "Dislocation generation due to differences between the coefficients of thermal expansion," *Materials Science and Engineering,* vol. 81, pp. 175-187, 1986.

[14] N. Chawla, U. Habel, Y. L. Shen, C. Andres, J. W. Jones, and J. E. Allison, "The effect of matrix microstructure on the tensile and fatigue behavior of SiC particle-reinforced 2080

Al matrix composites," *Metallurgical and Materials Transactions a-Physical Metallurgy and Materials Science,* vol. 31, pp. 531-540, 2000.

[15] T. H. Courtney, *Mechanical behavior of materials*, 2nd ed. Boston ; London: McGraw-Hill, 2000.

[16] V. C. Srivastava, V. Jindal, V. Uhlenwinkel, and K. Bauckhage, "Hot-deformation behaviour of spray-formed 2014 Al-SiCp metal matrix composites," *Materials Science and Engineering A,* vol. 477, pp. 86-95, 2008.

[17] S. Qu, T. Siegmund, Y. Huang, P. D. Wu, F. Zhang, and K. C. Hwang, "A study of particle size effect and interface fracture in aluminum alloy composite via an extended conventional theory of mechanism-based strain-gradient plasticity," *Composites Science and Technology,* vol. 65, pp. 1244-1253, 2005.

[18] M. Rajamuthamilselvan, S. Ramanathan, and S. Krishnamohan, "Deformation stability of Al 7075/20%SiCp (63μm) composites during hot compression," Nagapattinam, Tamil Nadu, 2012, pp. 281-286.

[19] (14-05-2014). Available: http://en.wikipedia.org/wiki/Rule_of_mixtures

[20] Y. Wu and E. J. Lavernia, "Strengthening behavior of particulate reinforced MMCs," *Scripta Metallurgica Et Materialia,* vol. 27, pp. 173-178, 1992.

[21] Z. Zhang and D. L. Chen, "Consideration of Orowan strengthening effect in particulate-reinforced metal matrix nanocomposites: A model for predicting their yield strength," *Scripta Materialia*, vol. 54, pp. 1321-1326, 2006.

[22] Y. Yang, J. Lan, and X. C. Li, "Study on bulk aluminum matrix nano-composite fabricated by ultrasonic dispersion of nano-sized SiC particles in molten aluminum alloy," *Materials Science and Engineering A,* vol. 380, pp. 378-383, 2004.

[23] B. W. Xiong, Z. F. Xu, Q. S. Yan, C. C. Cai, Y. H. Zheng, and B. P. Lu, "Fabrication of SiC nanoparticulates reinforced Al matrix composites by combining pressureless infiltration with ball-milling and cold-pressing technology," *Journal of Alloys and Compounds,* vol. 497, pp. L1-L4, 2010.

[24] A. Mazahery and M. Ostadshabani, "Investigation on mechanical properties of nano-Al_2O_3-reinforced aluminum matrix composites," *Journal of Composite Materials,* vol. 45, pp. 2579-2586, 2011.

[25] T. W. Clyne and P. J. Withers, *An introduction to metal matrix composites,* First paperback edition 1995. ed. Cambridge: Cambridge University Press, 1993.

[26] H. G. Yazdabadi, A. Ekrami, H. S. Kim, and A. Simchi, "An investigation on the fatigue fracture of P/M Al-SiC nanocomposites," *Metallurgical and Materials Transactions a-Physical Metallurgy and Materials Science,* vol. 44A, pp. 2662-2671, 2013.

[27] T. S. Srivatsan, M. Al-Hajri, M. Petraroli, B. Hotton, and P. C. Lam, "Influence of silicon carbide particulate reinforcement on quasi static and cyclic fatigue fracture behavior of 6061 aluminum alloy composites," *Materials Science and Engineering A,* vol. 325, pp. 202-214, 2002.

[28] J. N. Hall, J. W. Jones, and A. K. Sachdev, "Particle-size, volume fraction and matrix strength effects on fatigue behavior and particle fracture in 2124 aluminum-SiCp composites," *Materials Science and Engineering A,* vol. 183, pp. 69-80, 1994.

[29] N. Chawla, C. Andres, J. W. Jones, and J. E. Allison, "Effect of SiC volume fraction and particle size on the fatigue resistance of a 2080 Al/SiCp composite," *Metallurgical and Materials Transactions a-Physical Metallurgy and Materials Science,* vol. 29, pp. 2843-2854, 1998.

[30] Z. M. Gasem and S. S. Ali, "Low-cycle fatigue behavior of powder metallurgy 6061 aluminum alloy reinforced with submicron-scale Al_2O_3 particles," *Materials Science and Engineering A,* vol. 562, pp. 109-117, 2013.

[31] R. Sunder, W. J. Porter, and N. E. Ashbaugh, "Fatigue voids and their significance," *Fatigue & Fracture of Engineering Materials & Structures,* vol. 25, pp. 1015-1024, 2002.

[32] Q. Y. Wang, N. Kawagoishi, and Q. Chen, "Fatigue and fracture behaviour of structural Al-alloys up to very long life regimes," *International Journal of Fatigue,* vol. 28, pp. 1572-1576, 2006.

[33] W. T. Riddell and R. S. Piascik, "Stress ratio effects on crack opening loads and crack growth rates in aluminum alloy 2024," *ASTM Special Technical Publication,* pp. 407-425, 1999.

[34] A. Borrego, R. Fernandez, M. D. Cristina, J. Ibanez, and G. Gonzalez-Doncel, "Influence of extrusion temperature on the microstructure and the texture of 6061Al-15 vol. % SiCw PM composites," *Composites Science and Technology,* vol. 62, pp. 731-742, 2002.

[35] X. J. Wang, L. Xu, X. S. Hu, K. B. Nie, K. K. Deng, K. Wu, *et al.*, "Influences of extrusion parameters on microstructure and mechanical properties of particulate reinforced magnesium matrix composites," *Materials Science and Engineering A,* vol. 528, pp. 6387-6392, 2011.

[36] U. Cocen and K. Onel, "Ductility and strength of extruded SiCp/aluminium-alloy composites," *Composites Science and Technology,* vol. 62, pp. 275-282, 2002.

[37] R. R. Fard and F. Akhlaghi, "Effect of extrusion temperature on the microstructure and porosity of A356-SiC(p) composites," *Journal of Materials Processing Technology*, vol. 187, pp. 433-436, 2007.

[38] B. F. Luan, N. Hansen, A. Godfrey, G. H. Wu, and Q. Liu, "High strength Al-Al_2O_3p composites: Optimization of extrusion parameters," *Materials & Design,* vol. 32, pp. 3810-3817, 2011.

[39] C. Sun, R. J. Shen, and M. Song, "Effects of sintering and extrusion on the microstructures and mechanical properties of a SiC/Al-Cu composite," *Journal of Materials Engineering and Performance*, vol. 21, pp. 373-381, 2012.

[40] L. M. Tham, M. Gupta, and L. Cheng, "Effect of reinforcement volume fraction on the evolution of reinforcement size during the extrusion of Al-SiC composites," *Materials Science and Engineering A,* vol. 326, pp. 355-363, 2002.

[41] U. F. Kocks, C. N. Tomé, and H.-R. Wenk, *Texture and anisotropy : preferred orientations in polycrystals and their effect on materials properties*. New York ; Cambridge: Cambridge University Press, 1998.

[42] A. Poudens, B. Bacroix, and T. Bretheau, "Influence of microstructures and particle concentrations on the development of extrusion textures in metal-matrix composites," *Materials Science and Engineering A,* vol. 196, pp. 219-228, 1995.

[43] R. N. Lumley, *Fundamentals of aluminium metallurgy : production, processing and applications*. Cambridge: Woodhead Publishing Ltd, 2011.

[44] H. K. Ahn and C. H. Yu, "Effect of SiC volume fraction on the age-hardening behavior in SiC particulate-reinforced 6061 aluminum alloy composites," *Metals and Materials-Korea*, vol. 7, pp. 1-7, 2001.

[45] Y. Song and T. N. Baker, "A calorimetric and metallographic study of precipitation process in AA6061 and its composites," *Materials Science and Engineering A*, vol. 201, pp. 251-260, 1995.

[46] L. Zhen, W. D. Fei, S. B. Kang, and H. W. Kim, "Precipitation behaviour of Al-Mg-Si alloys with high silicon content," *Journal of Materials Science*, vol. 32, pp. 1895-1902, 1997.

[47] R. X. Li, R. D. Li, Y. H. Zhao, L. Z. He, C. X. Li, H. R. Guan, *et al.*, "Age-hardening behavior of cast Al-Si base alloy," *Materials Letters*, vol. 58, pp. 2096-2101, 2004.

[48] M. Wang, D. Chen, Z. Chen, Y. Wu, F. Wang, N. Ma, *et al.*, "Mechanical properties of in-situ TiB_2/A356 composites," *Materials Science and Engineering A,* vol. 590, pp. 246-254, 2014.

[49] S. M. R. M. Abarghouie and S. M. S. Reihani, "Aging behavior of a 2024 Al alloy-SiCp composite," *Materials & Design,* vol. 31, pp. 2368-2374, 2010.

[50] A. M. El-Sabbagh, M. Soliman, M. A. Taha, and H. Palkowski, "Effect of rolling and heat treatment on tensile behaviour of wrought Al-SiCp composites prepared by stir-casting," *Journal of Materials Processing Technology,* vol. 213, pp. 1669-1681, 2013.

[51] C. Badini, "SiC whiskers aluminum 6061 composite - microstructure and mechanical characteristic anisotropy," *Journal of Materials Science,* vol. 25, pp. 2607-2614, 1990.

[52] S. Rajasekaran, N. K. Udayashankar, and J. Nayak, "T4 and T6 treatment of 6061 Al-15 vol. % SiC_P composite," *ISRN Materials Science,* vol. 2012, p. 5, 2012.

[53] D. Poirier, R. A. L. Drew, M. L. Trudeau, and R. Gauvin, "Fabrication and properties of mechanically milled alumina/aluminum nanocomposites," *Materials Science and Engineering A,* vol. 527, pp. 7605-7614, 2010.

[54] R. George, K. T. Kashyap, R. Raw, and S. Yamdagni, "Strengthening in carbon nanotube/aluminium (CNT/Al) composites," *Scripta Materialia,* vol. 53, pp. 1159-1163, 2005.

[55] Z. Y. Liu, Q. Z. Wang, B. L. Xiao, and Z. Y. Ma, "Clustering model on the tensile strength of PM processed SiCp/Al composites," *Composites Part a-Applied Science and Manufacturing,* vol. 41, pp. 1686-1692, 2010.

[56] Z. W. Wang, M. Song, C. Sun, D. H. Xiao, and Y. H. He, "Effect of extrusion and particle volume fraction on the mechanical properties of SiC reinforced Al-Cu alloy composites," *Materials Science and Engineering A,* vol. 527, pp. 6537-6542, 2010.

[57] K. Mahadevan, K. Raghukandan, T. Senthilvelan, B. C. Pai, and U. T. S. Pillai, "Investigations on the high cycle fatigue behaviour of stir cast AA 6061-SiCp composites," *Journal of Materials Science,* vol. 41, pp. 5548-5555, 2006.

[58] C. S. Shin and J. C. Huang, "Effect of temper, specimen orientation and test temperature on the tensile and fatigue properties of SiC particles reinforced PM 6061 Al alloy," *International Journal of Fatigue,* vol. 32, pp. 1573-1581, 2010.

[59] A. Slipenyuk, V. Kuprin, Y. Milman, V. Goncharuk, and J. Eckert, "Properties of P/M processed particle reinforced metal matrix composites specified by reinforcement concentration and matrix-to-reinforcement particle size ratio," *Acta Materialia,* vol. 54, pp. 157-166, 2006.

[60] S. Pal, K. K. Ray, and R. Mitra, "Room temperature mechanical properties and tensile creep behavior of powder metallurgy processed and hot rolled Al and Al-SiCp composites," *Materials Science and Engineering A,* vol. 527, pp. 6831-6837, 2010.

[61] Y. C. Kang and S. L. I. Chan, "Tensile properties of nanometric Al_2O_3 particulate-reinforced aluminum matrix composites," *Materials Chemistry and Physics*, vol. 85, pp. 438-443, 2004.

5. Cold rolling of 6061Al/SiC composites

Chapter 4 studies the extruded bars of 6061Al alloy and 6061Al/SiC composites. Except the extruded bars, some of the as-received 6061Al/SiC billets and the compacted 6061Al billets were also extruded into strips, solution heat treated and subjected to cold rolling with multiple rolling passes up until a final thickness of ~1mm. Table 3.4 lists the sample information and rolling details for each sample. Further details of the production of the cold rolled samples can be found in Chapter 3. In the following text, samples will be designated by their conditions. For example, “6061Al(SH)” means as-extruded and solution heat treated 6061Al alloy and “6061Al(SH)$_{3.6}$” means as-extruded and solution heat treated 6061Al alloy cold rolled up to a rolling strain of 3.6.

Microstructural characterization (Section 5.1) including XRD, SEM, texture XRD and EBSD analysis was carried out to investigate the microstructure development and texture evolution during cold rolling.

Mechanical property tests (Section 5.2) including microhardness and three-point bending tests, were carried out to study the effect of cold rolling on the development of mechanical properties.

The effect of extrusion parameters, rolling process and rolling strains on the microstructure and mechanical properties of the composite samples and the additions of SiC particles to the macroscopic and microscopic texture development is discussed in Section 5.3.

5.1 Microstructural characterization of as-extruded and cold rolled 6061Al alloy and 6061Al/SiC composites

5.1.1 X-ray diffraction analysis

XRD analysis has been carried out on the normal plane (TD-ED/RD) of the as-extruded, solution heat treated strips and cold rolled 6061Al(SH) alloy and 6061Al/SiC(SH) composites. The diffractograms are shown in Figure 5.1. For as-extruded and solution heat treated 6061Al(SH) alloy, fcc-Al and intermetallic phases, Mg_2Si and α-AlFeSi [1, 2], are observed. After cold rolling, similar phases have been detected.

For as-extruded and solution heat treated 6061Al/SiC(SH) composites, XRD analysis identifies fcc-Al, 6H-SiC and α-AlFeSi intermetallic phases. No other phases such as Al_4C_3 [3] are observed indicating that no interfacial reaction is detected by XRD. The X-ray diffractograms of the cold rolled composites do not show much difference compared with that of the as-extruded composites, indicating that cold rolling did not promote interfacial reactions or other precipitation process.

Figure 5.2 shows the difference in the Al (3 1 1) peak of the as-extruded and cold rolled 6061Al(SH) samples. It can be seen that the XRD pattern shows a decrease in peak intensity and an increase in width at half peak after cold rolling. In addition, it is also noticed that the Cu $K\alpha_2$ reflection becomes invisible after cold rolling due to the reflection broadening effect. The peak broadening effect indicates enhanced lattice distortions of the samples resulting from cold work. Similar XRD results were also reported by Korchef and Kahoul [2] on commercial Al alloys processed by Equal Channel Angular Pressing (ECAP) and Zhao et al. [4] on mechanically alloyed $6061Al/SiC_p$ composite powders. The relative Al peak intensity change in as-extruded and cold rolled conditions is an indication that the Al grains have rotated to different orientations during cold rolling, forming certain textures in cold rolled samples. The texture development will be discussed in detail in sections 5.1.3, 5.1.4 and 5.1.5.

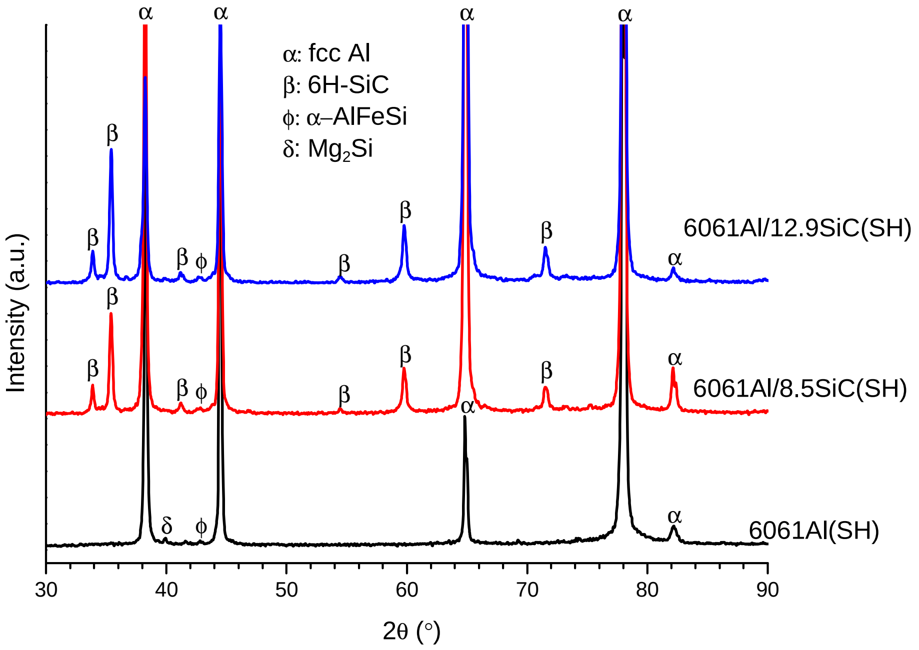

(a)

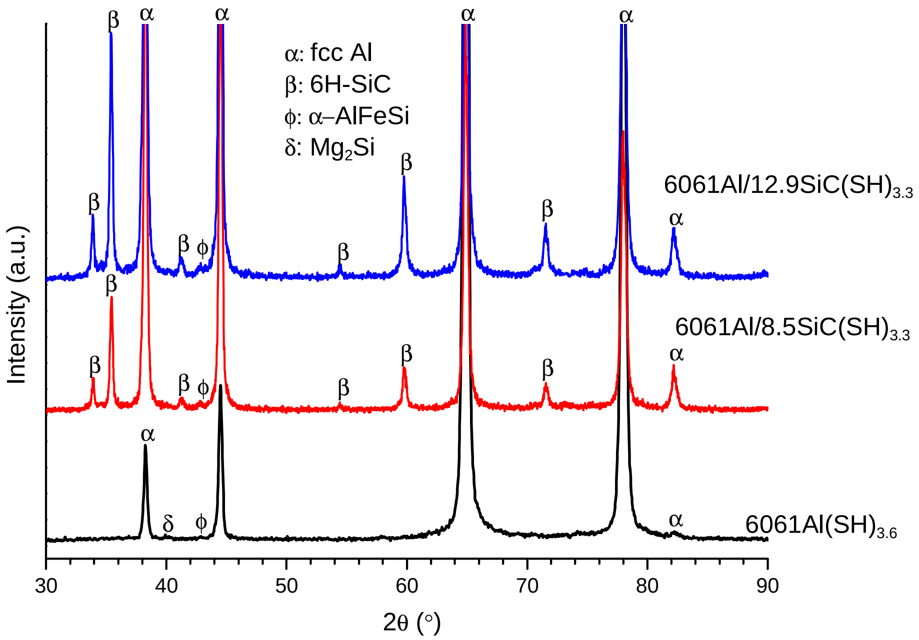

(b)

Figure 5.1: X-ray diffractograms of the normal plane (TD-ED/RD) of 6061Al(SH) alloy, 6061Al/8.5SiC(SH) and 6061Al/12.9SiC(SH) samples in (a) as-extruded and solution heat treated strips and (b) cold rolled conditions.

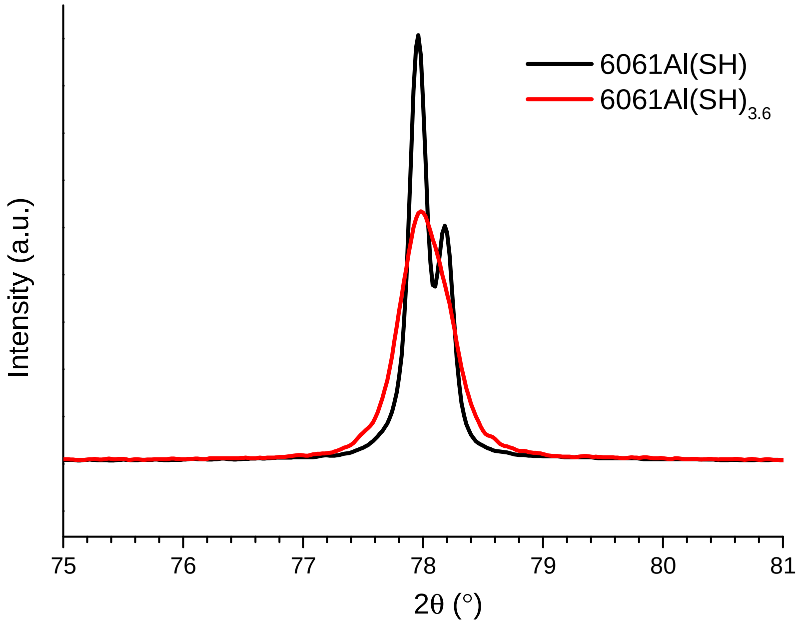

Figure 5.2: X-ray diffractograms of Al (3 1 1) peak of the normal plane (TD-ED/RD) of as-extruded, solution heat treated 6061Al(SH) and cold rolled 6061Al(SH)$_{3.6}$ samples.

5.1.2 Scanning electron microscopy analysis

Figure 5.3 shows the SEM images of as-extruded, solution heat treated strips and cold rolled 6061Al/SiC(SH) composites. From Figure 4.2, it has been observed that SiC particles are not homogeneously distributed in the as-received billets. There are some areas free of SiC particles. After extrusion into strips, those areas are observed as particle free bands with a width of 5-15μm along the extrusion direction (ED) (Figures 5.3(a) and (c)).

During cold rolling, with increasing rolling strains, the SiC particulate free zones became narrower and most of them disappeared after about 70% rolling reductions. Finally, a uniform distribution of SiC particles in the 6061Al matrix can be observed in Figures 5.3(b) and (d). Cracks began to develop at the side of the strips during cold rolling and grew inside with more rolling passes, especially for the 6061Al/12.9SiC(SH). However, no cracks were found in the middle of the strips.

Careful observation of Figures 5.3(b) and (d) also shows a reduced amount of porosity in the cold rolled composites when compared to the as-received or as-extruded samples. However, a small amount of SiC particle cracking perpendicular to the rolling direction was formed during cold rolling as illustrated in the inset pictures in Figures 5.3(b) and (d).

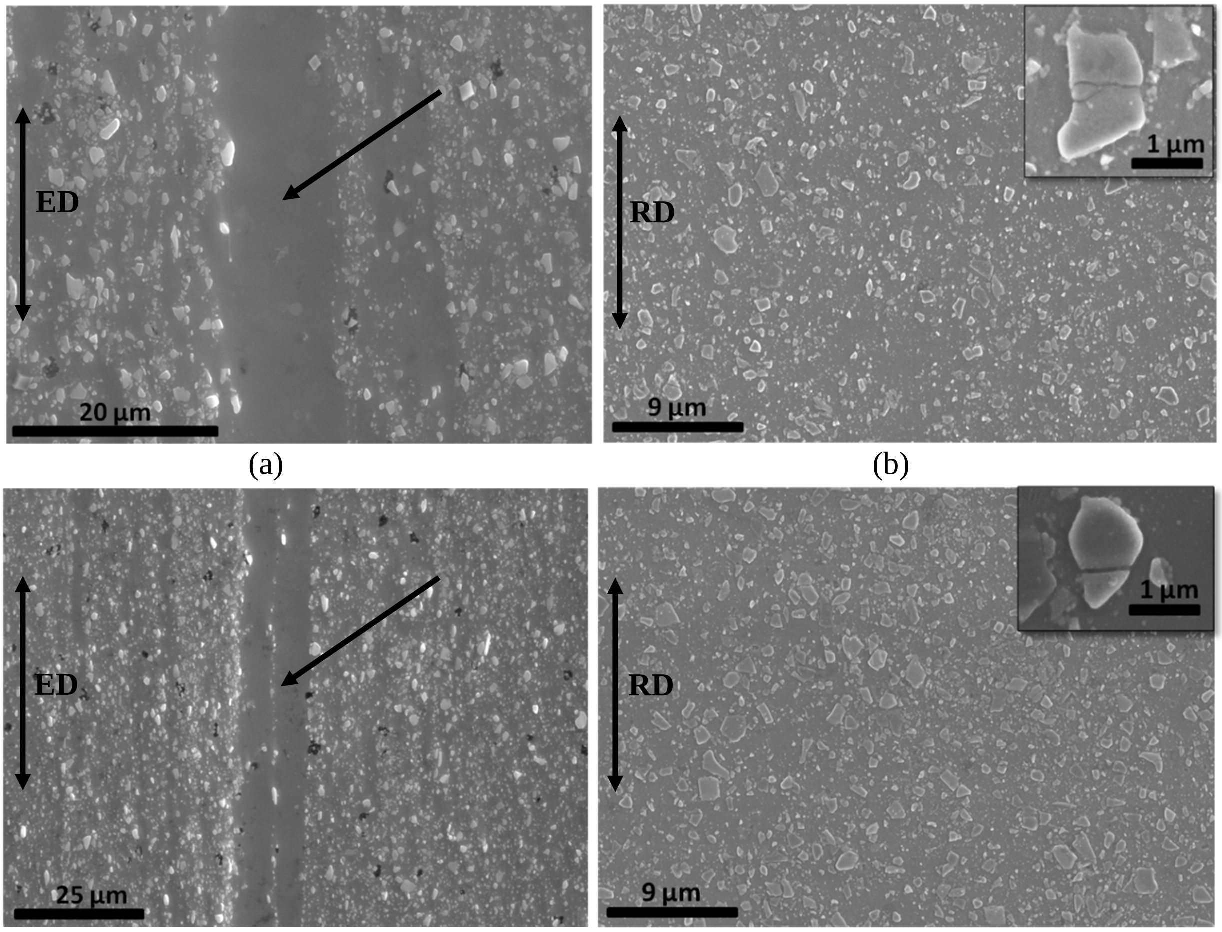

(a) (b)

(c) (d)

Figure 5.3: Secondary electron images in the normal plane (TD-ED/RD) of (a) as-extruded, solution heat treated 6061Al/8.5SiC(SH) strip; (b) cold rolled 6061Al/8.5SiC(SH)$_{3.3}$; (c) as-extruded, solution heat treated 6061Al/12.9SiC(SH) strip and (d) cold rolled 6061Al/12.9SiC(SH)$_{3.3}$. Arrows indicate particle free areas. Insets show cracked particles.

5.1.3 Macroscopic texture development during extrusion, solution heat treatment and cold rolling

ODFs of as-extruded 6061Al, 6061Al/8.5SiC and 6061Al/12.9SiC strips in constant φ_2 sections are shown in Figure 5.4. It can be seen from Figure 5.4(a) that for as-extruded 6061Al alloy, the extrusion texture can be described as a near β fibre mainly containing B' (Brass')-{1 0 1} <3 5 3> (φ_1=40°, Φ=45°, φ_2=0°), S'-{6 3 10} <6 10 7> (φ_1=60°, Φ=35°, φ_2=65°), C' (Copper')-{2 2 5} <5 4 4> (φ_1=90°, Φ=30°, φ_2=50°) and cube orientation. The texture components are totally different from the axial fibre textures obtained in Al alloys after extrusion into bars [5, 6], however, very similar to the typical β fibre texture obtained in cold and hot rolled Al, which contains Brass component ({1 0 1} <1 2 1>), S component ({1 2 3} <6 3 4>) and Copper component ({1 1 2} <1 1 1>) [7]. In the present work, the extruded samples have been compressed in the normal directions of the strips and elongated along the extrusion directions. Hence, it is not surprising that a near β fibre texture has formed after extrusion since the deformation state during extrusion of a circular bar to a flat strip is very similar to the plane strain rolling process [8].

For as-extruded 6061Al/SiC composites (Figures 5.4(b) and (c)), the texture components are quite similar with each other. Besides the random texture, there are three moderate strong texture components, which are B'-{1 0 1} <3 5 3> (φ_1=40°, Φ=45°, φ_2=0°) with a scatter along α fibre, S'-{5 3 10} <8 10 7> (φ_1=70°, Φ=30°, φ_2=60°), C'-{2 2 5} <5 4 4> (φ_1=90°, Φ=30°, φ_2=50°) and a weak scatter of the cube orientation. The three moderate strong texture components are near the typical β fibre texture components in both cold and hot rolled Al within several degree's tolerance.

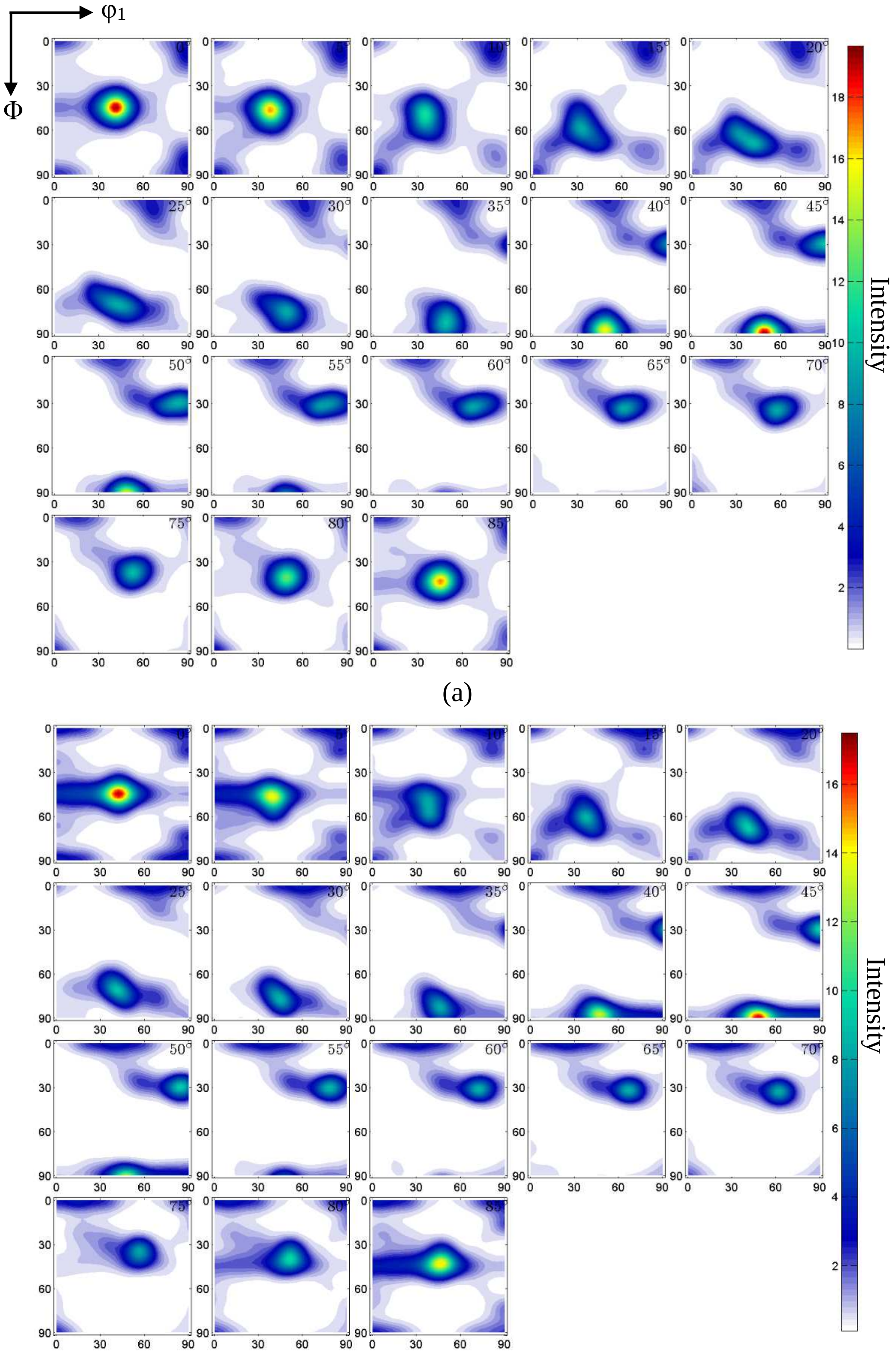

(a)

(b)

Figure 5.4: ODFs of (a) as-extruded 6061Al alloy, (b) as-extruded 6061Al/8.5SiC and (c) as-extruded 6061Al/12.9SiC samples in constant φ_2 sections.

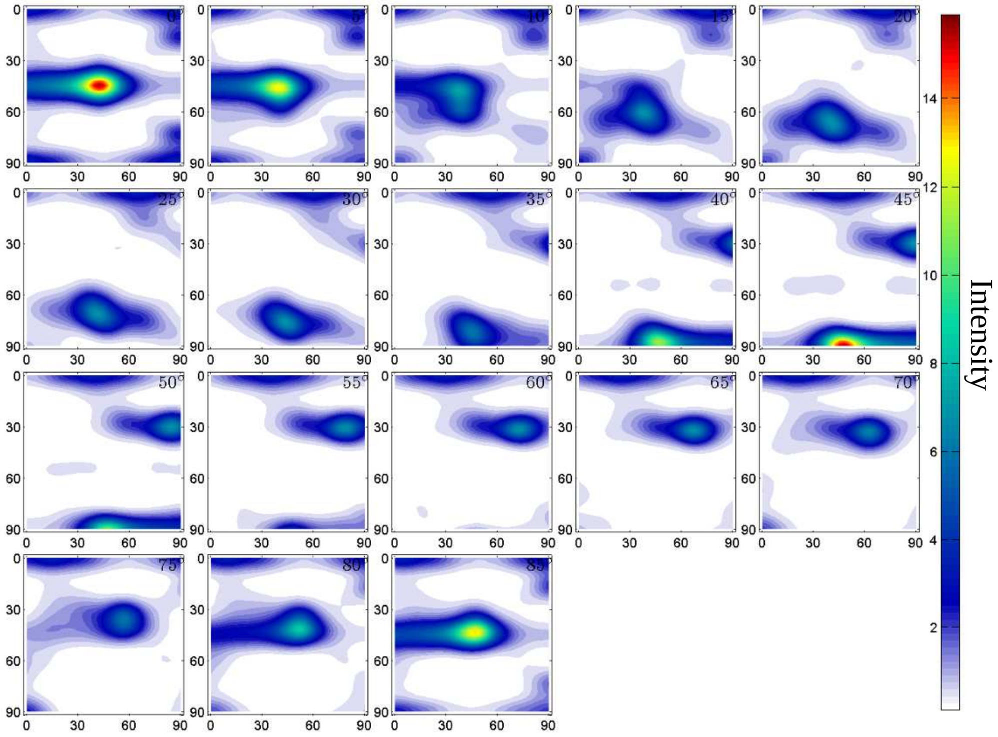

(c)

Figure 5.4: ODFs of (a) as-extruded 6061Al alloy, (b) as-extruded 6061Al/8.5SiC and (c) as-extruded 6061Al/12.9SiC samples in constant φ_2 sections.

Figure 5.5 shows the ODFs of as-extruded and solution heat treated 6061Al(SH), 6061Al/8.5SiC(SH) and 6061Al/12.9SiC(SH) strips in constant φ_2 sections. After solution heat treatment, the 6061Al(SH) alloy has similar near β fibre texture components with that of the as-extruded 6061Al sample observed in Figure 5.4(a), however, with a reduced intensity at B' and an increased intensity at cube component. Jata et al. [9] studied the hot deformation texture of as-extruded and solution heat treated Al-Li-Cu alloy and found that solution heat treatment following extrusion at lower temperatures (below 330°C) resulted in the loss of all the extrusion texture components due to recrystallization while solution heat treatment following elevated temperature extrusion (480°C) exhibited strong extrusion texture components due to negligible recrystallization. It is possible that in the present extrusion condition (extrusion temperature: 375°C, extrusion ratio: 6:1), localized Al grain recrystallization has occurred during solution heat treatment which has consumed some B' oriented grains and formed cube component, which is known as the most common recrystallization texture for Al alloys [10].

For the 6061Al/SiC(SH) composites (Figures 5.5(b) and (c)), the texture components are similar with that of the as-extruded composite samples, strongly suggesting that no recrystallization has occurred during solution heat treatment. The hard secondary phase particles have three main effects on recrystallization process according to Humphreys and Hatherly [10]:

1. Particles may increase the stored energy and hence the driving force for recrystallization may be increased;
2. Large particles (usually above 1μm) may act as nucleation sites for recrystallization (Particle stimulated nucleation-PSN);
3. Small and closely spaced particles may exert a significant pinning effect on both low and high angle grain boundaries (Zener drag).

The first two effects promote recrystallization while the last tends to hinder recrystallization. Hence, the overall recrystallization behaviour depends on which of these effects dominate [10]. Analysis of a large number of investigations show that the overall recrystallization behaviour is primarily a function of the volume fraction (f) and particle diameter (d) and recrystallization is impeded when $f/d > 0.1\mu m^{-1}$ [10, 11]. In the present work, f/d equals to $0.17\mu m^{-1}$ and $0.26\mu m^{-1}$ for 6061Al/8.5SiC(SH) and 6061Al/12.9SiC(SH) samples, respectively, strongly suggesting the retardation of recrystallization, thus leading to the unchanged texture after solution heat treatment.

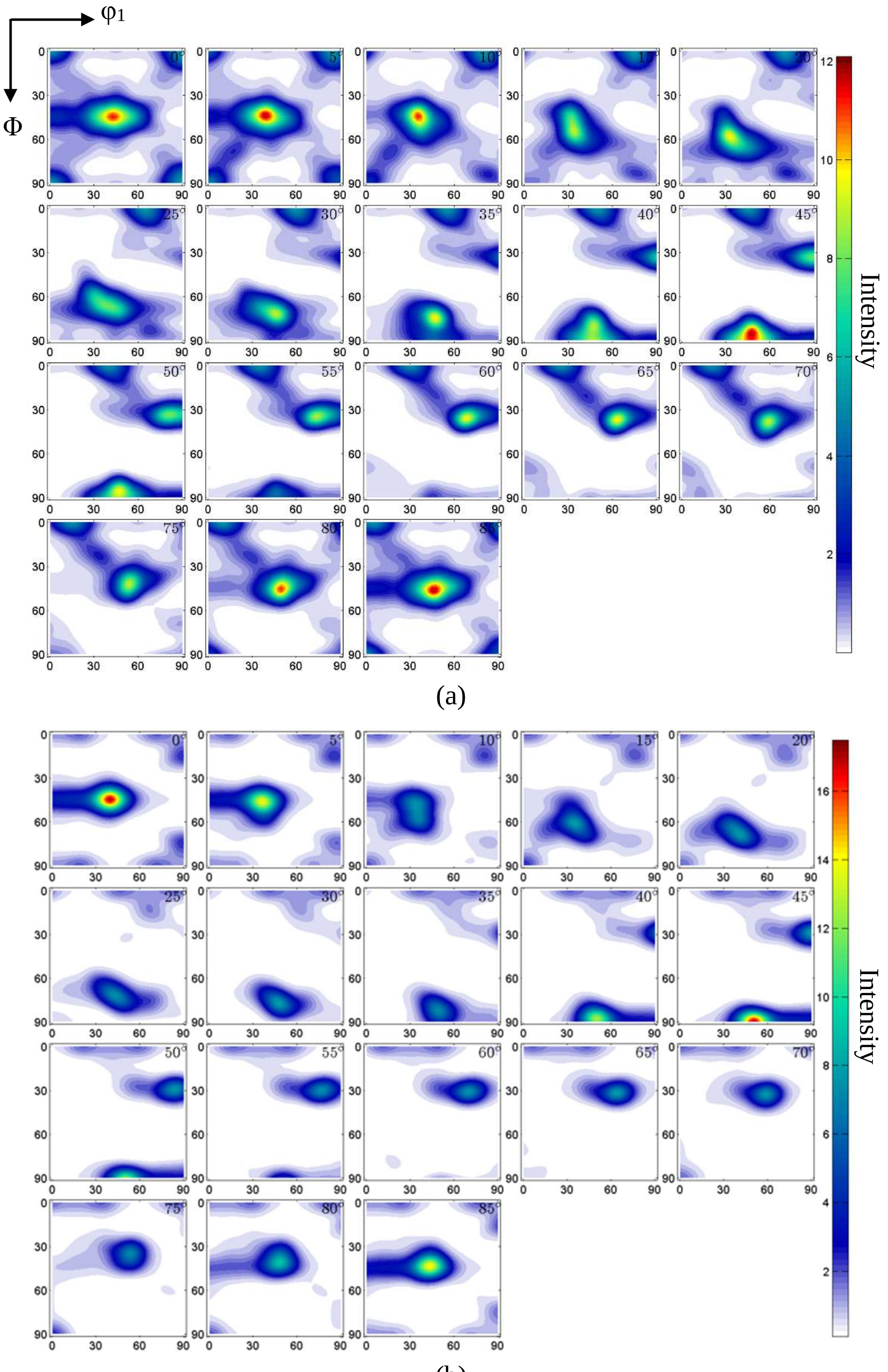

(a)

(b)

Figure 5.5: ODFs of as-extruded and solution heat treated (a) 6061Al(SH) alloy, (b) 6061Al/8.5SiC(SH) and (c) 6061Al/12.9SiC(SH) samples in constant φ_2 sections.

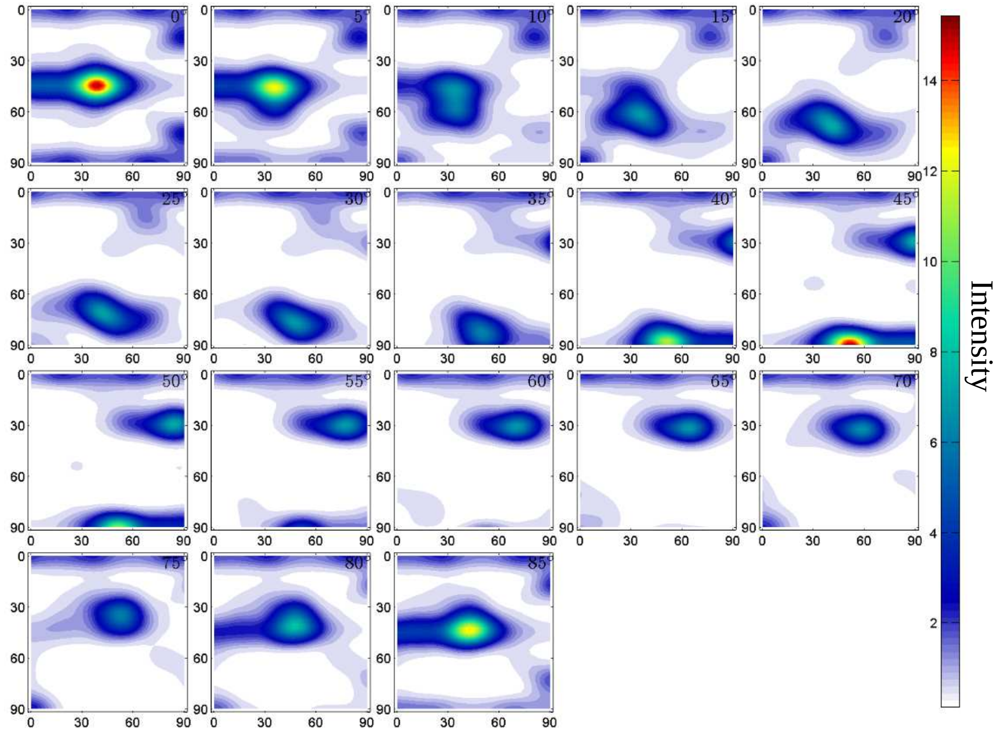

(c)

Figure 5.5: ODFs of as-extruded and solution heat treated (a) 6061Al(SH) alloy, (b) 6061Al/8.5SiC(SH) and (c) 6061Al/12.9SiC(SH) samples in constant φ_2 sections.

After cold rolling, for 6061Al(SH)$_{3.6}$ sample (Figure 5.6(a)), the texture components in the near β fibre have slightly evolved while with increased intensities. For 6061Al/SiC(SH)$_{3.3}$ composites (Figures 5.6(b) and (c)), the textures of the composites are quite random with a bit higher intensities near α fibre after cold rolling. All these features are more clearly shown in Figure 5.7 which depicts the intensities along β orientation lines of the Al matrix in solution heat treated and cold rolled samples.

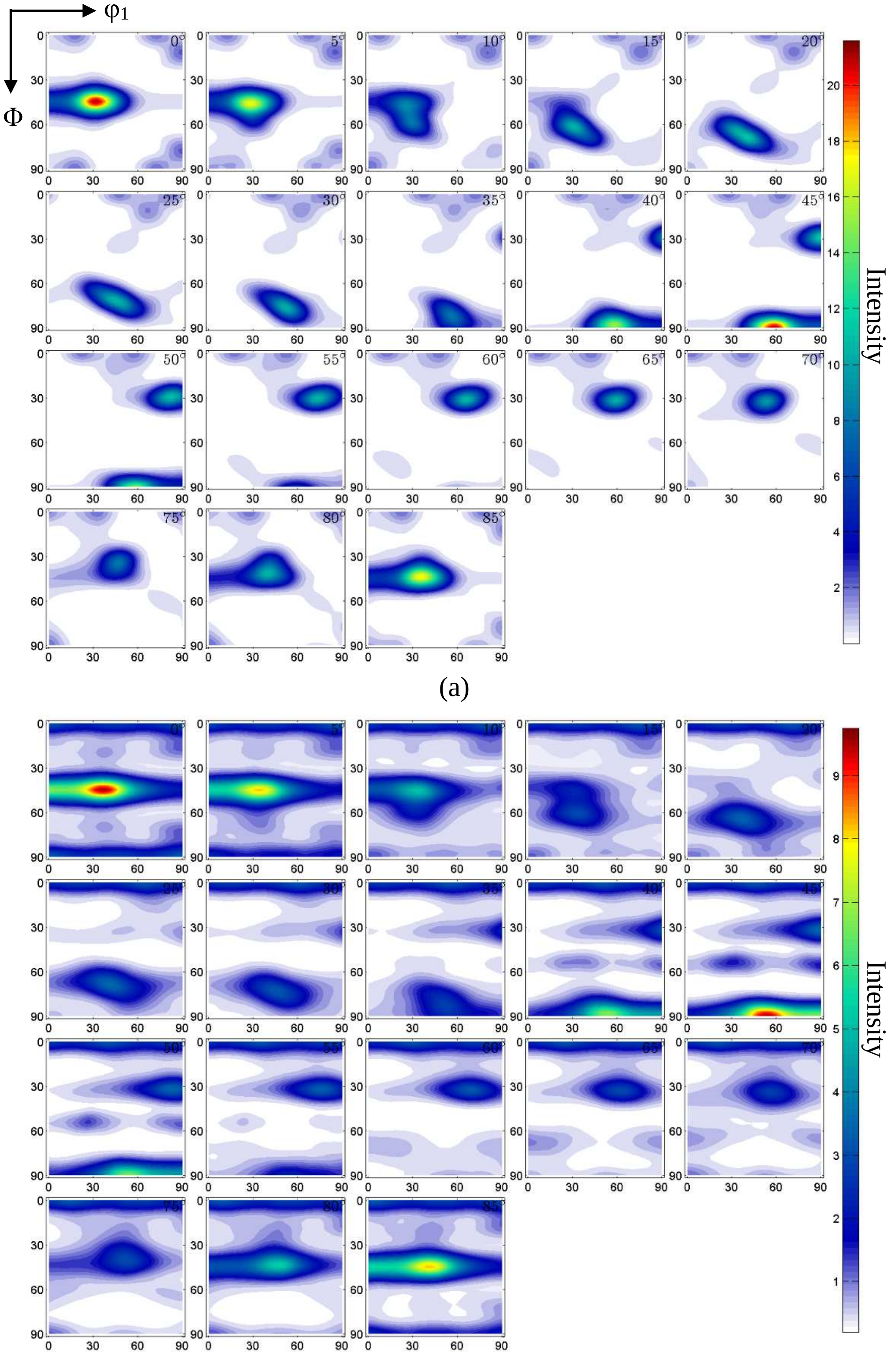

(a)

(b)

Figure 5.6: ODFs of cold rolled (a) 6061Al(SH)$_{3.6}$, (b) 6061Al/8.5SiC(SH)$_{3.3}$ and (c) 6061Al/12.9SiC(SH)$_{3.3}$ samples in constant φ_2 sections.

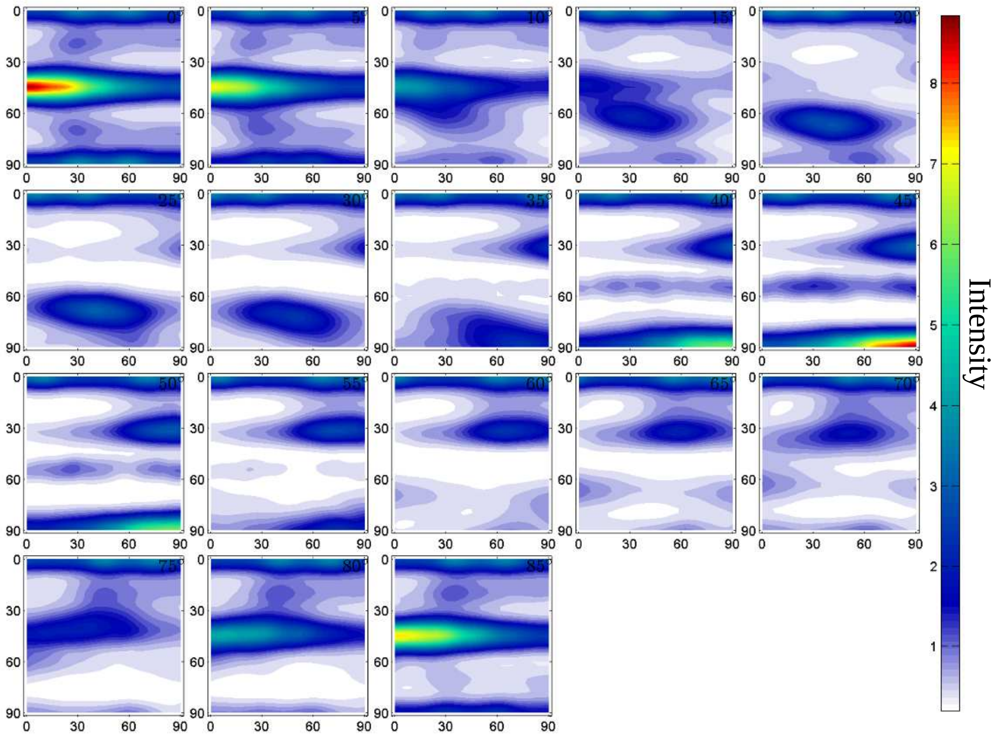

(c)

Figure 5.6: ODFs of cold rolled (a) 6061Al(SH)$_{3.6}$, (b) 6061Al/8.5SiC(SH)$_{3.3}$ and (c) 6061Al/12.9SiC(SH)$_{3.3}$ samples in constant φ_2 sections.

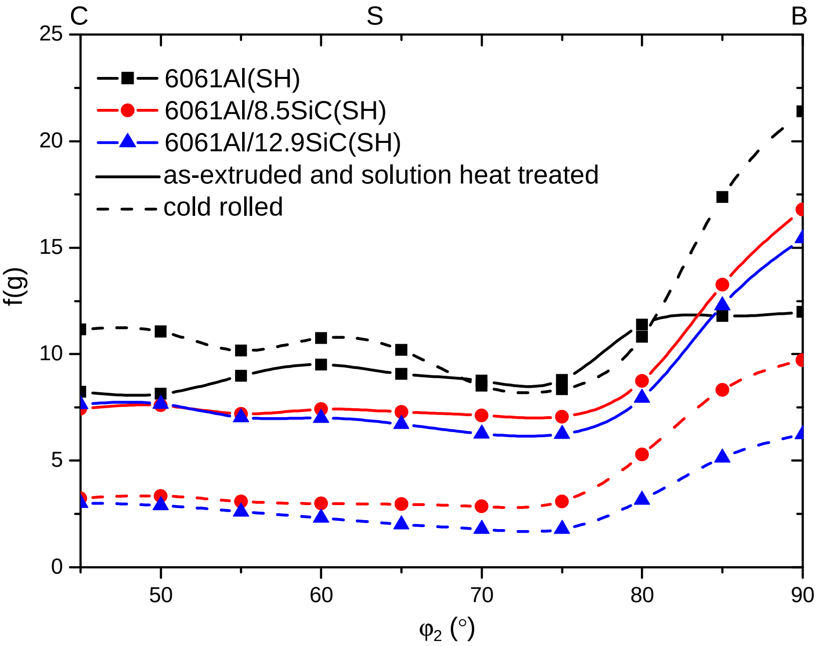

Figure 5.7: β fibre intensities of the Al matrix of as-extruded, solution heat treated strips and cold rolled 6061Al(SH)$_{3.6}$, 6061Al/8.5SiC(SH)$_{3.3}$ and 6061Al/12.9SiC(SH)$_{3.3}$ samples.

It can be seen from Figure 5.7 that for 6061Al(SH)$_{3.6}$, increased intensities near Copper, Brass and S components are observed after cold rolling, while for 6061Al/SiC(SH)$_{3.3}$, the intensities along β fibre have declined. With increased rolling strains, the texture components would normally become sharper [7], as is observed for 6061Al(SH) alloy. However, in the case of 6061Al/SiC(SH) composites, the texture intensities have dropped significantly indicating weaker and randomized texture with rolling strains.

5.1.4 Electron backscatter diffraction analysis of as-extruded strips

Texture XRD gives information about macroscopic texture development, to investigate the texture in microscopic level, EBSD analysis was also carried out.

Figure 5.8 shows the EBSD orientation maps of as-extruded 6061Al alloy, 6061Al/8.5SiC and 6061Al/12.9SiC strips with respect to the normal direction (ND). The black and white lines from the EBSD maps indicate the locations of high angle grain boundaries (≥15°) and low angle grain boundaries (2°-15°), respectively. Neighboring grains with misorientations less than 15° are considered as subgrain structure in the following text.

As can be seen in Figure 5.8(a), hot extrusion of 6061Al alloy has led to the formation of elongated grains aligned along the extrusion direction containing subgrain structures. The subgrain size is measured as an average width of 1.6±0.3μm and length of 2.0±0.2μm according to the mean linear intercept method (see section 3.3.3). The scattered inverse pole figure (IPF) data shows a typical near β fibre texture which is consistent with the ODF result obtained from Figure 5.4(a). The misorientation distribution plot shows that the Al grain boundary populations are not uniformly distributed. A peak exists in the range of 0-10°, which corresponds to a large fraction of low angle grain boundaries (about 25%-30%) located within the elongated grains.

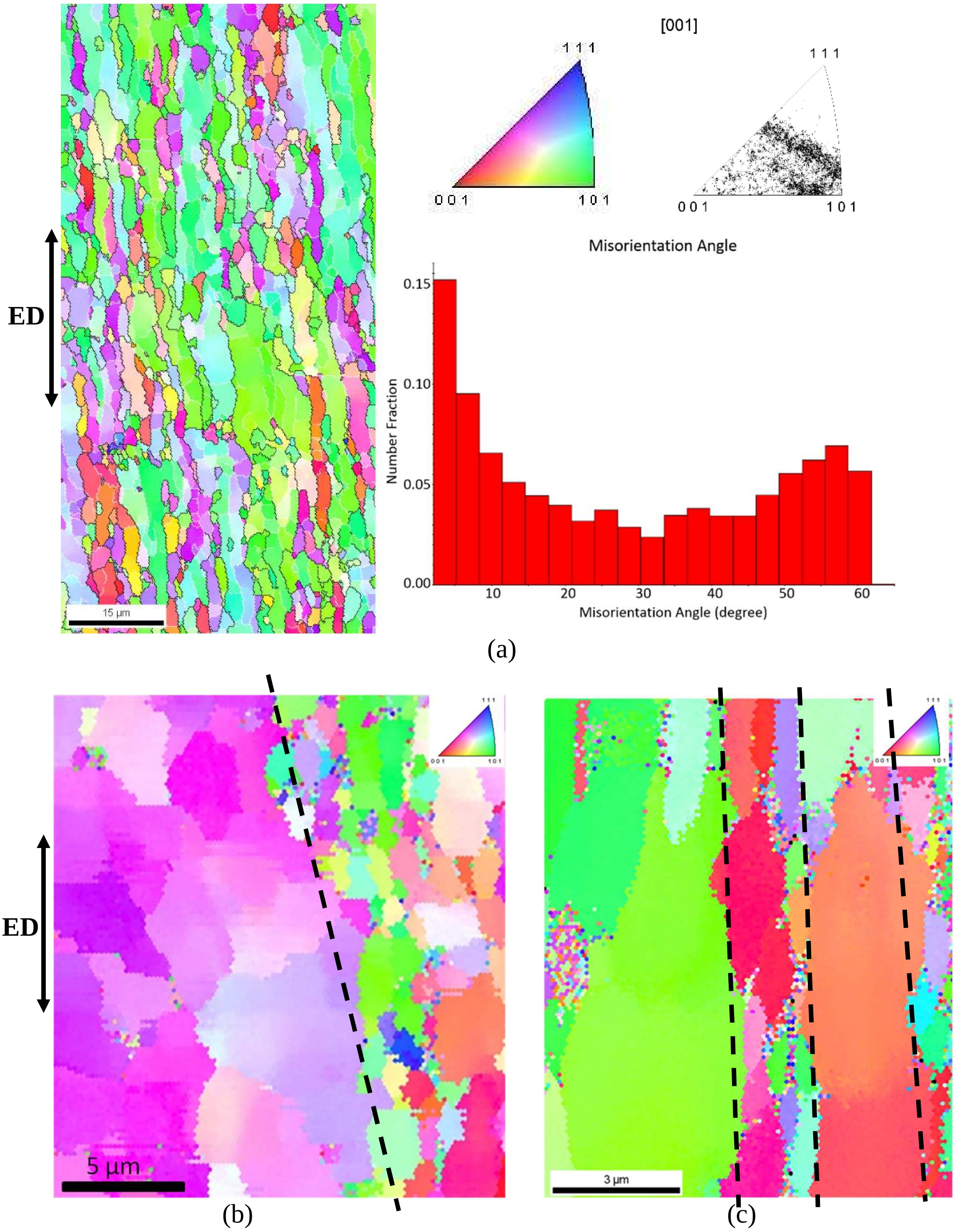

(a)

(b) (c)

Figure 5.8: (a) EBSD orientation map with scattered inverse pole figure (IPF) and misorientation distribution plot of as-extruded 6061Al alloy in the normal plane (TD-ED) (Black lines indicate high angle grain boundaries: θ≥15°, white lines indicate low angle grain boundaries: 2°<θ<15°), EBSD orientation maps of (b) as-extruded 6061Al/8.5SiC and (c) as-extruded 6061/12.9SiC strips in the normal plane (TD-ED).

Several EBSD measurements have been carried out on the particle free bands and particle rich zones of as-extruded 6061Al/8.5SiC and 6061Al/12.9SiC strips. Two representative EBSD orientation maps are shown in Figures 5.8(b) and (c). The particle free bands and particle rich zones are separated by the dash lines in the figure. It can be seen that the Al grain alignment near SiC particles is different from those in the particle free bands. Most of the Al grains in the particle free bands are elongated and have been rotated to similar orientations within several degree's tolerance (In most measurements, Al grains in the particle free bands have {1 1 2} or {1 0 1} planes nearly parallel to the extrusion plane). However, in the particle rich zones, much smaller Al grains with different orientations have been observed. In addition, most of the grains are nearly equiaxed instead of elongated towards ED.

A closer look of the particle rich zones in Figures 5.8(b) and (c) shows the presence of a small amount of Al grains having {0 0 1} planes nearly parallel to the extrusion plane, which is in agreement with the ODF results of a weak scattered cube component for the as-extruded 6061Al/SiC composites. The cube texture is known as the most common recrystallization texture for Al alloys [10]. In order to find out if any dynamic recrystallization happened for 6061Al/SiC composites during hot extrusion, EBSD scans were performed on the SiC rich areas of the as-received and as-extruded 6061Al/8.5SiC composites (Figure 5.9) where nearly equiaxed grains have been observed. The average Al matrix grain size is estimated as 1.3±0.4μm and 1.4±0.4μm for the as-received and as-extruded 6061Al/8.5SiC composites respectively according to the EBSD software analysis.

The comparison of the Al matrix grain size between the as-received and as-extruded 6061Al/8.5SiC samples shows no sign of grain refinement due to dynamic recrystallization in the particle rich zones and it is already mentioned in section 5.1.3 that fine closely spaced particles in the present composites suppress recrystallization. Hence, it can be said that there is hardly any dynamic recrystallization has happened for the composites during extrusion.

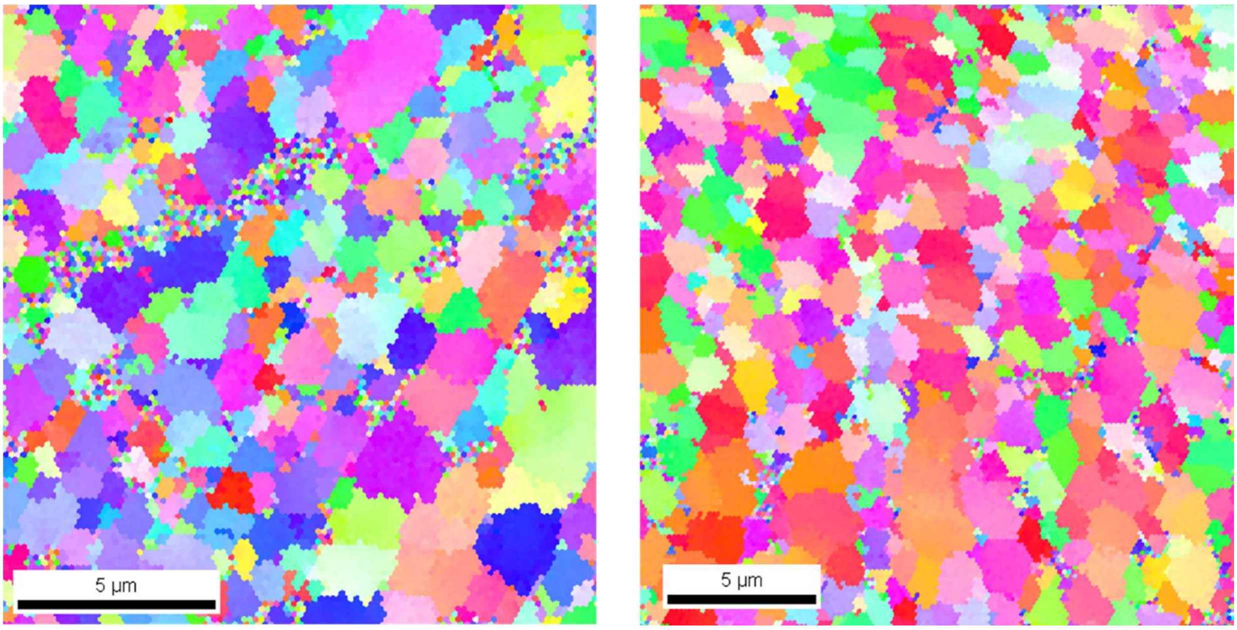

(a) (b)

Figure 5.9: EBSD orientation maps in SiC rich zones of (a) as-received 6061Al/8.5SiC composite in longitudinal plane and (b) as-extruded 6061Al/8.5SiC composite in the normal plane (TD-ED).

Another possible explanation for the presence of near cube component is the stability of the cube orientation during plastic deformation at high temperatures. Quantitative analysis on hot deformation textures of Al alloys suggests that the cube orientation is stable during large plane strain reductions at high temperatures [12-16]. Maurice and Driver [12, 13, 16] have studied and simulated the stability of cube component of Al alloys by channel die compression tests at different temperatures, which showed the appearance of a significant cube component after plane strain compression at 400ºC. It is suggested by Maurice and Driver [12, 13, 16] that at deformation temperatures above 300ºC and high strain rates, the original {1 1 1}<1 1 0> slip systems are replaced by {1 1 0}<1 1 0> type. The onset of {1 1 0}<1 1 0> non-octahedral slip systems stabilizes the cube component which would otherwise rotate towards other more stable orientations. Both experimental results and numerical simulations have verified the active non-octahedral slip systems for cube and near cube orientations and the stability of cube orientation during high temperature deformations. In the as-extruded 6061Al/SiC samples studied in the present work, it is possible that the near cube component is actually the cube orientation in the as-received samples which has survived through hot extrusion at 375ºC with just an ER of 6:1.

5.1.5 Electron backscatter diffraction analysis of cold rolled samples

EBSD analysis of cold rolled samples was also carried out and the results are shown in Figure 5.10. Figure 5.10(a) shows the EBSD orientation map with scattered IPF and misorientation distribution plot of cold rolled 6061Al(SH)$_{3.6}$ sample. After cold rolling, severely fragmented grains with a subgrain size of ~1μm are observed in Figure 5.10(a). The fractions of low angle grain boundaries (2°-15°) have increased from 37.1% in the as-extruded state to 52.8% after cold rolling, indicating the development of subgrain structure during cold rolling. In addition, the misorientation distribution plot shows increased fractions of low angle grain boundaries (about 45%-50%) within the range of 0-10° and largely decreased high angle grain boundaries compared with Figure 5.8(a), also suggesting the development of substructures. The scattered IPF data in Figure 5.10(a) shows the formation of a strong β fibre texture with the highest intensities near Brass and Copper components, which is consistent with the ODF results in section 5.1.3.

Figures 5.10(b) and (c) show the EBSD orientation maps for cold rolled 6061Al/8.5SiC(SH)$_{3.3}$ and 6061Al/12.9SiC(SH)$_{3.3}$ composites. It can be seen that both the cold rolled composites have nearly equiaxed grains with no preferred orientations, agreeing with the ODF results in Figure 5.6. In addition, the EBSD analysis shows both samples have more than 85% fractions of high angle grain boundaries after cold rolling. Similar results that an increased fraction of high angle grain boundaries and misorientation angle of the Al matrix have also been reported by Alizadeh et al. [17] on 1050Al/SiC$_p$ composites during accumulative roll bonding (ARB) process and were ascribed to the increased local strain and dislocation density in the matrix nearby the particles, enhancing local lattice rotations close to the particles and increasing the fraction of high angle grain boundaries.

Also, it is notable that the Al grains in cold rolled 6061Al/8.5SiC$(SH)_{3.3}$ and 6061Al/12.9SiC$(SH)_{3.3}$ composites are much smaller compared to the as-extruded composites probably due to the cold rolling process and the presence of SiC particles. According to EBSD analysis, the Al grain size for cold rolled 6061Al/8.5SiC$(SH)_{3.3}$ and 6061Al/12.9SiC$(SH)_{3.3}$ samples is 1.0±0.3μm and 0.9±0.3μm, respectively. During most deformation process, such as equal channel angular extrusion [18], high pressure torsion [19] and cold rolling [20], the original grains will be subdivided extensively and materials with very fine grains can be achieved. The presence of homogeneously distributed hard particles (SiC in the present work) can introduce more grain refinement probably due to the increased geometrically necessary dislocations around the particles as a result of the complicated local deformation near the hard particles [17] and the pinning effect where the particles can pin the movement of grain boundaries and inhibit grain growth [21]. Similar results of the formation of ultrafine Al matrix grains were also reported by Alizadeh et al. [17] on accumulative roll bonding (ARB) processed 1050Al/SiC_p composites and Ahn et al. [21] on friction stir welding (FSW) fabricated 5083Al/SiC_p composites.

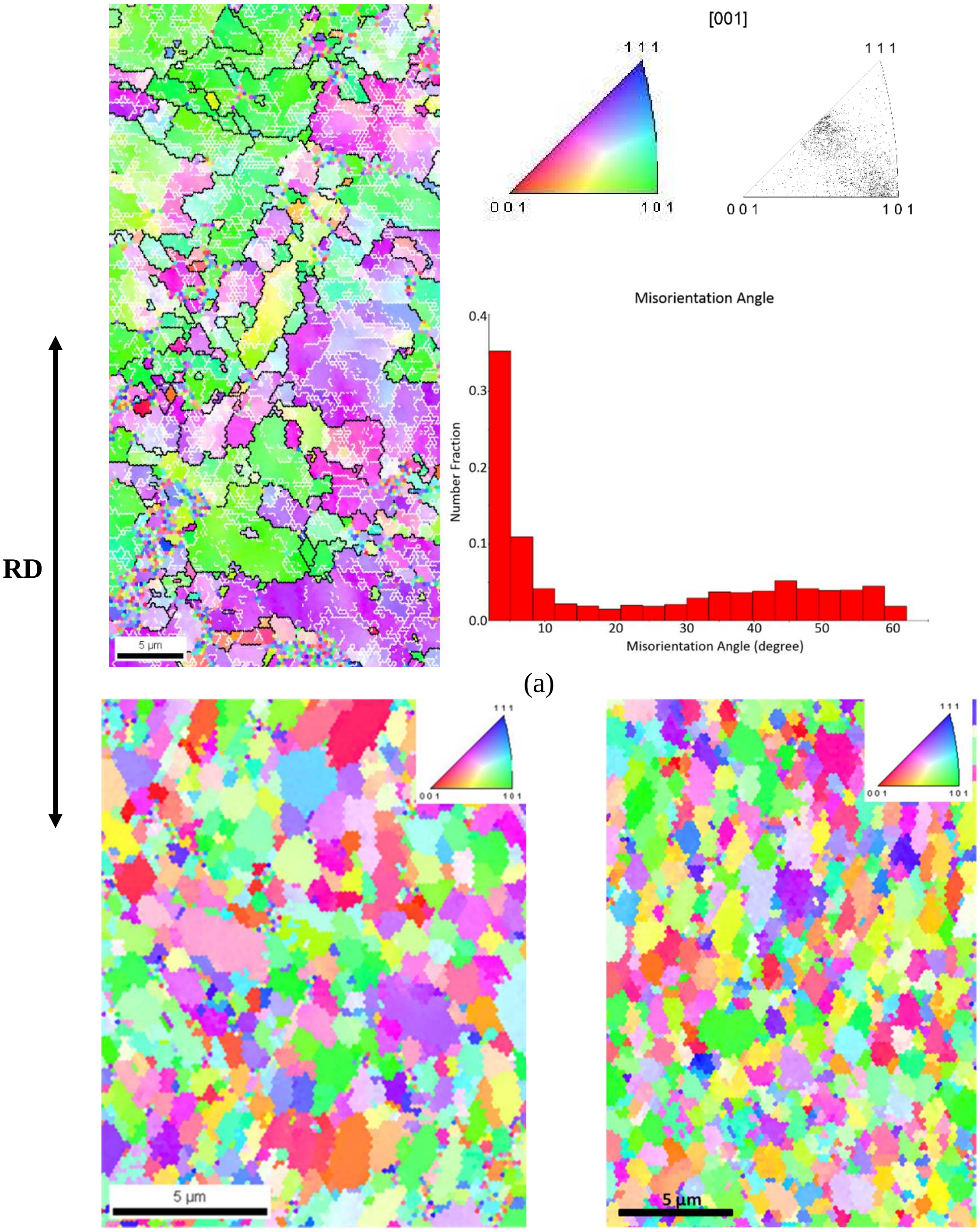

(a)

(b)

(c)

Figure 5.10: (a) EBSD orientation map with scattered inverse pole figure (IPF) and misorientation distribution plot of cold rolled 6061Al(SH)$_{3.6}$ sample in the normal plane (TD-RD) (Black lines indicate high angle grain boundaries: θ≥15°, white lines indicate low angle grain boundaries: 2°<θ<15°), EBSD orientation maps of (b) 6061Al/8.5SiC(SH)$_{3.3}$ and (c) 6061Al/12.9SiC(SH)$_{3.3}$ samples in the normal plane (TD-RD).

5.2 Mechanical properties and work hardening of as-extruded and cold rolled 6061Al alloy and 6061Al/SiC composites

5.2.1 Microhardness analysis

Microhardness tests were carried out on as-extruded and cold rolled 6061Al(SH) and 6061Al/SiC(SH) samples after every rolling pass and the results are plotted as a function of the rolling true strain in Figure 5.11.

Figure 5.11 shows that the microhardness of all samples increase with increasing rolling strains due to work hardening up to a maximum limit value. All of the values for the composites are much higher than those of the unreinforced alloy indicating effective strengthening from the SiC particles. In addition, the samples exhibit different work hardening capacities. For 6061Al(SH) alloy, the microhardness values have increased ~100%, from 60±1μHV$_{200}$ to about 126±1μHV$_{200}$. While for 6061Al/8.5SiC(SH) composite, the values have increased ~39%, from 109±3μHV$_{200}$ to 152±2μHV$_{200}$. It seems that the 6061Al(SH) alloy has a larger work hardening capacity than the 6061Al/SiC(SH) composites.

The empirical power-law relationship developed by Holloman [22] has been used to describe the microhardness-strain curves:

$$\mu HV = \mu HV_0 + K \cdot (\varepsilon - \varepsilon_0)^m \qquad (5.1)$$

where μHV is the microhardness as a function of rolling strain (ε), μHV$_0$ is the initial microhardness value in the as-extruded condition, K and m are fitting parameters dependent on the material and the testing temperature, ε_0 is the initial strain value after extrusion, which equals to 1.77 in the present work.

The fitted lines in Figure 5.11 show that the initial work hardening rate is high and then decreases with increasing strains for all materials. The work hardening rate is governed by dislocation accumulations and dynamic recovery rate [23]. At the beginning of deformation, the number of dislocations increases as deformation proceeds. Dislocations on different slip systems intersect and the intersections block the dislocations from further motion, causing rapid work hardening rate [23]. Then at a certain point, cross slip or climb of dislocations is launched, causing dislocations with opposite signs to meet and annihilate, a lowering work hardening ability is developed. With further deformations, a balance between dislocation generation and annihilation is created where no more hardening happens and a stress limit is reached [24].

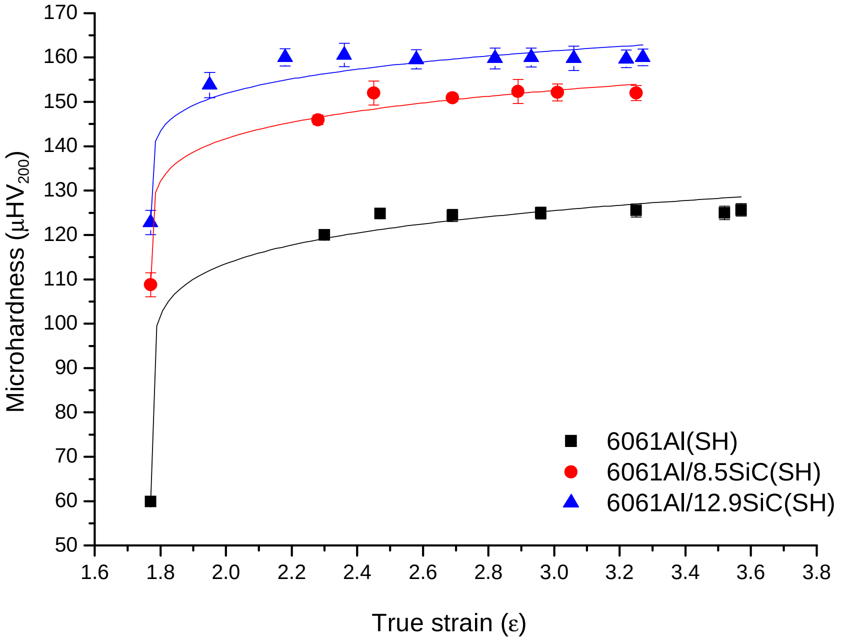

Figure 5.11: Microhardness of as-extruded and cold rolled 6061Al(SH), 6061Al/8.5SiC(SH) and 6061Al/12.9SiC(SH) samples as a function of the rolling true strain and microhardness fitted lines based on eq. 5.1.

5.2.2 Three-point bending tests of as-extruded, solution heat treated and cold rolled samples

Three-point bending tests of as-extruded, solution heat treated and cold rolled samples were carried out for 6061Al alloy, 6061Al/SiC samples. The calculated flexural stress–flexural strain curves for different samples are plotted in Figure 5.12 and the yield stress values are summarized and plotted as a function of the volume fractions of SiC particles in Table 5.1 and Figure 5.13, respectively. It should be noted that none of the samples have fractured during the tests since the equipment limitation has reached.

From Figures 5.12 and 5.13, it can be observed that the solution heat treated samples have higher yield strength compared to the as-extruded samples due to solid solution strengthening and the cold rolled samples have the highest yield strength due to work hardening. For example, the yield strength of cold rolled 6061Al(SH)$_{3.6}$ and 6061Al/12.9SiC(SH)$_{3.3}$ samples has increased by almost 100% and 28% compared with solution heat treated samples, respectively. Compared to 6061Al alloy samples, the yield strength of the composites increases with increasing volume fraction of SiC particles and the correlation seems to be linear.

The extent of the increase in yield strength due to the additions of SiC particles of cold rolled samples has declined compared to as-extruded or solution heat treated samples. For example, the yield strength of solution heat treated and cold rolled 6061Al/12.9SiC(SH) composites has increased by almost 105% and 31% compared with solution heat treated and cold rolled 6061Al(SH) alloy, respectively. This could be due to multiple reasons. One could be the increasing amount of SiC particle cracking during cold rolling, as shown in Figure 5.3. Another reason could be the texture strengthening effect. Texture analysis in sections 5.1.3, 5.1.4 and 5.1.5 suggests that with further rolling passes, the composites have no preferred orientations while the 6061Al(SH) alloy has developed a sharp β fibre texture, causing a reduced amount of texture strengthening for cold rolled 6061Al/SiC(SH)$_{3.3}$ composites when compared to cold rolled 6061Al(SH)$_{3.6}$ alloy.

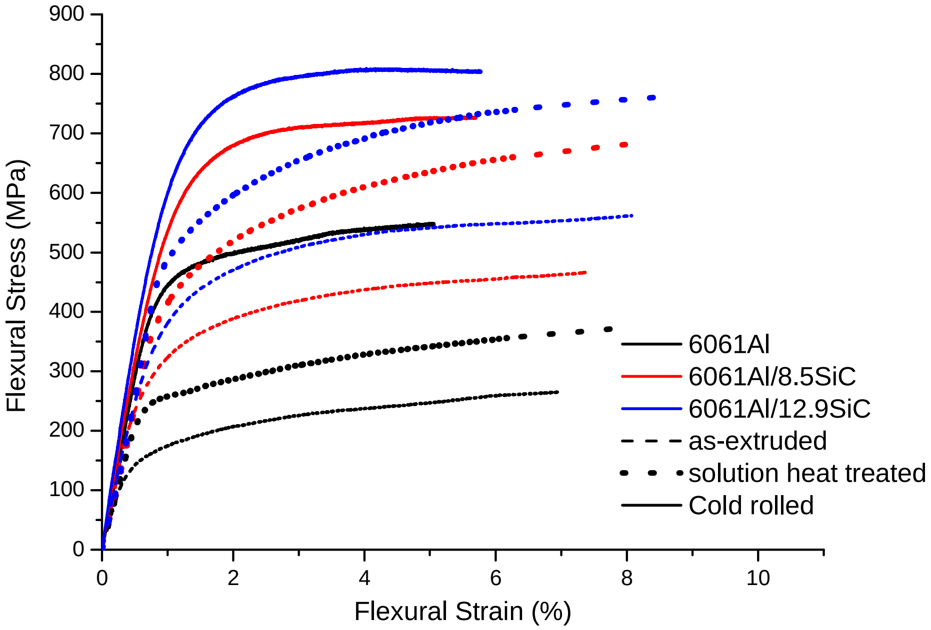

Figure 5.12: Three-point bending curves for as-extruded, solution heat treated and cold rolled 6061Al alloy, 6061Al/8.5SiC and 6061Al/12.9SiC composite samples. Cold rolled samples were tested under a condition of true strain values of 3.6 and 3.3 for the alloys and the composites respectively.

Materials	Condition	Stress at Yield (MPa)
6061Al	as-extruded	157±11
	solution heat treated	235±17
	cold rolled with a strain of 3.6	471±21
6061Al/8.5SiC	as-extruded	299±26
	solution heat treated	427±14
	cold rolled with a strain of 3.3	574±7
6061Al/12.9SiC	as-extruded	368±1
	solution heat treated	482±28
	cold rolled with a strain of 3.3	616±15

Table 5.1: Three-point bending properties for as-extruded, solution heat treated and cold rolled 6061Al alloy, 6061Al/8.5SiC and 6061Al/12.9SiC composite samples.

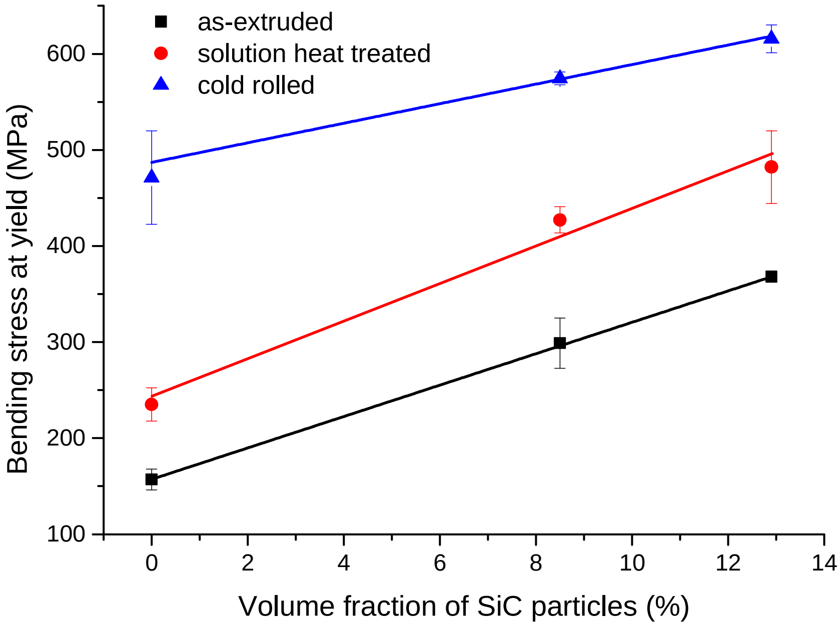

Figure 5.13: Bending stress at yield of as-extruded, solution heat treated and cold rolled 6061Al alloy, 6061Al/8.5SiC and 6061Al/12.9SiC composite samples as a function of volume fraction of SiC particles.

5.3 Discussion

5.3.1 Effect of extrusion parameters

In section 5.1.2, Figures 5.3(a) and (c) show that the SiC particle free areas in the as-received billets have developed into particle free bands with a width of 5-15μm along the extrusion direction (ED) after extrusion into strips.

This banded structure, with particle free zones, has been observed previously for this type of composites [6, 25-28]. Sun et al. [27] studied the microstructure of Al/SiC$_p$ composites after hot extrusion with different extrusion ratios ranging from 11:1 to 39:1 and found out that there were many dark bands (SiC rich areas) and bright belts parallel to the extrusion direction. The boundaries between bright and dark bands became diluted with increasing extrusion ratios. Similar results were also reported by Wang et al. [28] indicating a less uniform distribution of SiC particles when the extrusion ratio was 5:1 and the particle distribution was significantly improved when the extrusion ratio increased to 12:1. The banded structure observed in the present work after extrusion, with an ER of 6:1, is in agreement with those results found by Sun et al. [27] and Wang et al. [28].

Other authors [6, 25, 28] have analysed the effect of the extrusion temperature on the microstructure of Al alloy matrix composites and found out a more uniform particle distribution with increasing extrusion temperature up to a certain value. If the temperature is not high enough, it cannot facilitate the flow of the matrix alloy under the applied stress resulting in a non-homogeneous distribution of the particles. If extrusions are carried out at a relatively high temperature, partial melting of the matrix alloy at the grain boundaries happens causing the particles to get suspended in the melt matrix near the grain boundaries [25]. In the present work, both composites were extruded at 375°C which is lower than the average extrusion temperature at about 500°C for 6061Al alloy matrix composites reinforced with similar amount of SiC particles reported in literature [6]. The combined effects of a small extrusion ratio and a low extrusion temperature will certainly lead to a non-sufficient flow of the matrix alloy, resulting in a non-uniform distribution of SiC particles among the Al alloy matrix generating a banded structure.

5.3.2 Effect of rolling process and rolling strain

Rolling, similar to extrusion, can greatly influence materials' microstructure and in turn the overall mechanical properties.

According to Figure 5.3, a more uniform distribution of SiC particles has been achieved for the cold rolled composite materials with a reduced number of pores. Similar results showing better reinforcement particle distribution and reduced porosity after rolling were also observed elsewhere [17, 26, 29] on Al alloy matrix composites, indicating that rolling is another effective processing technique to homogenize the microstructure, improve the interfacial bonding strength and reduce the number of pores. Because of the high pressure involved during rolling, the matrix flow can easily remove porosity and improve interfacial bonding, leading to an increased density after cold rolling [30].

The negative effect of rolling is the reinforcement particle fracture also observed in Figure 5.3. It is believed that the substantial increase in rolling pressure, which is associated with an increase in the hardness of the matrix during cold rolling, is the main reason for such cracking [26]. The brittle SiC particles will fracture once the stress concentration reaches the fracture strength of the particles, especially for relatively larger particles.

The mechanical properties of the produced composites have been investigated by microhardness and three-point bending tests. Compared with as-extruded samples, the microhardness increases with increasing rolling strain until a saturation limit has been reached. The three-point bending tests show significantly improved yield stress when compared to as-extruded or solution heat treated samples, indicating effective work hardening from cold rolling process.

5.3.3 Effect of SiC particles

According to the macroscopic texture analysis in section 5.1.3, the extrusion of 6061Al alloy and 6061Al/SiC composites has led to the development of near β fibre texture which contains three main components of B’, S’ and C’ with other minor texture components. Figure 5.14 shows the maximum texture intensities for the three dominant texture components near Brass (B’), Copper (C’) and S (S’) positions. From the figure, it can be seen that for all the as-extruded samples, the texture intensities near Brass (B’) component are highest compared to C’ and S’ components. This observation is similar to the results reported by Maurice and Driver [12, 13], Contrepois et al. [31] and Bate et al. [32] on hot rolled Al alloys. These authors found that at elevated temperature and certain strain levels, there was significant increase of Brass component at the expense of other β fibre components.

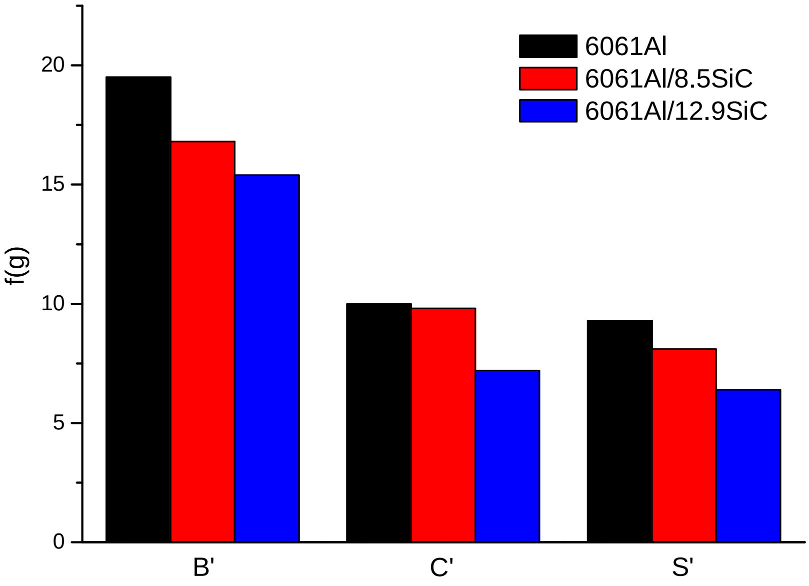

Figure 5.14: Maximum intensity of main texture components near Brass (B'), Copper (C') and S (S') position in as-extruded 6061Al, 6061Al/SiC strips.

It is also noticeable that the maximum texture intensities of 6061Al alloy are higher than those of the 6061Al/SiC composites at all three orientations and with the additions of SiC particles, the intensities of the major textures become weaker. The above difference in texture intensities is believed to be mainly due to the additions of non-deformable SiC particles. For 6061Al alloy, during extrusion, the Al grains are elongated along the extrusion direction and a strong deformation texture can be developed. For 6061Al/SiC composites, however, the texture formation would be limited to some extent.

During deformation of MMCs, localised strain incompatibility between the deforming matrix and non-deformable second phase particles can develop. Such strain incompatibility could be accomplished by the generation of dislocations at the particle-matrix interface [11]. At very low strains (much less than 1%), load is transferred to the particles by unrelaxed dislocation structures such as Orowan loops, but with increased deformation strains, the resulting stress on the non-deformable reinforcement will rapidly rise to a level where local plastic relaxation in the matrix will be occurred to relieve the stress [10]. For small particles (<0.1μm) and low strains, plastic relaxation generally involves the generation of prismatic dislocation loops while for large particles and large strains, more complex dislocation structures associated with local lattice rotations close to the particles are formed and these regions are termed as particle deformation zones [10], which can help weaken or randomize the matrix texture [33]. Figure 5.15 summarizes the deformation mechanisms at particles in Al as a function of strain and particle diameter [34].

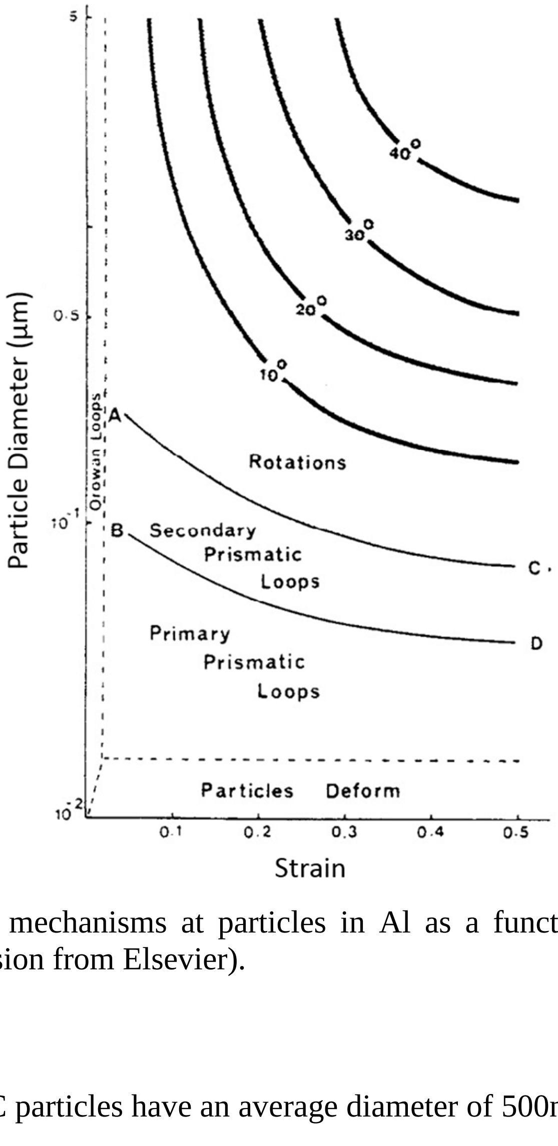

Figure 5.15: Deformation mechanisms at particles in Al as a function of strain and particle diameter [34] (with permission from Elsevier).

In the present work, the SiC particles have an average diameter of 500nm and the extrusion gives a true strain value of 1.8. Clearly, particle deformation zones around the SiC particles have formed where the normal Al deformation texture is disrupted. The grains in these regions cannot rotate to the same orientations as the rest of the matrix, resulting in a weaker deformation texture in the composites than that of 6061Al alloy. With the additions of SiC particles, more deformation zones will be formed resulting in more reductions in the texture intensities. Similar results showing reduced matrix texture intensities with increasing reinforcement volume fractions have also been reported by Humphreys et al. [35] on hot rolling texture of Al/SiC$_p$ (7μm) composites and He et al. [36] on hot extrusion texture of Al/SiC$_p$ (3.5μm) composites.

After cold rolling, based on Figures 5.6 and 5.7, instead of getting sharper texture components, the texture intensities of cold rolled 6061Al/SiC(SH) composites have decreased with increasing rolling strains and randomized texture has been developed in the final cold rolled samples. This may be explained by the microstructure evolution during cold rolling. As discussed in section 5.1.2, the as-extruded 6061Al/SiC composites have particle free bands and particle rich zones. It is believed that the particle free bands are the areas with preferred orientations while the particle rich zones are the areas with weakened or randomized texture due to the formation of particle deformation zones in the vicinity of the SiC particles. During cold rolling, most of the particle free bands have disappeared after more than 70% of rolling reductions. The disappearance of particle free bands could lead to the randomized texture in cold rolled 6061Al/SiC(SH) composites since the Al grains have no preferred orientations when they are around SiC particles.

The above explanation can be further supported by the EBSD results in sections 5.1.4 and 5.1.5. The EBSD orientation maps (Figures 5.8(b) and (c)) for as-extruded 6061Al/8.5SiC and 6061Al/12.9SiC strips show typical plane strain deformation texture ({1 1 2} or {1 0 1} planes nearly parallel to the extrusion plane in most measurements) in the particle free bands and randomized orientations in the particle rich zones, proving that the additions of SiC particles will weaken the amount of major textures. After cold rolling, the EBSD maps (Figures 5.10(b) and (c)) for cold rolled 6061Al/8.5SiC(SH)$_{3.3}$ and 6061Al/12.9SiC(SH)$_{3.3}$ composites show equiaxed grains with no preferred orientations. The comparison of the EBSD maps for as-extruded and cold rolled composite samples corroborates that the disappearance of the particle free bands during cold rolling is the main reason for the randomized texture in cold rolled composites.

5.4 Summary

6061Al/SiC composites were successfully produced by powder metallurgy using ball milling process followed by extrusion into strip shape and cold rolling. During extrusion into strips, SiC particles show a non-homogeneous distribution within the matrix due to a combination of the inhomogeneity in the as-received materials, a low extrusion ratio and a low extrusion temperature. Banded structures composed by particle free bands and SiC rich zones have been formed in the as-extruded composites. After cold rolling, a significant redistribution of SiC particles has been obtained. Most of the particle free bands in the as-extruded condition have disappeared, resulting in a homogeneous distribution of SiC particles within 6061Al matrix. A reduced amount of porosity and an increased amount of SiC particle fracture have also been formed in cold rolling process.

The extrusion texture of 6061Al/SiC composites consists of three moderate strong texture components, which are B’-{1 0 1} <3 5 3> with a scatter along α fibre, S’-{5 3 10} <8 10 7>, C’-{2 2 5} <5 4 4> and a weak scatter of the cube orientation. The three moderate strong texture components are close to the typical β fibre texture components in deformed fcc metals. Compared to 6061Al alloy, the intensities of the extrusion texture of 6061Al/SiC composites decrease with increasing volume fractions of SiC particles due to the formation of particle deformation zones around SiC particles where the normal Al deformation texture is disrupted. During cold rolling, 6061Al(SH) alloy has developed a stronger β fibre texture while for 6061Al/SiC(SH) composites, the texture intensities have dropped significantly and a randomized texture with very small grains has achieved due to the presence of non-deformable SiC particles and the disappearance of particle free bands.

Despite the increasing amount of SiC particle cracking during cold rolling, all the cold rolled samples exhibit improved strength respect to the as-extruded samples in both microhardness testing and three-point bending tests.

Overall, the cold rolling process on 6061Al/SiC composites improves homogeneity of the microstructure and increases the strength considerably. Also, it does not introduce anisotropy as crystallographic texture in 6061Al alloy matrix is quite random.

5.5 References

[1] R. Thomas, "Microstructure development in multicomponent alloys," D Phil, University of Oxford, 1998.

[2] A. Korchef and A. Kahoul, "Corrosion behavior of commercial aluminum alloy processed by equal channel angular pressing," *International Journal of Corrosion,* vol. 2013, 2013.

[3] R. Mitra, V. S. C. Rao, R. Maiti, and M. Chakraborty, "Stability and response to rolling of the interfaces in cast Al-SiCp and Al-Mg alloy-SiCp composites," *Materials Science and Engineering A,* vol. 379, pp. 391-400, 2004.

[4] N. Q. Zhao, P. Nash, and X. J. Yang, "The effect of mechanical alloying on SiC distribution and the properties of 6061 aluminum composite," *Journal of Materials Processing Technology,* vol. 170, pp. 586-592, 2005.

[5] A. Poudens, B. Bacroix, and T. Bretheau, "Influence of microstructures and particle concentrations on the development of extrusion textures in metal-matrix composites," *Materials Science and Engineering A,* vol. 196, pp. 219-228, 1995.

[6] A. Borrego, R. Fernandez, M. D. Cristina, J. Ibanez, and G. Gonzalez-Doncel, "Influence of extrusion temperature on the microstructure and the texture of 6061Al-15 vol. % SiCw PM composites," *Composites Science and Technology,* vol. 62, pp. 731-742, 2002.

[7] U. F. Kocks, C. N. Tomé, and H.-R. Wenk, *Texture and anisotropy : preferred orientations in polycrystals and their effect on materials properties*. New York ; Cambridge: Cambridge University Press, 1998.

[8] L. Q. Chen and N. Kanetake, "Hot-extruded and cold-rolled textures of the matrix aluminum in deformation processed two-phase Nb/Al metal-metal composites," *Textures and Microstructures,* vol. 35, pp. 273-282, 2003.

[9] K. V. Jata, S. Panchanadeeswaran, and A. K. Vasudevan, "Evolution of texture, microstructure and mechanical property anisotropy in an Al-Li-Cu alloy," *Materials Science and Engineering A,* vol. 257, pp. 37-46, 1998.

[10] F. J. Humphreys and M. Hatherly, *Recrystallization and related annealing phenomena*. Oxford: Pergamon, 1995.

[11] F. J. Humphreys, "The thermomechanical processing of Al-SiC particulate composites," *Materials Science and Engineering A,* vol. 135, pp. 267-273, 1991.

[12] C. Maurice and J. H. Driver, "Hot rolling textures of fcc metals .1. Experimental results on Al single and polycrystals," *Acta Materialia,* vol. 45, pp. 4627-4638, 1997.

[13] C. Maurice and J. H. Driver, "Hot rolling textures of fcc metals .2. Numerical simulations," *Acta Materialia,* vol. 45, pp. 4639-4649, 1997.

[14] O. Daaland and E. Nes, "Origin of cube texture during hot rolling of commercial Al-Mn-Mg alloys," *Acta Materialia,* vol. 44, pp. 1389-1411, 1996.

[15] S. Panchanadeeswaran and D. P. Field, "Texture evolution during plane-strain deformation of aluminum," *Acta Metallurgica Et Materialia,* vol. 43, pp. 1683-1692, 1995.

[16] C. Maurice, D. Piot, H. Klocker, and J. H. Driver, "Hot plane strain compression testing of aluminum alloys by channel-die compression," *Metallurgical and Materials Transactions a-Physical Metallurgy and Materials Science,* vol. 36A, pp. 1039-1047, 2005.

[17] M. Alizadeh, M. H. Paydar, D. Terada, and N. Tsuji, "Effect of SiC particles on the microstructure evolution and mechanical properties of aluminum during ARB process," *Materials Science and Engineering A,* vol. 540, pp. 13-23, 2012.

[18] M. Reihanian, R. Ebrahimi, N. Tsuji, and M. M. Moshksar, "Analysis of the mechanical properties and deformation behavior of nanostructured commercially pure Al processed by equal channel angular pressing (ECAP)," *Materials Science and Engineering A,* vol. 473, pp. 189-194, 2008.

[19] A. Azushima, R. Kopp, A. Korhonen, D. Y. Yang, F. Micari, G. D. Lahoti*, et al.,* "Severe plastic deformation (SPD) processes for metals," *Cirp Annals-Manufacturing Technology,* vol. 57, pp. 716-735, 2008.

[20] J. G. Sevillano, P. Vanhoutte, and E. Aernoudt, "Large strain work-hardening and textures," *Progress in Materials Science,* vol. 25, pp. 69-412, 1980.

[21] B.-W. Ahn, D.-H. Choi, Y.-H. Kim, and S.-B. Jung, "Fabrication of SiCp/AA5083 composite via friction stir welding," *Transactions of Nonferrous Metals Society of China,* vol. 22, Supplement 3, pp. s634-s638, 2012.

[22] J. H. Hollomon, "Tensile deformation," *Transactions of the American Institute of Mining and Metallurgical Engineers,* vol. 162, pp. 268-290, 1945.

[23] W. F. Hosford, *Mechanical behavior of materials,* 2nd ed. Cambridge: Cambridge University Press, 2010.

[24] M. Zehetbauer and S. V, "Cold work-hardening in stage-IV and stage-V of fcc metals .1. Experiments and interpretation," *Acta Metallurgica Et Materialia,* vol. 41, pp. 577-588, 1993.

[25] R. Rahmani Fard and F. Akhlaghi, "Effect of extrusion temperature on the microstructure and porosity of A356-SiCp composites," *Journal of Materials Processing Technology,* vol. 187-188, pp. 433-436, 2007.

[26] J. C. Lee and K. N. Subramanian, "Effect of cold-rolling on the tensile properties of $(Al_2O_3)_P$/Al composites," *Materials Science and Engineering A,* vol. 159, pp. 43-50, 1992.

[27] Y. P. Sun, H. G. Yan, B. Su, L. Jin, and J. M. He, "Microstructure and mechanical properties of spray deposition Al/SiCp composite after hot extrusion," *Journal of Materials Engineering and Performance,* vol. 20, pp. 1697-1702, 2011.

[28] X. J. Wang, L. Xu, X. S. Hu, K. B. Nie, K. K. Deng, K. Wu*, et al.*, "Influences of extrusion parameters on microstructure and mechanical properties of particulate reinforced magnesium matrix composites," *Materials Science and Engineering A,* vol. 528, pp. 6387-6392, 2011.

[29] S. Amirkhanlou, M. R. Rezaei, B. Niroumand, and M. R. Toroghinejad, "High-strength and highly-uniform composites produced by compocasting and cold rolling processes," *Materials & Design,* vol. 32, pp. 2085-2090, 2011.

[30] T. W. Clyne and P. J. Withers, *An introduction to metal matrix composites*, First paperback edition 1995. ed. Cambridge: Cambridge University Press, 1993.

[31] Q. Contrepois, C. Maurice, and J. H. Driver, "Hot rolling textures of Al-Cu-Li and Al-Zn-Mg-Cu aeronautical alloys: Experiments and simulations to high strains," *Materials Science and Engineering A,* vol. 527, pp. 7305-7312, 2010.

[32] P. S. Bate, Y. Huang, and F. J. Humphreys, "Development of the "brass" texture component during the hot deformation of Al-6Cu-0.4Zr," *Acta Materialia,* vol. 52, pp. 4281-4289, 2004.

[33] L. C. L. Ko, "Particle stimulated nucleation: deformation around particles," PhD, Engineering and Physical Sciences, University of Manchester, 2014.

[34] F. J. Humphreys, "Local lattice rotations at 2nd phase particles in deformed metals," *Acta Metallurgica,* vol. 27, pp. 1801-1814, 1979.

[35] F. J. Humphreys, W. S. Miller, and M. R. Djazeb, "Microstructural development during thermomechanical processing of particulate metal-matrix composites," *Materials Science and Technology,* vol. 6, pp. 1157-1166, 1990.

[36] C. L. He, J. M. Wang, and Q. K. Cai, "Effects of particle size and volume fraction on extrusion texture of SiCp/Al metal matrix composites," *Advanced Engineering Materials, Pts 1-3,* vol. 194-196, pp. 1437-1441, 2011.

6. Cold rolling of 6061Al/$Al_{93}Fe_3Cr_2Ti_2$ alloy particle composites

Chapter 6 comprises the studies of extrusion and cold rolling behaviour of 6061Al/$Al_{93}Fe_3Cr_2Ti_2$ alloy particle composites. The compacted composite billets were extruded into strips and then subjected to cold rolling. For comparison purposes, the compacted billets were also extruded into bars under the same extrusion conditions. Table 3.4 lists the sample information and rolling details for each sample. For convenience purposes, “NQX” has been used as an acronym for $Al_{93}Fe_3Cr_2Ti_2$ particles in the following texts. Further details of the production of the composites can be found in Chapter 3.

Section 6.1 comprises the studies of the effect of cold rolling on the microstructural development and texture evolution by different means of characterization techniques.

The effect of cold rolling on the mechanical properties and work hardening behaviour of the composites are studied in Section 6.2.

Section 6.3 contains the discussions and partial conclusions about the effect of rolling strains on the microstructure and mechanical properties of the composites and the effect of NQX particles on the texture development during cold rolling.

6.1 Microstructural characterization of as-extruded and cold rolled 6061Al/$Al_{93}Fe_3Cr_2Ti_2$ alloy particle composites

6.1.1 X-ray diffraction analysis

XRD analysis has been carried out on as-received and sieved NQX powders, as-extruded 6061Al/NQX composite bars in longitudinal planes, as-extruded 6061Al strip and cold rolled 6061Al/$NQX_{3.6}$ samples in normal planes (TD-ED/RD) and the diffractograms are shown in Figure 6.1.

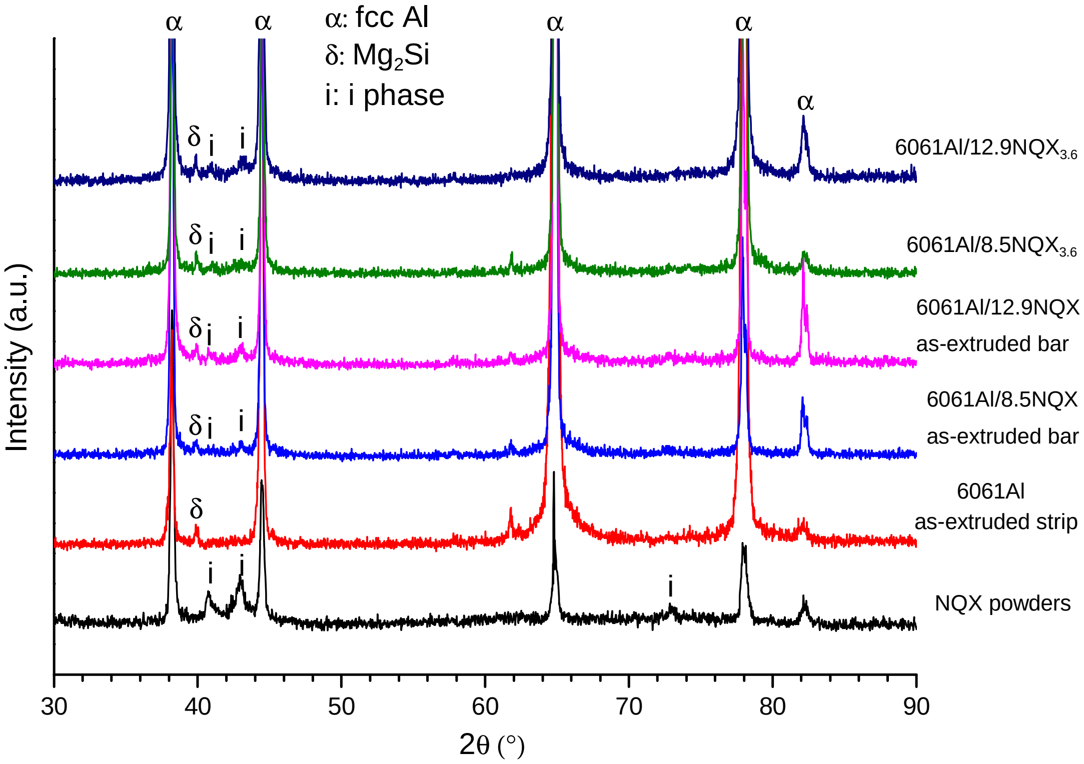

(a)

Figure 6.1: X-ray diffractograms of as-received NQX powders, as-extruded 6061Al strip in normal plane (TD-ED), as-extruded 6061Al/NQX composite bars in longitudinal planes and cold rolled 6061Al/$NQX_{3.6}$ samples in normal planes (TD-RD). (a) 2θ values between 30° and 90° and (b) 2θ values between 35° and 50°.

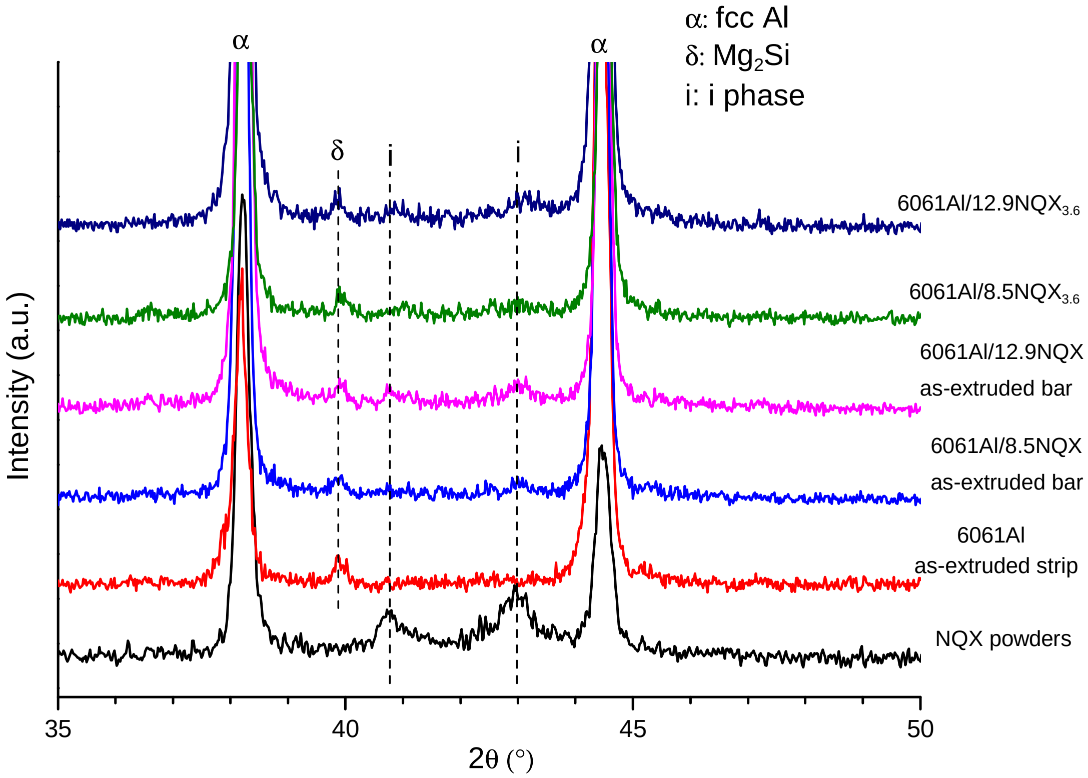

(b)

Figure 6.1: X-ray diffractograms of as-received NQX powders, as-extruded 6061Al strip in normal plane (TD-ED), as-extruded 6061Al/NQX composite bars in longitudinal planes and cold rolled 6061Al/$NQX_{3.6}$ samples in normal planes (TD-RD). (a) 2θ values between 30° and 90° and (b) 2θ values between 35° and 50°.

The as-received NQX powders consist of the icosahedral quasicrystalline phase (2θ=40.98°, 43.24° and 73.22°) [1, 2] embedded in an fcc-Al matrix. After extrusion the mixed 6061Al/NQX powders into composite bars and cold rolling, low intensity icosahedral quasicrystalline phase peaks can be observed at 2θ values of 40.98° and 43.24° (see Figure 6.1(b)) due to the low volume fractions of icosahedral quasicrystalline phase in the produced composites. In addition, intermetallic phase Mg_2Si has been observed in all the as-extruded and cold rolled samples. An unidentified peak at a 2θ value of 61.78° has been observed which might be due to other intermetallic phase in 6061Al matrix or impurities brought in during the fabrication process.

6.1.2 Scanning electron microscopy and optical microscopy analysis

SEM analysis has been carried out on as-received and sieved NQX powders and the micrographs are shown in Figure 6.2. Well-sieved spherical NQX particles within 25μm in diameter/thickness can be observed in Figure 6.2(a). The particle size distribution is not very uniform with some small particles with a diameter of ~5μm. Powder particles are pulled into a spherical shape by surface tension [1]. The smaller the powder particle is, the larger the driving force will be. However, sometimes premature freezing occurs and the molten droplets freeze before the metal is pulled to a spheroidal shape during gas atomisation, leading to small fractions of non-spherical powder particles [3, 4]. A closer look of one of the NQX particle is shown in Figure 6.2(b) which shows the internal microstructure with near-spherical particles of a size of 100-200nm embedded in Al matrix.

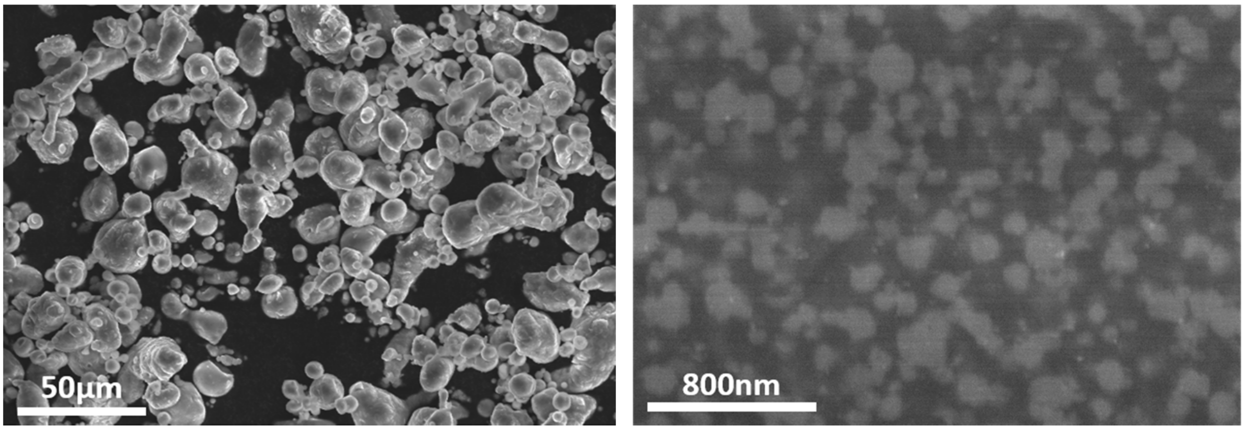

(a) (b)

Figure 6.2: Secondary electron images of as-received NQX powders showing (a) well-sieved NQX powders under 25μm and (b) the internal microstructure of the NQX powders.

Figure 6.3 shows the SEM images of the 6061Al/NQX composites in longitudinal sections after extrusion into bars. It can be seen from Figures 6.3(a) and (b) that the NQX particles have a uniform distribution in the 6061Al matrix. In addition, cracks and porosities exist at the tip of the particles, which might be detrimental to the overall mechanical properties.

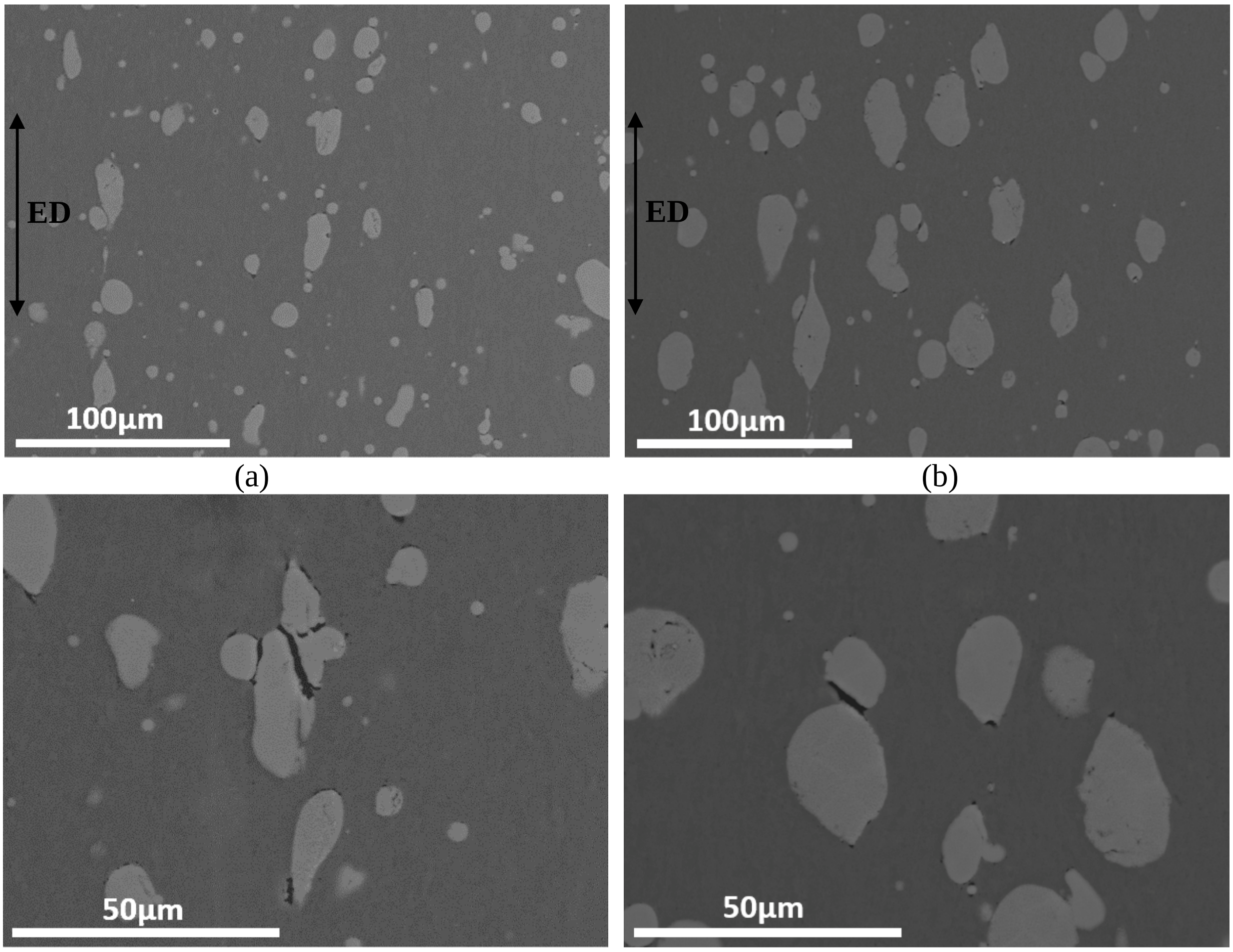

(a) (b)

(c) (d)

Figure 6.3: Secondary electron images of (a) 6061Al/8.5NQX and (b) 6061Al/12.9NQX composites in longitudinal sections after extrusion into bars, (c) and (d) show the presence of cracks and porosity in the corresponding sample.

The 6061Al/NQX composite microstructure after extrusion into strips and cold rolling is shown in Figure 6.4. Figures 6.4(a) and (b) show that there is a major crack in the middle layer of the as-extruded strips. The observed crack is called Chevron cracking or Central burst which is one of the commonly occurred extrusion defects [5]. The formation of Chevron cracking during extrusion is shown in Figure 6.5. It can be seen that if the two plastic deformation zones are not large enough to meet, Chevron cracking occurs in the middle layer of the extrusion products. The plastic deformation zone size varies with different materials and extrusion conditions. It is reported that increasing extrusion ratio or increasing the extrusion temperature can avoid the formation of Chevron cracking [5]. In the present work, the low extrusion ratio (6:1) and the materials used might have caused small plastic deformation zones during extrusion, leading to the formation of Chevron cracking. Despite the Chevron cracking, the NQX particles have been distributed uniformly among the 6061Al matrix in the as-extruded strips according to Figures 6.4(c) and (d). Cracks and porosities are also observed. With further rolling strains, major cracks in sizes of hundreds of microns have been observed in the final cold rolled samples which probably evolve from the Chevron cracking or due to the coalesce of the cracks and interfacial debonding during cold rolling process. One of the examples is shown in Figure 6.6 for 6061Al/12.9$NQX_{3.6}$ sample.

Careful observation of Figure 6.4 also shows conical voids (see arrows) in the matrix-NQX interfacial areas aligned along the ED/RD directions (located both at front or back sides of the particles). Conical voids are frequently formed at the ends of hard inclusions in metal forming process [6, 7] and the formation mechanism has been discussed in literature. According to Baker and Charles [8], the voids appear because of the instability of the matrix to flow around the hard particles whilst maintaining contact with them. The matrix-particle interfaces separate and create voids due to the insufficient interface strength to withstand the longitudinal tensile stress caused by the deformation of the surrounding matrix. Luo [7] simulated the void formation and evolution around an inclusion in a uniform matrix under the condition of compressive deformation by finite element method and found that the tangential shear stresses or tensile normal stresses at the interface between the inclusion and the matrix were considered to be responsible for debonding and void formation. The conical cavities could be filled or minimised by flowing matrix under high processing pressure and temperature [9].

A high magnification SEM image of interfacial regions for cold rolled 6061Al/12.9$NQX_{3.6}$ sample is shown in Figure 6.7 showing a clean interface between 6061Al matrix and NQX particles.

Figures 6.3 and 6.4 show a large amount of cracks in as-extruded or cold rolled 6061Al/NQX composites, indicating poor mechanical properties. Although this material may not be suitable for practical applications, it is still scientifically important to understand the processing/microstructure/property relationships involved, especially considering there is currently no published work about using NQX alloy particles as reinforcement. It is hoped that the knowledge gained through such study will help tailor the processing conditions in the future to improve the properties of this material.

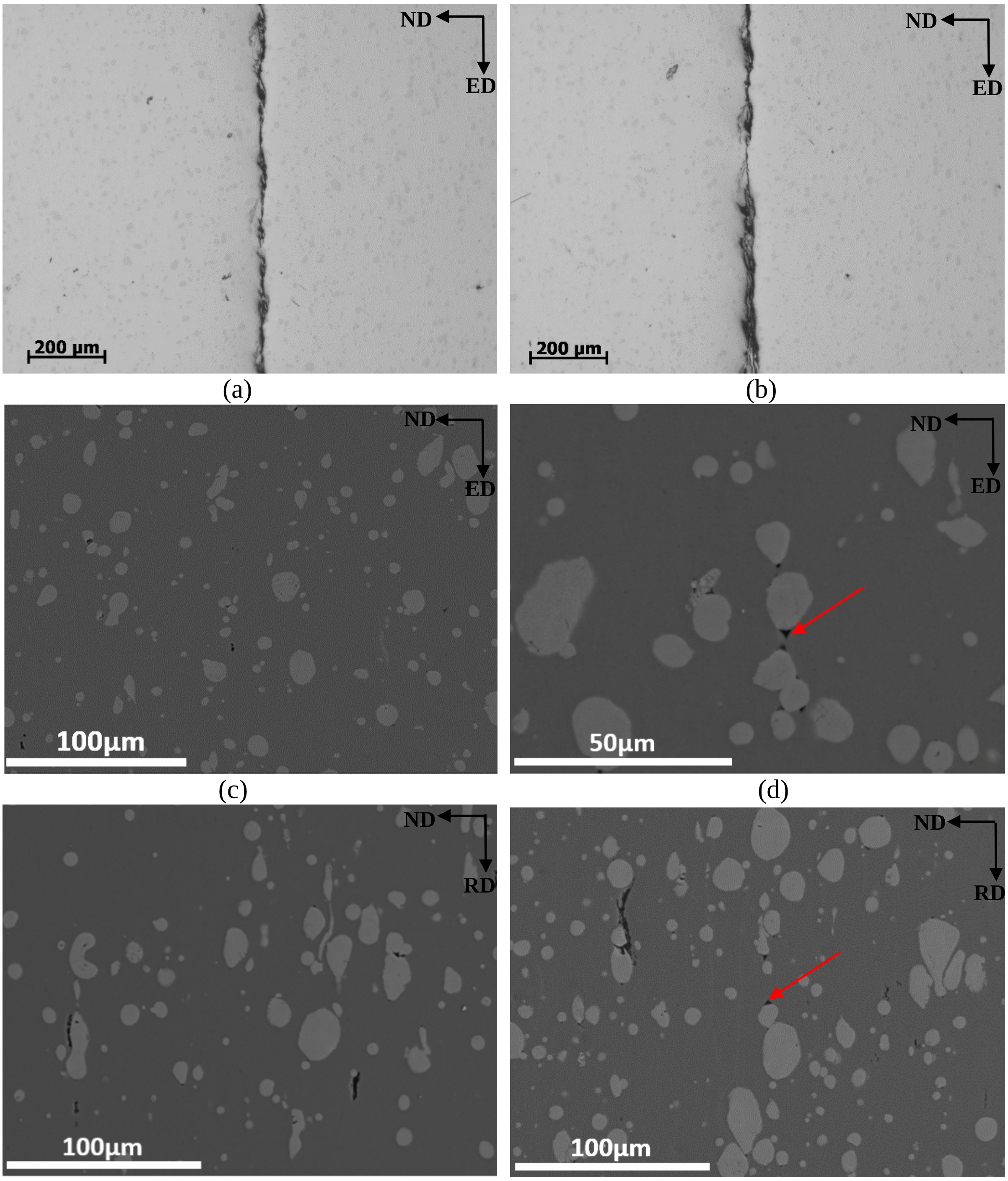

(a) (b)

(c) (d)

(e) (f)

Figure 6.4: Optical micrographs of (a) as-extruded 6061Al/8.5NQX strip and (b) as-extruded 6061Al/12.9NQX strip showing major cracks and secondary electron images of (c) as-extruded 6061Al/8.5NQX strip, (d) as-extruded 6061Al/12.9NQX strip, (e) cold rolled 6061Al/8.5NQX$_{3.6}$ and (f) cold rolled 6061Al/12.9NQX$_{3.6}$ in longitudinal plane (ND-ED/RD) (Arrows indicate conical voids).

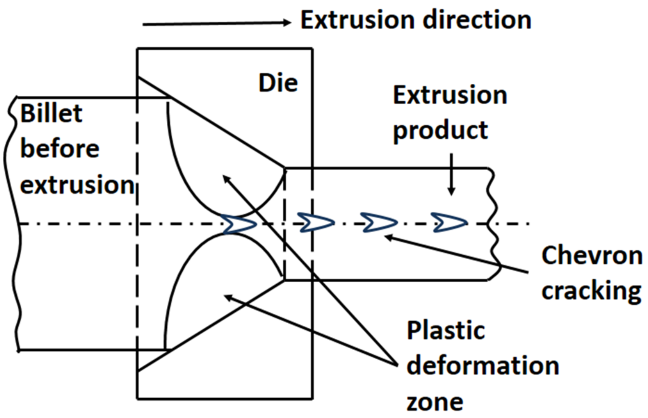

Figure 6.5: Schematic illustration of the formation of Chevron cracking during extrusion [5].

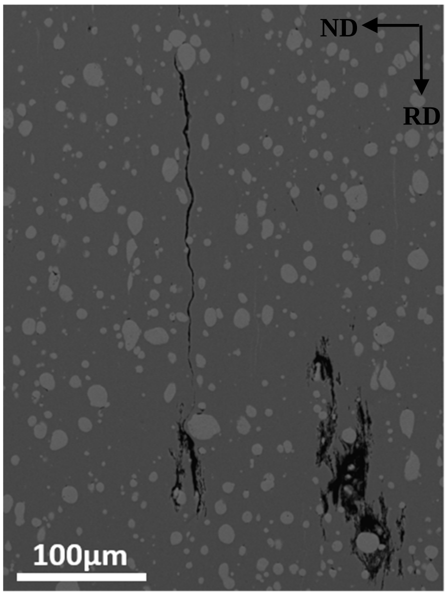

Figure 6.6: Secondary electron image of cold rolled 6061Al/12.9$NQX_{3.6}$ sample in longitudinal plane (ND-RD) showing major cracks.

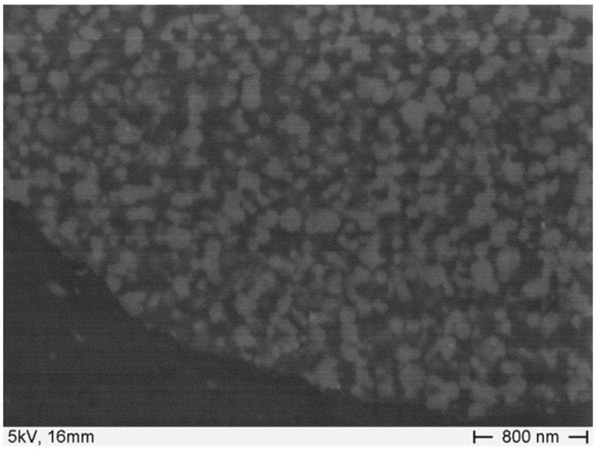

Figure 6.7: Secondary electron image of cold rolled 6061Al/12.9$NQX_{3.6}$ sample showing interfacial areas.

6.1.3 Transmission electron microscopy analysis

TEM was used to further investigate the microstructure of the final cold rolled 6061Al/12.9$NQX_{3.6}$ sample in the rolling plane (RD-TD). Figure 6.8(a) shows a spherical NQX particle with a diameter of ~4µm imbedded in the 6061Al matrix. The internal microstructure of the NQX particle is shown in Figure 6.8(b) with near-spherical particles of a size of ~100nm embedded in Al matrix. The ~100nm sized particles are believed to be icosahedral quasicrystalline phase based on the XRD results in section 6.1.1 and the similar morphology of the icosahedral particles reported by Galano et al. [2, 10] on melt spun $Al_{93}Fe_3Cr_2Ti_2$ alloys which remained a near-spherical shape up to a heat treatment temperature at 450°C. The icosahedral phase in the present work has obviously survived the extrusion carried out at 375°C and the cold rolling process.

Figure 6.8(c) shows the interfacial areas between the NQX particles and the matrix along with several sub-micron Al grains or subgrains adjacent to the NQX particles. No interfacial reaction products have been observed at the interfacial areas which is consistent with Figure 6.7. In addition, a thin layer of oxide (see the arrow) is observed around the NQX particle. EDX analysis has been carried out on regions 1 (Al matrix), 2 (interface) and 3 (NQX particles) and the spectra are shown in Figure 6.8(d). It can be seen that the EDX spectrum on the interface exhibits a higher level of O when compared to regions 1 and 3, strongly suggesting the existence of oxide layers around the NQX particles.

The deformation microstructure of the matrix Al grains was also investigated. It is generally accepted that the original grains will be subdivided into cell blocks or subgrains during deformation process for fcc metals [11-15]. One example is displayed in Figure 6.8(e) showing an elongated Al grain containing several subgrains with a size of 0.2-0.4µm. The substructure seems to consist of continuous dislocation walls surrounding areas of smaller dislocation density. Similar substructure of deformed Al alloys was also reported elsewhere [11, 16].

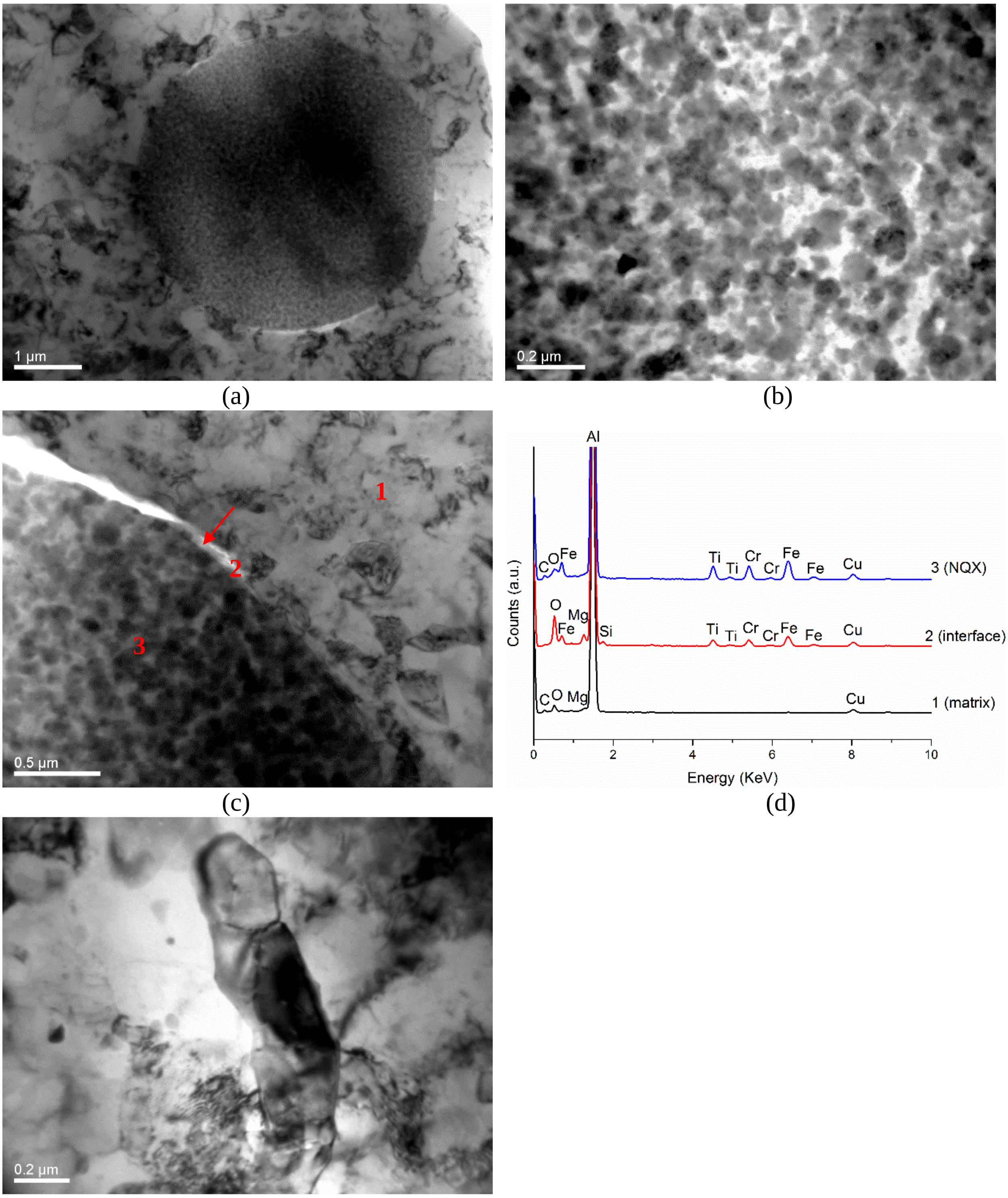

(a) (b)

(c) (d)

(e)

Figure 6.8: TEM bright field images of cold rolled 6061Al/12.9NQX$_{3.6}$ sample showing (a) NQX particle in the 6061Al matrix, (b) microstructure inside the NQX particle, (c) interfacial border between the NQX particle and 6061Al matrix, (d) EDX spectra for regions 1-3 and (e) Al grains in the matrix.

6.1.4 Macroscopic texture development during extrusion and cold rolling

ODFs of as-extruded and cold rolled 6061Al/8.5NQX and 6061Al/12.9NQX strips in constant φ_2 sections are shown in Figures 6.9 and 6.10, respectively.

For as-extruded 6061Al/8.5NQX strip, the sample has a strong rotated-cube-{0 0 1}<5 3 0> (φ_1=30º, Φ=0º, φ_2=0º), a moderate α fibre and a weak γ fibre (φ_1=0-90º, Φ=54.7º, φ_2=45º, {1 1 1} planes parallel to the extrusion plane [17]). During the first cold rolling pass (ε=2.4), rotated-cube component and γ fibre have weakened and a stronger scatter along α fibre as well as a weak Copper-{1 1 2}<1 1 1> (φ_1=90º, Φ=35º, φ_2=45º) component has been developed. With further rolling passes, the scattered intensity along α fibre has concentrated around Brass-{1 1 0}<1 1 2> (φ_1=35º, Φ=45º, φ_2=0º) component and a stronger Copper component has appeared. In the final cold rolled 6061Al/8.5$NQX_{3.6}$ sample, a sharp β fibre texture has formed where the main orientation components go from Brass to Copper through S [18].

The overall texture development of cold rolled 6061Al/12.9NQX strip is similar with that of the 6061Al/8.5NQX strip except that the as-extruded texture contains a stronger α fibre and a weak γ fibre while no strong rotated-cube component has been observed. Although the main texture components in both the cold rolled 6061Al/$NQX_{3.6}$ samples are quite similar, the orientation densities have weakened with increasing volume fractions of NQX reinforcement.

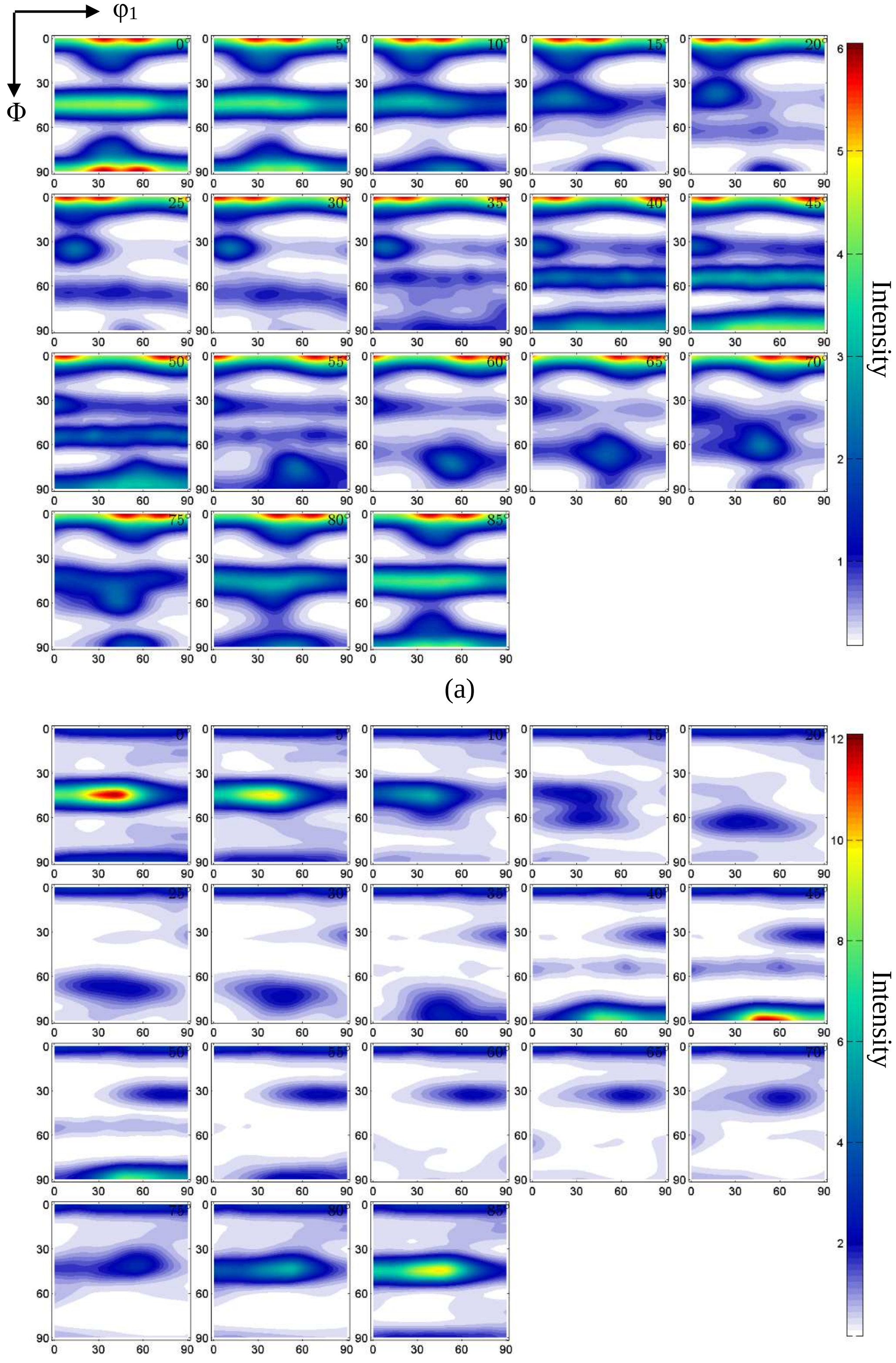

(a)

(b)

Figure 6.9: ODFs of (a) as-extruded 6061Al/8.5NQX strip; (b) cold rolled 6061Al/8.5$NQX_{2.4}$; (c) cold rolled 6061Al/8.5$NQX_{2.8}$ and (d) cold rolled 6061Al/8.5$NQX_{3.6}$.

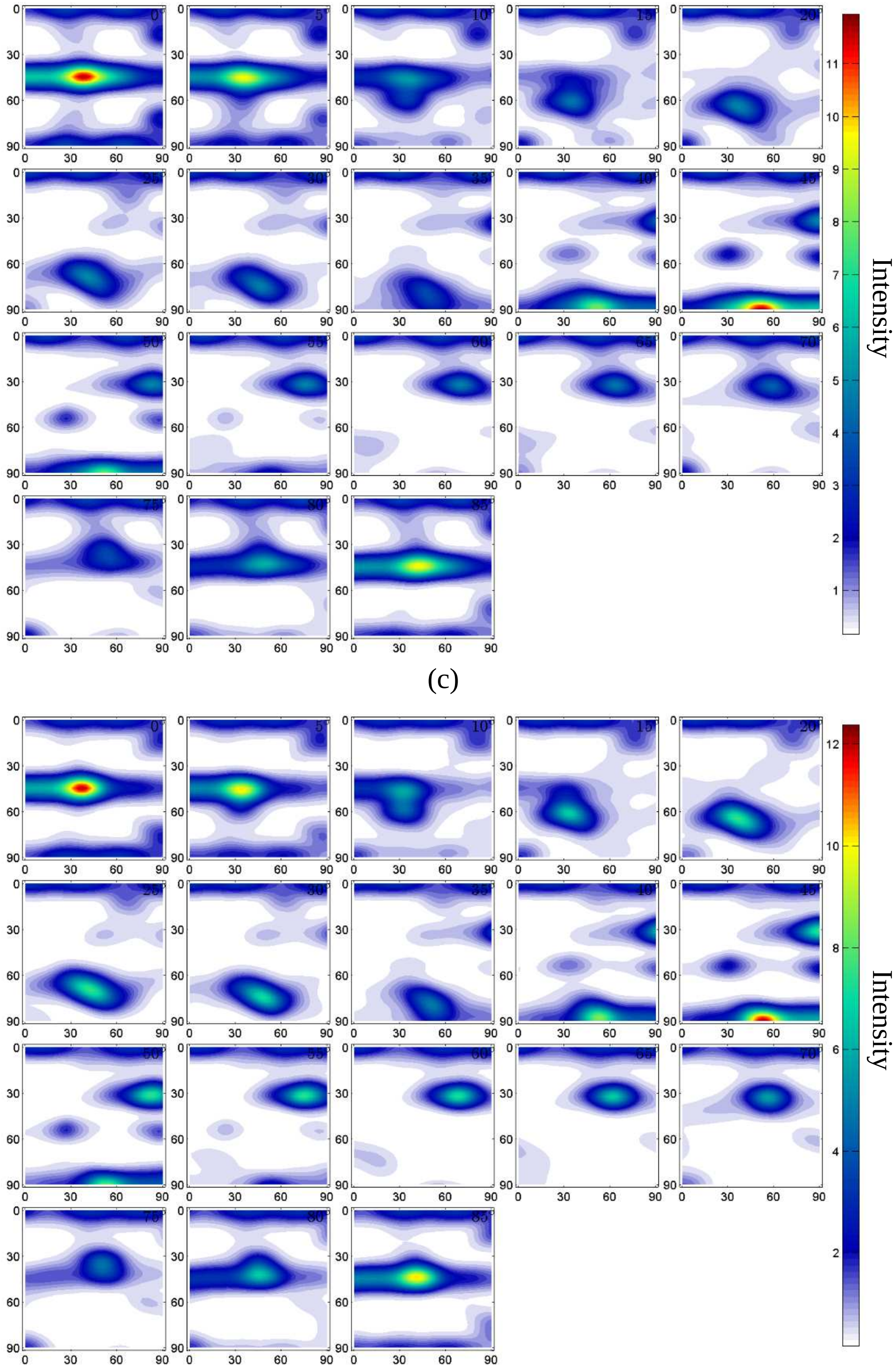

(c)

(d)

Figure 6.9: ODFs of (a) as-extruded 6061Al/8.5NQX strip; (b) cold rolled 6061Al/8.5NQX$_{2.4}$; (c) cold rolled 6061Al/8.5NQX$_{2.8}$ and (d) cold rolled 6061Al/8.5NQX$_{3.6}$.

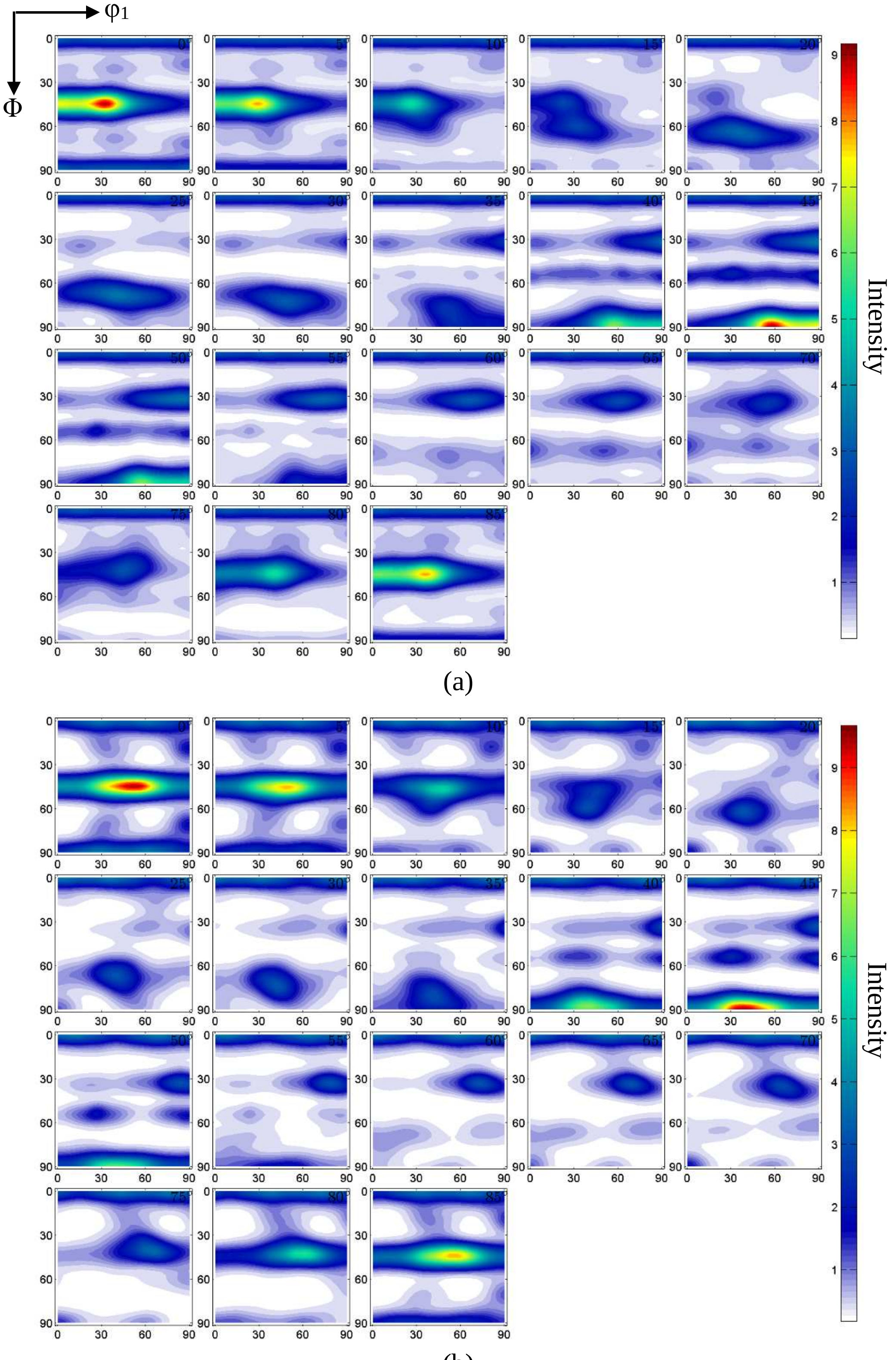

(a)

(b)

Figure 6.10: ODFs of (a) as-extruded 6061Al/12.9NQX strip; (b) cold rolled 6061Al/12.9NQX$_{2.0}$; (c) cold rolled 6061Al/12.9NQX$_{2.7}$ and (d) cold rolled 6061Al/12.9NQX$_{3.6}$.

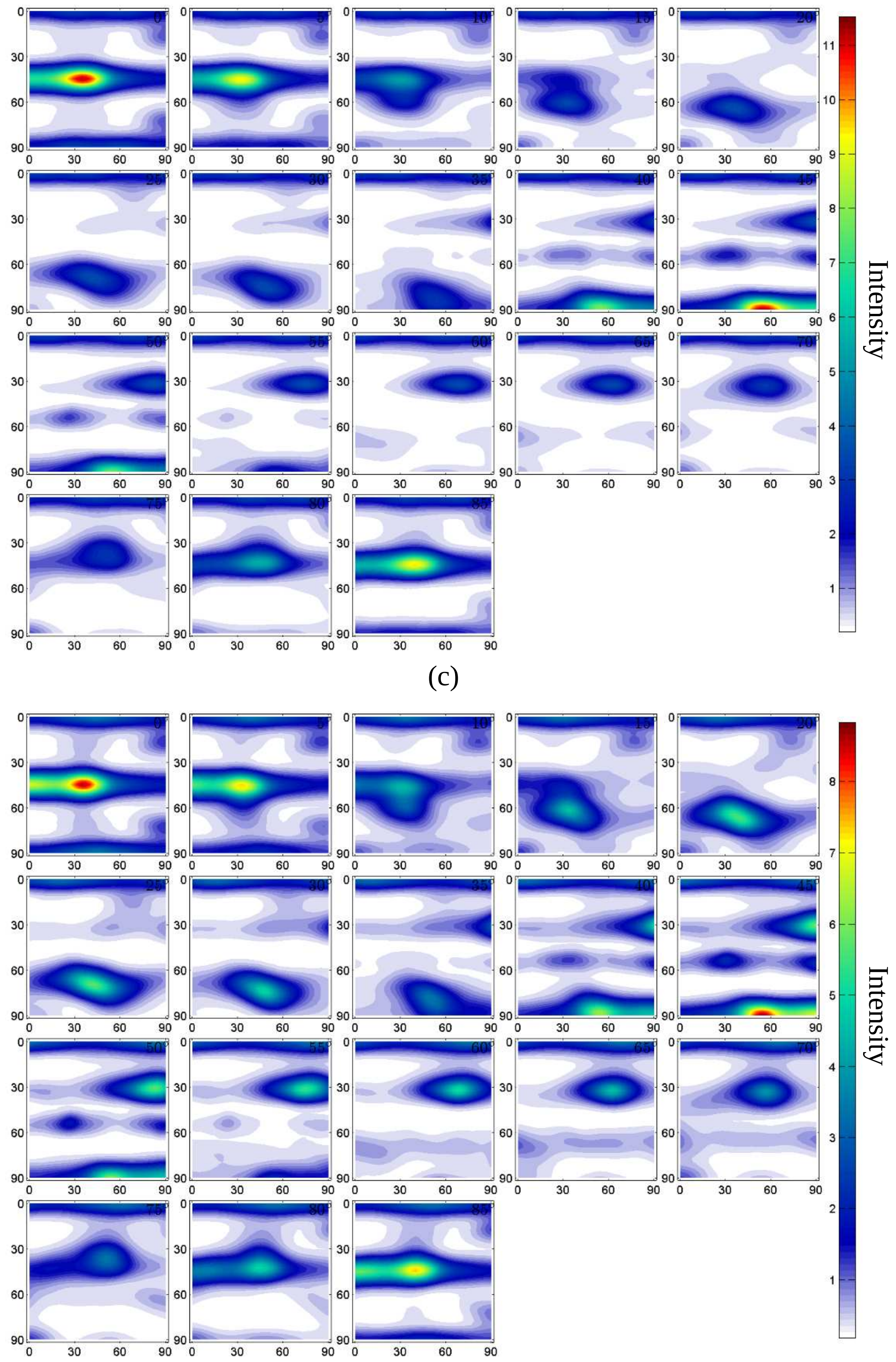

(c)

(d)

Figure 6.10: ODFs of (a) as-extruded 6061Al/12.9NQX strip; (b) cold rolled 6061Al/12.9NQX$_{2.0}$; (c) cold rolled 6061Al/12.9NQX$_{2.7}$ and (d) cold rolled 6061Al/12.9NQX$_{3.6}$.

The α and β fibre intensity plots in Figures 6.11 and 6.12 were depicted to further clarify the evolution of texture during cold rolling process. For as-extruded 6061Al/8.5NQX strip, the α fibre can be described as a relatively homogeneous orientation tube. After a rolling strain of 2.4, increased intensities along α fibre have been observed with a stronger Goss-{1 1 0}<0 0 1> (φ_1=0º, Φ=45º, φ_2=0º) component and a broad peak near B'-{0 1 1}<5 3 3> (φ_1=40º, Φ=45º, φ_2=0º). With increasing rolling strains, Goss component has gradually weakened and the initial homogeneous orientation tube has deteriorated into peak type texture with the highest intensity at Brass component. For β fibre, in as-extruded condition, the orientation intensities are distributed more or less homogeneously along the fibre over the whole length with relatively higher intensity near Brass component. With increasing rolling strains, Brass, Copper and S orientations increase rapidly. Especially Brass component, it has increased by more or less two times compared with Copper component. Overall, the average intensities of β fibre have been enhanced with further rolling strains.

For 6061Al/12.9NQX strip, an α fibre with higher intensities near Goss and Brass components have already been developed after extrusion. With rolling strains, increased intensity near Brass and decreased intensity at Goss have been observed. The observation is in agreement with the rotation path from Goss orientation to Brass orientation reported in literature for fcc metals [19-21], indicating that the unstable Goss component has gradually moved towards Brass component during cold rolling of 6061Al/12.9NQX strip. The β fibre intensity plot shows increased Copper and S orientations while decreased Brass orientation after a rolling strain of 2.7 indicating that more Copper and S have been formed at the expense of Brass during further deformation.

A comparison between both 6061Al/$NQX_{3.6}$ samples show that with increasing volume fractions of NQX reinforcement, the texture intensities at Copper, Brass and S components become weaker and compared with the cold rolled 6061Al(SH)$_{3.6}$ alloy in section 5.1.3, the main texture intensities are significantly lower.

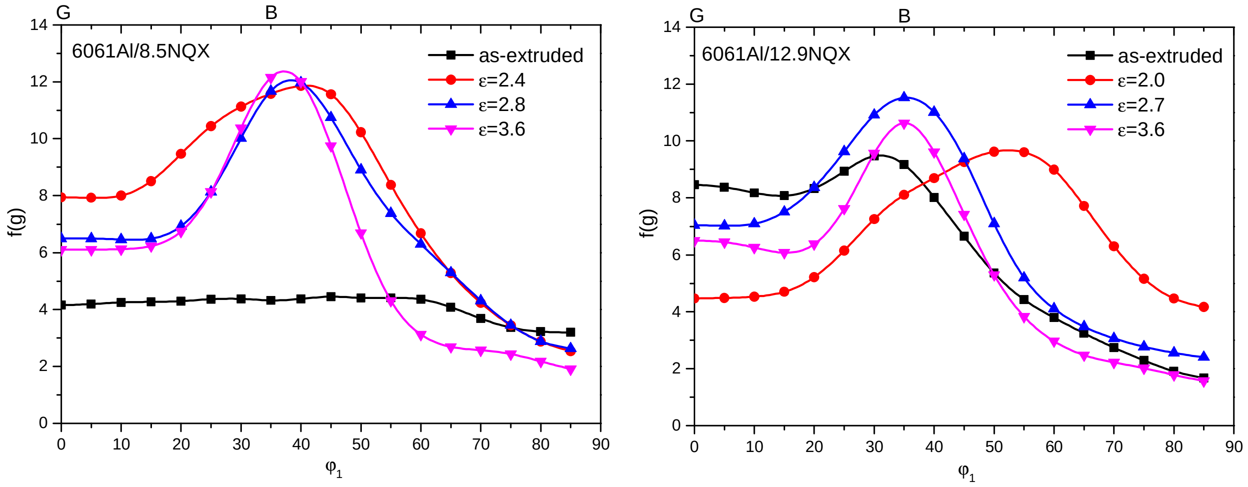

(a) (b)

Figure 6.11: α fibre intensity plots of (a) 6061Al/8.5NQX and (b) 6061Al/12.9NQX.

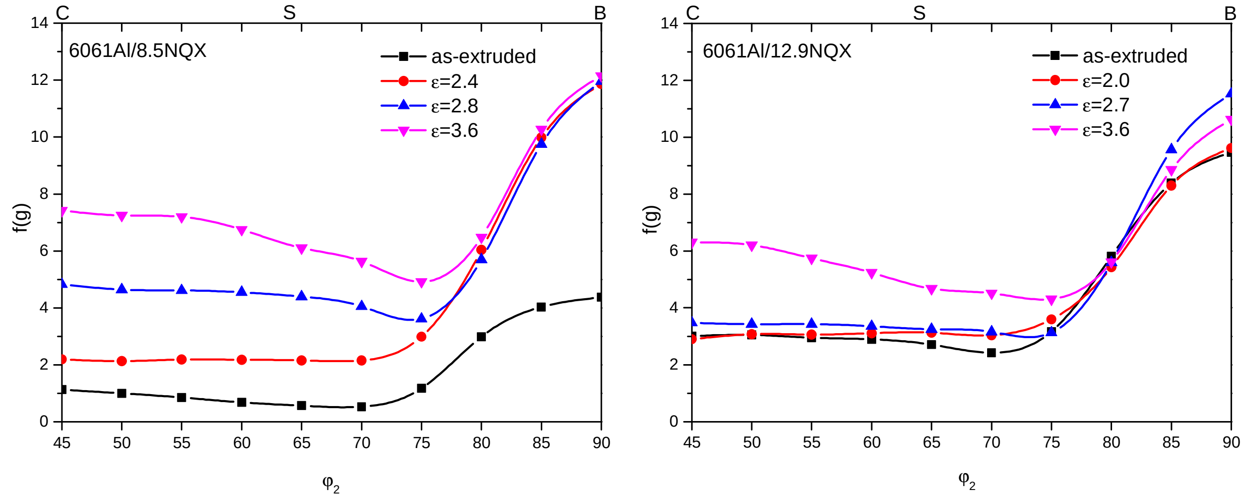

(a) (b)

Figure 6.12: β fibre intensity plots of (a) 6061Al/8.5NQX and (b) 6061Al/12.9NQX.

The volume fractions of main texture components (Copper, S and Brass) were calculated by Mtex [22, 23] within a range of 15° tolerance and the results are plotted as a function of the rolling strains in Figure 6.13. The volume fractions of Copper and S components increase from the beginning of rolling. For Brass component, it increases significantly in the first few rolling passes and then nearly levels off or even decreases a little with further rolling strain. The volume fraction of β fibre, which was estimated by the sum of Copper, S and Brass components, increases with the rolling strain and achieves more than 50% of the overall texture components in the final cold rolled samples. The volume fraction of β fibre for 6061Al/12.9NQX$_{3.6}$ is lower than that for 6061Al/8.5NQX$_{3.6}$ which is in agreement with the intensity difference observed in the ODFs.

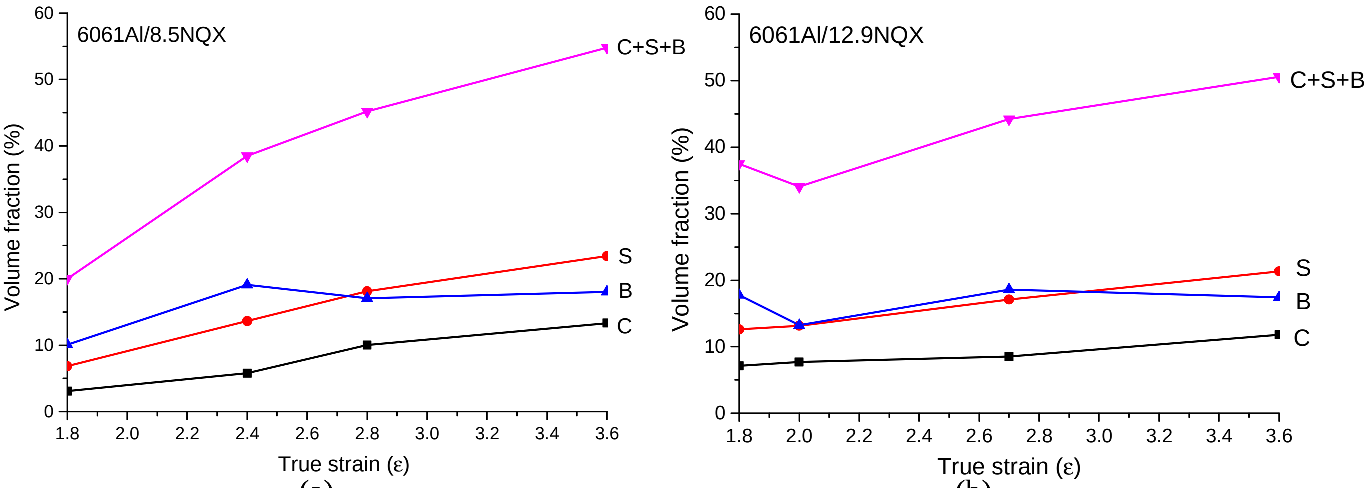

(a) (b)

Figure 6.13: Volume fractions of main texture components (Copper, S and Brass) of (a) 6061Al/8.5NQX and (b) 6061Al/12.9NQX.

6.1.5 Electron backscatter diffraction analysis

Figures 6.14-6.17 show EBSD orientation maps of as-extruded and cold rolled 6061Al/NQX samples with respect to the normal direction. Each point is painted with a color according to the crystal orientation. The black and white lines from the EBSD maps indicate the locations of high angle grain boundaries (≥15°) and low angle grain boundaries (2°-15°), respectively. The fractions of low angle grain boundaries (2°-15°) measured by the EBSD analysis are summarized in Table 6.1.

Figures 6.14 and 6.16 show that hot extrusion of 6061Al/NQX strips has led to the formation of slighted elongated Al matrix grains aligned along the extrusion direction with subgrain structures. The subgrains have an average width of 1.5±0.1μm and length of 2.4±0.2μm for as-extruded 6061Al/8.5NQX strip and an average width of 1.5±0.2μm and length of 2.1±0.2μm for as-extruded 6061Al/12.9NQX strip according to the mean linear intercept method (see section 3.3.3). The substructure size is similar with that of the as-extruded 6061Al alloy which has an average width of 1.6±0.3μm and length of 2.0±0.2μm based on Figure 5.8(a).

Figures 6.14 and 6.16 also show the localized Al grain orientations for the as-extruded 6061Al/NQX strips. The IPF map of as-extruded 6061Al/8.5NQX in Figure 6.14 shows most of the Al grains having {0 0 1} to {1 1 1} planes parallel to the extrusion plane which is more or less consistent with the ODF result in Figure 6.9(a) showing the presence of ND rotated-cube component and γ fibre texture for as-extruded 6061Al/8.5NQX strip. For as-extruded 6061Al/12.9NQX sample (see Figure 6.16), the IPF map shows the orientations mostly concentrate close to <1 0 1> in the ND direction suggesting most of the Al {1 0 1} planes nearly parallel to the extrusion plane along with other random orientations. This is also compatible with Figure 6.10(a) showing the formation of α fibre for as-extruded 6061Al/12.9NQX strip.

A closer look of Figures 6.14 and 6.16 also shows the presence of very small Al grains in the vicinity of NQX particles which might be the result of dynamic recrystallization due to particle stimulated nucleation (PSN) in the particle deformation zones during extrusion. PSN has already mentioned in section 5.1.3 as a form of recrystallization which occurs during static annealing. In fact, PSN can also happen during high temperature deformation as a form of dynamic recrystallization if high densities of dislocations accumulate at the particles during deformation and provide the driving force for nucleation in particle deformation zones [24]. One example of dynamic recrystallization by PSN is reported by Giribaskar et al. [25] on Al-Li based alloy during Equal Channel Angular Extrusion (ECAE) where ultrafine crystallites have been observed in the vicinity of non-deformable Al_3Zr-Al_3Li precipitates by TEM. Despite of the smaller Al grains in the vicinity of the NQX particles, the Al grain structure in the atomised NQX particles can also be observed in Figures 6.14 and 6.16. It can be seen that smaller sized NQX particles (6-15μm) consist of 1~2 grains while the relatively large NQX particle (~20μm) comprises of multiple grains with no preferred orientations. From the above observations, it seems that the formation of particle deformation zones and possibly dynamic recrystallized Al matrix grains around NQX particles and the Al grains in the NQX particles have led to weaker deformation texture when compared with unreinforced 6061Al alloy sample (Figure 5.8(a)) after extrusion.

After cold rolling with a true strain of 3.6, the Al matrix grains have been further subdivided into smaller subgrains with an average size of less than 1μm with lower aspect ratios (Figures 6.15 and 6.17). The results are consistent with the fractions of low angle grain boundaries summarized in Table 6.1 showing the fractions have increased from 26.0% in as-extruded state to 63.5% after cold rolling for 6061Al/8.5NQX and from 23.4% to 50.8% for 6061Al/12.9NQX, indicating severe grain fragmentation. In addition, the misorientation distribution plots in Figures 6.15 and 6.17 show increased fractions of low angle grain boundaries within the misorientation range of 0-10°, also suggesting the development of subgrain structure. The IPF maps in Figures 6.15 and 6.17 show the formation of near β fibre in cold rolled 6061Al/$NQX_{3.6}$ samples, agreeing with the ODF results.

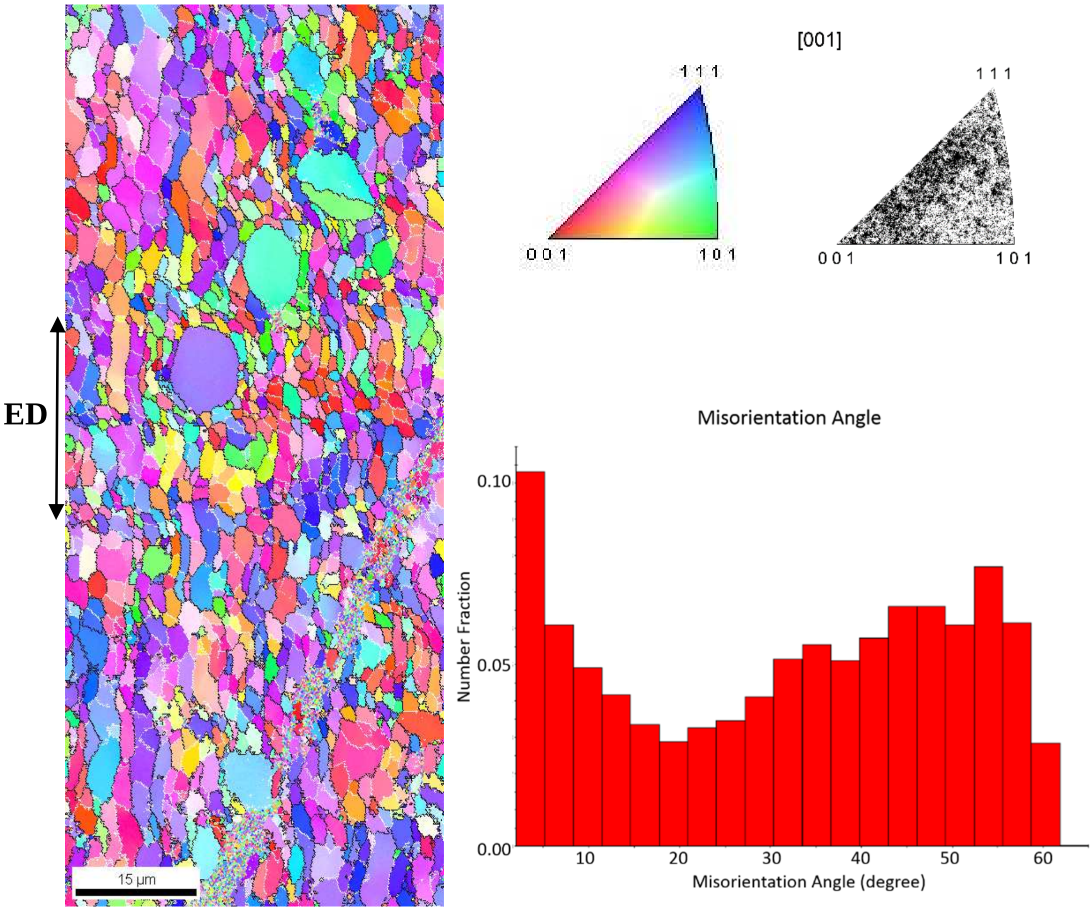

Figure 6.14: EBSD orientation map with IPF and misorientation distribution plot of as-extruded 6061Al/8.5NQX strip with respect to ND.

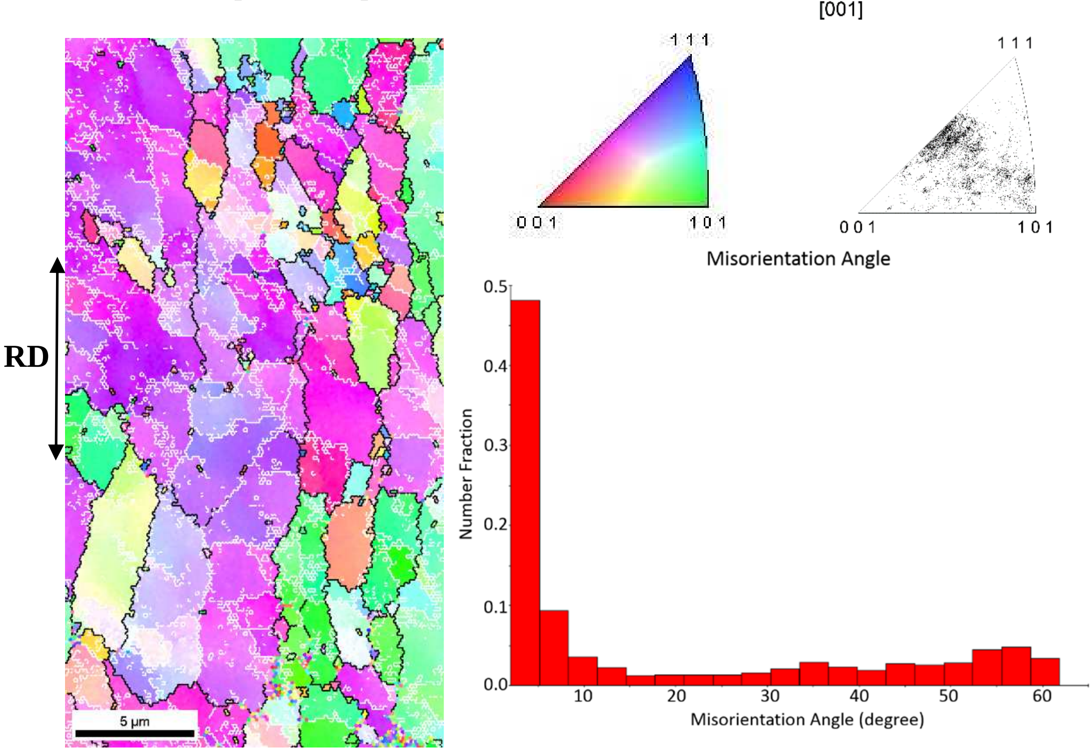

Figure 6.15: EBSD orientation map with IPF and misorientation distribution plot of cold rolled 6061Al/8.5NQX$_{3.6}$ with respect to ND.

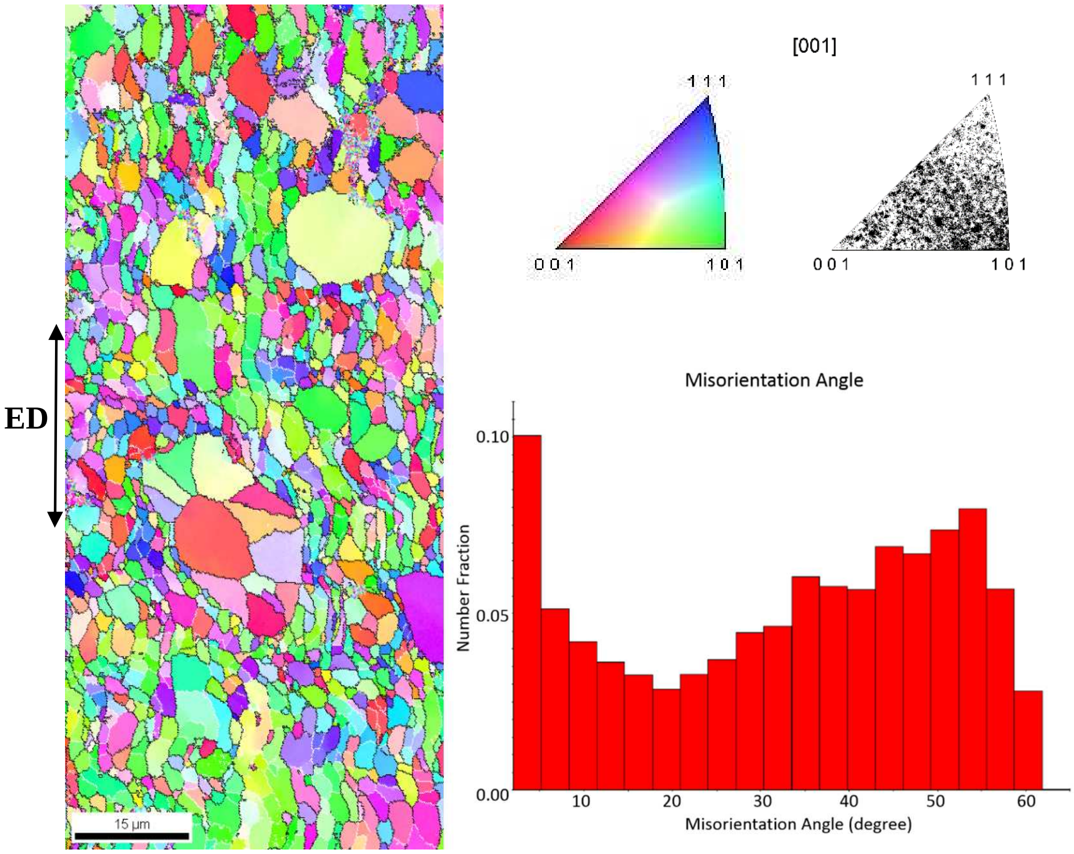

Figure 6.16: EBSD orientation map with IPF and misorientation distribution plot of as-extruded 6061Al/12.9NQX strip with respect to ND.

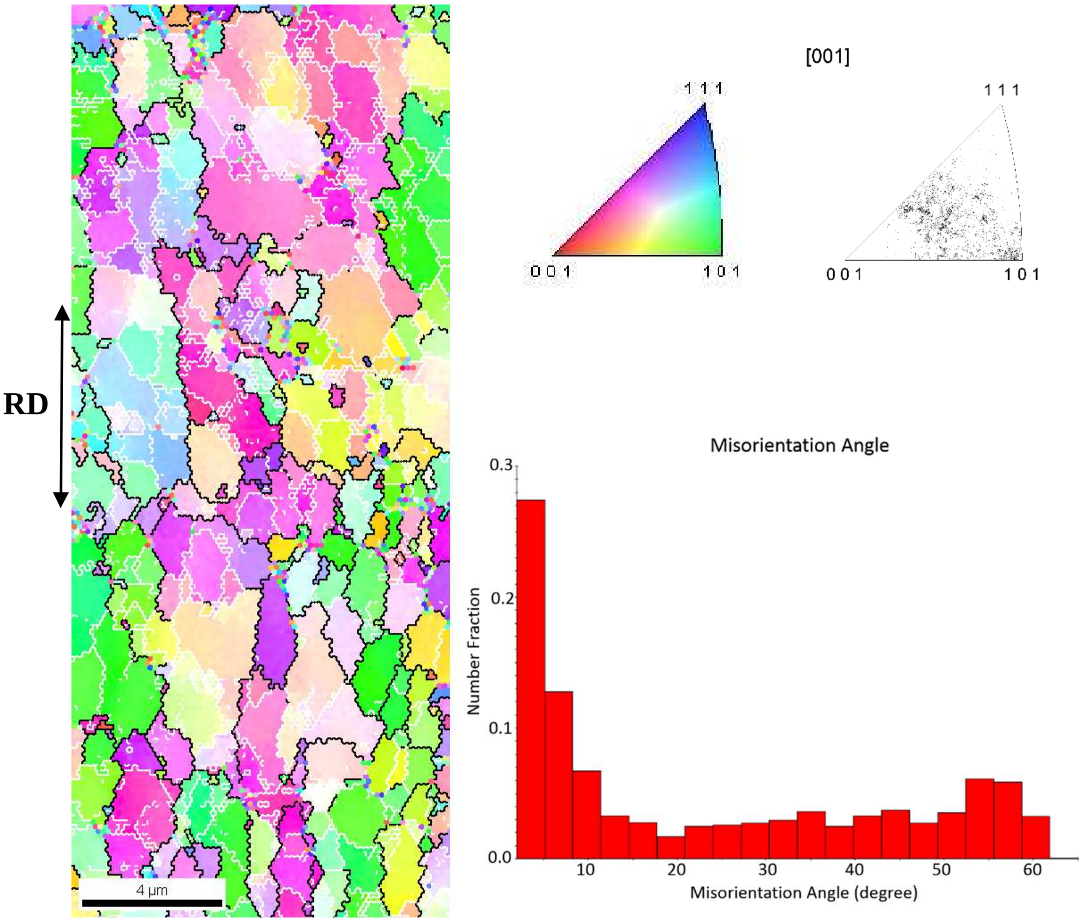

Figure 6.17: EBSD orientation map with IPF and misorientation distribution plot of cold rolled 6061Al/12.9NQX$_{3.6}$ with respect to ND.

Materials	**As-extruded strip**	**Cold rolled sample up to 3.6 of true strain**
6061Al/8.5NQX	26.0%	63.5%
6061Al/12.9NQX	23.4%	50.8%

Table 6.1: Fractions of low angle grain boundaries (2º-15º) measured from EBSD analysis for as-extruded and cold rolled 6061Al/NQX samples.

6.2 Mechanical properties and work hardening of as-extruded and cold rolled 6061Al/$Al_{93}Fe_3Cr_2Ti_2$ alloy particle composites

6.2.1 Microhardness analysis

Microhardness results on as-extruded and cold rolled 6061Al/NQX samples after each rolling pass are plotted in Figure 6.18 as a function of rolling strains. It can be seen that the microhardness of both samples increases with increasing rolling strains due to work hardening effect. All of the values for 6061Al/12.9NQX sample are higher than that for 6061Al/8.5NQX sample, indicating effective strengthening from additional NQX reinforcement.

The empirical power-law relationship based on eq. 5.1 [26] was also used to describe the microhardness-strain curves and the fitted lines are shown in Figure 6.18 as well. It can be seen that the fitted curves for the two composite samples have similar work hardening capabilities and the work hardening rate is initially high and then decreases with increasing strains for both composites. The similar behaviour is also observed in Figure 5.11 for cold rolled 6061Al(SH) alloy and 6061Al/SiC(SH) samples. The additions of reinforcement particles would normally lead to higher work hardening rates due to the increased dislocation densities in the vicinity of the particles [27], however, particle fracture, interfacial debonding and the possibly recrystallized Al matrix grains around the NQX particles in the present work could lead to localized strain softening and a decrease in the overall work hardening rates.

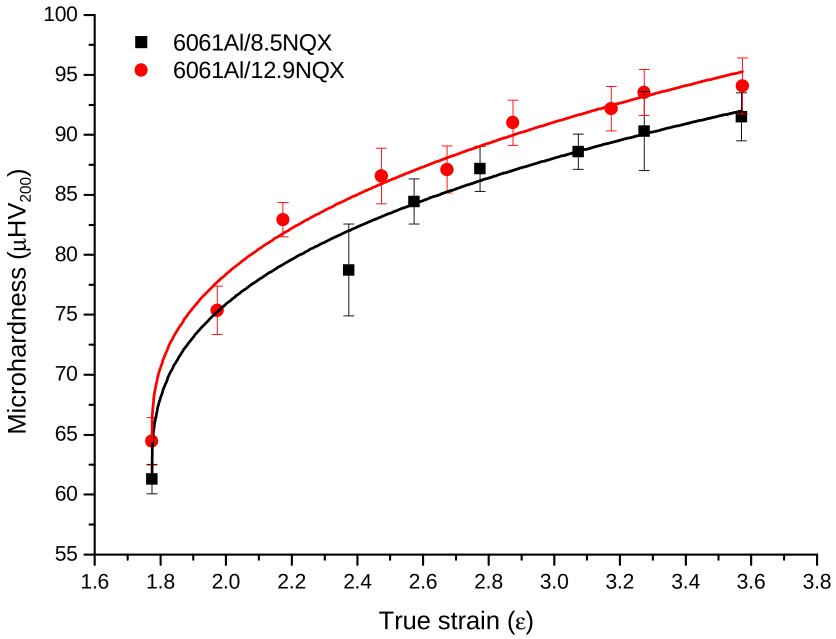

Figure 6.18: Microhardness of as-extruded and cold rolled 6061Al/8.5NQX and 6061Al/12.9NQX strips as a function of the rolling true strain and microhardness fitted lines based on eq. 5.1.

6.2.2 Three-point bending tests of cold rolled samples

Three-point bending tests were conducted on the final cold rolled samples such that the bending axis was perpendicular to the rolling direction. Flexural stress-strain curves for the cold rolled 6061Al/$NQX_{3.6}$ bending samples are shown in Figure 6.19 and strength values are summarized in Table 6.2. For comparison purposes, the test results on cold rolled $6061Al_{4.0}$ sample from as-extruded bars are also included. It should be noted that none of the samples have been fully broken during the tests since the equipment limitation has reached.

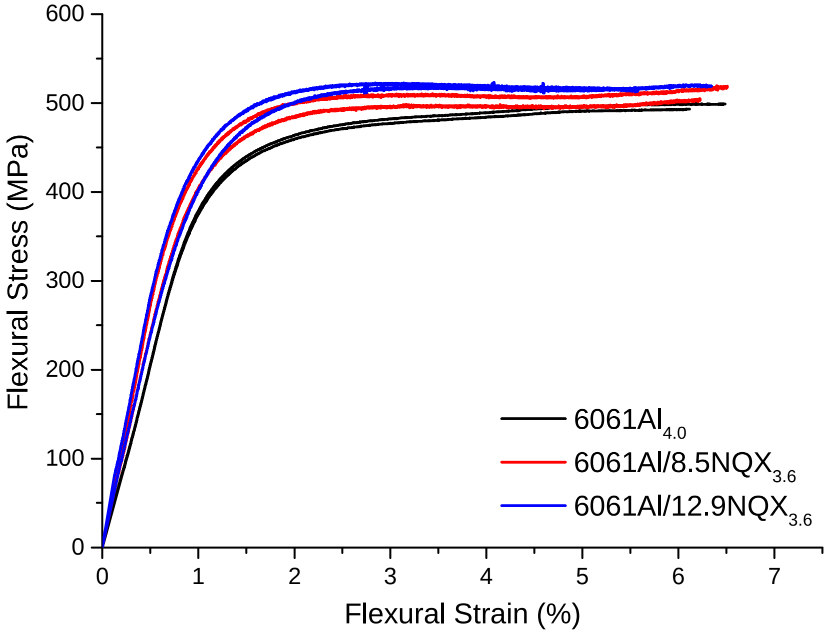

Figure 6.19: Three-point bending tests of cold rolled $6061Al_{4.0}$, $6061Al/8.5NQX_{3.6}$ and $6061Al/12.9NQX_{3.6}$ samples.

Materials	Stress at yield (MPa)	Bending flow stress (MPa)
$6061Al_{4.0}$	396±3	496±4
$6061Al/8.5NQX_{3.6}$	422±7	512±10
$6061Al/12.9NQX_{3.6}$	429±7	523±1

Table 6.2: Three-point bending properties of cold rolled $6061Al_{4.0}$, $6061Al/8.5NQX_{3.6}$ and $6061Al/12.9NQX_{3.6}$ samples.

From Figure 6.19 and Table 6.2, it can be seen that the bending strength has increased with increasing volume fraction of NQX reinforcement. The longitudinal planes (RD-ND) of the plastically bent composite samples were examined under SEM to investigate the failure behaviour and the images are shown in Figures 6.20 and 6.21. For the cold rolled $6061Al/8.5NQX_{3.6}$ sample, no macro-cracks have been observed under low magnification. A closer look on the tension side of the sample shows debonded interfaces which could act as failure initiation points. For cold rolled $6061Al/12.9NQX_{3.6}$ sample, macro-cracks have been developed on the tension side and grown along the bending axis. A higher magnification image shows that the cracks grow along debonded NQX particle/matrix interfaces.

The fracture behaviour of bending samples is quite complex and is generally governed by many factors, such as micro-voids formation around large second phase particles, strain localization and propagation of macroscopic shear bands [28]. In the present work, the composite samples developed conical voids around the NQX particles aligned along the rolling direction according to section 6.1.2. When the samples are subjected to bending, they experience a range of stresses across the sample thickness, such as shown in Figure 6.22 [29]. The tension stress is maximized at the convex surface of the loading position and favors the growth of the pre-existed conical voids. The growth and coalesce of the voids create a crack path that goes from particle to particle, leaving a zigzag crack path, such as shown in Figure 6.21.

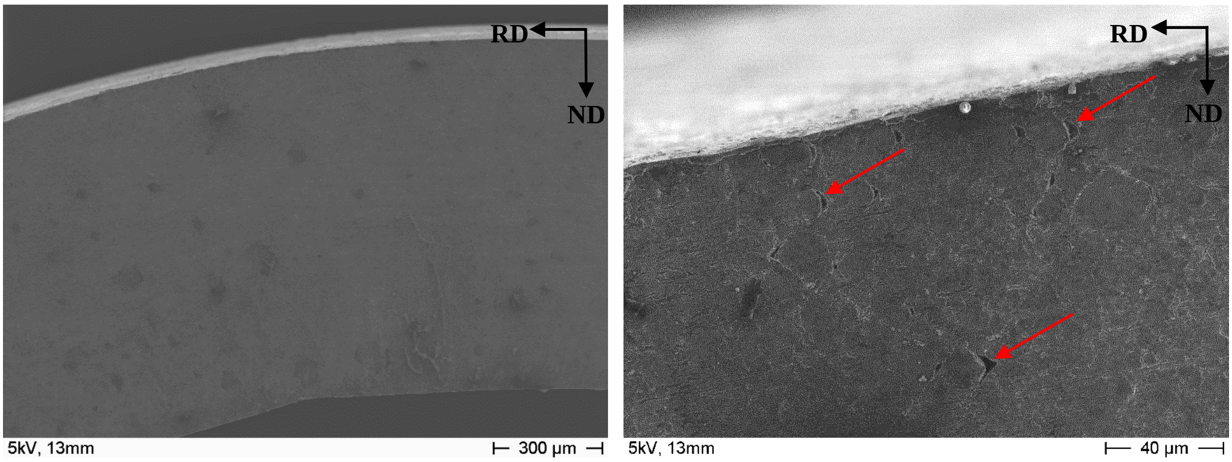

(a) (b)

Figure 6.20: Secondary electron images of the longitudinal plane (RD-ND) of the plastically bent cold rolled 6061Al/8.5$NQX_{3.6}$ samples showing (a) general microstructure; (b) micro-cracks (see arrows).

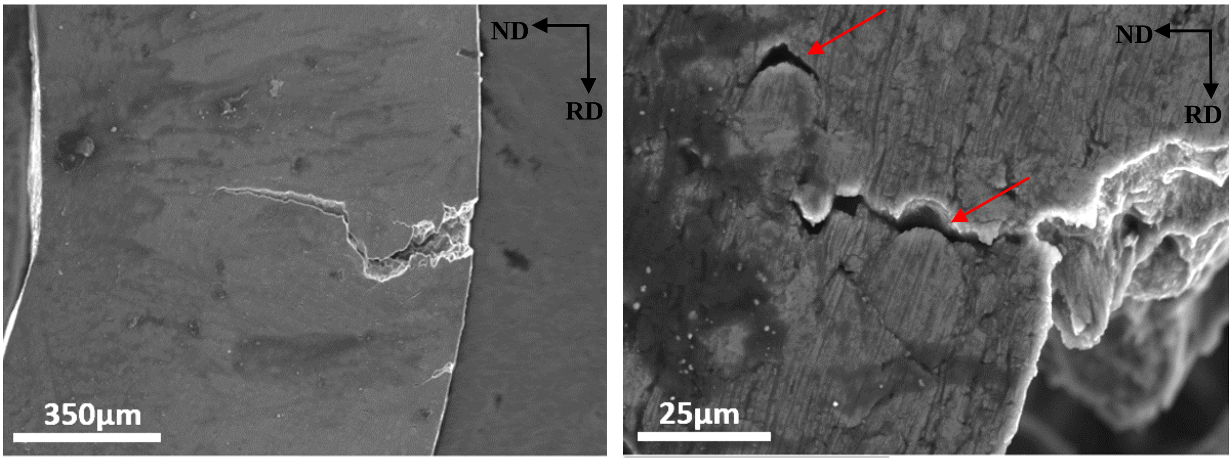

(a) (b)

Figure 6.21: Secondary electron images of the longitudinal plane (RD-ND) of the plastically bent cold rolled 6061Al/12.9$NQX_{3.6}$ samples showing (a) general microstructure; (b) micro-cracks (see arrows).

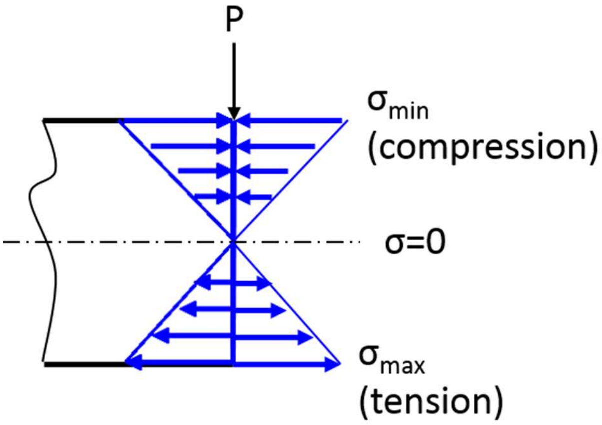

Figure 6.22: Bending stress distribution across sample thickness [29].

6.2.3 Tensile tests of as-extruded and cold rolled samples

Room temperature tensile tests were performed at a constant strain rate of $10^{-4}s^{-1}$ on the as-extruded composite bars and the final cold rolled samples. Engineering stress-strain curves for the tensile tests are shown in Figure 6.23. The tensile strength values are summarized in Table 6.3 as well as the tensile properties of as-extruded 6061Al alloy bar (section 4.2.3) and a 94% cold rolled 6061Al alloy reported by El-Sabbagh et al. [30] for comparison purposes.

According to Table 6.3, compared to the as-extruded 6061Al alloy bar, the as-extruded composite bars show slight improvement in UTS (5-7MPa) with slightly reduced ductility. The current increment of the composite bars in tensile strength is relatively low possibly due to poor load transfer and the size of NQX particles. In addition, the yield strength of the as-extruded 6061Al/12.9NQX bar is lower (~2MPa) than that of the as-extruded 6061Al/8.5NQX bar probably due to the increased microstructural defects related with increasing volume fractions of NQX reinforcements.

After cold rolling, the UTS of the cold rolled samples increases significantly with greatly reduced ductility. For example, the UTS of cold rolled 6061Al/8.5$NQX_{3.6}$ and 6061Al/12.9$NQX_{3.6}$ samples has increased by ~40% and ~45% when compared to as-extruded strength values, respectively, indicating effective strengthening from work hardening. In addition, compared with the UTS data of 94% cold rolled 6061Al alloy reported by El-Sabbagh et al. [30], the cold rolled 6061Al/8.5$NQX_{3.6}$ and 6061Al/12.9$NQX_{3.6}$ samples show ~40MPa and ~60MPa improvement in UTS due to the additions of NQX particles.

Despite the increased UTS, there is a decrease in stiffness and even a load/stress drop at the tensile curves for all the cold rolled samples in the red circled region. This phenomenon has rarely been reported in the literature. Guo et al. [31] has observed a sudden reduction of overall stress level in the tensile curve for cold rolled alumina dispersion strengthened copper (ADSC) alloys and named the phenomenon as “twice fracture”. He explained the “twice fracture” as a result of the growth and coalesce of the cracks initiated at the matrix/particle interface. Other researchers [32, 33] have observed tensile stress-strain curves with three distinct regions for MMCs. The first region is a linear region in which the macroscopic behaviour is elastic and the matrix and the reinforcement remain well bonded. The second region is a near linear region with a lower stiffness due to the damage in the microstructure which could be in the form of cracking of reinforcement, matrix,

matrix-reinforcement reaction zone or debonding at the interface. Finally, the third region is nonlinear due to significant inelasticity in the matrix upon fracture. Based on these reports, it is likely that deformation by damage has occurred in the red circled region which could be due to the growth and coalesce of the conical voids observed in Figure 6.4 or the major cracks in sizes of hundreds of microns observed in Figure 6.6. Afterwards, the well-bonded areas continue to deform until final failure. Further work, such as unload at the circled regions, needs to be done to understand the stress/load drop phenomenon.

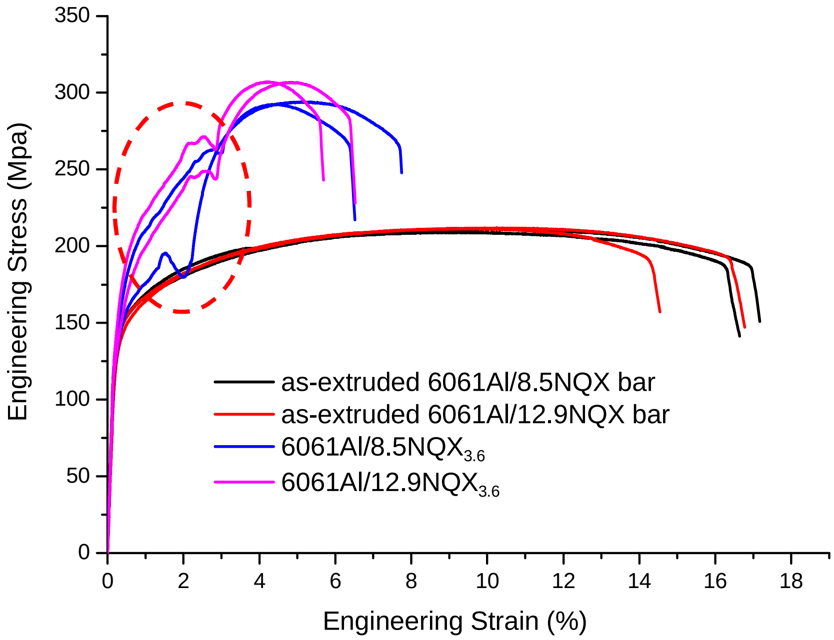

Figure 6.23: Room temperature tensile results for as-extruded 6061Al/NQX composite bars and cold rolled 6061Al/8.5$NQX_{3.6}$, 6061Al/12.9$NQX_{3.6}$ samples.

Materials	Yield stress (MPa)	UTS (MPa)	ε_f (%)
as-extruded 6061Al bar (section 4.2.3)	131±5	205±5	19±1
as-extruded 6061Al/8.5NQX bar	148±1	210±2	18±1
as-extruded 6061Al/12.9NQX bar	146±2	212±1	17±1
94% cold rolled 6061Al [30]	-	250	5
cold rolled 6061Al/8.5$NQX_{3.6}$	-	293±1	8±1
cold rolled 6061Al/12.9$NQX_{3.6}$	-	307±1	7±1

Table 6.3: Mechanical properties of as-extruded 6061Al/NQX composite bars and cold rolled 6061Al/8.5$NQX_{3.6}$, 6061Al/12.9$NQX_{3.6}$ samples extracted from Figure 6.23. Mechanical properties of as-extruded 6061Al alloy (section 4.2.3) are included for comparison. Mechanical properties of 94% cold rolled 6061Al alloy reported by El-Sabbagh et al. [30] are also included.

Figure 6.24 shows the fracture surfaces of as-extruded 6061Al/8.5NQX composite bar. Figure 6.24(a) shows the fracture surface overview with necking, indicating ductile fracture. Two different sizes of dimples have been observed. One is relatively large with the size of NQX particles as shown in Figure 6.24(b) with some particles still present inside the dimples. EDX analysis (Figure 6.24(e)) on particles 1 and 2 suggests they could be NQX particles. A significant macro-crack due to the interconnecting of debonding initiated cracks can be seen in Figure 6.24(c). It seems that interfacial debonding and the coalesce of the debonding initiated cracks have led to the final failure. The other type of dimple occurs in the 6061Al matrix with an average size of 1.2±0.3μm as shown in Figure 6.24(d).

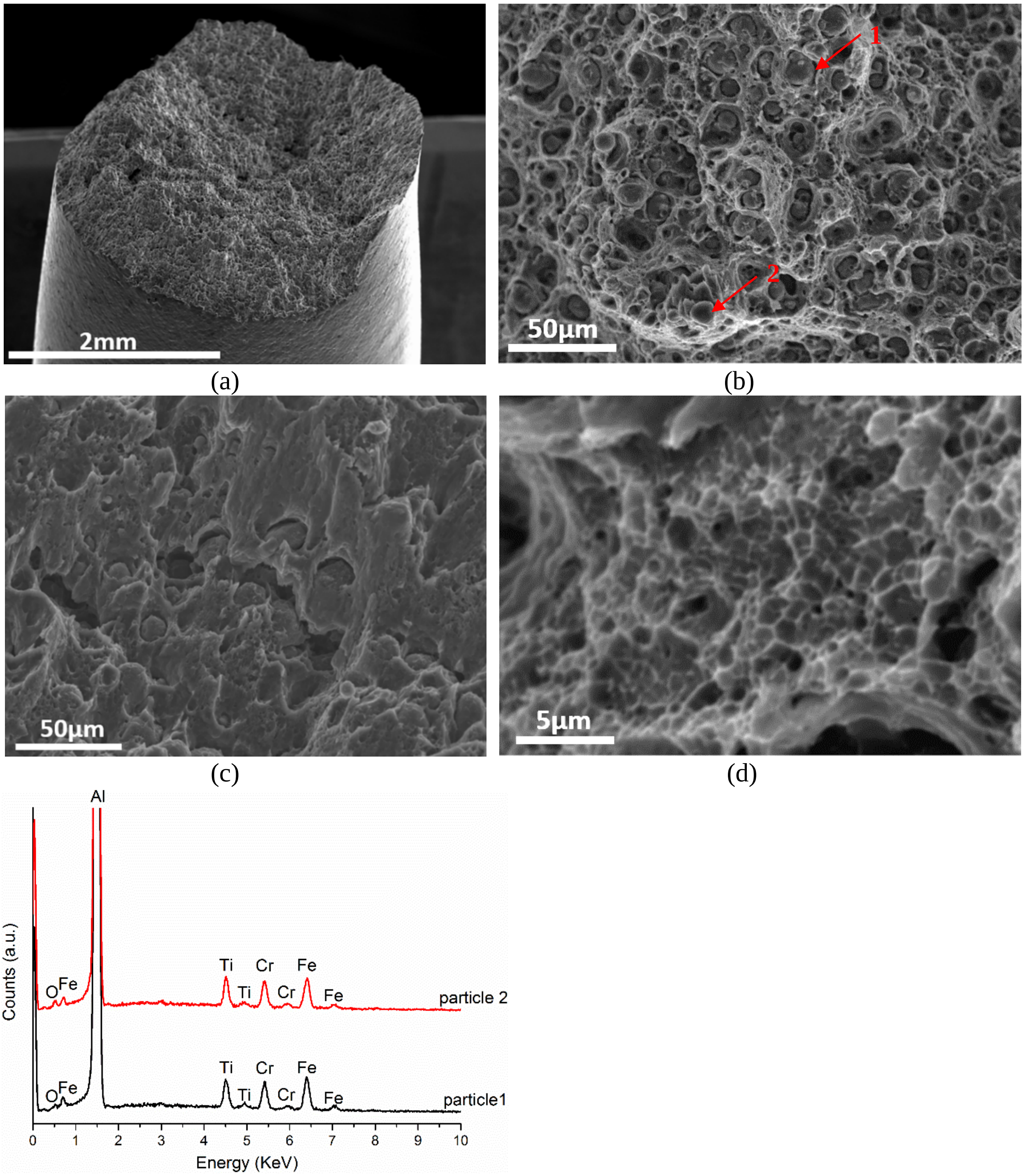

(a) (b)

(c) (d)

(e)

Figure 6.24: Fracture surfaces of as-extruded 6061Al/8.5NQX composite bar showing (a) overview of the fractured section, (b) dimples related with NQX, (c) macro-cracks, (d) Al matrix dimple and (e) EDX spectra for particles 1 and 2.

The fracture surfaces of cold rolled 6061Al/8.5$NQX_{3.6}$ sample are shown in Figure 6.25. From Figure 6.25(a), the cold rolled sample has a relatively flat fracture surface with an angle of ~45° with no obvious necking, indicating that the failure mode has changed from necking to shear fracture after cold rolling. Similar failure mode transition has also been observed by Panigrahi and Jayaganthan [34] on cryorolled 7075Al alloy and Fang et al. [35] on Al-Mg alloy after equal channel angular pressing (ECAP). A higher magnification image in Figure 6.25(b) shows debonded NQX particles (particles 1-6 have been confirmed by EDX analysis) indicating that the main failure mechanism is still the pull-out of the reinforcement particles. Figure 6.25(c) shows shallow dimples slightly elongated along the shear direction with an average size of 0.8±0.3μm in Al matrix indicating less plastic deformation when compared to the as-extruded bars. The reduction in dimple size is in agreement with the reduced ductility observed in Figure 6.23 for cold rolled 6061Al/$NQX_{3.6}$ samples and is reported to be due to grain refinement and work hardening associated with cold rolling process [34, 36, 37].

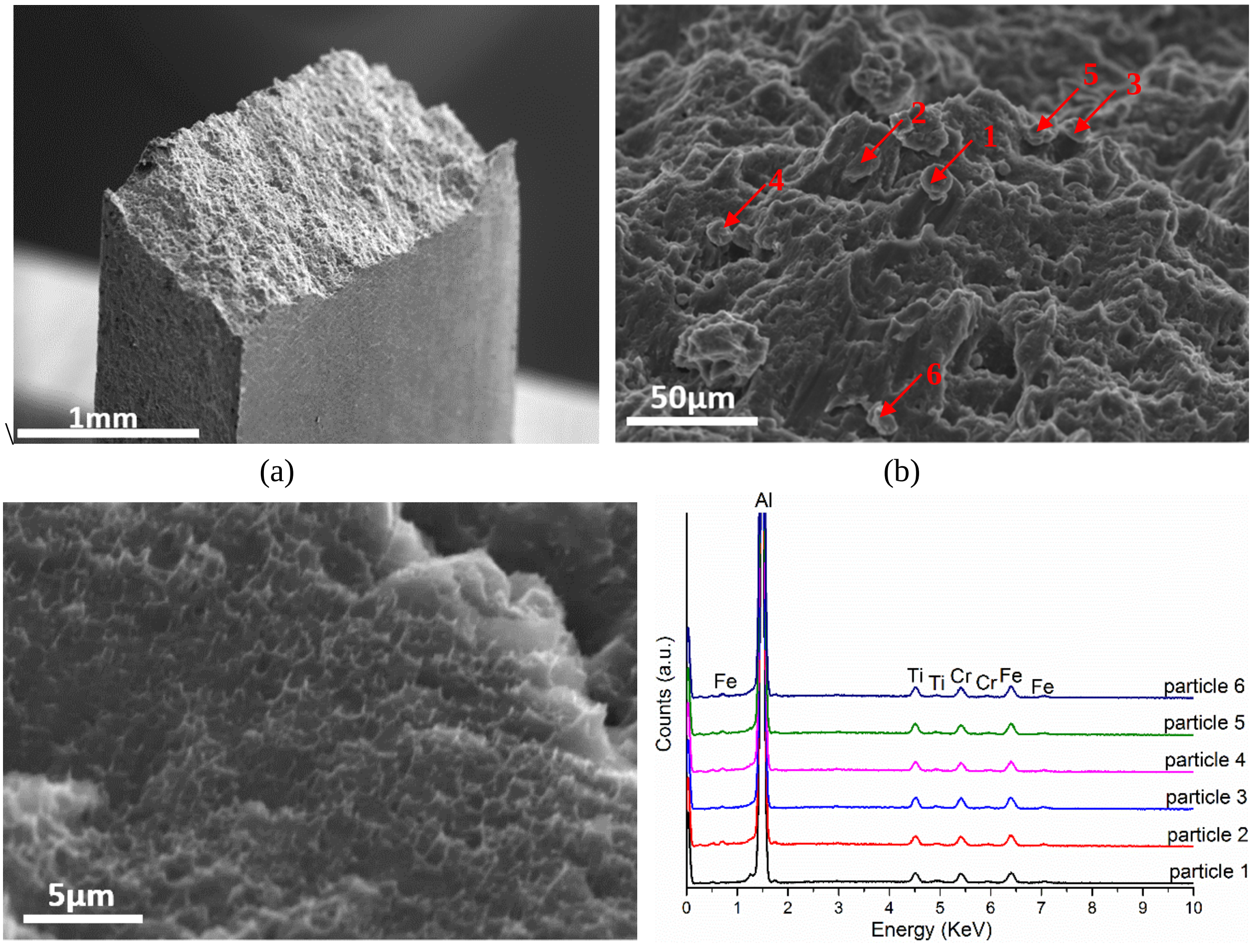

(a) (b)

(c) (d)

Figure 6.25: Fracture surfaces of cold rolled 6061Al/8.5NQX$_{3.6}$ showing (a) overview of the fractured section, (b) debonded NQX particles (c) Al matrix dimple and (d) EDX spectra for particles 1-6.

6.3 Discussion and future work

6.3.1 Effect of rolling strain

The influence of rolling strain to the composite microstructure has been analyzed in detail by means of SEM, TEM, texture XRD and EBSD. SEM analysis shows a uniform distribution of NQX particles embedded in 6061Al matrix during cold rolling. However, microstructure defects, such as cracks, conical voids, interfacial debonding, have occurred and major cracks in sizes of hundreds of microns have been observed in the final cold rolled composite samples (see Figures 6.4 and 6.6). TEM and EBSD measurements show the development of substructures in the 6061Al matrix. During cold rolling, elongated Al grains have been subdivided. The subgrain size has reduced from 1.5-2.4µm with an aspect ratio of 1.4-1.6 in the as-extruded condition to less than 1µm (0.2-0.4µm observed in TEM analysis) after a rolling strain of 3.6. The reduced subgrain size is believed to be the result of the increased dislocation densities induced by cold rolling process forming dislocation walls as subgrain boundaries [16], agreeing with the TEM observation in Figure 6.8(e).

The effect of rolling strain on the mechanical properties of the composites have been studied in terms of microhardness, three-point bending tests and tensile tests. The microhardness and UTS of the cold rolled composites with a rolling strain of 3.6 have increased from 60-65µHV_{200} in the as-extruded state to 90-95µHV_{200} and 210-212MPa to 293-307MPa, respectively, due to work hardening effect. However, decreased stiffness and a stress/load drop phenomenon have been observed in the tensile tests for the cold rolled samples which might be due to the development of microstructure defects during cold rolling. The bending tests were only carried out on cold rolled samples so the work hardening effect cannot be investigated.

6.3.2 Effect of NQX particles

Sections 6.1.4 and 6.1.5 studies the macroscopic and localized texture development during extrusion and cold rolling for 6061Al/NQX composites by texture XRD and EBSD. After extrusion into strips, the 6061Al/8.5NQX strip has a strong rotated-cube, a moderate α fibre and a weak γ fibre along with other random orientations while the as-extruded 6061Al/12.9NQX strip has a stronger α fibre (higher intensities near Brass component) and a weak γ fibre. Consistent results were also observed in the EBSD analysis. Generally speaking, the increasing volume fractions of micron-sized hard reinforcement particles would lead to a decrease in the matrix texture intensity due to the formation of particle deformation zones adjacent to the particles [38-41]. However, Poudens et al. [38] have found an increase in the main texture intensity of the Al matrix with an increase in the hard phase percentage for 6061Al/SiC_p (3μm) composites which was attributed to the more deforming matrix as the SiC content increases to accommodate the same macroscopic strain. It is likely that in the present work, the Al matrix in the as-extruded 6061Al/12.9NQX strip undergoes higher degree of deformation leading to the transformation of the rotated-cube component to the more stable α fibre texture (especially near Brass component). The rotation path that the ND rotated-cube component transforms to Brass component after certain deformation degree is reported by Liu and Morris [42] on AA3105 Al alloys. It should be noted that the above explanation is a possible mechanism while the actual reasons are unclear and need further work. Compared with the texture of the as-extruded 6061Al alloy in section 5.1.3 where a near β fibre has formed, the additions of NQX particles have led to the development of intermediate and unstable texture components.

During cold rolling, the intermediate and unstable texture components have gradually re-oriented and a sharp β fibre texture has formed for both composites. The maximum texture intensities for the three dominant texture components near Brass (B’), Copper (C’) and S (S’) positions have been plotted in Figure 6.26 as well as the texture intensities for $6061Al_{3.6}$ alloy sample (section 5.1.3). It can be seen that similar with Figure 5.14, the additions of NQX particles have led to a reduction in the main texture intensities. The additions of NQX particles have similar effect as SiC particles that they all weaken the texture intensities. However, for cold rolled $6061Al/NQX_{3.6}$ samples, a sharp β fibre texture has formed while the cold rolled $6061Al/SiC(SH)_{3.3}$ samples have no preferred orientations possibly due to the difference in interparticle spacing arised from different particle diameters.

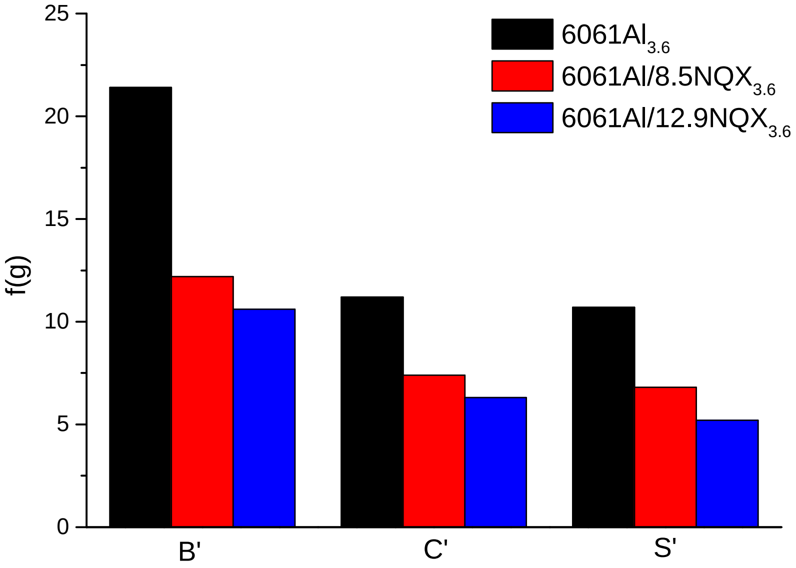

Figure 6.26: Maximum intensity of main texture components near Brass (B'), Copper (C') and S (S') position in cold rolled $6061Al_{3.6}$, $6061Al/8.5NQX_{3.6}$ and $6061Al/12.9NQX_{3.6}$ samples.

6.3.3 Future work

The present work shows that mixing, compaction, extrusion and cold rolling are not appropriate techniques to fabricate Al alloy composites reinforced with nanoquasicrystalline $Al_{93}Fe_3Cr_2Ti_2$ alloy particles. Poor interfacial bonding and large cracks have been observed which seriously deteriorate the mechanical properties. For future work, methods to improve the interfacial bonding, such as high energy ball milling to break the oxide layers around the particles, should be carried out. Hot rolling instead of cold rolling, which would facilitate the matrix flow more easily to avoid the formation of micro-cracks should be further tested.

6.4 References

[1] N. J. Rounthwaite, "Development of bulk nanoquasicrystalline alloys for high strength elevated temperature applications," Doctor of Philosophy, Department of Materials, University of Oxford, 2012.

[2] M. Galano, F. Audebert, I. C. Stone, and B. Cantor, "Nanoquasicrystalline Al-Fe-Cr-based alloys. Part I: Phase transformations," *Acta Materialia,* vol. 57, pp. 5107-5119, 2009.

[3] B. L. Zheng, Y. J. Lin, Y. Z. Zhou, and E. J. Lavernia, "Gas atomization of amorphous aluminum powder: Part II. Experimental investigation," *Metallurgical and Materials Transactions B-Process Metallurgy and Materials Processing Science,* vol. 40, pp. 995-1004, 2009.

[4] J. Zhou, J. Duszczyk, and B. M. Korevaar, "A study on an atomized Al-Fe-Mo-Zr powder to be processed for high-temperature applications," *Journal of Materials Science,* vol. 26, pp. 3292-3304, 1991.

[5] B. Avitzur, "Analysis of central bursting defects in extrusion and wire drawing," *Journal of Engineering for Industry-Transactions of the Asme,* vol. 90, pp. 79-90, 1968.

[6] C. Luo, "Modeling the behavior of inclusions in plastic deformation of steels," PhD, Division of Materials Forming, Department of Production Engineering, Royal Institute of Technology, 2001.

[7] C. H. Luo, "Evolution of voids close to an inclusion in hot deformation of metals," *Computational Materials Science,* vol. 21, pp. 360-374, 2001.

[8] T. J. Baker and J. A. Charles, "Deformation of Mns inclusions in steel," *Journal of the Iron and Steel Institute,* vol. 210, p. 680, 1972.

[9] G. I. Belchenko and S. I. Gubenko, "Deformation of non-metallic inclusions during steel rolling," *Russian Metallurgy,* pp. 66-69, 1983.

[10] M. Galano, F. Audebert, B. Cantor, and I. Stone, "Structural characterisation and stability of new nanoquasicrystalline Al-based alloys," *Materials Science and Engineering A,* vol. 375, pp. 1206-1211, 2004.

[11] Ø. Ryen, "Work hardening and mechanical anisotropy of aluminium sheets and profiles," Norwegian University of Science and Technology, 2003.

[12] B. Bay, N. Hansen, D. A. Hughes, and D. Kuhlmannwilsdorf, "Overview no-96 - Evolution of fcc deformation structures in polyslip," *Acta Metallurgica Et Materialia,* vol. 40, pp. 205-219, 1992.

[13] Q. Liu and N. Hansen, "Deformation microstructure and orientation of fcc crystals,"

Physica Status Solidi a-Applied Research, vol. 149, pp. 187-199, 1995.

[14] Q. Liu, X. Huang, D. J. Lloyd, and N. Hansen, "Microstructure and strength of commercial purity aluminium (AA 1200) cold-rolled to large strains," *Acta Materialia,* vol. 50, pp. 3789-3802, 2002.

[15] F. J. Humphreys, P. B. Prangnell, J. R. Bowen, A. Gholinia, and C. Harris, "Developing stable fine-grain microstructures by large strain deformation," *Philosophical Transactions of the Royal Society a-Mathematical Physical and Engineering Sciences,* vol. 357, pp. 1663-1680, 1999.

[16] J. G. Sevillano, P. Vanhoutte, and E. Aernoudt, "Large strain work-hardening and textures," *Progress in Materials Science,* vol. 25, pp. 69-412, 1980.

[17] V. Randle and O. Engler, *Introduction to texture analysis : macrotexture, microtexture and orientation mapping*. Amsterdam: Gordon & Breach;, 2000.

[18] U. F. Kocks, C. N. Tomé, and H.-R. Wenk, *Texture and anisotropy : preferred orientations in polycrystals and their effect on materials properties*. New York ; Cambridge: Cambridge University Press, 1998.

[19] W. C. Liu and J. G. Morris, "Lattice rotation and stability of 22.5 degrees ND rotated cube orientation in cold rolled polycrystalline AA 5182 aluminum alloy," *Materials Science and Engineering A,* vol. 380, pp. 147-154, 2004.

[20] H. Masui, "Simulation for f.c.c. deformation texture by modified pencil glide theory," *Acta Materialia,* vol. 47, pp. 4283-4298, 1999.

[21] J. Hirsch and K. Lucke, "Mechanism of deformation and development of rolling textures in polycrystalline fcc metals .2. Simulation and interpretation of experiments on the basis of taylor-type theories," *Acta Metallurgica,* vol. 36, pp. 2883-2904, 1988.

[22] R. Hielscher and H. Schaeben, "A novel pole figure inversion method: specification of the MTEX algorithm," *Journal of Applied Crystallography,* vol. 41, pp. 1024-1037, 2008.

[23] (08-10-2013). Available: https://code.google.com/p/mtex/

[24] F. J. Humphreys and M. Hatherly, *Recrystallization and related annealing phenomena*. Oxford: Pergamon, 1995.

[25] S. Giribaskar, Gouthama, and R. Prasad, "Dynamic recrystallization in Al-Li based alloy during Equal Channel Angular Extrusion," *Recrystallization and Grain Growth Iv,* vol. 715-716, pp. 286-291, 2012.

[26] J. H. Hollomon, "Tensile deformation," *Transactions of the American Institute of Mining and Metallurgical Engineers,* vol. 162, pp. 268-290, 1945.

[27] M. Rajamuthamilselvan, S. Ramanathan, and S. Krishnamohan, "Deformation stability of

Al 7075/20%SiCp (63μm) composites during hot compression," Nagapattinam, Tamil Nadu, 2012, pp. 281-286.

[28] A. Davidkov, R. H. Petrov, P. De Smet, B. Schepers, and L. A. I. Kestens, "Microstructure controlled bending response in AA6016 Al alloys," *Materials Science and Engineering A*, vol. 528, pp. 7068-7076, 2011.

[29] (25-03-2014). Available: http://en.wikipedia.org/wiki/Flexural_strength

[30] A. M. El-Sabbagh, M. Soliman, M. A. Taha, and H. Palkowski, "Effect of rolling and heat treatment on tensile behaviour of wrought Al-SiCp composites prepared by stir-casting," *Journal of Materials Processing Technology*, vol. 213, pp. 1669-1681, 2013.

[31] M. X. Guo, M. P. Wang, K. Shen, L. F. Cao, R. S. Lei, and S. M. Li, "Effect of cold rolling on properties and microstructures of dispersion strengthened copper alloys," *Transactions of Nonferrous Metals Society of China*, vol. 18, pp. 333-339, 2008.

[32] R. K. Goldberg and S. M. Arnold, "A study of influencing factors on the tensile response of a titanium matrix composite with weak interfacial bonding," *NASA/TM*, vol. 209798, 2000.

[33] B. S. Majumdar and G. M. Newaz, "Inelastic deformation of metal matrix composites - plasticity and damage mechanisms," *Philosophical Magazine a-Physics of Condensed Matter Structure Defects and Mechanical Properties*, vol. 66, pp. 187-212, 1992.

[34] S. K. Panigrahi and R. Jayaganthan, "Development of ultrafine grained high strength age hardenable Al 7075 alloy by cryorolling," *Materials & Design*, vol. 32, pp. 3150-3160, 2011.

[35] D. R. Fang, Q. Q. Duan, N. Q. Zhao, J. J. Li, S. D. Wu, and Z. F. Zhang, "Tensile properties and fracture mechanism of Al-Mg alloy subjected to equal channel angular pressing," *Materials Science and Engineering A*, vol. 459, pp. 137-144, 2007.

[36] A. Vinogradov, T. Ishida, K. Kitagawa, and V. I. Kopylov, "Effect of strain path on structure and mechanical behavior of ultrafine grain Cu-Cr alloy produced by equal-channel angular pressing," *Acta Materialia*, vol. 53, pp. 2181-2192, 2005.

[37] Y. G. Ko, D. H. Shin, K. T. Park, and C. S. Lee, "An analysis of the strain hardening behavior of ultra-fine grain pure titanium," *Scripta Materialia*, vol. 54, pp. 1785-1789, 2006.

[38] A. Poudens, B. Bacroix, and T. Bretheau, "Influence of microstructures and particle concentrations on the development of extrusion textures in metal-matrix composites," *Materials Science and Engineering A*, vol. 196, pp. 219-228, 1995.

[39] L. Q. Chen and N. Kanetake, "Finite element polycrystal model simulation of cold rolling

textures in deformation processed two-phase Nb/Al metal-metal composites," *Transactions of Nonferrous Metals Society of China*, vol. 15, pp. 64-71, 2005.

[40] F. J. Humphreys, W. S. Miller, and M. R. Djazeb, "Microstructural development during thermomechanical processing of particulate metal-matrix composites," *Materials Science and Technology,* vol. 6, pp. 1157-1166, 1990.

[41] F. J. Humphreys and P. N. Kalu, "The plasticity of particle-containing polycrystals," *Acta Metallurgica Et Materialia,* vol. 38, pp. 917-930, 1990.

[42] J. T. Liu and J. G. Morris, "Macro-, micro- and mesotexture evolutions of continuous cast and direct chill cast AA 3105 aluminum alloy during cold rolling," *Materials Science and Engineering A,* vol. 357, pp. 277-296, 2003.

7. Cold rolling of Al/Nb and 6061Al/Nb composites

Deformation processed metal-metal composites (DPMMCs) have superior mechanical properties at room temperature or elevated temperatures [1-9]. Considering the promising mechanical properties of DPMMCs, the advantages of powder metallurgy and the potential applications of Al sheet composites, Al and 6061Al alloy reinforced with Nb particles have been chosen to produce DPMMCs by powder metallurgy routes followed with hot extrusion and cold rolling.

The compacted composite billets were extruded into strips and subjected to cold rolling process. For improved mechanical properties, one of the as-extruded 6061Al/Nb composite strips were solution heat treated before cold rolling and designated as “6061Al/Nb(SH)” in the following text. For comparison purposes, pure Al powders were prepared in the same way to provide the reference data. Table 3.4 lists the sample information, heat treatment and rolling details for each sample. Further details of the production of the composites can be found in Chapter 3.

Section 7.1 comprises the studies of the effect of cold rolling on the microstructure development and texture evolution. Section 7.2 comprises the studies of the mechanical properties and work hardening behaviour of the composites during cold rolling in terms of microhardness, three-point bending tests and tensile tests. Discussion and partial conclusions can be found in Section 7.3.

7.1 Microstructural Characterization of as-extruded and cold rolled Al/Nb and 6061Al/Nb composites

7.1.1 X-ray diffraction analysis

XRD analysis has been carried out on the normal planes (TD-ED/RD) of the as-extruded and cold rolled Al/Nb, 6061Al/Nb and 6061Al/Nb(SH) samples to identify the phases present before and after cold rolling and the diffractograms are shown in Figure 7.1.

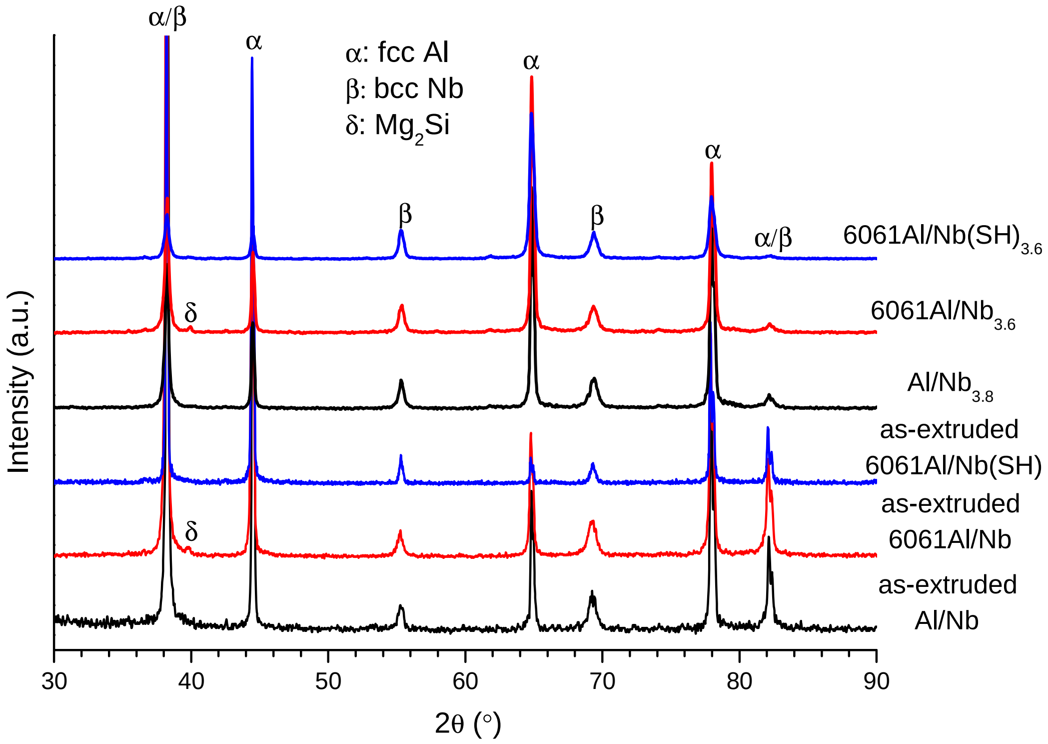

Figure 7.1: X-ray diffractograms of as-extruded and cold rolled Al/Nb, 6061Al/Nb and 6061Al/Nb(SH) samples in normal planes (TD-ED/RD).

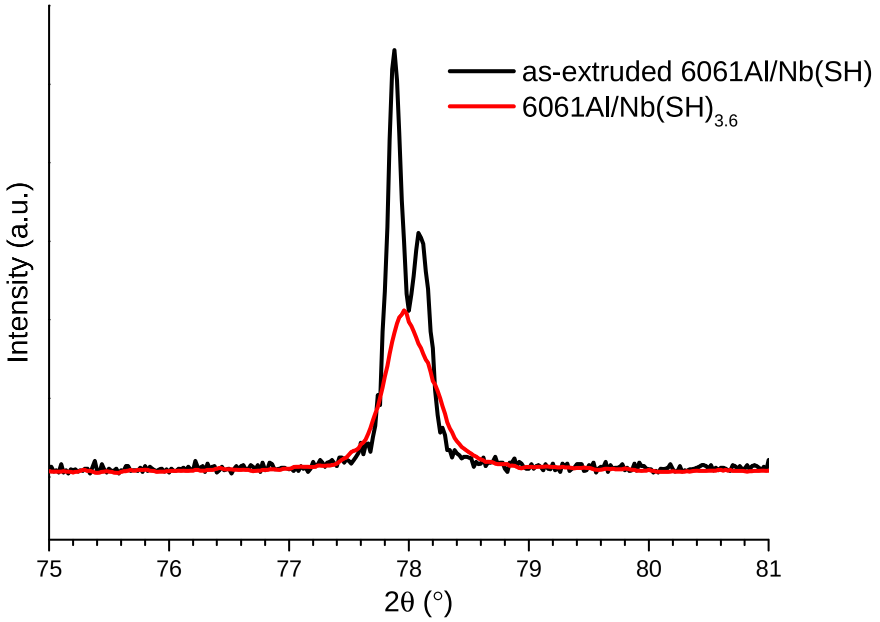

Figure 7.2: X-ray diffractograms of Al (3 1 1) peak of the normal plane (TD-ED/RD) of as-extruded 6061Al/Nb(SH) and cold rolled 6061Al/Nb$(SH)_{3.6}$.

For all as-extruded samples, fcc-Al, bcc-Nb (2θ=38.5°, 55.3°, 69.4° and 82.2°) have been identified. For as-extruded 6061Al/Nb sample, also Mg_2Si intermetallic phase is observed while for as-extruded 6061Al/Nb(SH) sample, this phase is not present perhaps due to the dissolution of the intermetallics during solution heat treatment. No other intermetallic phases, such as Al_3Nb or $AlNb_2$ [10, 11] have been detected after extrusion and cold rolling, suggesting no significant interfacial reactions have occurred during extrusion and cold rolling.

Figure 7.2 shows the Al (3 1 1) peak of the as-extruded and cold rolled 6061Al/Nb(SH) samples. Peak broadening and the disappearance of Cu $K\alpha_2$ reflection have been observed for cold rolled 6061Al/Nb$(SH)_{3.6}$ sample indicating enhanced lattice distortions after cold work. Similar XRD results were also observed in Chapter 5 for cold rolled 6061Al$(SH)_{3.6}$ alloy. The relative intensities of Al peaks have changed in as-extruded and cold rolled samples, indicating the development of certain texture after cold rolling which will be discussed in detail in sections 7.1.3 and 7.1.4.

7.1.2 Scanning electron microscopy and Optical microscopy analysis

Figure 7.3 shows the morphology of as-received Nb powders. The Nb particles have an irregular shape with an average particle size of about 130±57μm.

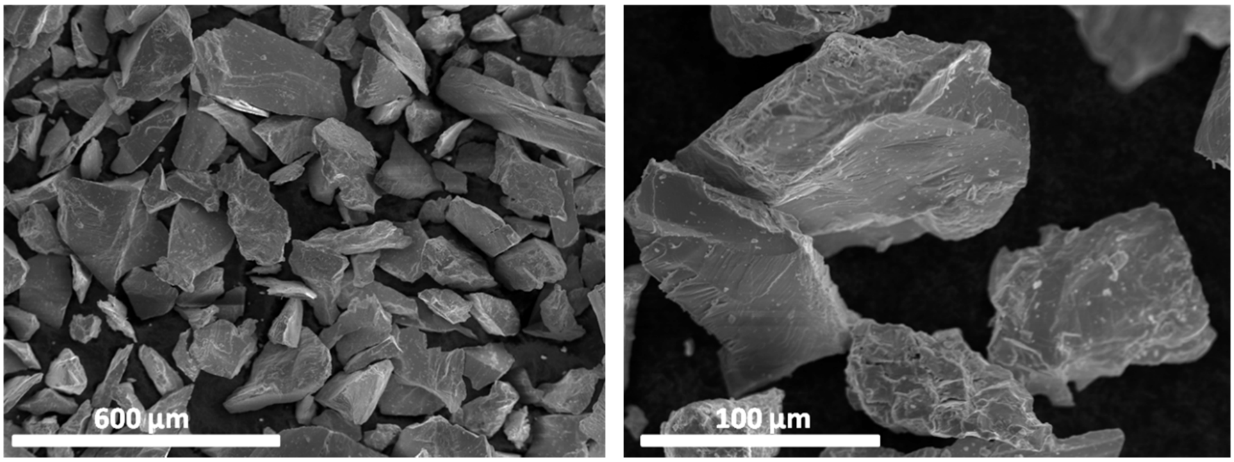

Figure 7.3: Secondary electron images of as-received Nb powders.

Optical microscope (OM) has been used to characterize the morphology development during extrusion and cold rolling. Figures 7.4-7.6 show representative OM images for as-extruded Al/Nb strip, cold rolled Al/$Nb_{2.4}$ and Al/$Nb_{3.8}$ samples in cross section plane (ND-TD), longitudinal plane (ND-ED/RD) and rolling plane (TD-ED/RD), respectively.

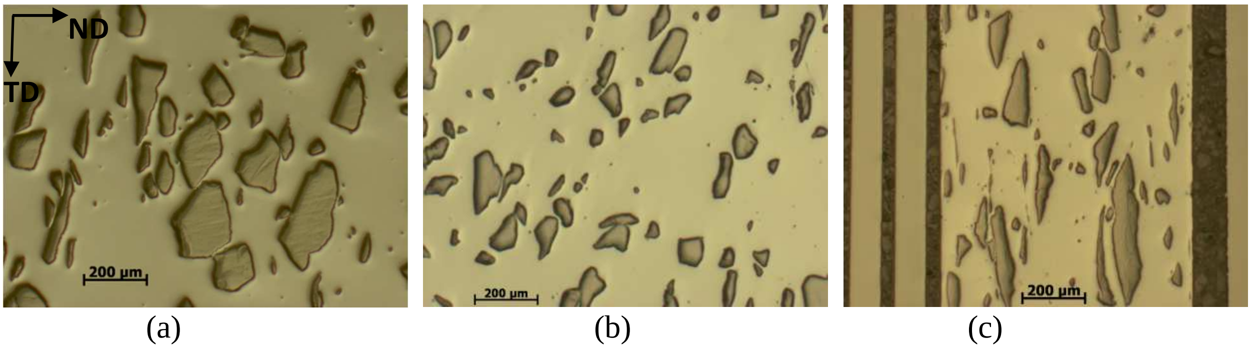

Figure 7.4: Optical images of (a) as-extruded Al/Nb strip, (b) cold rolled Al/$Nb_{2.4}$ and (c) cold rolled Al/$Nb_{3.8}$ in cross section plane (ND-TD).

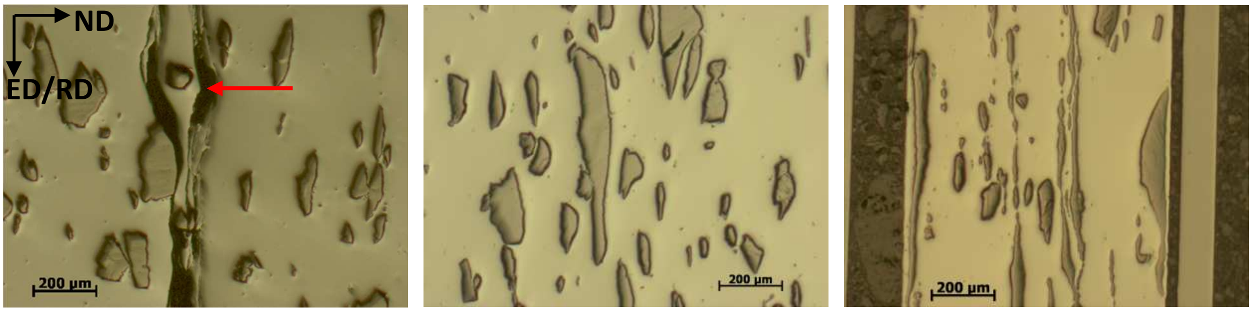

(a) (b) (c)

Figure 7.5: Optical images of (a) as-extruded Al/Nb strip, (b) cold rolled Al/$Nb_{2.4}$ and (c) cold rolled Al/$Nb_{3.8}$ in longitudinal plane (ND-ED/RD). Red arrow indicates Chevron cracking in the middle layer of the as-extruded Al/Nb strip.

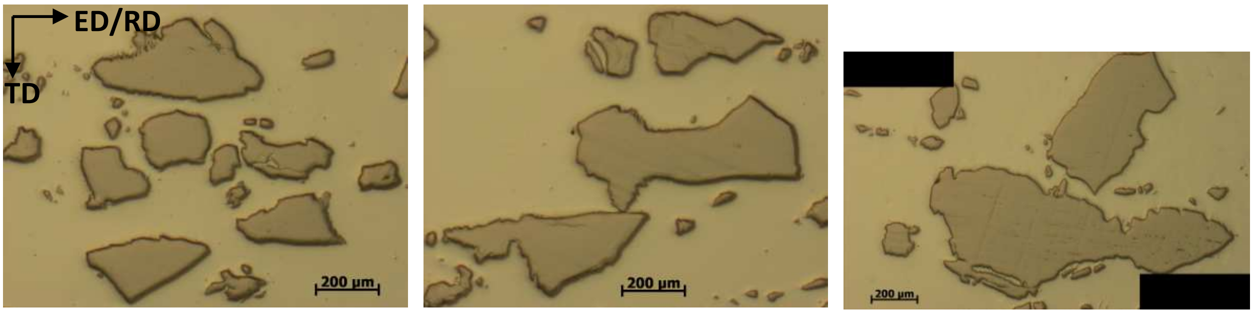

(a) (b) (c)

Figure 7.6: Optical images of (a) as-extruded Al/Nb strip, (b) cold rolled Al/$Nb_{2.4}$ and (c) cold rolled Al/$Nb_{3.8}$ in rolling plane (TD-ED/RD).

In as-extruded condition, most Nb particles remain undeformed. Some Nb particles show slight deformation possibly due to their specific crystal orientation related to the extrusion direction. Similar Chevron cracking [12] observed in the as-extruded 6061Al/NQX strips in Chapter 6 also occurs in the middle layer of the as-extruded Al/Nb strip (see the arrow in Figure 7.5(a)). During cold rolling, the Chevron cracks developed in extrusion seem bonded after multiple rolling passes indicating that rolling is an effective secondary processing technique to eliminate porosity and other defects from the previous consolidation steps.

The Nb particles become more and more flattened and expanded in rolling plane and elongated along rolling direction with further rolling passes. Finally, the Nb particles have developed into flattened ribbons of irregular cross section as revealed in Figure 7.5(c). Similar microstructure development has also occurred for 6061Al/Nb and 6061Al/Nb(SH) strips during cold rolling and the representative OM images in the longitudinal planes are displayed in Figures 7.7 and 7.8, showing the formation of Nb ribbons after cold rolling. The observed microstructure development is in agreement with Chen and Kanetake's results for cold rolled Al-Nb MMCs [13].

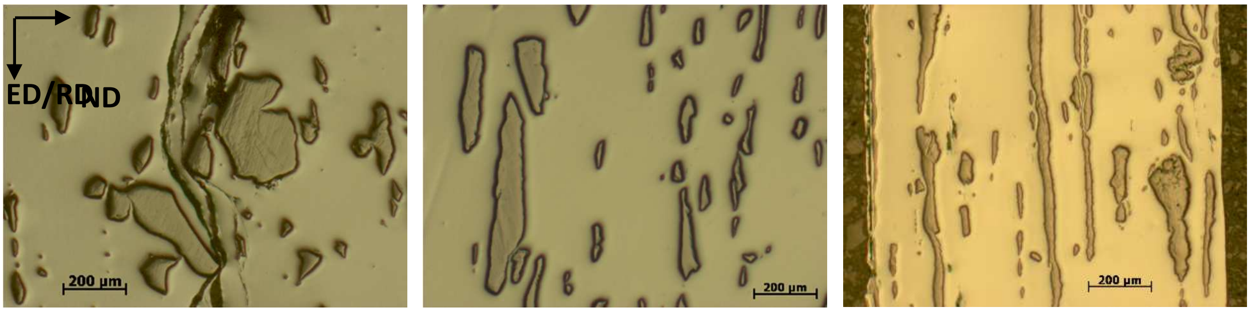

(a) (b) (c)

Figure 7.7: Optical images of (a) as-extruded 6061Al/Nb strip, (b) cold rolled 6061Al/Nb$_{2.4}$ and (c) cold rolled 6061Al/Nb$_{3.6}$ in longitudinal plane (ND-ED/RD).

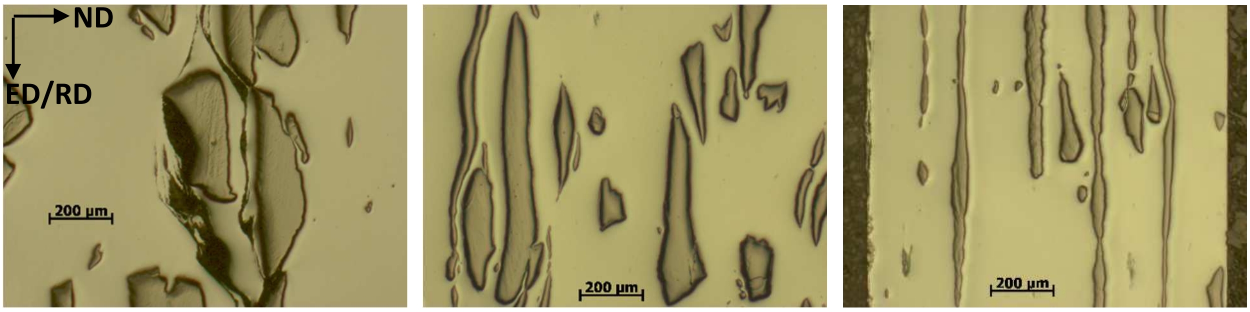

(a) (b) (c)

Figure 7.8: Optical images of (a) as-extruded 6061Al/Nb(SH) strip, (b) cold rolled 6061Al/Nb(SH)$_{2.5}$ and (c) cold rolled 6061Al/Nb(SH)$_{3.6}$ in longitudinal plane (ND-ED/RD).

The interparticle spacings and Nb ribbon thickness have been measured according to the longitudinal OM images and the results are plotted in Figure 7.9 as a function of rolling strains. The average Nb particle spacing is 221±67μm for as-extruded Al/Nb sample and after cold rolling it reduces to 116±29μm for Al/Nb$_{3.8}$ sample. The Nb ribbon thickness has changed from 102±53μm for as-extruded Al/Nb to 30±16μm for cold rolled Al/Nb$_{3.8}$ accordingly. The large measurement variations are mainly due to the broad Nb size distribution used. The interparticle spacing and Nb ribbon thickness developed for 6061Al/Nb and 6061Al/Nb(SH) samples follow similar trends with that of the Al/Nb composite.

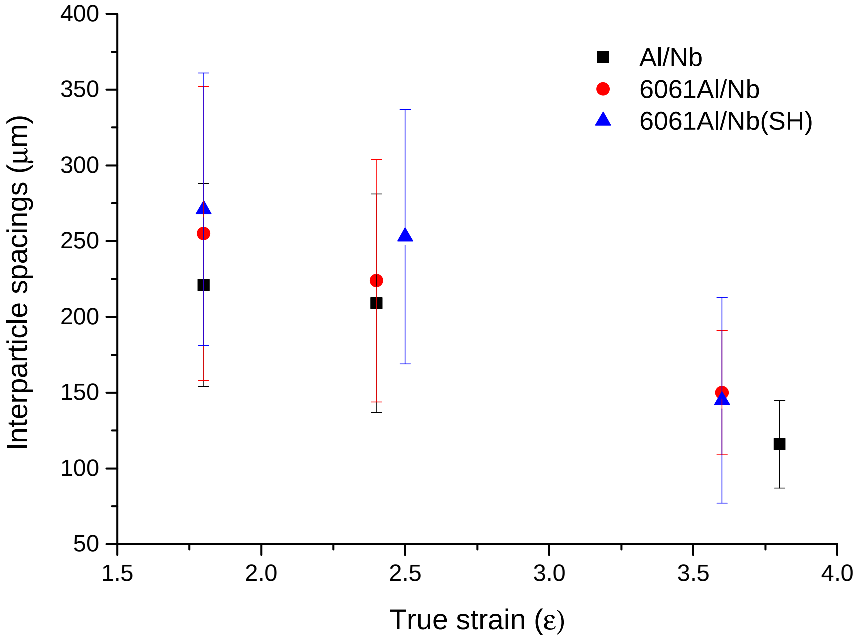

(a)

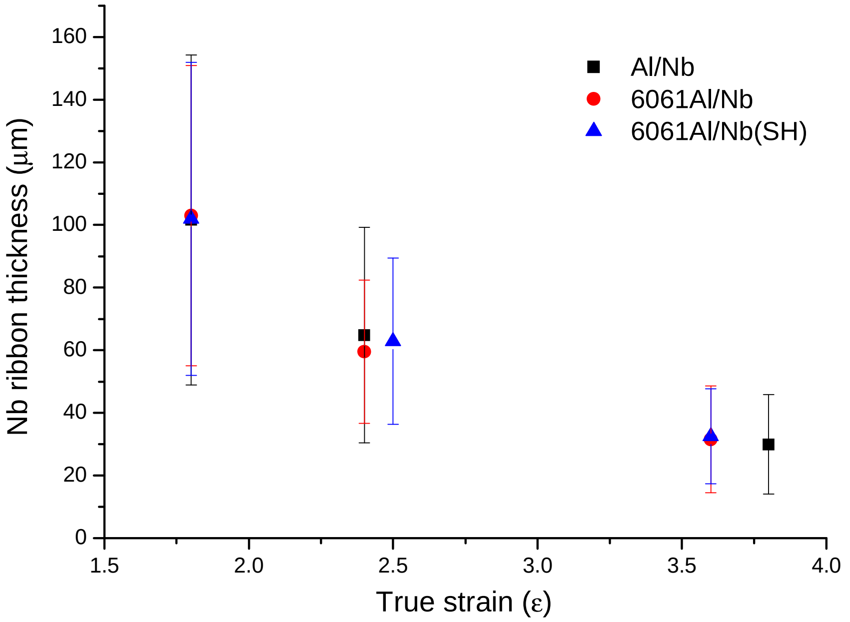

(b)

Figure 7.9: Comparisons of (a) measured interparticle spacings and (b) measured Nb ribbon thickness in the longitudinal planes (ND-ED/RD) as a function of true strain for Al/Nb, 6061Al/Nb and 6061Al/Nb(SH) samples.

7.1.3 Macroscopic texture development during extrusion and cold rolling

ODFs of as-extruded and cold rolled pure Al strip sample in constant φ_2 sections are shown in Figure 7.10. Similar to the texture of the as-extruded 6061Al alloy shown in section 5.1.3, the as-extruded pure Al strip also has a near β fibre texture mainly containing B'-{0 1 1}<10 7 7> (φ_1=45º, Φ=45º, φ_2=0º), S'-{5 2 10}<7 10 6> (φ_1=65º, Φ=30º, φ_2=65º) and C'-{2 2 5}<5 5 4> (φ_1=90º, Φ=30º, φ_2=45º) components with highest intensities at B'. During cold rolling, the main texture stays nearly the same.

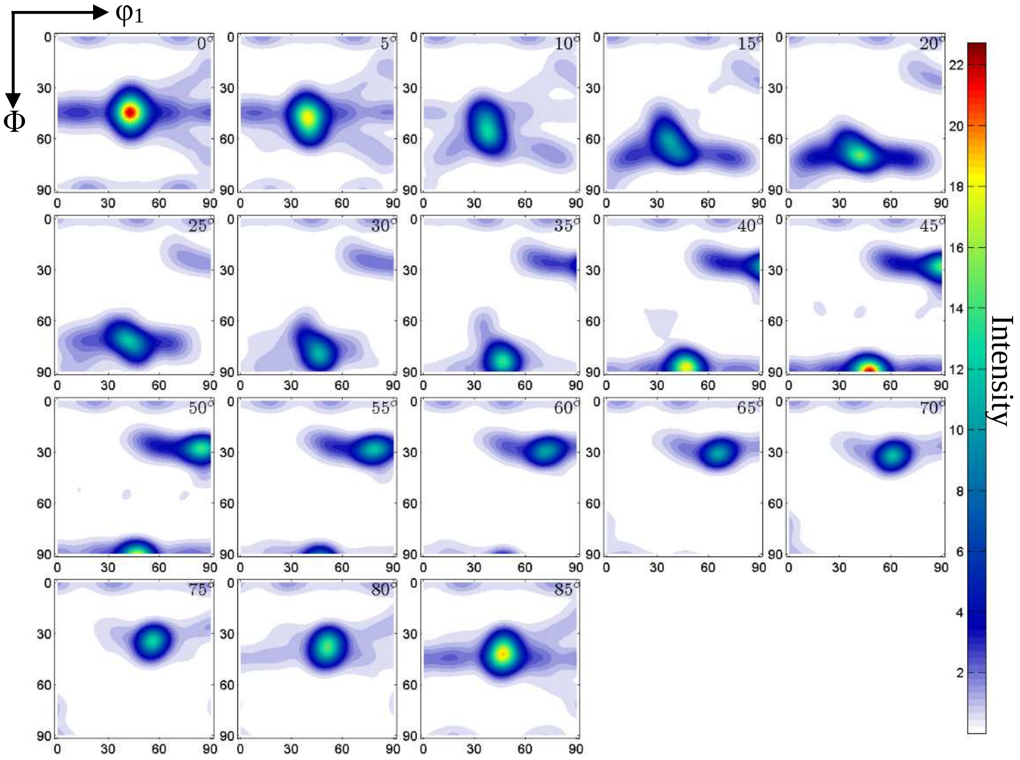

(a)

Figure 7.10: ODFs of (a) as-extruded Al strip; (b) cold rolled $Al_{2.3}$; (c) cold rolled $Al_{2.7}$ and (d) cold rolled $Al_{3.4}$.

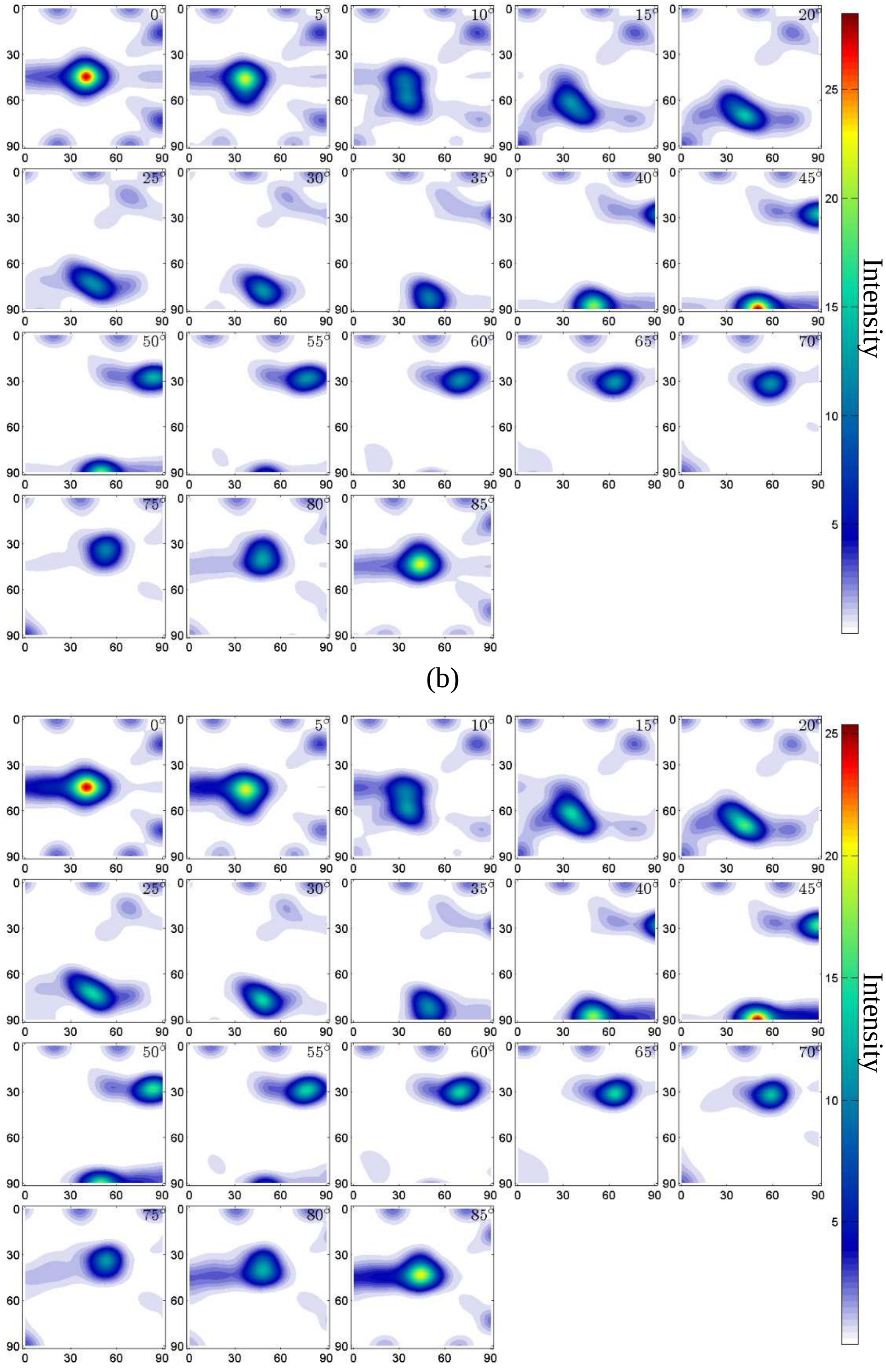

(b)

(c)

Figure 7.10: ODFs of (a) as-extruded Al strip; (b) cold rolled $Al_{2.3}$; (c) cold rolled $Al_{2.7}$ and (d) cold rolled $Al_{3.4}$.

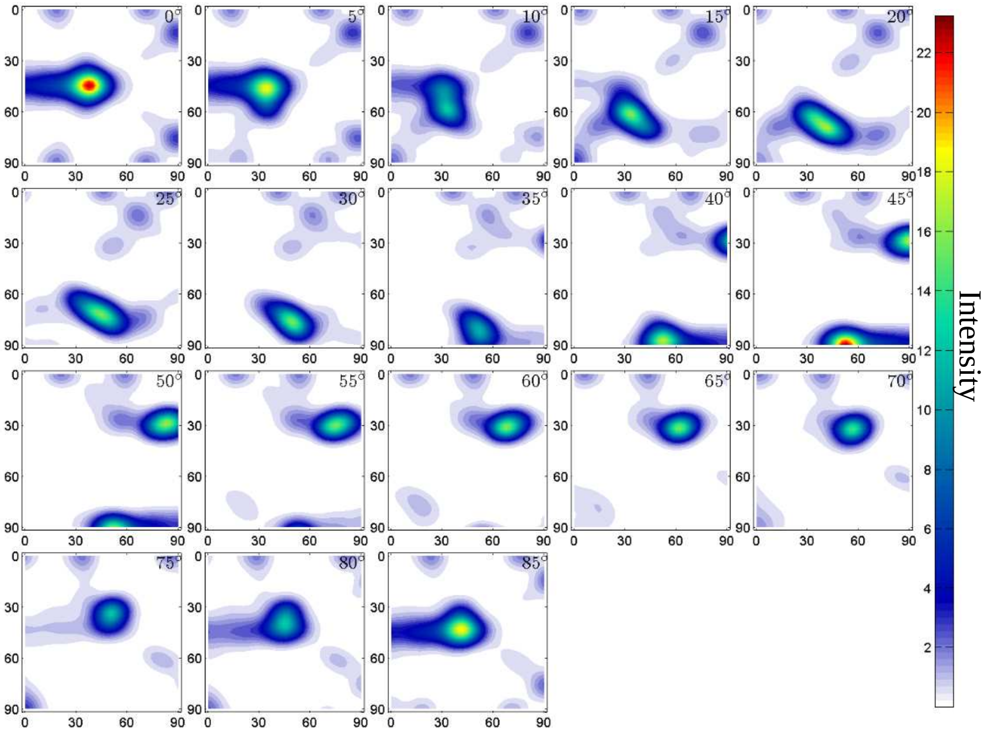

(d)

Figure 7.10: ODFs of (a) as-extruded Al strip; (b) cold rolled $Al_{2.3}$; (c) cold rolled $Al_{2.7}$ and (d) cold rolled $Al_{3.4}$.

Figure 7.11 shows the texture development for Al/Nb sample. After extrusion, the strip sample has a strong cube-{0 0 1}<1 0 0> (φ_1=0°, Φ=0°, φ_2=0°) component, a weak α fibre and a weak γ fibre. In the case of lower cold rolling strains, for example, Figure 7.11(b), a stronger α fibre with higher intensities near Brass component and Goss-{1 1 0}<0 0 1> (φ_1=0°, Φ=45°, φ_2=0°) component appear as well as an increased intensity near Copper component. As the rolling strains increase, the initial cube component weakens and a typical fcc cold rolling β fibre texture is developed within the Al matrix with highest texture intensities near Copper.

Similar texture evolution behaviour has been found for 6061Al/Nb and 6061Al/Nb(SH) samples, as seen in Figures 7.12 and 7.13, respectively, with a minor difference that the as-extruded texture contains a rotated-cube-{0 0 1}<1 1 0> (φ_1=45°, Φ=0°, φ_2=0°) component instead of a cube component as observed for Al/Nb sample. In addition, the cold rolled $6061Al/Nb_{3.6}$ and

6061Al/Nb(SH)$_{3.6}$ samples develop a similar β fibre texture with highest texture intensities near Brass component instead of Copper.

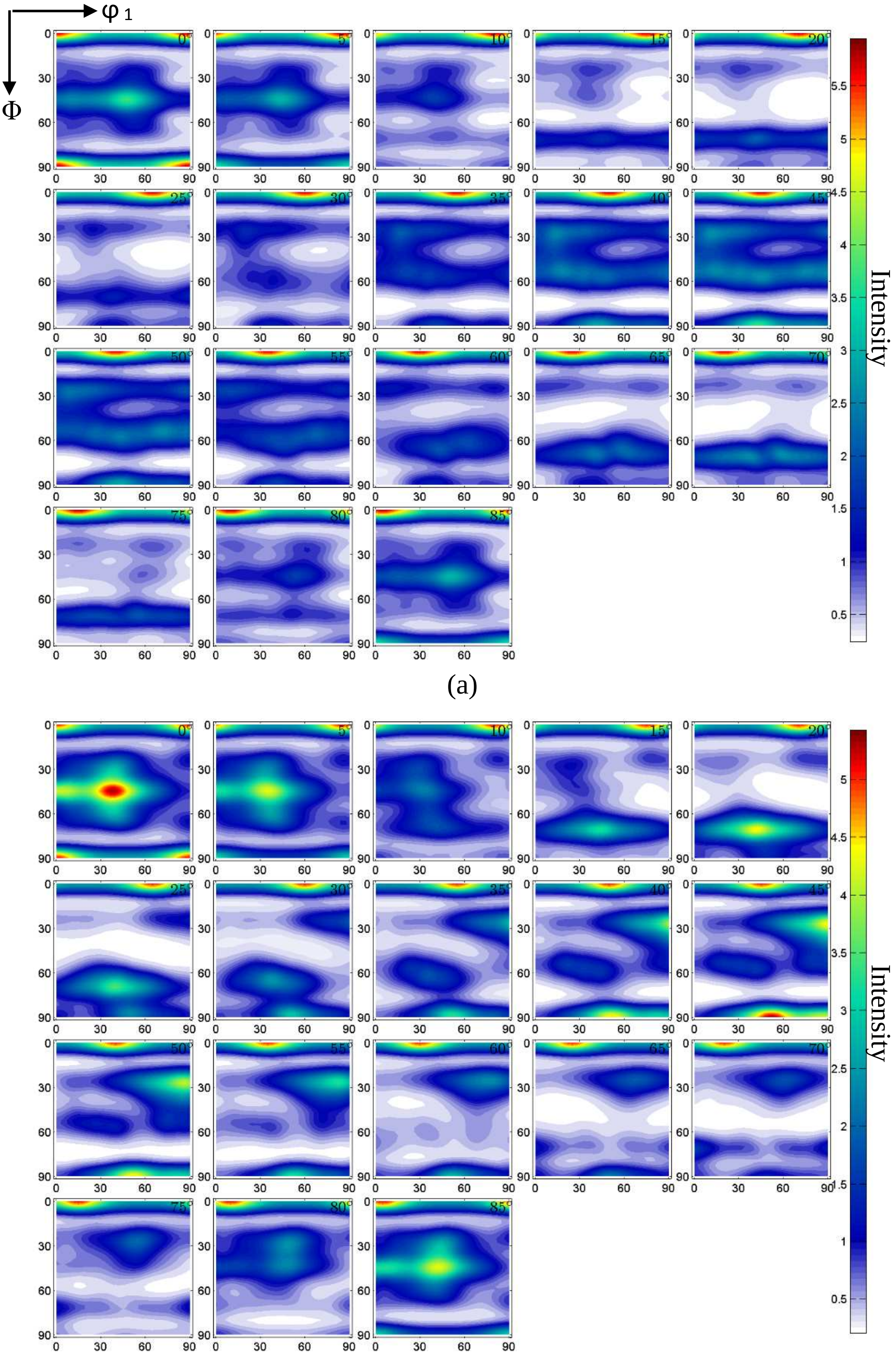

(a)

(b)

Figure 7.11: ODFs of (a) as-extruded Al/Nb strip; (b) cold rolled Al/Nb$_{2.4}$; (c) cold rolled Al/Nb$_{3.3}$ and (d) cold rolled Al/Nb$_{3.8}$.

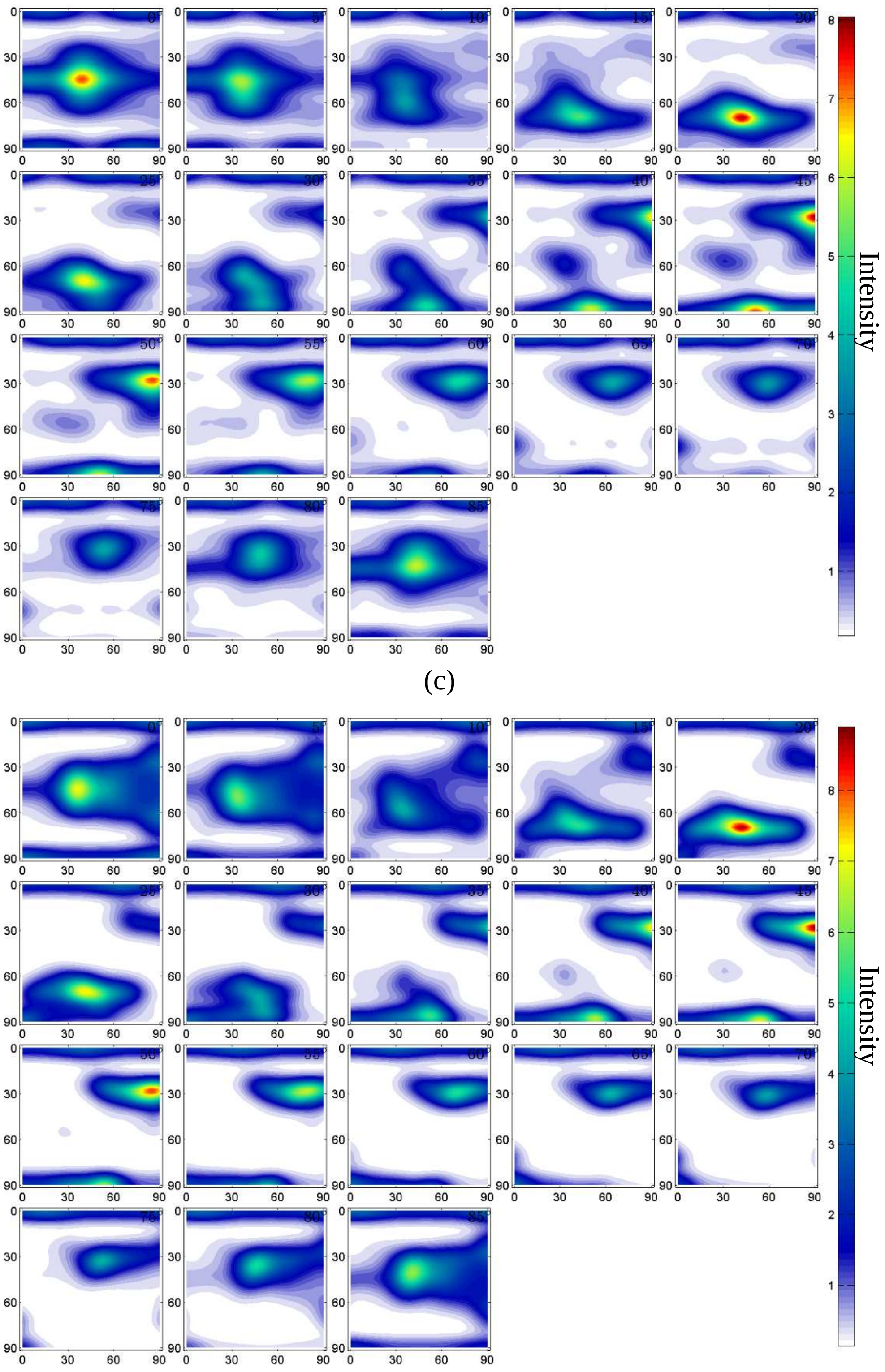

(c)

(d)

Figure 7.11: ODFs of (a) as-extruded Al/Nb strip; (b) cold rolled Al/Nb$_{2.4}$; (c) cold rolled Al/Nb$_{3.3}$ and (d) cold rolled Al/Nb$_{3.8}$.

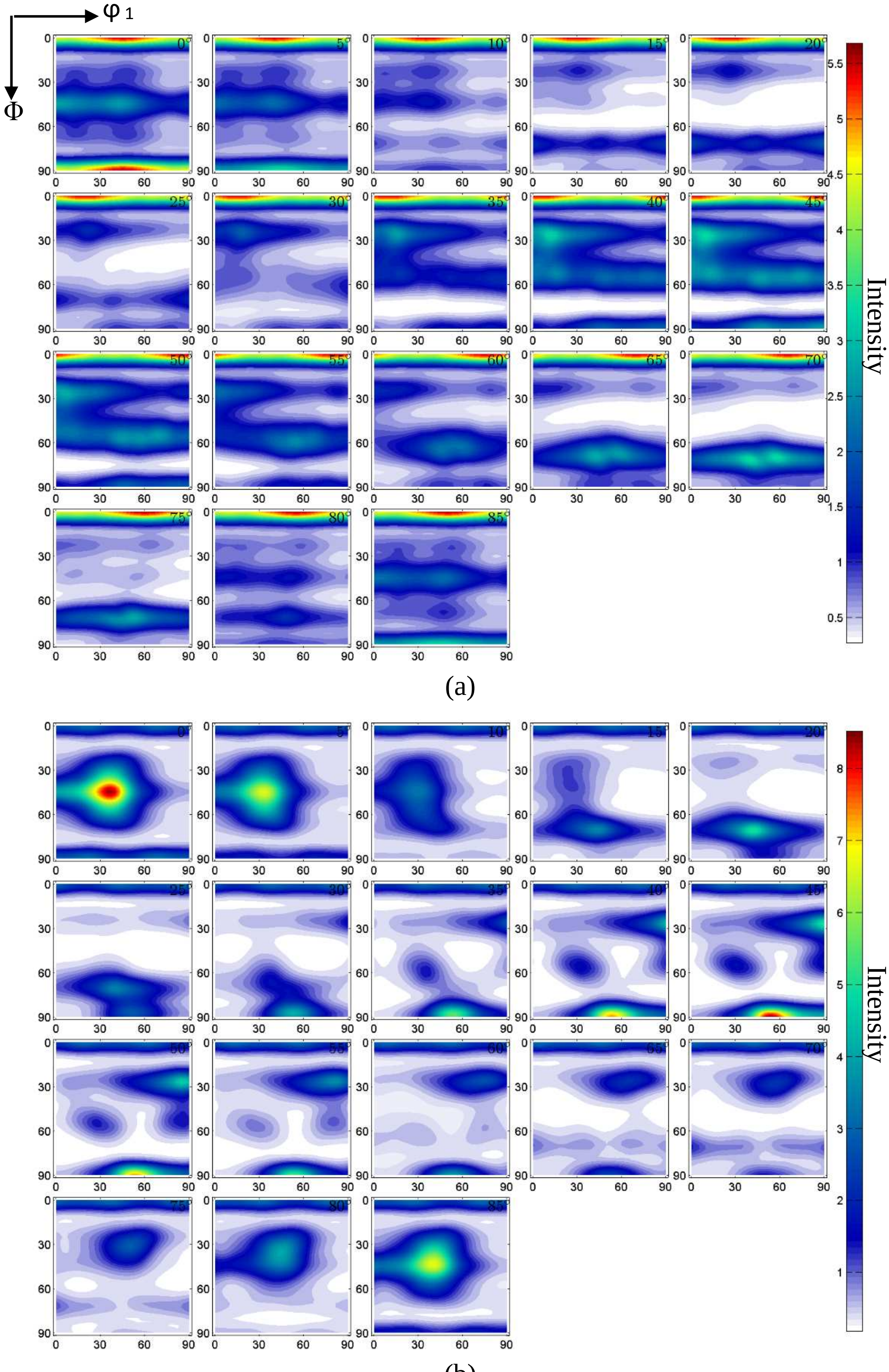

(a)

(b)

Figure 7.12: ODFs of (a) as-extruded 6061Al/Nb strip; (b) cold rolled 6061Al/$Nb_{2.4}$; (c) cold rolled 6061Al/$Nb_{2.8}$ and (d) cold rolled 6061Al/$Nb_{3.6}$.

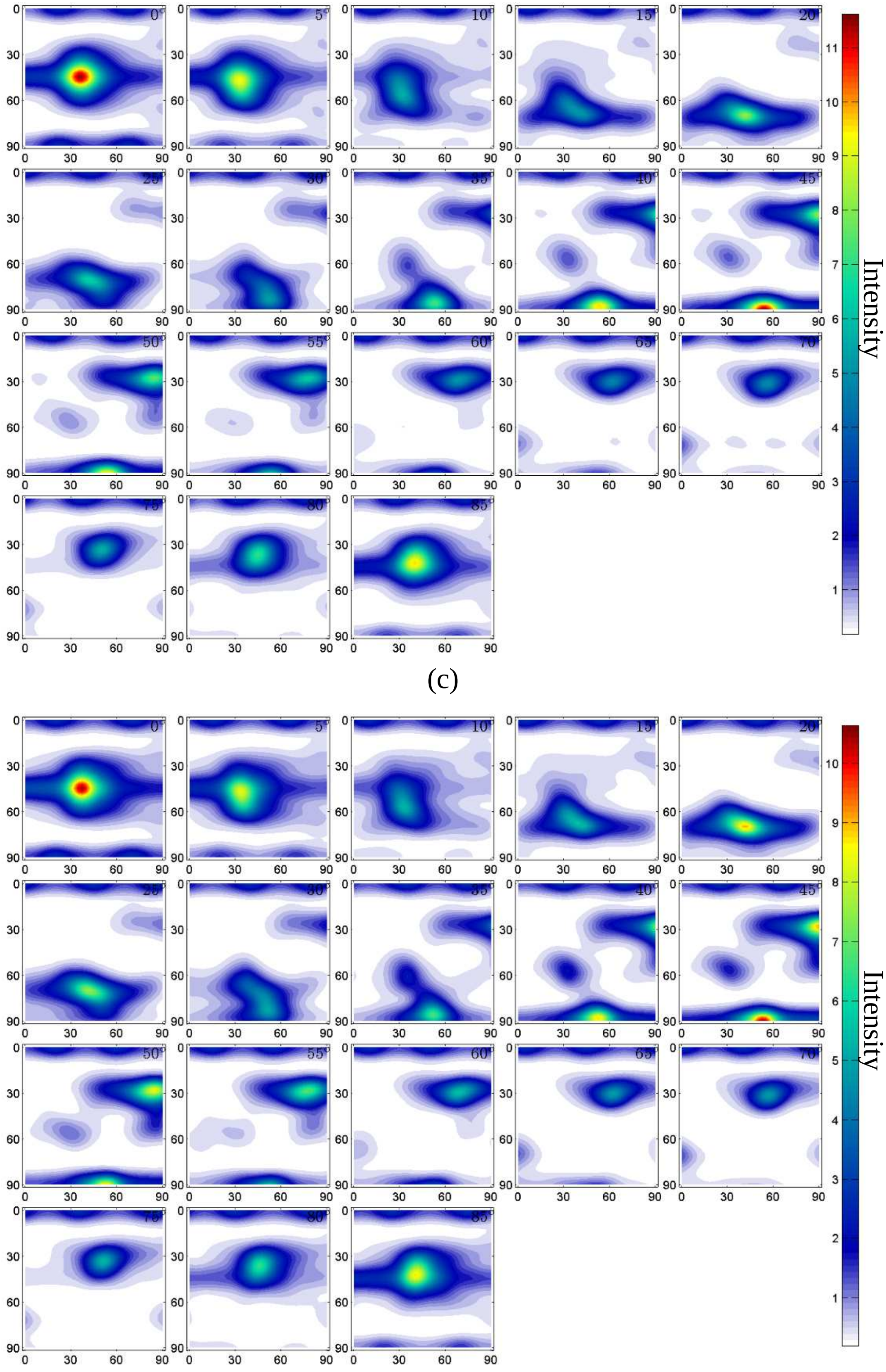

(c)

(d)

Figure 7.12: ODFs of (a) as-extruded 6061Al/Nb strip; (b) cold rolled 6061Al/Nb$_{2.4}$; (c) cold rolled 6061Al/Nb$_{2.8}$ and (d) cold rolled 6061Al/Nb$_{3.6}$.

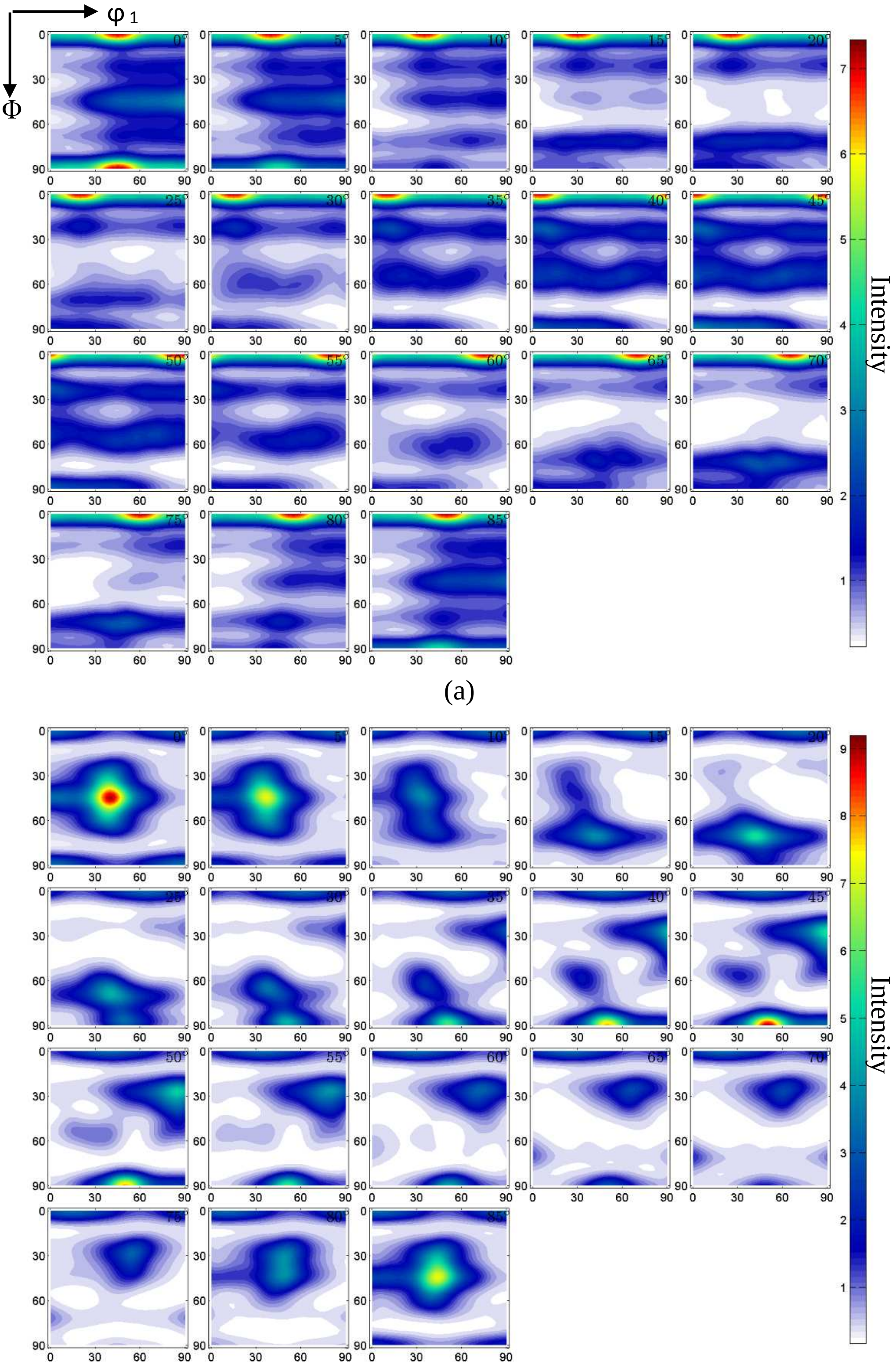

(a)

(b)

Figure 7.13: ODFs of (a) as-extruded 6061Al/Nb(SH) strip; (b) cold rolled 6061Al/Nb$(SH)_{2.0}$; (c) cold rolled 6061Al/Nb$(SH)_{2.9}$ and (d) cold rolled 6061Al/Nb$(SH)_{3.6}$.

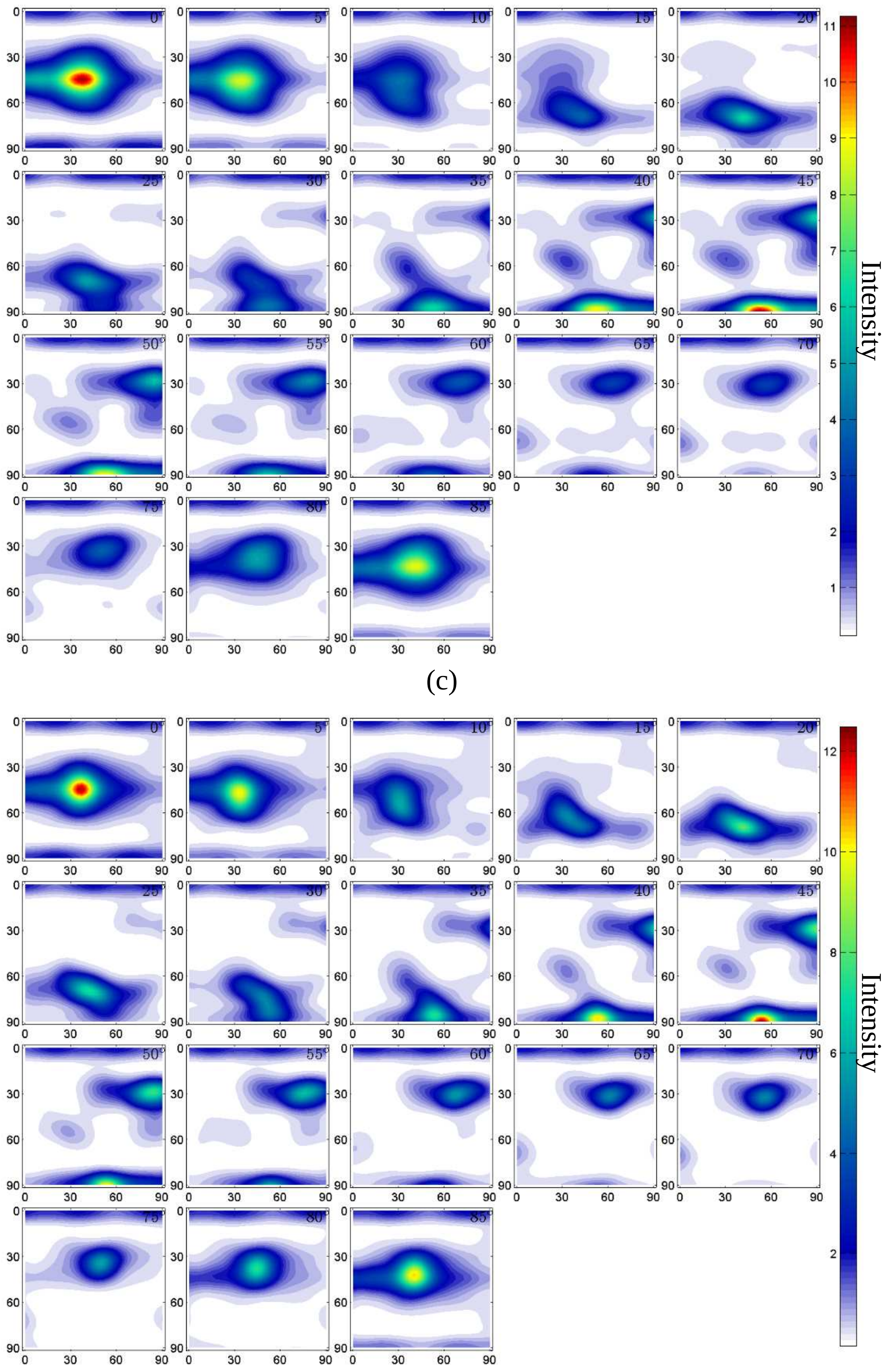

(c)

(d)

Figure 7.13: ODFs of (a) as-extruded 6061Al/Nb(SH) strip; (b) cold rolled 6061Al/Nb(SH)$_{2.0}$; (c) cold rolled 6061Al/Nb(SH)$_{2.9}$ and (d) cold rolled 6061Al/Nb(SH)$_{3.6}$.

To further clarify the texture evolution during cold rolling, the α and β fibre intensity plots were depicted in Figures 7.14 and 7.15, respectively. The α fibre intensity plot in Figure 7.14(a) shows a sharp peak at B'-{0 1 1}<10 7 7> (φ_1=45º, Φ=45º, φ_2=0º) for as-extruded Al strip. With further rolling strains, the peak intensity increases to a rolling strain of 2.3 and then decreases and the peak position gradually moves to stable Brass-{1 1 0}<1 1 2>(φ_1=35º, Φ=45º, φ_2=90º). The β fibre intensity plot in Figure 7.15(a) has a prominent peak near Brass in the as-extruded condition. After the first rolling pass (ε=2.3), the intensities near Brass and S components increase strongly. With further rolling passes, the intensities near Copper and S increase while the intensity near Brass drops gradually. It seems that more Copper and S components are formed during high strain cold rolling at the expense of Brass component for pure Al strip.

For as-extruded Al/Nb sample (Figures 7.14(b) and 7.15(b)), the intensities along α and β fibres are distributed more or less homogeneously along the whole fibre length with much lower intensity values than that of the pure Al sample. With increasing rolling strains, Figure 7.14(b) shows Goss component and B' component first increase and then decrease with B' gradually transforms into stable Brass-{1 1 0}<1 1 2>. Figure 7.15(b) shows an enhanced overall intensities along the β fibre with higher intensities at Brass, Copper and S orientations in the final cold rolled $Al/Nb_{3.8}$ sample. Similar trends to the Al/Nb composite are also observed for 6061Al/Nb and 6061Al/Nb(SH) samples but with higher intensities for the Brass component than the observed for the Al/Nb sample.

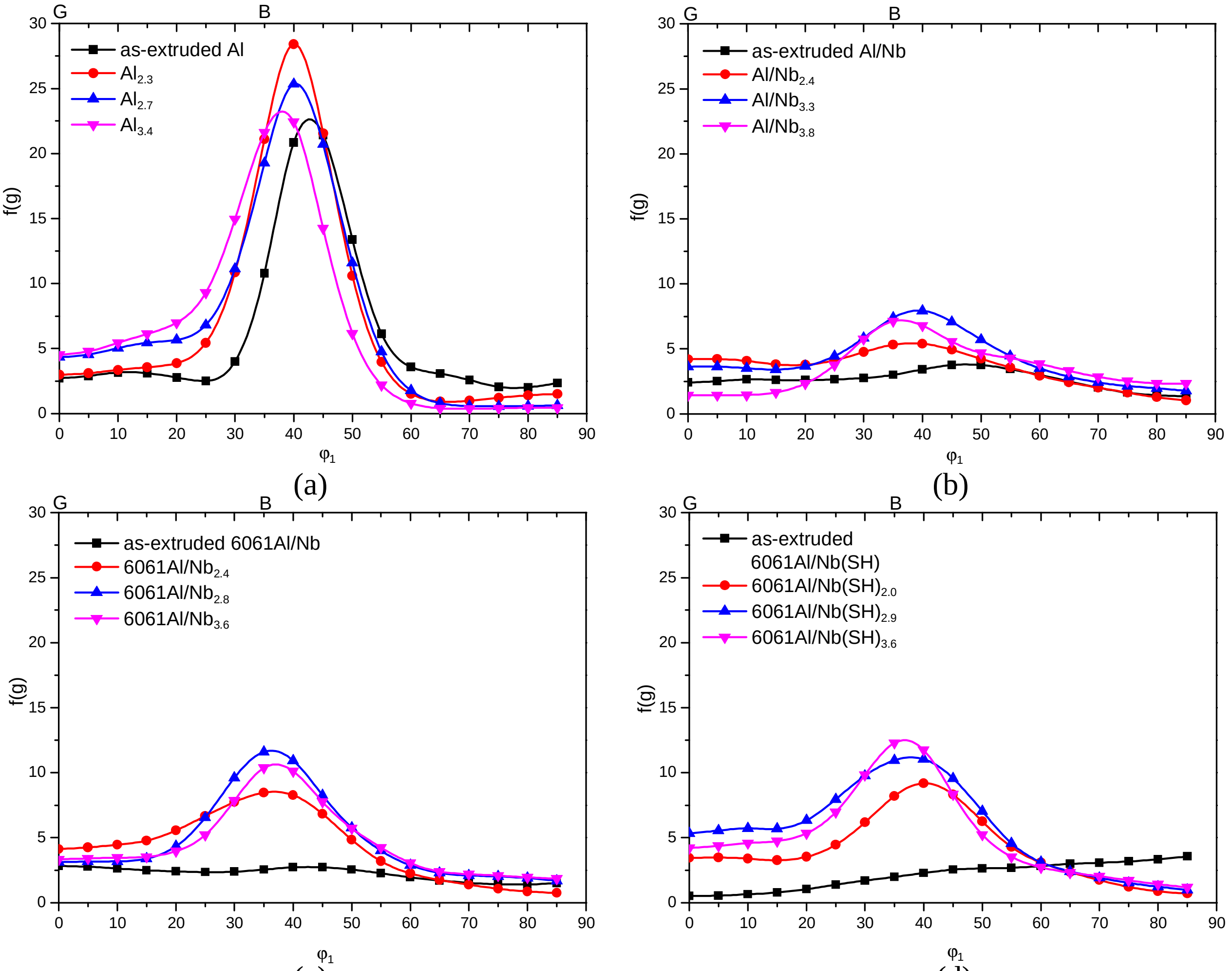

(a) (b) (c) (d)

Figure 7.14: α fibre intensity plots of (a) pure Al; (b) Al/Nb; (c) 6061Al/Nb and (d) 6061Al/Nb(SH).

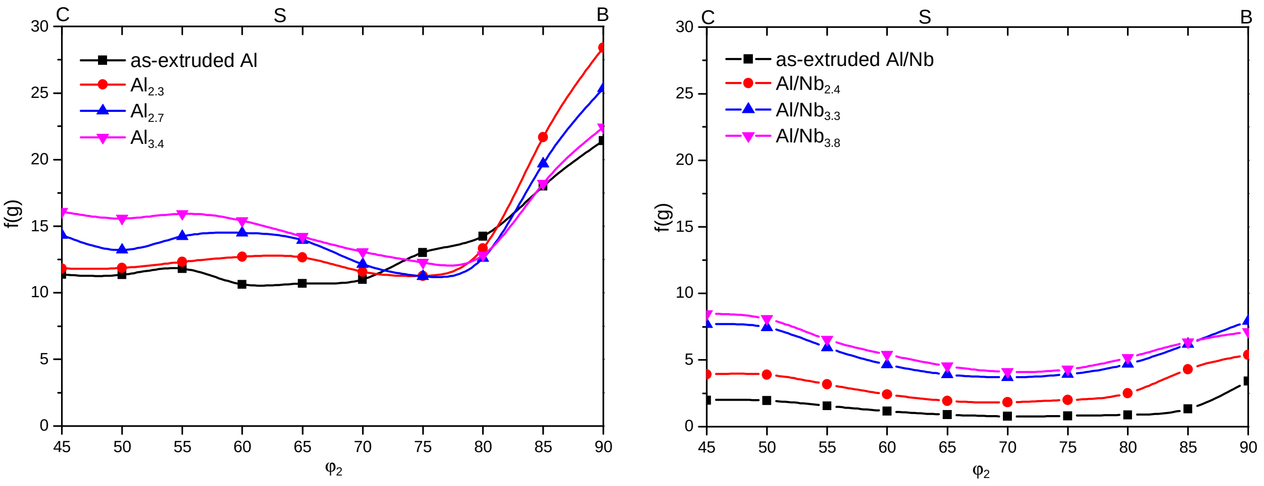

(a) (b)

Figure 7.15: β fibre intensity plots of (a) pure Al; (b) Al/Nb; (c) 6061Al/Nb and (d) 6061Al/Nb(SH).

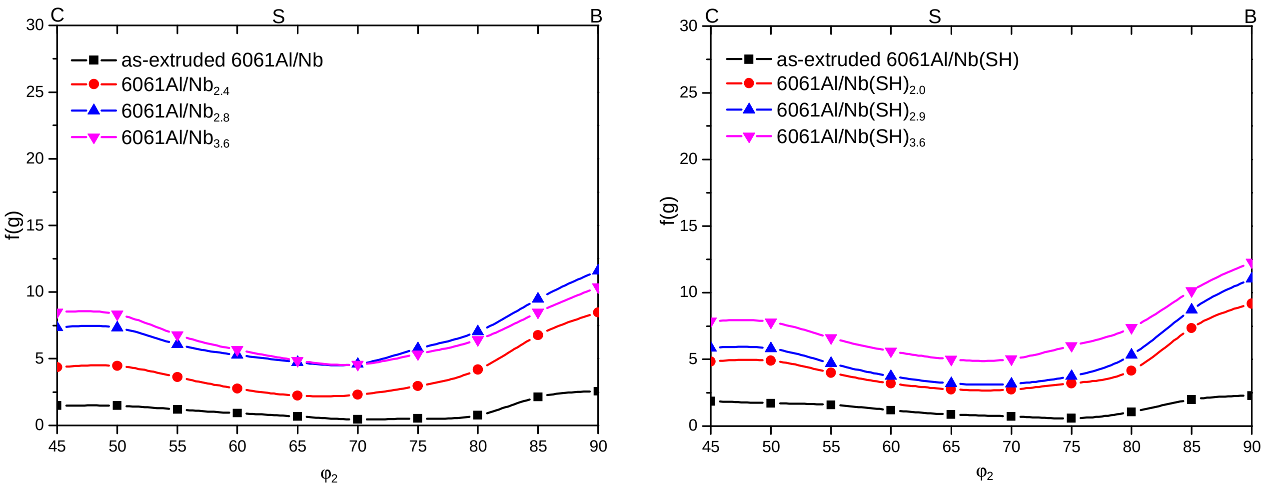

(c) (d)

Figure 7.15: β fibre intensity plots of (a) pure Al; (b) Al/Nb; (c) 6061Al/Nb and (d) 6061Al/Nb(SH).

The volume fractions of main texture components were calculated by Mtex [14, 15] within a range of 15° tolerance and the results are plotted as a function of the rolling strains in Figure 7.16. It can be seen that for all the samples (especially the composites), the volume fractions of Copper, S and Brass components increase significantly in the first few rolling passes and the increment rates become slower and nearly reach saturation points in the final cold rolled samples. The volume fraction of β fibre was estimated as the sum of Copper, S and Brass components. From Figure 7.16, it can be observed that the volume fractions of β fibre increase with increasing rolling strains and achieve a ~80% and ~55% of the overall rolling components for cold rolled pure Al and the composite samples, respectively.

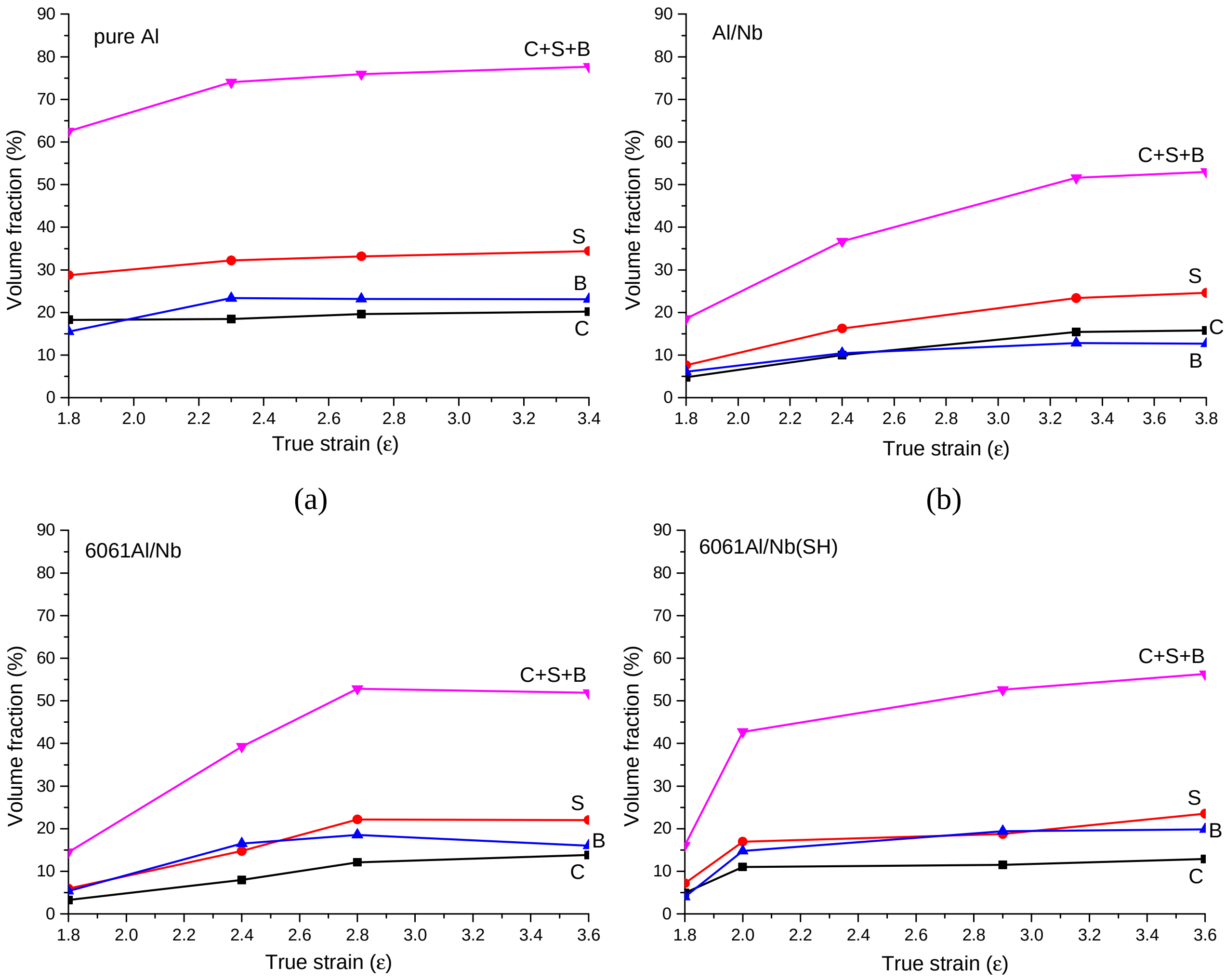

(a) (b)

(c) (d)

Figure 7.16: Volume fractions of main texture components of (a) pure Al; (b) Al/Nb; (c) 6061Al/Nb and (d) 6061Al/Nb(SH) samples as a function of rolling strains.

As summary, for pure Al strip, the extrusion texture can be represented by a near β fibre containing the components of B'-{0 1 1}<10 7 7>, S'-{5 2 10}<7 10 6> and C'-{2 2 5}<5 5 4>. When it is subjected to cold rolling, B' component will gradually transform into stable Brass component and more Copper and S components are formed at the expense of Brass. For the composites, the main extrusion texture is either cube component or rotated-cube component with weak α and γ fibres and other random texture. During low reduction cold rolling, α fibre with stronger Goss and Brass components first evolves as well as Copper component, with further rolling strains, Goss component weakens and a stronger β fibre with more intensities near Brass, Copper and S orientations will be developed. Compared to pure Al strip, the composites generally have much lower texture intensities.

7.1.4 Electron backscatter diffraction analysis of Al matrix

EBSD scans conducted on the rolling planes (TD-ED/RD) of as-extruded strips and cold rolled samples were carried out to study their microscopic texture. Figures 7.17 and 7.18 show the EBSD orientation maps of as-extruded and cold rolled pure Al samples with respect to the normal direction. Each point is painted with a color according to the crystal orientation. The black and white lines from the EBSD maps indicate the locations of high angle grain boundaries (≥15°) and low angle grain boundaries (2°-15°), respectively. The fractions of low angle grain boundaries (2°-15°) measured by EBSD analysis are summarized in Table 7.1.

As can be seen from Figure 7.17, similar with the results of the as-extruded 6061Al alloy strip (Figure 5.8(a)), hot extrusion of pure Al strip has led to the formation of elongated grains aligned along the extrusion direction with some grain fragmentation. The Al subgrain size is measured as a width of 1.4±0.2μm and a length of 2.1±0.3μm according to the mean linear intercept method (see section 3.3.3). The scattered IPF data shows a near β fibre texture with other random orientations, agreeing with the ODF results in Figure 7.10(a). Similar to Figure 5.8(a) for as-extruded 6061Al alloy, the misorientation distribution plot also shows a peak in the range of 0-10°, which corresponds to a large fraction of low angle grain boundaries (about 25%-30%) located within the elongated grains.

After cold rolling of a true strain of 3.4, severely fragmented and elongated grains with a subgrain size of 1.3±0.2μm in width and 1.7±0.3μm in length aligned along the rolling direction are shown in Figure 7.18. The misorientation distribution plot shows increased fractions of grain boundaries (about 37%-41%) misoriented less than 10º and largely decreased high angle grain boundaries compared with Figure 7.17, indicating the development of subgrain structure in the parallel bands of elongated grains during cold rolling, which is in agreement with the data summarized in Table 7.1 showing the fractions of low angle grain boundaries (2°-15°) have increased from 33.7% in the as-extruded state to 44.0% after a rolling strain of 3.4. In addition, the IPF in Figure 7.18 shows the formation of a stronger β fibre texture with less scatter.

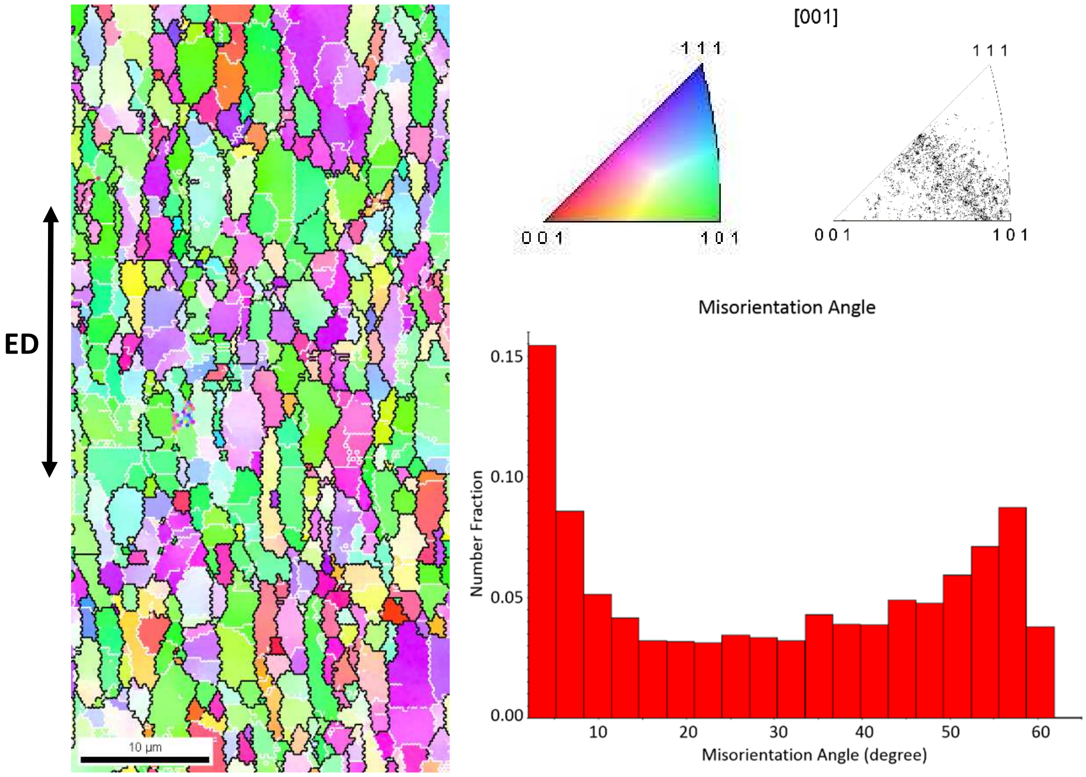

Figure 7.17: EBSD orientation map with IPF and misorientation distribution plot of as-extruded pure Al strip with respect to ND.

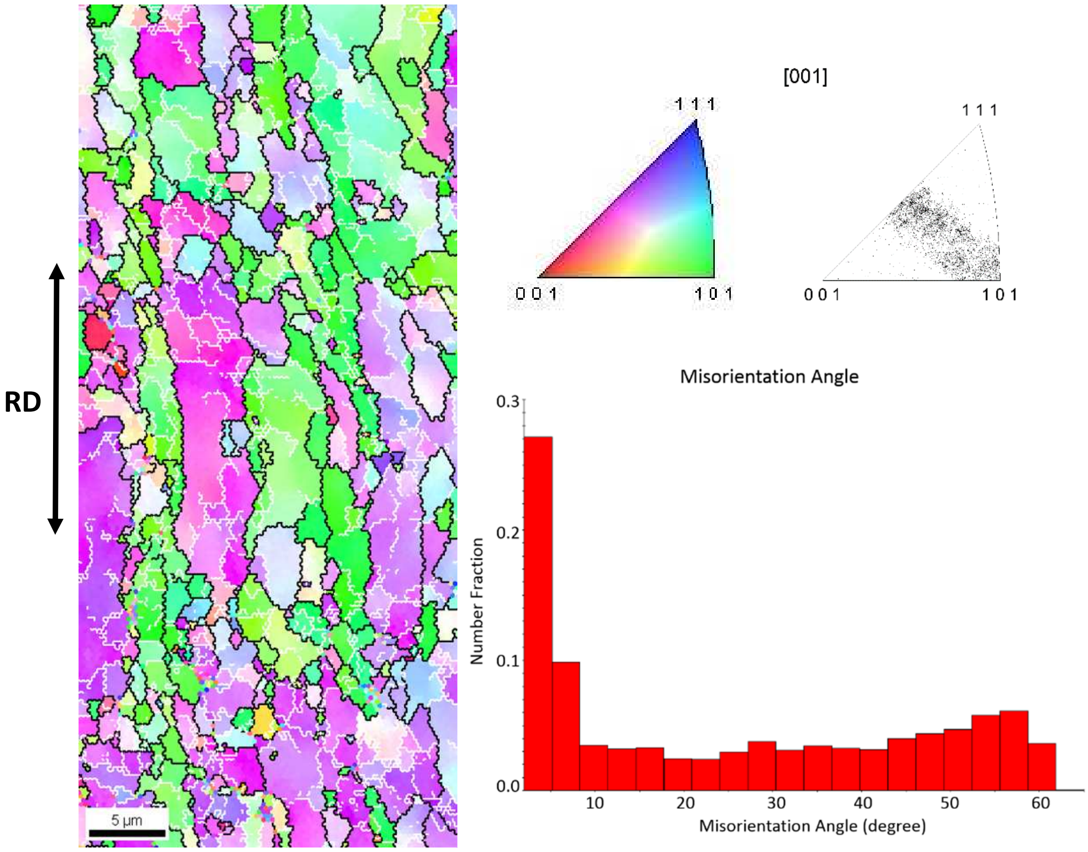

Figure 7.18: EBSD orientation map with IPF and misorientation distribution plot of cold rolled $Al_{3.4}$ sample with respect to ND.

Materials	As-extruded sample	Cold rolled sample
Pure Al	33.7%	44.0% ($Al_{3.4}$)
Al/Nb	22.2% (Figure 7.19(a))	49.1% ($Al/Nb_{3.8}$)

Table 7.1: Fractions of low angle grain boundaries (2°-15°) measured from EBSD analysis for the as-extruded and cold rolled pure Al, Al/Nb samples.

Figures 7.19(a) and (b) show the Al matrix EBSD orientation maps for as-extruded Al/Nb samples away from Nb particles and in the vicinity of Nb particles, respectively. Similar with the results for pure Al strip, Figure 7.19(a) shows that the as-extruded Al/Nb sample exhibits elongated Al matrix grains with an average subgrain size of 1.2±0.2μm in width and 1.9±0.3μm in length. While Figure 7.19(b) exhibits a near equiaxed Al grain morphology with an average subgrain size of 1.2±0.2μm. No preferred grain orientation has been developed in the as-extruded state according to the scattered IPF maps. The two EBSD maps show that the Al grain morphology strongly depends on the neighboring areas. The large Nb particles could produce particle deformation zones and restrict Al grain rotations, discouraging the formation of elongated Al grains in the vicinity of Nb particles after extrusion.

After cold rolling with a true strain of 3.8, Figure 7.20 shows Al grains with nearly equiaxed subgrains of less than 1μm with a strong β fibre. The fractions of low angle grain boundaries (2º-15º) have increased from 22.2% in the as-extruded state to 49.1% after cold rolling, indicating severe grain break-up or grain fragmentation. The comparison of the misorientation distribution plots between Figures 7.19 and 7.20 also suggests the development of subgrain structure with majority (about 37%-44%) of the Al grains misoriented within 10º after cold rolling. Similar EBSD results were also found for as-extruded and cold rolled 6061Al/Nb and 6061Al/Nb(SH) samples.

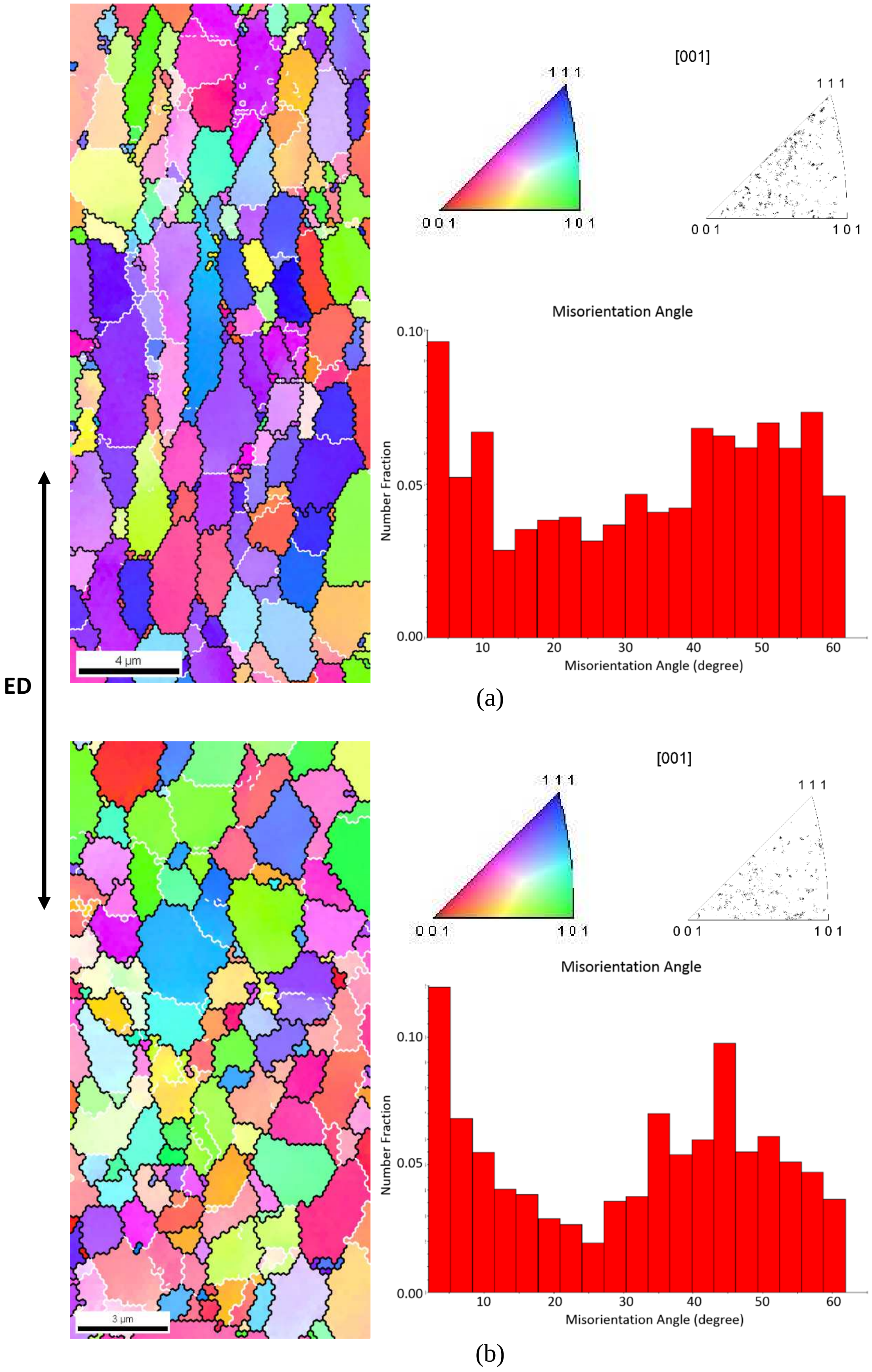

Figure 7.19: Al matrix EBSD orientation maps with IPF and misorientation distribution plots of as-extruded Al/Nb strip with respect to ND. (a) Al matrix away from Nb and (b) Al matrix near Nb.

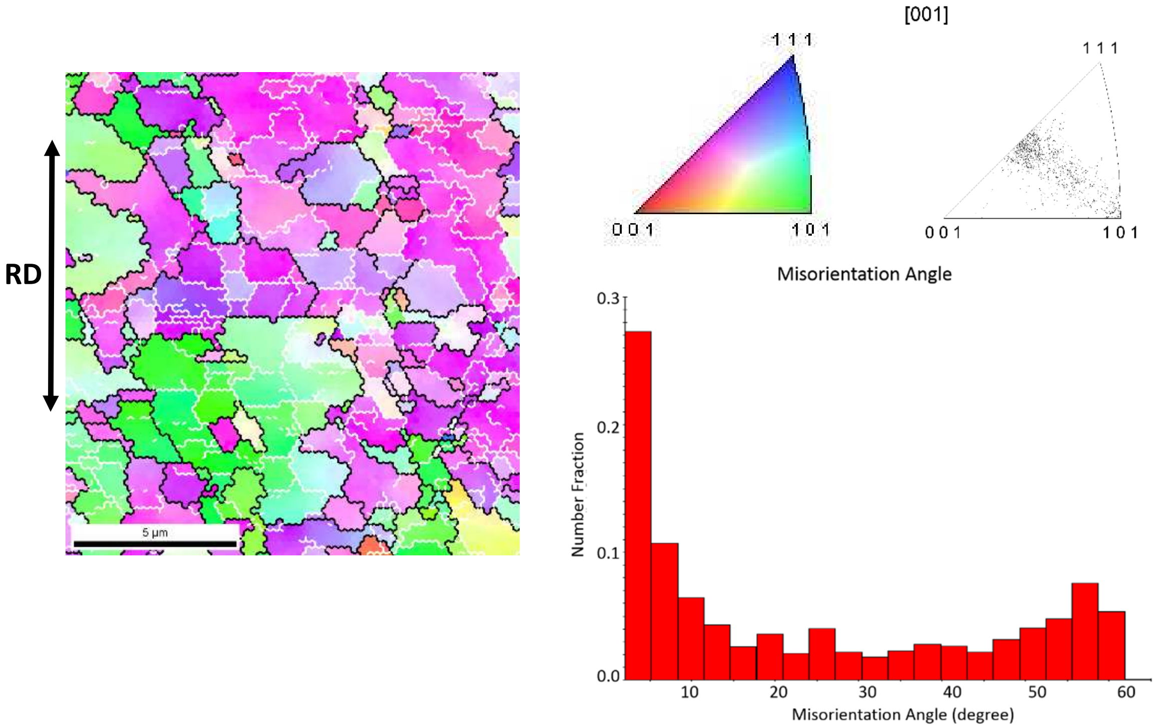

Figure 7.20: Al matrix EBSD orientation map with IPF and misorientation distribution plot of cold rolled Al/$Nb_{3.8}$ with respect to ND.

7.1.5 Electron backscatter diffraction analysis of Nb particles

EBSD scans over large areas were carried out by Dr. Singh Ubhi from Oxford Instruments on cold rolled Al/$Nb_{3.8}$ sample to collect the texture information of Nb particles. Figure 7.21 shows EBSD maps for cold rolled Al/$Nb_{3.8}$ sample and the generated Nb ODF plot in φ_2=45° section is shown in Figure 7.22 as well as the ideal texture components for rolled bcc metals in φ_2=45° section for comparison purposes [16].

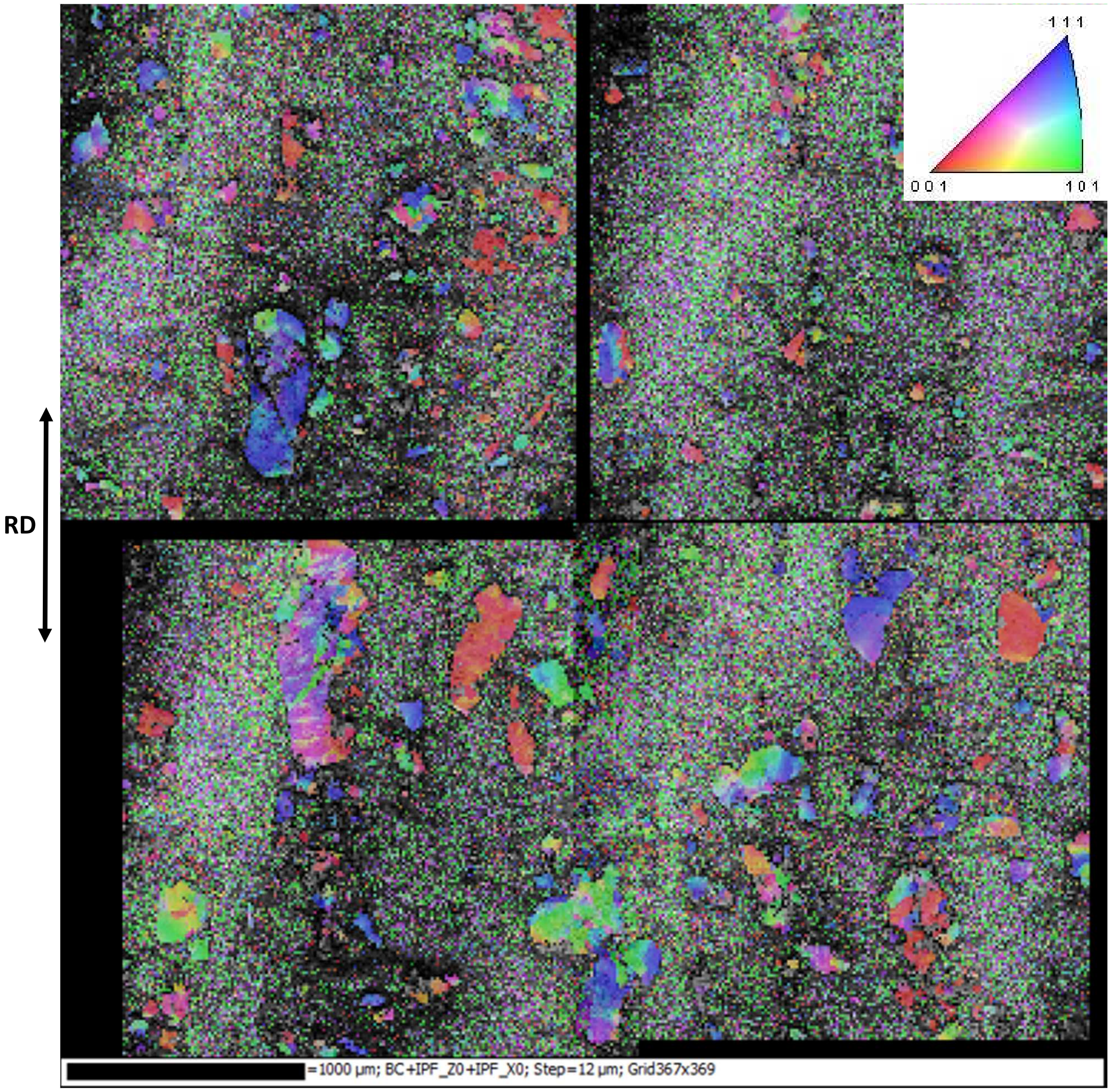

Figure 7.21: EBSD orientation maps for cold rolled Al/Nb$_{3.8}$ sample with respect to ND (courtesy of Dr. Singh Ubhi).

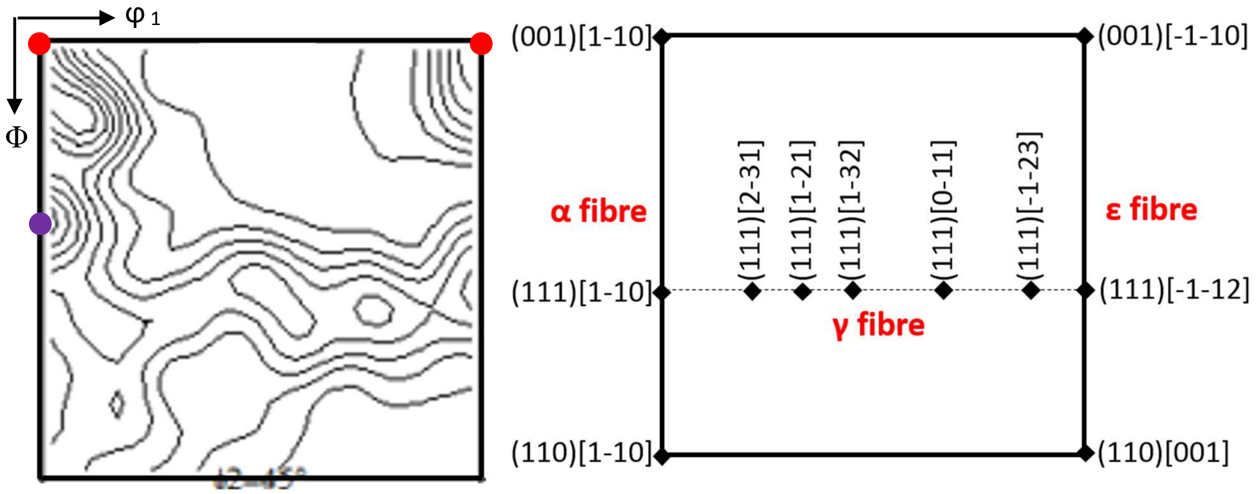

(a) (b)

Figure 7.22: (a) ODF plot in φ_2=45° section of Nb particles constructed from EBSD analysis for cold rolled Al/$Nb_{3.8}$ sample, red and purple circles represent {0 0 1}<1 1 0> and {1 1 2}<1 1 0> orientations, respectively (courtesy of Dr. Singh Ubhi) and (b) Ideal texture components for rolled bcc metals in φ_2=45° section [16].

The rolling textures of bcc metals have been reported by many research groups. In general, bcc metals exhibit the development of α and γ fibres during deformation and heat treatments [17, 18]. The α fibre represents <1 1 0> direction aligned along the rolling direction and the γ fibre represents a texture condition where {1 1 1} planes are preferentially aligned parallel to the rolling plane [19]. For the present material, after a cold rolling strain of 3.8, a strong α fibre and a relatively weak γ fibre are observed according to Figure 7.22(a) with the highest intensities at {0 0 1}<1 1 0> and {1 1 2}<1 1 0> orientations. These findings agree with the results reported by Raabe and Luecke [20] showing {0 0 1}<1 1 0> and {1 1 2}<1 1 0> orientations as dominant texture components for deformed pure Nb. Similar results were also reported by Jiang et al. [19], Borodkina et al. [21] and Abreu et al. [22] for deformed pure Nb and Nb alloys. It seems that the texture development of Nb reinforcement in cold rolled Al/$Nb_{3.8}$ sample is the same with that of the deformed pure Nb and Nb alloys.

7.2 Mechanical properties and work hardening of as-extruded and cold rolled Al/Nb and 6061Al/Nb composites

7.2.1 Microhardness analysis

Microhardness results on as-extruded and cold rolled samples after each rolling pass are plotted as a function of rolling true strains in Figure 7.23. Microhardness tests were performed on both the Al matrix and the Nb particles of as-extruded and cold rolled Al/Nb, 6061Al/Nb and 6061Al/Nb(SH) samples and Rule of Mixtures (ROM) [23] calculation was applied to get the microhardness data for the composites.

From Figure 7.23, it can be observed that the microhardness of all samples increase with increasing strains due to work hardening up to a maximum limit value. In addition, the samples show different work hardening capacities. For instance, the microhardness values of 6061Al/Nb(SH) sample have increased about ~50%, from 88±3μHV$_{200}$ in the as-extruded condition to 132±5μHV$_{200}$ after cold rolling at a true strain of 3.6; while for Al/Nb sample, the microhardness values have only increased about ~19%.

The empirical power-law relationship based on eq. 5.1 [24] was used to describe the microhardness-strain curves and the fitted lines are also included in Figure 7.23. It can be seen that the initial work hardening rate is high and then decreases with increasing strains for all materials, similar with the work hardening behaviour of 6061Al alloy, 6061Al/SiC composites and 6061Al/NQX composites shown in the previous chapters. It is also noticeable that the work hardening rates of 6061Al/Nb and 6061Al/Nb(SH) samples are higher than those of the Al/Nb and pure Al samples. This is probably due to the precipitates or solid solution elements in the 6061Al alloy matrix. For 6061Al/Nb sample, a higher work hardening rate is observed possibly due to effective dislocation accumulations because of the presence of fine precipitates in the matrix [25]. For 6061Al/Nb(SH) sample, in solid solution state, solute atoms would have a pinning effect on the gliding dislocations and could effectively reduce the dynamic recovery rate, leading to high work hardening capabilities [26].

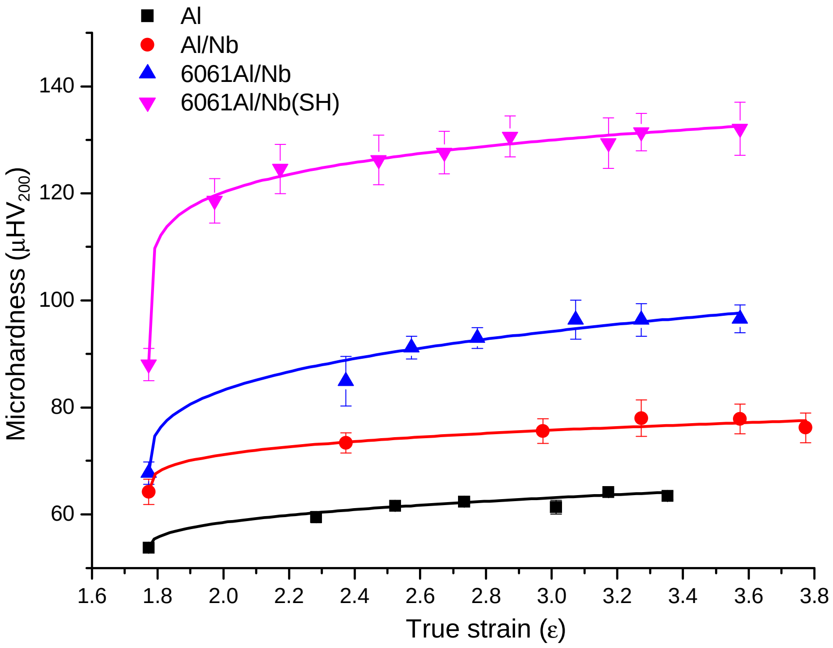

Figure 7.23: Microhardness of as-extruded and cold rolled pure Al, Al/Nb, 6061Al/Nb and 6061Al/Nb(SH) strips as a function of the rolling true strain and microhardness fitted lines based on eq. 5.1.

7.2.2 Three-point bending tests of cold rolled samples

Three-point bending tests were conducted on the final cold rolled samples. Flexural stress-strain curves for the pure Al, Al/Nb, 6061Al/Nb and 6061Al/Nb(SH) bending samples are shown in Figure 7.24 and the strength values are summarized in Table 7.2. All the tests were stopped due to equipment limitations. None of the samples have been fully broken during the tests.

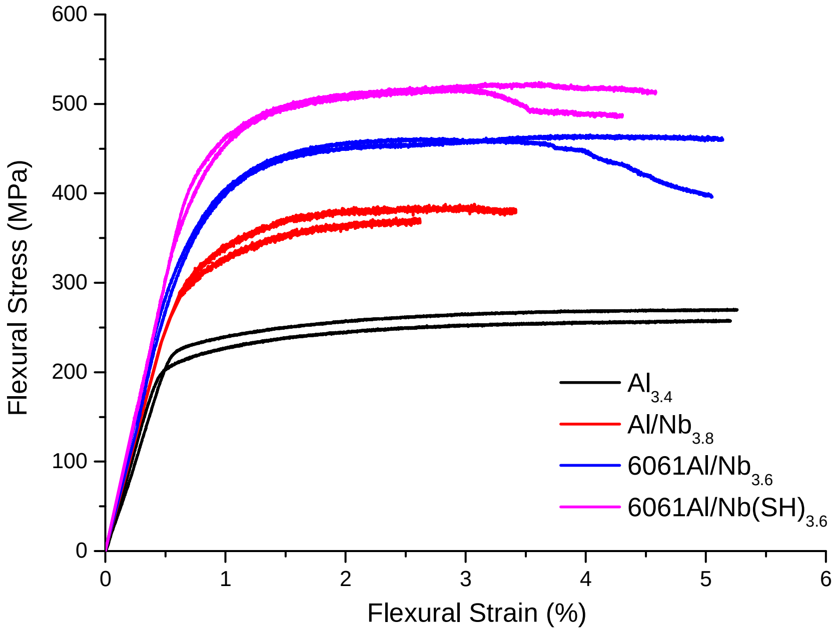

Figure 7.24: Three-point bending tests of cold rolled $Al_{3.4}$, $Al/Nb_{3.8}$, $6061Al/Nb_{3.6}$ and $6061Al/Nb(SH)_{3.6}$ samples.

Materials	Stress at yield (MPa)	Bending flow stress (MPa)
$Al_{3.4}$	224±10	272±18
$Al/Nb_{3.8}$	312±8	380±11
$6061Al/Nb_{3.6}$	380±1	464±3
$6061Al/Nb(SH)_{3.6}$	448±13	521±4

Table 7.2: Three-point bending properties of cold rolled $Al_{3.4}$, $Al/Nb_{3.8}$, $6061Al/Nb_{3.6}$ and $6061Al/Nb(SH)_{3.6}$ samples.

Compared with cold rolled $Al_{3.4}$ sample, the yield stress of cold rolled $Al/Nb_{3.8}$ sample has increased by ~39%, indicating effective strengthening from Nb ribbons. The strengthening mechanisms of DPMMCs have been subjected to extensive research due to their high strengths [27-32]. The achieved high strength can be ascribed to the individual phase undergoing large deformations and extensive work hardening at low strains [32] and dislocation interactions with the ribbon-matrix boundaries at higher strains [31]. In the present work, according to Figure 7.9, although the spacings of Nb particles have reduced with rolling passes, the spacings are not uniform and are highly dispersed and the Al-Nb boundaries are not close enough to effectively interact with dislocations. In addition, during cold rolling, the Nb particles have gradually developed into flattened ribbons with different lengths due to the broad Nb size distribution used and aligned parallel to the sheet surface, which prevents them from being effective barriers to dislocations compared to wire drawn composites [32], hence the increased strength of cold rolled Al/Nb$_{3.8}$ sample compared with cold rolled Al$_{3.4}$ is probably just related to the individual Nb phase undergoing rolling deformations. Compared with cold rolled Al$_{3.4}$ and Al/Nb$_{3.8}$ samples, the 6061Al/Nb$_{3.6}$ and 6061Al/Nb(SH)$_{3.6}$ samples show higher bending strength due to the higher strength of their matrix.

To study the failure behaviour, investigations of the longitudinal planes (ND-RD) of the plastically bent samples were carried out under OM and the images are shown in Figure 7.25. It can be observed that although none of the samples have fully broken during the tests, the fractures have initiated as shear cracks on the tension sides of all the samples. A closer look of the longitudinal planes of the test samples also shows the presence of intense shear bands across the matrix and Nb ribbons. The pairs of intersecting shear bands (inclined by 40°-50° with respect to the rolling plane) have passed through the Nb ribbons and generated cracks at the intersection points. The cracks would grow larger along the shear bands or at the matrix-Nb boundaries with further deformations and lead to the final fracture of the samples.

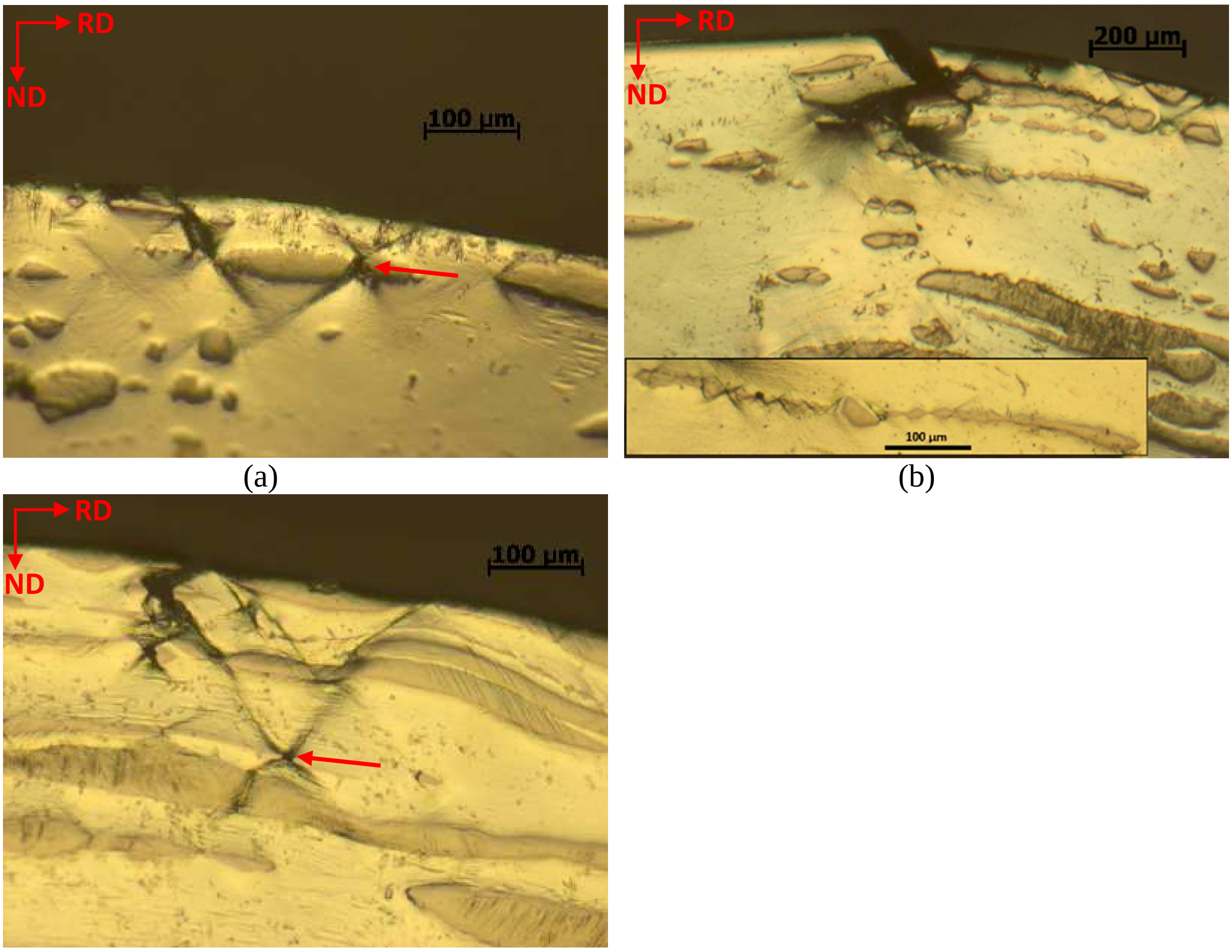

(a) (b)

(c)

Figure 7.25: Optical images of the longitudinal plane (ND-RD) of the plastically bent (a) Al/Nb$_{3.8}$, (b) 6061Al/Nb$_{3.6}$ and (c) 6061Al/Nb(SH)$_{3.6}$ samples. Arrows and the inset image show intersecting shear bands cutting through Nb ribbons.

7.2.3 Tensile tests of as-extruded and cold rolled samples

Room temperature tensile tests were performed with final cold rolled samples at a constant strain rate at $10^{-4}s^{-1}$. For comparison purposes, 6061Al alloy reinforced with 12.9vol.% of Nb particles were mixed and compacted in the same way and then extruded into a bar of a diameter of 7.5mm at the same extrusion conditions. Tensile samples were machined from the as-extruded 6061Al/Nb bar according to ASTM E8M-08 standard.

Engineering stress-strain curves for the tensile tests are shown in Figure 7.26. The tensile strength values are summarized in Table 7.3, for comparison purposes, the tensile strength of as-extruded

6061Al alloy bar in section 4.2.3 and the UTS data of 90% cold rolled pure Al and Al/20vol.%Nb sheet reported by Chen and Kanetake [13] are also included. The Al/20vol.%Nb composite sheet was prepared by powder metallurgy routes including compaction, flat extrusion and cold rolling.

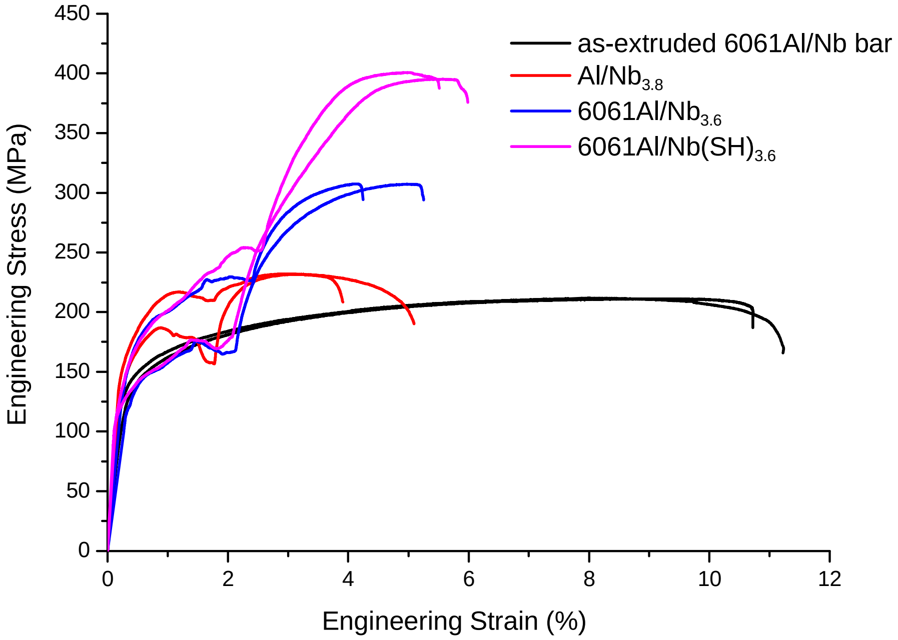

Figure 7.26: Room temperature tensile test results for as-extruded 6061Al/Nb bars, cold rolled $Al/Nb_{3.8}$, $6061Al/Nb_{3.6}$ and $6061Al/Nb(SH)_{3.6}$ samples.

Materials	Yield stress (MPa)	UTS (MPa)	ε_f (%)
as-extruded 6061Al/Nb bar	141±1	212±1	11±1
$Al/Nb_{3.8}$	-	232±1	5±1
$6061Al/Nb_{3.6}$	-	307±1	5±1
$6061Al/Nb(SH)_{3.6}$	-	398±4	6±1
as-extruded 6061Al bar (section 4.2.3)	131±5	205±5	19±1
90% cold rolled pure Al [13]	-	180	-
90% cold rolled Al/20vol.%Nb [13]	-	210	-

Table 7.3: Mechanical properties of as-extruded 6061Al/Nb, cold rolled $Al/Nb_{3.8}$, $6061Al/Nb_{3.6}$ and $6061Al/Nb(SH)_{3.6}$ samples extracted from Figure 7.26 and as-extruded 6061Al alloy in section 4.2.3 together with UTS data of 90% cold rolled pure Al and Al/20vol.%Nb sheet reported by Chen and Kanetake [13].

According to Table 7.3, compared to the as-extruded 6061Al alloy bar, the as-extruded 6061Al/Nb bar shows slight improvement in tensile strength (~7MPa superior) with reduced ductility. Based on literature [6, 33, 34], the UTS value of commercial Nb is in the range of 275-350MPa, hence the additions of 12.9vol.% of Nb particles should result in an increase of UTS of 9-19MPa for 6061Al/Nb sample according to Rule of Mixtures (ROM) [23]. The current improvement in tensile strength (~7MPa) is reasonable considering a few microstructural defects, such as interfacial debonding or particle broken, which will be discussed later in the fracture behaviour of as-extruded 6061Al/Nb sample.

After cold rolling, the UTS of the sheet composites increases substantially with rolling strains coupled with drastically reduced ductility. For example, the UTS of cold rolled 6061Al/Nb$_{3.6}$ sample reaches 307±1MPa, which has increased by ~45% when compared to as-extruded 6061Al/Nb bar, indicating effective strengthening from cold work. In addition, it can also been seen from Table 7.3 that the cold rolled Al/Nb$_{3.8}$ sample has a UTS of 232±1MPa, which is ~52MPa higher than that of the 90% cold rolled pure Al reported [13], indicating effective strengthening from Nb ribbons as well. The tensile results of the cold rolled samples show substantial improvement which is similar to the behaviour of other DPMMCs produced by drawing or swaging methods [3, 5, 35]. However, the improvement in tensile strength is relatively limited due to the nature of the cold rolling process that it becomes more and more difficult to conduct when the rolling reductions reach 90% (ε=2.3) or more while DPMMCs produced by drawing or swaging can easily reach true strain values larger than 10 [5].

The anomalous increase in tensile strength of DPMMCs is widely accepted to be closely related with the microstructural changes during deformation [4, 5, 35]. In the early stages of cold working (low to medium strains), the tensile strength increases due to work hardening effect and this effect saturates when dislocation accumulation and dynamic recovery rates reach a balance [36]. At larger deformations, strength increases significantly again when the average inter-fibre spacing becomes small enough (<0.1μm) that they can act as effective barriers for the matrix dislocations [3, 5, 13]. For the present cold rolled composites, the interparticle spacing is in the range of 100-150μm according to Figure 7.9(a), which is a lot larger than the dislocation mean free path in the Al or 6061Al matrix. Hence, it can be said that almost all of the tensile strength of cold rolled composites just comes from work hardening effect and probably a very small portion of the strength comes from localized closely spaced Nb ribbons being close enough to directly influence the dislocation motions.

Despite the increased UTS, all the tensile curves of cold rolled samples have decreased stiffness and a load/stress drop which is also observed in the tensile curves of cold rolled 6061Al/NQX$_{3.6}$ samples in Chapter 6. The mechanism behind the load/stress drop is still unclear. It is possible that during tensile tests, cracks have been produced on the Al and Nb phase boundaries and continue to expand along the phase boundaries till to the tip of Nb ribbons. If enough Nb ribbons split from the matrix at the same time, a load drop before final fracture can be observed especially considering the relatively large size of Nb particles. With further deformation, the matrix and the remaining bonded Nb ribbons continue to deform until final fracture. Further work needs to be done to understand the load/stress drop phenomenon.

The fracture surfaces of the as-extruded 6061Al/Nb bar samples are shown in Figure 7.27. Figures 7.27(a) and (b) show the overview of a ~45° fracture surface and dimples within the 6061Al matrix indicating ductile fracture, respectively. In order to have a comprehensive understanding of failure mode, both halves of the fracture surfaces have been examined under SEM and the images are shown in Figures 7.27(c)-(f). Figures 7.27(c) and (d) are matching points on both halves. It is observed that the Nb particles have broken into two halves due to their large particle size. Figures 7.27(e) and (f) are also matching points from both halves, the Nb particle with a smaller size (see arrows), has been pulled out from the matrix which suggests that interfacial debonding has occurred. In addition, the inset image in Figure 7.27(e) also shows the cracking of Nb particles and the interfacial debonding between 6061Al matrix and Nb particles. Hence, it can be said that both reinforcement cracking and interfacial debonding have happened during tensile tests, the initiated cracks followed by the growth and link-up of voids have resulted in the final failure. The failure initiation is closely related to the particle size and shape.

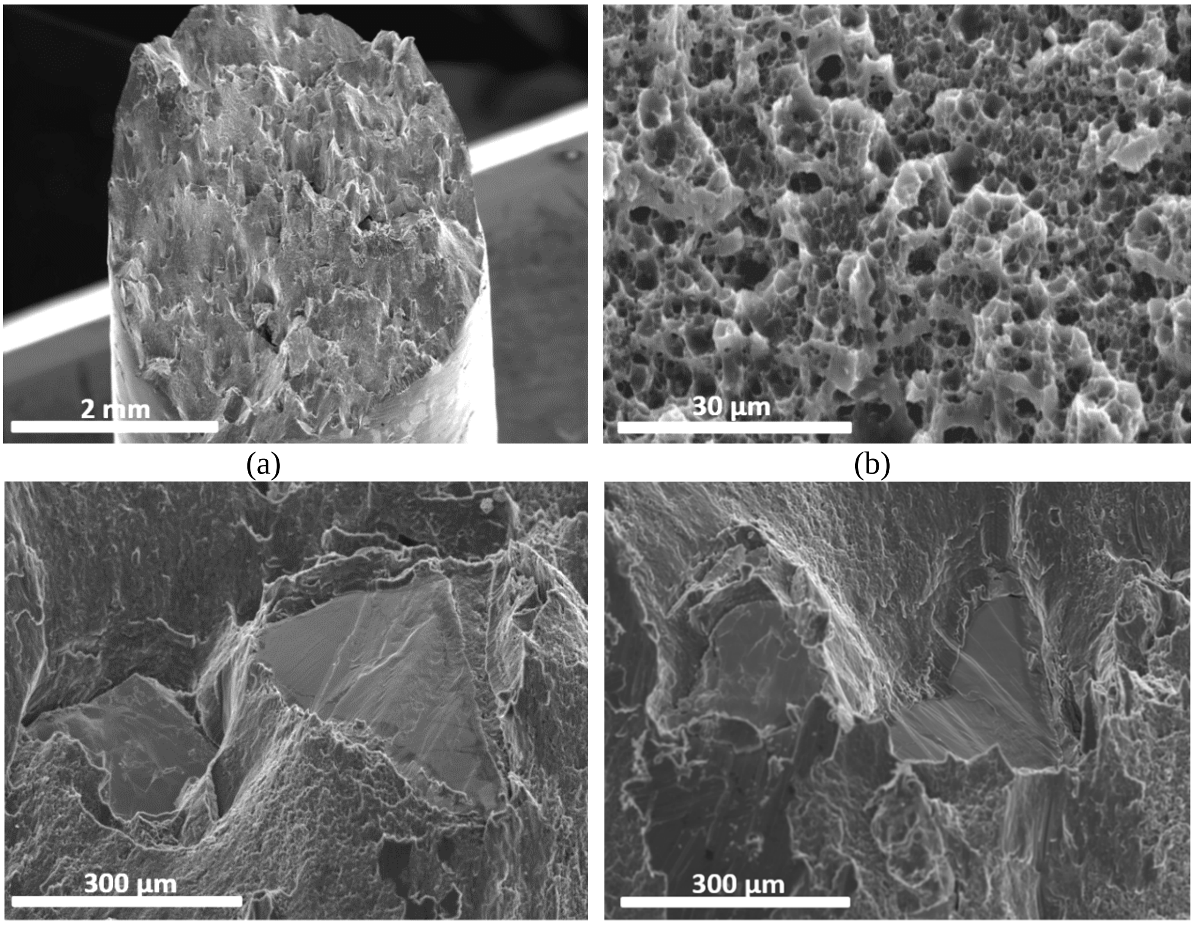

(a) (b)

(c) (d)

Figure 7.27: Fracture surface analysis of as-extruded 6061Al/Nb sample (arrows show matching point from two halves).

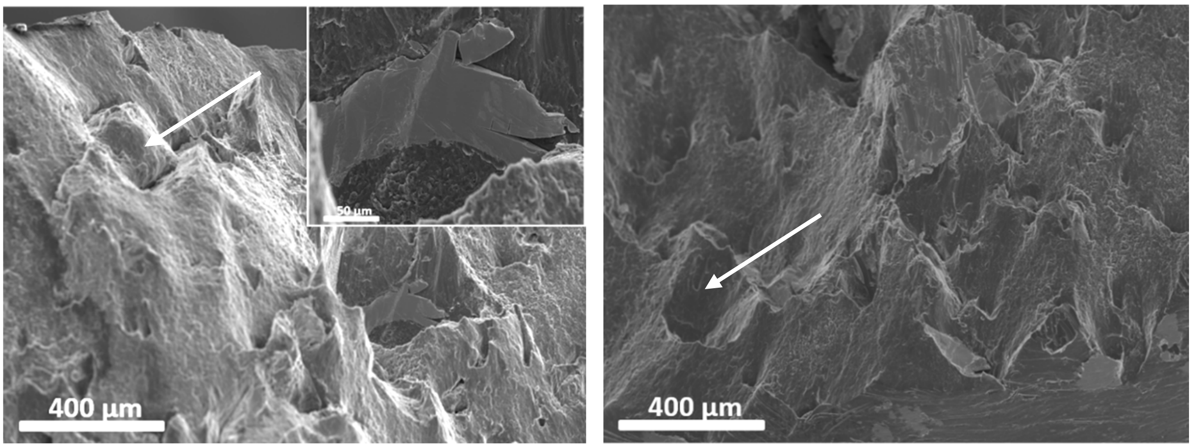

(e) (f)

Figure 7.27: Fracture surface analysis of as-extruded 6061Al/Nb sample (arrows show matching point from two halves).

The fracture surfaces of cold rolled 6061Al/$Nb_{3.6}$ sample are shown in Figure 7.28. Figure 7.28(a) shows that the cold rolled 6061Al/$Nb_{3.6}$ sample has a ~45º fracture surface with no obvious necking. The fracture feature of 6061Al matrix in Figure 7.28(b) shows cleavage-like features with very shallow dimples, indicating less plastic deformation and more brittle failure compared to the as-extruded 6061Al/Nb bar sample. Figures 7.28(c) and (d) are representative figures for two different failure mechanisms of particle cracking and particle pull-out (see arrows). It is observed that cold rolling has led to the transition of ductile to brittle failure of tensile samples since the cold rolling has resulted in an increase in yield stress and caused a lack of plastic deformation, also the long grain boundaries and Nb ribbons can act as suitable sites for crack initiation and interfacial debonding and preferential direction for crack growth. The fracture surfaces of cold rolled Al/$Nb_{3.8}$ and 6061Al/Nb$(SH)_{3.6}$ samples show similar features.

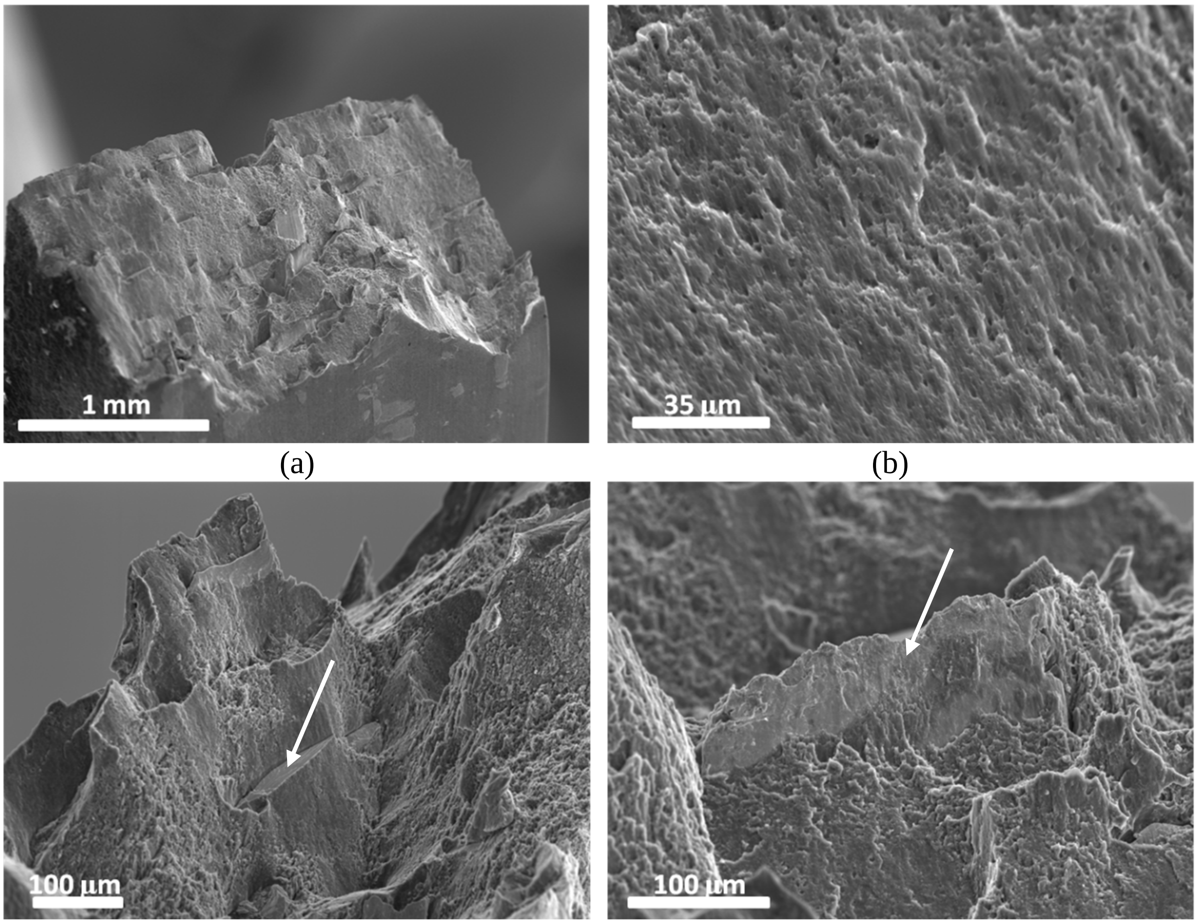

(a) (b)

(c) (d)

Figure 7.28: Fracture surface analysis of cold rolled 6061Al/Nb$_{3.6}$ sample (arrows show particle broken and pull-out).

7.3 Discussion and future work

7.3.1 Effect of rolling strain

Pure Al and 6061Al alloy reinforced with 12.9vol.% Nb particles were produced by extrusion and cold rolling. During cold rolling, Nb particles have gradually developed into flattened ribbons of irregular cross section aligned parallel to the rolling plane. The interparticle spacings and Nb ribbon thickness decrease with increasing rolling strains. The Chevron cracks in the as-extruded condition have bonded after multiple rolling passes indicating that rolling is an effective secondary processing technique to eliminate porosity and other defects from the previous consolidation steps.

The macroscopic texture analysis shows that the extrusion texture can be represented by a near β fibre containing the components of B’-{0 1 1}<10 7 7>, S’-{5 2 10}<7 10 6> and C’-{2 2 5}<5 5 4> for pure Al strip. When it is subjected to cold rolling, B’ component will gradually transform into stable Brass-{1 1 0}<1 1 2> component and more Copper and S components are formed at the expense of Brass. For the composites, the main extrusion texture is either cube component or rotated-cube component with weak α and γ fibres and other random texture. During low reduction cold rolling, α fibre with stronger Goss and Brass components first evolves as well as Copper component, with further rolling strains, Goss component weakens and a stronger β fibre with more intensities near Brass, Copper and S orientations will be developed.

The microscopic texture analysis by EBSD shows similar results that the Al matrix of the composites develops a strong β fibre texture after cold rolling while the Nb particles develop both α and γ fibre textures. EBSD also shows the development of Al subgrains during cold rolling. The elongated Al grains in the as-extruded condition have been subdivided and severely fragmented with rolling strains into substructures with increased fractions of low angle grain boundaries. The similar behaviour of substructure development during extrusion and cold rolling was also observed in Chapters 5 and 6 for 6061Al alloy and 6061Al/NQX composites.

The mechanical properties of the cold rolled composites exhibit significant improvement respect to the as-extruded samples or pure Al sample in both microhardness testing and three-point bending tests, showing effective strengthening from cold working and Nb ribbons. The cold rolled 6061Al/Nb(SH)$_{3.6}$ sample exhibits highest microhardness values and bending strength of all the samples due to the higher strength of the matrix. The tensile tests, however, show an abrupt stress drop in the middle of the tests and limited UTS values, probably due to the interfacial debonding of Al or 6061Al matrix and Nb ribbons resulting in ineffective load transfer and early failure.

7.3.2 Effect of Nb particles

The texture development during extrusion and cold rolling has been investigated in sections 7.1.3 and 7.1.4 by texture XRD and EBSD analysis. The as-extruded pure Al strip has developed a near β fibre texture while the composites have cube or rotated-cube component with weak α and γ fibres and other random texture after extrusion. The maximum texture intensities for the three dominant texture components near Brass (B’), Copper (C’) and S (S’) positions of the as-extruded samples have been plotted in Figure 7.29(a) showing almost randomized texture for the as-extruded composites due to the additions of Nb particles when compared to pure Al strip.

After cold rolling, the main texture stays nearly the same with slightly enhanced intensities (especially near Copper and S components) for pure Al strip. For the composites, increased intensities at B’, C’ and S’ positions have been observed as shown in Figure 7.29(b) indicating the development of β fibre formation with rolling strains. However, similar with SiC and NQX reinforcement studied in Chapters 5 and 6, the additions of Nb particles have led to a significant reduction in the main texture intensities. Similar results were also observed by Chen and Kanetake [37] on cold rolled Al/Nb composites and they suggested that secondary particles, especially large-sized particles, will give rise to heterogeneity of the deformation region and lead to independent deformation and rotations of the grains around the Nb particles, resulting in a weaker deformation texture in the matrix composite than that of pure Al strip.

The EBSD analysis in section 7.1.4 shows consistent texture results with the texture XRD analysis. Figure 7.19(b) shows localized Al grain orientation maps in the vicinity of Nb particles. Equiaxed Al grains around the Nb particles have been observed, indicating that the large Nb particles could produce particle deformation zones and restrict Al grain rotations, discouraging the formation of elongated Al grains in the vicinity of Nb particles and leading to weaker texture components when compared to pure Al strip.

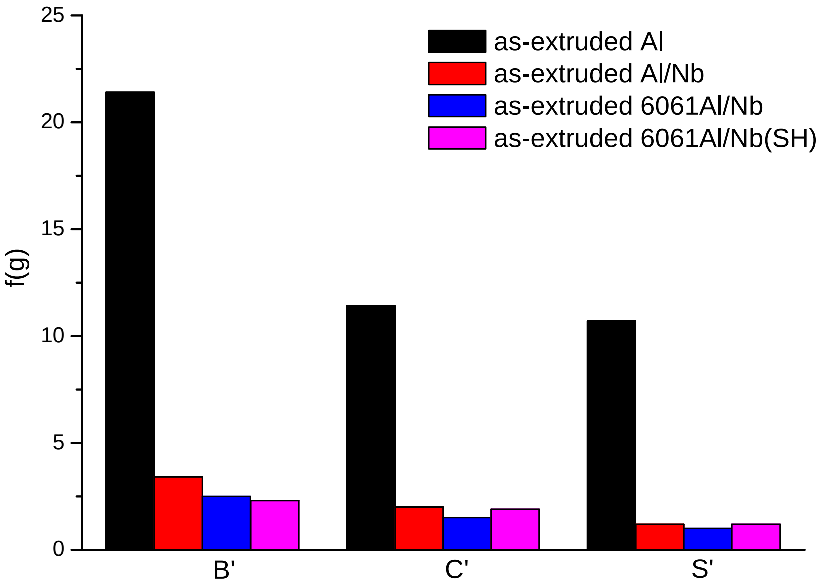

(a)

Figure 7.29: Maximum intensity of main texture components near Brass (B’), Copper (C’) and S (S’) positions in (a) as-extruded and (b) cold rolled pure Al, Al/Nb, 6061Al/Nb and 6061Al/Nb(SH) samples.

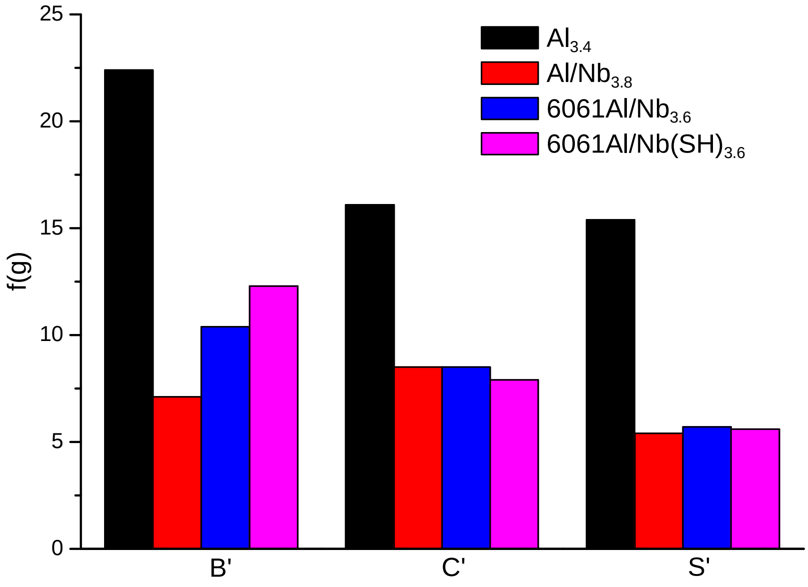

(b)

Figure 7.29: Maximum intensity of main texture components near Brass (B’), Copper (C’) and S (S’) positions in (a) as-extruded and (b) cold rolled pure Al, Al/Nb, 6061Al/Nb and 6061Al/Nb(SH) samples.

7.3.3 Future work

The present work shows the possibility of developing high strength Al alloy/Nb composites by severe deformation. For future work, ways to improve the interfacial bonding strength of Al based matrix and Nb particles need to be found out. In addition, at the current rolling strains, the Nb interparticle spacings are not close enough to act as effective barriers to mobile dislocations, larger deformation to further decrease the Nb interparticle spacings needs to be carried out to study the effect of closely aligned Nb ribbons on the mechanical properties despite the work hardening effect.

7.4 References

[1] H. P. Wahl and G. Wasserma, "Anomalies of properties of thin iron-silver alloy wires," *Zeitschrift Fur Metallkunde,* vol. 61, p. 326, 1970.

[2] G. Wasserma, "Deformation mechanism and properties of 2 phase composite wires," *Zeitschrift Fur Metallkunde,* vol. 64, pp. 844-848, 1973.

[3] J. Bevk, J. P. Harbison, and J. L. Bell, "Anomalous increase in strength of in situ formed Cu-Nb multifilamentary composites," *Journal of Applied Physics,* vol. 49, pp. 6031-6038, 1978.

[4] J. J. Petrovic and A. K. Vasudevan, "Rolling deformation of 2-ductile-phase Ag-Ni alloys," *Materials Science and Engineering,* vol. 34, pp. 39-51, 1978.

[5] W. A. Spitzig, A. R. Pelton, and F. C. Laabs, "Characterization of the strength and microstructure of heavily cold-worked Cu-Nb composites," *Acta Metallurgica,* vol. 35, pp. 2427-2442, 1987.

[6] W. A. Spitzig, C. L. Trybus, and F. C. Laabs, "Structure properties of heavily cold-drawn niobium," *Materials Science and Engineering A,* vol. 145, pp. 179-187, 1991.

[7] P. D. Funkenbusch, T. H. Courtney, and D. G. Kubisch, "Fabricability of an microstructural development in cold-worked metal matrix composites," *Scripta Metallurgica,* vol. 18, pp. 1099-1104, 1984.

[8] S. I. Hong, M. A. Hill, Y. Sakai, J. T. Wood, and J. D. Embury, "On the stability of cold drawn, 2-phase wires," *Acta Metallurgica Et Materialia,* vol. 43, pp. 3313-3323, 1995.

[9] S. I. Hong and M. A. Hill, "Microstructural stability of Cu-Nb microcomposite wires fabricated by the bundling and drawing process," *Materials Science and Engineering A,* vol. 281, pp. 189-197, 2000.

[10] I. S. Ahn, K. C. Jung, S. S. Kim, and Y. Y. Kim, "Mechanical behavior and microstructure of Al-10wt. % Nb alloy fabricated by mechanical alloying," *Metals and Materials-Korea,* vol. 5, pp. 619-624, 1999.

[11] I. S. Ahn, S. S. Kim, M. W. Park, and K. M. Lee, "Phase characteristics of mechanically alloyed Al-10wt.%Nb alloy," *Journal of Materials Science Letters,* vol. 19, pp. 2015-2018, 2000.

[12] B. Avitzur, "Analysis of central bursting defects in extrusion and wire drawing," *Journal of Engineering for Industry-Transactions of the Asme,* vol. 90, pp. 79-90, 1968.

[13] L. Q. Chen and N. Kanetake, "Fabrication and mechanical behavior of powder metallurgy processed in situ Nb/Al sheet metal-metal composites," *Materials Science and Engineering A,* vol. 367, pp. 295-300, 2004.

[14] R. Hielscher and H. Schaeben, "A novel pole figure inversion method: specification of the MTEX algorithm," *Journal of Applied Crystallography,* vol. 41, pp. 1024-1037, 2008.

[15] (08-10-2013). Available: https://code.google.com/p/mtex/

[16] R. K. Ray, J. J. Jonas, and R. E. Hook, "Cold rolling and annealing textures in low carbon and extra low carbon steels," *International Materials Reviews,* vol. 39, pp. 129-172, 1994.

[17] B. Vishwanadh, K. V. Mani Krishna, A. K. Revelly, I. Samjdar, R. Tewari, and G. K. Dey, "Textural and microstructural evolutions during deformation and annealing of Nb-1% Zr-0.1% C (wt%) alloy," *Materials Science and Engineering A,* vol. 585, pp. 343-355, 2013.

[18] D. Raabe and K. Lucke, "Annealing textures of bcc metals," *Scripta Metallurgica Et Materialia,* vol. 27, pp. 1533-1538, 1992.

[19] H. Jiang, T. R. Bieler, C. Compton, and T. L. Grimm, "Cold rolling evolution in high purity niobium using a tapered wedge specimen," *Physica C-Superconductivity and Its Applications,* vol. 441, pp. 118-121, 2006.

[20] D. Raabe and K. Lucke, "Rolling and annealing textures of bcc metals," *Proceedings of the 10th International Conference on Textures of Materials, Pts 1 and 2 - Icotom-10,* vol. 157-, pp. 597-610, 1994.

[21] M. M. Borodkina, G. F. Chusova, Y. A. Gruznov, and L. N. Fedotov, "Texture of niobium bands," *Metal Science and Heat Treatment*, vol. 17, pp. 540-541, 1975.

[22] H. F. G. Abreu, S. S. M. Tavares, S. S. Carvalho, T. H. T. Eduardo, A. D. S. Bruno, and M. H. Prado da Silva, "Texture and microstructure of cold rolled and recrystallized pure niobium," *Thermec 2006, Pts 1-5,* vol. 539-543, pp. 3436-3441, 2007.

[23] (14-05-2014). Available: http://en.wikipedia.org/wiki/Rule_of_mixtures

[24] J. H. Hollomon, "Tensile deformation," *Transactions of the American Institute of Mining and Metallurgical Engineers,* vol. 162, pp. 268-290, 1945.

[25] R. K. Goswami, A. Dhar, A. K. Srivastava, A. K. Gupta, O. P. Grover, and U. C. Jindal, "Effect of deformation and ceramic reinforcement on work hardening behaviour of hot extruded 2124 Al-SiCp metal matrix composites," *Journal of Composite Materials,* vol. 33, pp. 1160-1172, 1999.

[26] O. Ryen, O. Nijs, E. Sjolander, B. Holmedal, H. E. Ekstrom, and E. Nes, "Strengthening mechanisms in solid solution aluminum alloys," *Metallurgical and Materials Transactions a-Physical Metallurgy and Materials Science,* vol. 37A, pp. 1999-2006, 2006.

[27] W. A. Spitzig, J. D. Verhoeven, C. L. Trybus, and L. S. Chumbley, "On the role of interphase barrier and substructural strengthening in deformation processed composite-materials - comment," *Scripta Metallurgica Et Materialia*, vol. 24, pp. 1171-1174, 1990.

[28] W. A. Spitzig, J. D. Verhoeven, C. L. Trybus, and L. S. Chumbley, "On the role of interphase barrier and substructural strengthening in deformation processed composite-materials - reply," *Scripta Metallurgica Et Materialia*, vol. 24, pp. 1181-1182, 1990.

[29] P. D. Funkenbusch and T. H. Courtney, "On the role of interphase barrier and substructural strengthening in deformation processed composite-materials - comment," *Scripta Metallurgica Et Materialia*, vol. 24, pp. 1175-1180, 1990.

[30] P. D. Funkenbusch and T. H. Courtney, "Strengthening in deformation processed composite-materials (DPCM) - comment," *Scripta Metallurgica Et Materialia*, vol. 24, pp. 1183-1184, 1990.

[31] S. Pourrahimi, H. Nayebhashemi, and S. Foner, "Strength and microstructure of powder-metallurgy processed restacked Cu-Nb microcomposites," *Metallurgical Transactions a-Physical Metallurgy and Materials Science*, vol. 23, pp. 573-586, 1992.

[32] C. L. Trybus and W. A. Spitzig, "Characterization of the strength and microstructural evolution of a heavily cold-rolled Cu-20-percent Nb composite," *Acta Metallurgica*, vol. 37, pp. 1971-1981, 1989.

[33] R. T. Begley and J. H. Bechtold, "Effect of alloying on the mechanical properties of niobium," *Journal of the Less-Common Metals*, vol. 3, pp. 1-12, 1961.

[34] S. Nemat-Nasser and W. G. Guo, "Flow stress of commercially pure niobium over a broad range of temperatures and strain rates," *Materials Science and Engineering A*, vol. 284, pp. 202-210, 2000.

[35] W. A. Spitzig and P. D. Krotz, "A comparison of the strength and microstructure of heavily cold-worked Cu-20-percent Nb composites formed by different melting procedures," *Scripta Metallurgica*, vol. 21, pp. 1143-1146, 1987.

[36] M. Zehetbauer and S. V, "Cold work-hardening in stage-IV and stage-V of fcc metals .1. Experiments and interpretation," *Acta Metallurgica Et Materialia*, vol. 41, pp. 577-588, 1993.

[37] L. Chen and N. Kanetake, "Hot-extruded and cold-rolled textures of the matrix aluminum in deformation processed two-phase Nb/Al metal–metal composites," *Textures and Microstructures*, vol. 35, pp. 273-282, 2003.

8. General Discussion

8.1 Summary of the produced composites

In the present work, the fabrication of Al or 6061Al based composites with three types of reinforcements of different size ranges has been carried out. The detailed information of the used reinforcements is summarized in Table 8.1.

Reinforcements	**Size**	**Volume fraction (%)**	**Hardness (Vickers)**
SiC	~500nm	8.5; 12.9	2500 [1]
$Al_{93}Fe_3Cr_2Ti_2$ (NQX)	<25μm	8.5; 12.9	220-240 [2]
Nb	130±57 μm	12.9	120-150 (see Chapter 7)

Table 8.1: Properties of used reinforcements at room temperature.

The compacted composite billets have been extruded into bars, strips and some extruded samples were cold rolled until a final thickness of ~1mm. The representative SEM and OM images (from Chapters 4 to 7) of 6061Al/12.9SiC, 6061Al/12.9NQX and 6061Al/12.9Nb composites after extrusion into bars, strips and final cold rolled samples ($6061Al/12.9SiC(SH)_{3.3}$, $6061Al/12.9NQX_{3.6}$ and $6061Al/12.9Nb_{3.6}$) are listed in Figure 8.1. The micrographs of other produced composites have not been included since composites reinforced with the same reinforcement share the similar trend in microstructural development.

It can be seen from Figure 8.1 that the microstructural development has been largely affected by the additions of different reinforcement type, size, rolling strains and other factors. The microstructural development related to the reinforcement, matrix and interface during extrusion and cold rolling will be discussed in detail in Section 8.2.

Materials	Extrusion into bars	Extrusion into strips	Final cold rolled sample
6061Al/ 12.9SiC	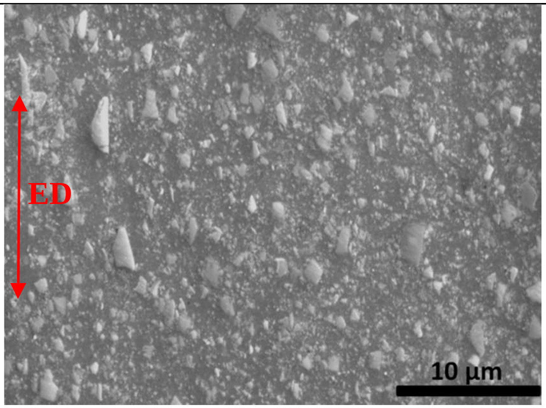 (a)	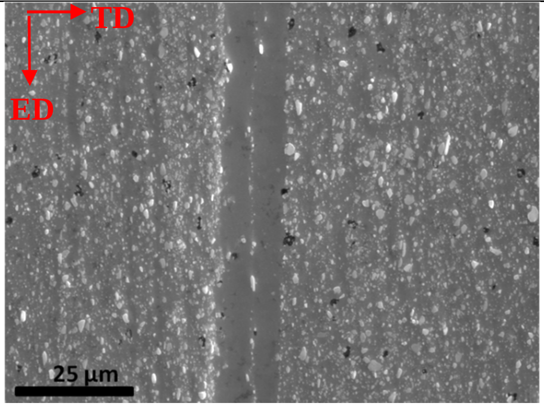 (b)	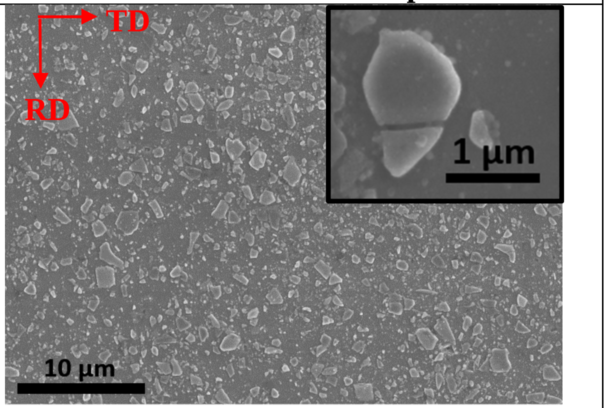 (c) ε=3.3
6061Al/ 12.9NQX	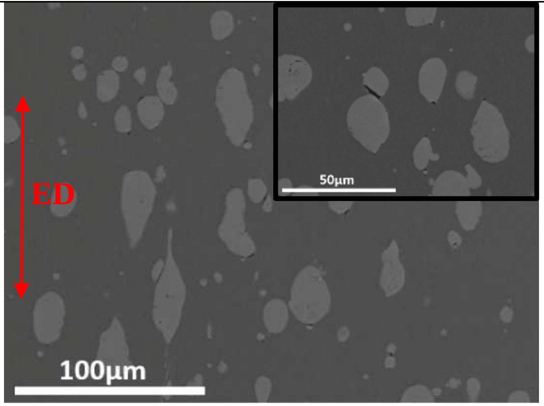 (d)	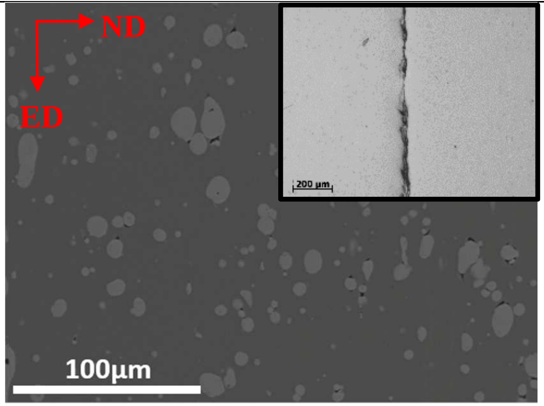 (e)	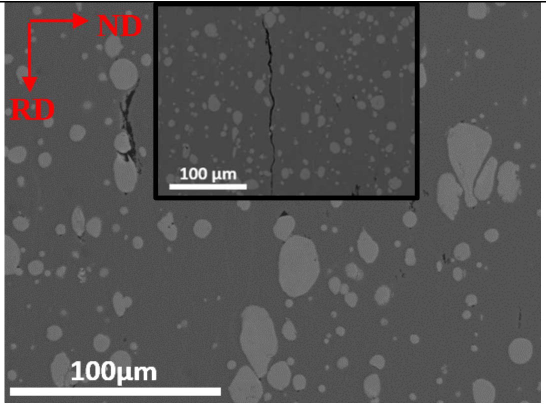 (f) ε=3.6
6061Al/ 12.9Nb	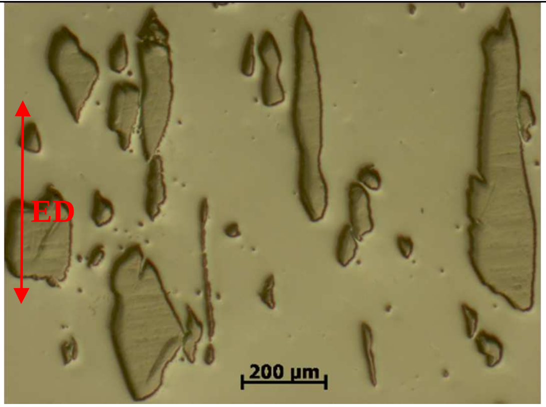 (g)	 (h)	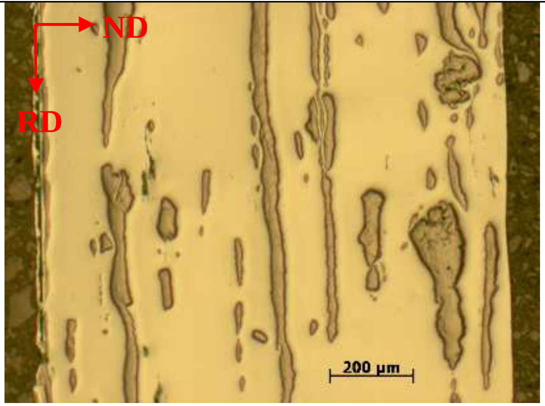 (i) ε=3.6

Figure 8.1: Representative secondary electron images and optical images of 6061Al/12.9SiC, 6061Al/12.9NQX and 6061Al/12.9Nb samples after extrusion into bars, extrusion into strips and final cold rolled samples.

8.2 Microstructural development during extrusion and cold rolling

8.2.1 Microstructural development related to the reinforcement

Extrusion is known to further consolidate the materials and help homogenize the microstructure. It can be seen from Figures 8.1(a), (d) and (g) that after extrusion into bars (ER: 16), all the composite samples have a uniform distribution of reinforcement particles. However, after extrusion into strips (see Figures 8.1(b), (e) and (h)) (ER: 6), a homogeneous microstructure has been observed for micro-sized NQX and Nb reinforced Al composites while particle free bands and particle rich zones have been observed for 6061Al/SiC composites due to the nano-sized SiC particles, the inhomogeneity of the as-received billets (produced by high energy ball milling and HIPing) and the inappropriate extrusion conditions (low extrusion ratio and extrusion temperature). A detailed discussion regarding the extrusion parameters on the microstructure can be found in section 5.3.1. It can be seen that although it is difficult to obtain an even distribution of nano-sized reinforcement due to the large surface-to-volume ratio that produces agglomeration [3], a homogeneous microstructure can still be achieved by extrusion given the right processing conditions.

Extrusion has also generated defects in some of the produced composites. It can be seen from Figures 8.1(e) and (h) that Chevron cracking [4] has occurred for NQX and Nb reinforced Al composites after extrusion into strips possibly due to the initial poor bonded compacted billets and a low extrusion ratio (ER: 6). In addition, particle coexisted voids or cracks have been observed for hard reinforcement particles reinforced composites (SiC and NQX in the present work) after extrusion into bars and strips. In particular, conical voids have been observed at the interfacial areas of the as-extruded 6061Al/NQX samples aligned along the ED directions (located both at front or back sides of the NQX particles). The cavities could be filled by flowing matrix under high processing pressure and temperature [5].

After cold rolling, it can be seen from Figures 8.1(c), (f) and (i) that a homogeneous distribution of the reinforcement particles has been achieved for all composites. Some of the larger SiC particles were broken during the cold rolling, and some cracks have been observed for NQX reinforced Al composites, which could be related to the Chevron cracking in the as-extruded strip samples and/or the cavities at the Al/NQX interface found after extrusion. Whereas, only elongated Nb fibres and not cracks have been observed for Nb reinforced Al composites. It seems that for hard particles with limited plasticity, severe damages can happen during cold rolling. In addition, the amount of damage is directly related to the volume fraction and size of the reinforcement. For a given volume fraction of particles, larger particles generally have greater damages since the nucleation of voids is easier around large particles and the growth rate of the voids is proportional to the particle size [6].

It can be seen from the above discussion that damages can happen during plastic deformation, especially cold working, where the difference of the plasticity between the matrix and the reinforcement is very important. Two main damage modes, including debonding of the matrix-particle interface and particle fracture, can take place mainly depending on the relationship between the particle-matrix interface stiffness and the particle stiffness. Other factors, such as the shape, size and distribution of the reinforcement and local parameters such as localised stress and strain field around the particles and the effect of neighbouring particles, etc. all play a role in the damage nucleation and growth [6]. With appropriate processing conditions, the damages can be minimised, especially during extrusion.

8.2.2 Microstructural development related to the matrix

It is already known that extrusion can influence the crystallographic texture in Al alloys [7]. In section 4.3.1, the as-extruded 6061Al and 6061Al/SiC bar samples have developed a sharp <1 1 1> fibre along the extrusion direction within the matrix. Similar texture analysis has also been performed by calculating the intensity ratios between the (1 1 1) α-Al peak and the (2 0 0), (2 2 0) and (3 1 1) peaks based on the XRD data of cross sectional planes of 6061Al/NQX composites after extrusion into bars with the relative intensity of a standard Al powder sample (see Figure 8.2). The as-extruded 6061Al/Nb sample is not included in the analysis since the (1 1 1) α-Al peak overlaps with (1 1 0) Nb peak. Figure 8.2 shows that the Al phase in the as-extruded 6061Al/NQX bars have the same trend in texture oriented in <1 1 1> but weaker than the as-extruded 6061Al and 6061Al/SiC samples, which could be due to the combined effect of the Al grains in the matrix with the non-deformed Al grains in the NQX particles and the relatively large NQX particle size.

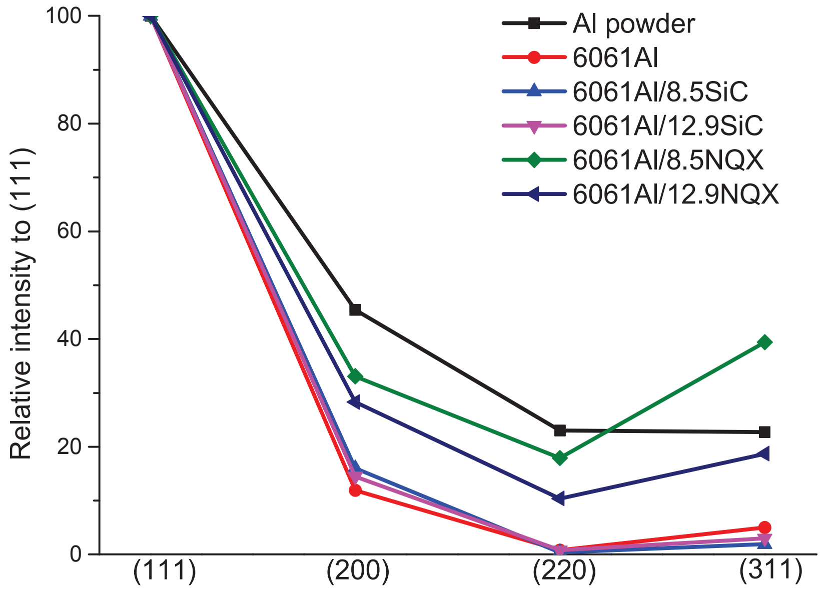

Figure 8.2: Texture analysis of the cross sectional planes of 6061Al, 6061Al/SiC and 6061Al/NQX samples after extrusion into bars as well as the pure Al powder as a reference.

After extrusion into strips, the Al texture has been analysed by texture XRD. There was observed that the Al texture is composed of different texture components with varied intensities (Chapters 5 to 7). The maximum intensities of main texture components near B', C' and S' positions in the as-extruded Al, 6061Al and composite strips are summarized and plotted in Figure 8.3.

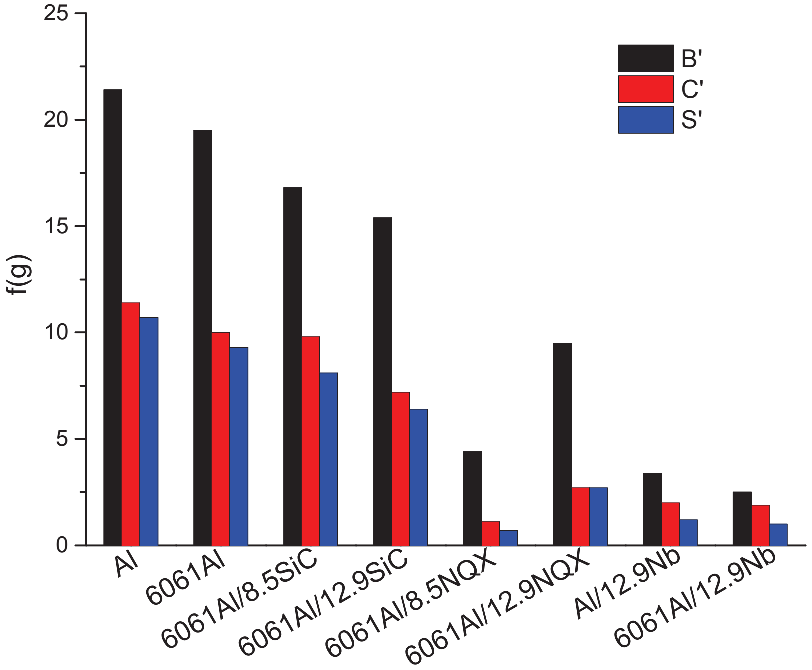

Figure 8.3: Maximum intensities of main texture components near B', C' and S' positions in as-extruded Al, 6061Al, 6061Al/SiC, 6061Al/NQX, Al/Nb and 6061Al/Nb strips.

Figure 8.3 shows that the extrusion of pure Al and 6061Al has led to the formation of sharp β fibre texture with highest intensities near Brass. For the composites, a reduction in the texture intensities has been achieved and the reduction extent seems to increase with increasing reinforcement size and reinforcement volume fractions. These observations are in agreement with the literature [8-11]. It should be noted that the texture behaviour of the as-extruded 6061Al/12.9NQX strip is unusual and the possible explanation has been addressed in section 6.3.2.

The additions of reinforcement mainly have two effects on the matrix texture development during deformation. With the additions of hard reinforcements, the matrix must deform more to accommodate the same macroscopic strain, which would lead to an increase in the matrix texture intensity [8]. On the other hand, particle deformation zones adjacent to the particles are formed, which increase with reinforcement particle size and volume fraction [8-11]. The formation of particle deformation zones can weaken or randomize the texture [12]. In addition, the high deformation zones could lead to a dynamic recrystallization process depending of the local strain grade and the deformation temperature, which will also reduce the matrix texture intensity.

After cold rolling, it can be summarized from Chapters 5 to 7 that the cold rolled Al and 6061Al(SH) strips have developed stronger β fibre texture with rolling strains. For the composites, the NQX and Nb reinforced composites have developed moderate β fibre texture while the cold rolled 6061Al/SiC(SH)$_{3.3}$ samples have randomized texture with reduced intensities. It can be seen that the β fibre texture in Al alloys would normally be enhanced with further cold rolling deformation and similar texture development can be found for MMCs with low volume fraction of reinforcements. However, for high volume fraction of reinforcements [10] or for fine reinforcement where the interparticle spacing is comparable to the particle diameter or to the particle deformation zones around the particles, the texture development is much more complicated, such as the case for the cold rolled 6061Al/SiC(SH)$_{3.3}$ samples.

The microstructure of the as-extruded and cold rolled strips has been further analysed by EBSD techniques. The extrusion of pure Al (Figure 7.17) and 6061Al alloy (Figure 5.8(a)) strips has led to the formation of elongated grains (subgrain aspect ratio: 1.2-1.5) aligned along the extrusion direction. For the as-extruded composite strips, elongated Al matrix grains (subgrain aspect ratio: 1.4-1.6 for NQX and Nb reinforced composites) have been observed in the areas away from reinforcement particles while highly-misoriented equiaxed grains with random texture have been observed in the vicinity of the reinforcement particles.

The formation of particle deformation zones in the as-extruded SiC, NQX and Nb reinforced composite strips has been proven based on Figure 5.15 where the deformation mechanisms at particles in Al as a function of strain and particle diameter has been shown. If high densities of dislocations accumulate at the particles during deformation and provide the driving force for nucleation, dynamic recrystallization by PSN can happen in particle deformation zones [13]. The effect of the particles on the recrystallization behaviour of the surrounding matrix during deformation can be quantitatively studied by the Zener-Hollomon parameter (Z). During hot deformation, thermally activated deformation and restoration processes result in a microstructure evolution dependent on the deformation temperature and strain rate, which are often incorporated in to a single parameter, the Zener-Hollomon parameter (Z) [13]:

$$Z = \dot{\varepsilon} exp(\frac{Q}{RT}) \tag{8.1}$$

where Q is the activation energy for Al self diffusion (142kJ/mol), R is the gas constant (8.31J/K·mol) and T is the deformation temperature (K). For extrusion, the average strain rate ($\dot{\varepsilon}$) is defined as [14]:

$$\dot{\varepsilon} = \frac{6VD_{in}^2 InER}{D_{in}^3 - D_{out}^3} \tag{8.2}$$

where V is the ram velocity, D_{in} is the billet diameter before extrusion, ER is the extrusion ratio and D_{out} is billet diameter after extrusion.

According to Humphreys and Hatherly [13], dynamic recrystallization by PSN can occur for larger particles, lower temperatures and higher strain rates (higher Z) and there is a particle-dependent lower limit to Z below which the nucleation of PSN will not happen. Figure 8.4 shows the critical particle diameters for PSN as a function of Zener-Hollomon parameter (Z) [13]. In the present work, the extrusion of billets (30mm in diameter) into strips (20x6mm, equivalent diameter: 12.4mm) at 375°C gives a strain rate of $3.0s^{-1}$ and a Z value of $8.1x10^{11}s^{-1}$. Based on the calculation and Figure 8.4, it can be said that PSN has happened for NQX and Nb reinforced Al composites during extrusion into strips while no PSN has happened for 6061Al/SiC composites, which is consistent with the experimental observations in Figure 5.9(b). For 6061Al/SiC composites, closely spaced SiC particles pin the grain or subgrain boundaries and recrystallization is therefore impeded.

Figure removed due to copyright reasons

Figure 8.4: The effect of particle diameter on PSN [13].

After cold rolling, the Al matrix grains have been severely fragmented and subdivided into smaller subgrains with lower aspect ratios for Al, 6061Al(SH), NQX and Nb reinforced composites while for cold rolled 6061Al/SiC(SH) samples, fine grains with increased fractions of high angle grain boundaries have been achieved.

The deformation microstructure development of fcc metals at room temperature has been studied extensively [15-17]. During plastic deformation, the initial randomly oriented grains rotate to their preferred orientations, resulting in grain convergence and a reduction of high angle grain boundaries as deformation proceeds [18]. At the same time, the initial grains will be separated into cellular or subgrain structures due to the interconnected dislocation tangles. With increasing deformation strains, the cell dimensions decrease rapidly and cell multiplication (i.e. the creation of new walls) take place up until a steady state has been reached, typically within a subgrain size of 0.2-0.5μm [16, 17]. It is believed that the observed reduced subgrain size in the present work for cold rolled Al, 6061Al(SH), NQX and Nb reinforced composites is the result of the increased dislocation densities induced by cold rolling process forming dislocation walls as subgrain boundaries. Consistent TEM micrograph is also observed in Figure 6.8(e) for cold rolled 6061Al/12.9NQX$_{3.6}$ showing Al subgrain structure (0.2-0.4μm) separated by dislocation walls.

The misorientation distribution plots of as-extruded and cold rolled 6061Al, 6061Al/12.9NQX and Al/12.9Nb samples are summarized in Figure 8.5 further supporting the development of substructure during cold rolling. It can be seen that higher fractions of low angle misorientation boundaries have been observed after cold rolling indicating the development of subgrain structure. Similar results showing the development of subgrains after plastic deformation have also been reported by Panigrahi and Jayaganthan [19] on cryorolled 7075Al alloy.

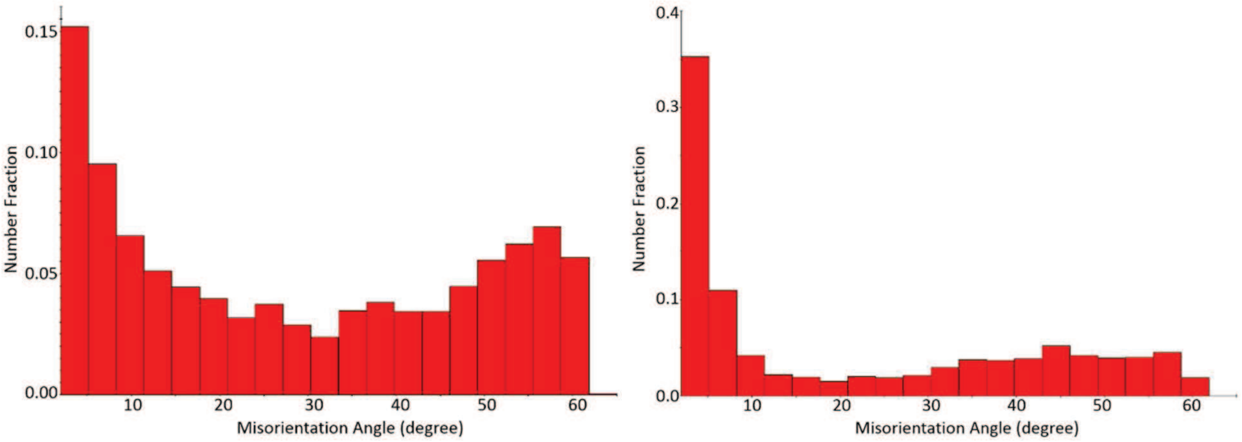

(a) as-extruded 6061Al (b) 6061Al(SH)$_{3.6}$

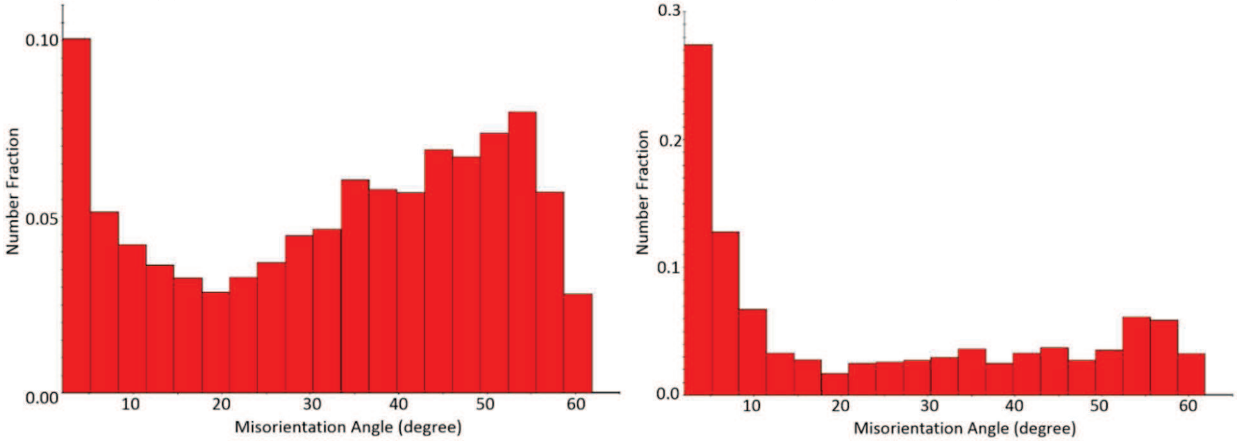

(c) as-extruded 6061Al/12.9NQX (d) 6061Al/12.9NQX$_{3.6}$

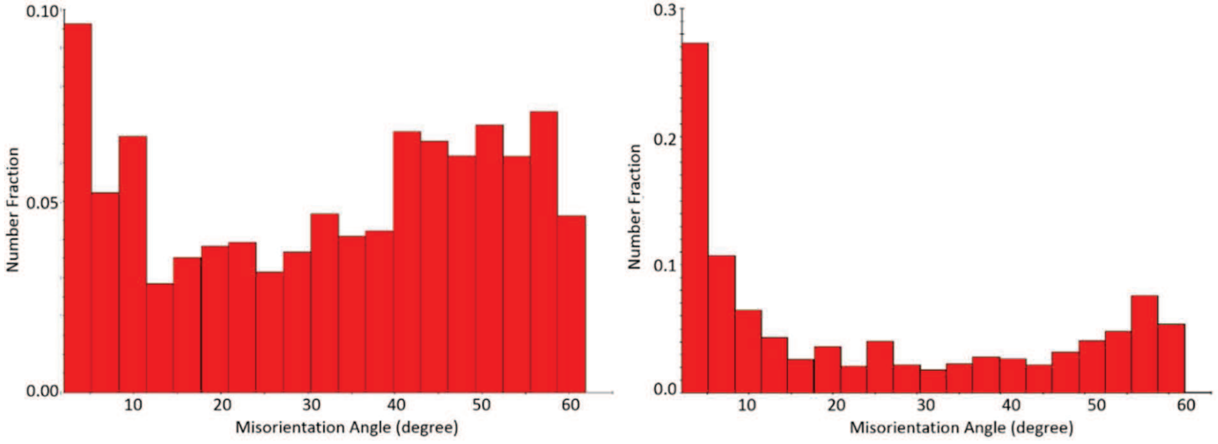

(e) as-extruded Al/Nb (f) Al/Nb$_{3.8}$

Figure 8.5: Misorientation distribution plot of (a) as-extruded 6061Al strip, (b) cold rolled 6061Al(SH)$_{3.6}$, (c) as-extruded 6061Al/12.9NQX strip, (d) cold rolled 6061Al/12.9NQX$_{3.6}$, (e) as-extruded Al/Nb strip and (f) cold rolled Al/Nb$_{3.8}$.

8.2.3 Microstructural development related to interface

Interface plays a very important role in composites. Based on the XRD analysis from Chapters 4 to 7, it can be seen that no interfacial reaction products, such as Al_4C_3, Al_3Nb or $AlNb_2$, have been detected after extrusion and cold rolling, which is one of the advantages of powder metallurgy compared with liquid phase processing techniques that involve high temperatures [20].

For Al-SiC composite systems, as SiC is thermodynamically unstable in Al, the Al_4C_3 phase is normally formed at the interface during the composite fabrication with molten Al in the temperature range from 675°C to 900°C [21-23]. In the present work, the whole process was performed at the solid state which hindered the formation of any carbides or intermetallics at the interface. It has also been found that Mg or other solute atoms in the matrix have a tendency to segregate at the phase boundaries (see Figure 4.10) and possibly forming MgO or $MgAl_2O_4$ at the interface, which can act as diffusion barrier, further restricting reactions between the matrix and reinforcement particles [24].

For 6061Al/NQX composite samples, no interfacial reaction products have been observed by XRD and TEM analysis. In addition, a thin layer of oxides confirmed by EDX has been observed around the NQX particles. The existence of oxide layers can prevent interfacial reactions as discussed above, however, may also degrade the interfacial bonding strength, as implied from the studies of 6061Al/NQX composite samples.

The defects of the interfacial areas during extrusion and cold rolling, such as interfacial debonding and voids formation, have been discussed in section 8.2.1 as well as the effect of particle size, volume fraction and particle type.

8.3 Mechanical properties after extrusion and cold rolling

8.3.1 Mechanical properties after extrusion into bars

The microhardness and tensile properties of as-extruded 6061Al, 6061Al/SiC, 6061Al/NQX and 6061Al/Nb bars have been studied and described in details in Chapters 4 to 7. Table 8.2 summarizes the values obtained for the mechanical properties.

Materials	**Microhardness ($\mu HV_{500/200}$)**	**σ_y (MPa)**	**UTS (MPa)**	**ε_f (%)**
6061Al	57±2	131±5	205±5	19±1
6061Al/8.5SiC	88±2	192±1	287±1	15±1
6061Al/12.9SiC	102±2	229±6	329±2	14±1
6061Al/8.5NQX	61±1	148±1	210±2	18±1
6061Al/12.9NQX	64±2	146±2	212±1	17±1
6061Al/12.9Nb	68±2	141±1	212±1	11±1

Table 8.2: Summary of the microhardness and tensile properties of as-extruded 6061Al, 6061Al/SiC, 6061Al/NQX and 6061Al/Nb composite bars.

A linear behaviour between microhardness and yield stress of the as-extruded samples has been found. A linear fit (see Figure 8.6) gives the relationship to be:

$$\sigma_y = (2.2 \pm 0.1) \times \mu HV_{500/200} \tag{8.3}$$

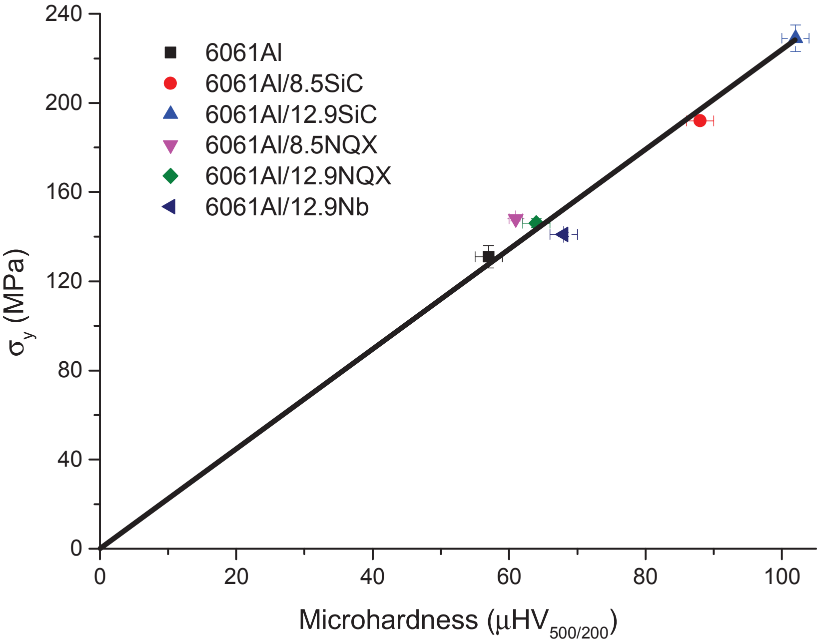

Figure 8.6: Linear relationship between yield strength and microhardness of as-extruded bars.

It can also be seen from Table 8.2 that at a given volume fraction, the SiC particles have a more effective strengthening effect than NQX or Nb particles possibly due to the size effect. It is well accepted that a reduction of particle size from micron to nano-size will lead to a significant improvement of mechanical properties especially due to the effect of Orowan strengthening and thermal mismatch [25]. The increment in yield strength due to Orowan strengthening can be estimated by Ashby-Orowan equation [26-29],

$$\Delta\sigma_{Orowan} = \frac{\alpha MGb}{\pi\lambda}\frac{\ln(\frac{\sqrt{\frac{2}{3}}d}{b})}{\sqrt{1-\upsilon}} \tag{8.4}$$

$$\lambda = \sqrt{\frac{2}{3}}d\left(\sqrt{\frac{\pi}{4V_p}} - 1\right) \tag{8.5}$$

$$G = \frac{E}{2(1+\upsilon)} \tag{8.6}$$

Where $\Delta\sigma_{Orowan}$ is the incremental yield strength due to Orowan strengthening, α is a geometric factor having a magnitude of 0.2-0.4 for fcc metals (assume α is 0.3) [30, 31], M is the mean orientation factor, G is the shear modulus of the matrix, b is the Burgers vector of the matrix, ν is Poisson's ratio, E is Young's modulus of the matrix, λ is the average interparticle spacing and d is the particle diameter. The parameters used for calculation are listed in Table 8.3.

Parameters	**Value**
α [30, 31]	0.3
M [25, 26, 28, 32, 33]	3.06
b (nm) [25, 26, 28, 32, 33]	0.286nm
ν [25, 26, 28, 32, 33]	0.33
E (GPa) (Table 4.7)	69GPa
G (GPa) (Eq. 8.6)	25.9GPa

Table 8.3: Parameters used for calculation.

After applying the above values in Eq. 8.4, the increment in tensile yield strength due to Orowan strengthening for the three types of composites studied can be estimated as a function of the average particle diameter d and the volume fraction of the reinforcement V_p using the following equation,

$$\Delta\sigma_{Orowan} = \frac{3243.65}{0.89{V_p}^{-0.5}-1}\frac{\ln(2.86d)}{d} \tag{8.7}$$

Figure 8.7 presents the effect of average particle diameter and the volume fractions of particles on the incremental yield strength based on Eq. 8.7. It is seen that particle size and volume fractions have a strong influence of the modelled yield strength. The increment in yield strength due to Orowan strengthening increases with increasing volume fractions of particles, while drops rapidly when the particles become larger. An average particle diameter of 500nm gives an incremental yield strength of 23MPa and 32MPa at a reinforcement volume fraction of 8.5% (6061Al/8.5SiC) and 12.9% (6061Al/12.9SiC), respectively. For as-extruded 6061Al/NQX and 6061Al/Nb composites, the Orowan strengthening can be neglected due to the relatively large particle size and interparticle spacing.

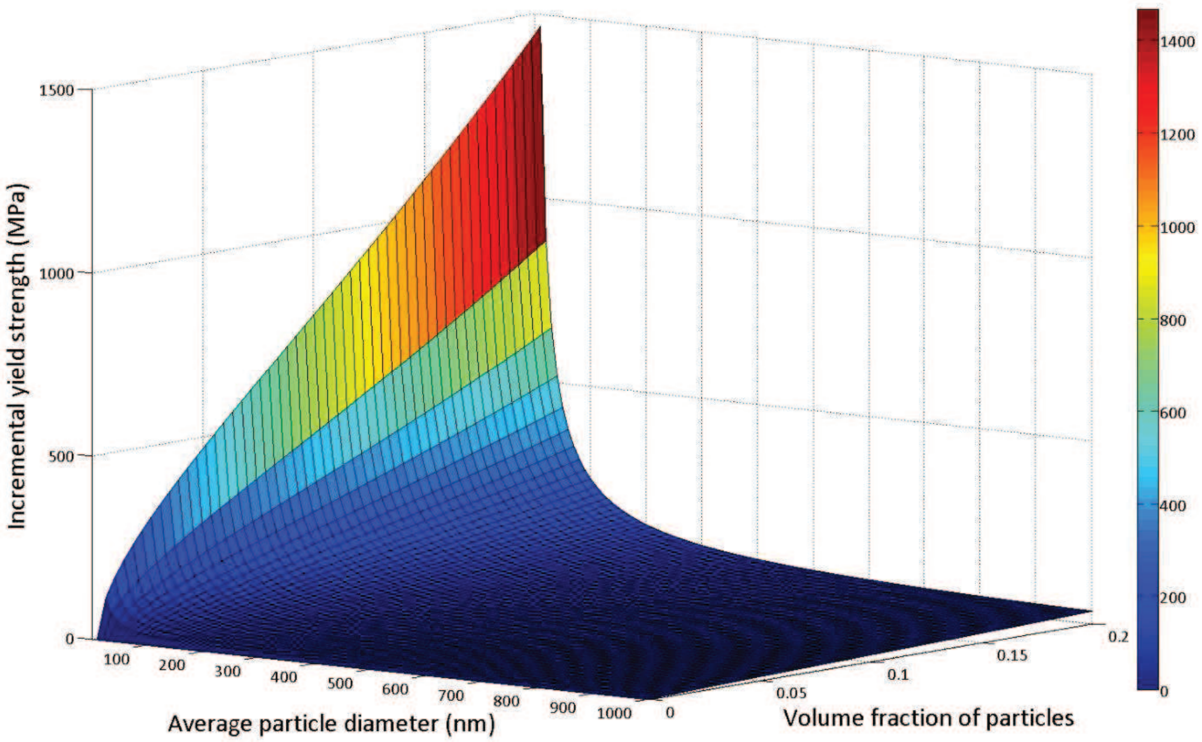

Figure 8.7: Incremental yield strength due to Orowan strengthening as a function of average particle diameter and volume fraction of particles for as-extruded 6061Al alloy based composites according to Eqs. 8.4 to 8.7.

Thermal mismatch, similar to Orowan strengthening, is another indirect strengthening mechanism due to the microstructural changes of the matrix as a result of the additions of the reinforcement [34]. The increment in yield strength due to dislocations generated by thermal mismatch can be calculated by the following equation [26, 27, 32, 35, 36],

$$\Delta\sigma_{CTE} = \alpha \cdot M \cdot G \cdot \rho_{CTE}{}^{1/2} \cdot b \tag{8.8}$$

where ρ is the increased dislocation density due to the residual plastic strain developed due to the difference between the coefficients of thermal expansions of the matrix and reinforcements during post-fabrication cooling [36]. The increased dislocation density can be expressed as [25, 32, 36],

$$\rho_{CTE} = \frac{12 \cdot \Delta\alpha \cdot \Delta T \cdot V_p}{b \cdot t \cdot (1 - V_p)} \tag{8.9}$$

where Δα is the difference in the coefficients of thermal expansion ($\Delta\alpha=\alpha_{Al}-\alpha_{SiC}=24\times10^{-6}\ {}^{o}C^{-1}-4.3\times10^{-6}\ {}^{o}C^{-1}=19.7\times10^{-6}\ {}^{o}C^{-1}$ for 6061Al/SiC composites [26, 32]), ΔT is the difference between the processing and test temperature (ΔT=450ºC-25ºC=425ºC for 6061Al/SiC according to Table 3.2) and t is the particle diameter.

After applying all the parameters, the incremental yield strength due to thermal mismatch is also a function of particle diameter and particle volume fractions. The plotted figure for as-extruded 6061Al/SiC composites is shown in Figure 8.8. It is quite obvious from Figure 8.8 that the gains in yield strength due to thermal mismatch have the similar trend with the gains due to Orowan strengthening that it increases with increasing volume fractions of reinforcement particles while drops drastically when the particle becomes larger. For 6061Al/8.5SiC and 6061Al/12.9SiC composites, the modelled increment in yield strength due to thermal mismatch is 55MPa and 70MPa, respectively. For 6061Al/NQX and 6061Al/Nb composites, the incremental yield strength is almost negligible due to the similar thermal expansion coefficients of the matrix and reinforcement for 6061Al/NQX and relatively large reinforcement size for 6061Al/Nb composites. For example, the modelled increment in yield strength due to thermal mismatch is calculated to be 4MPa for as-extruded 6061Al/12.9Nb sample.

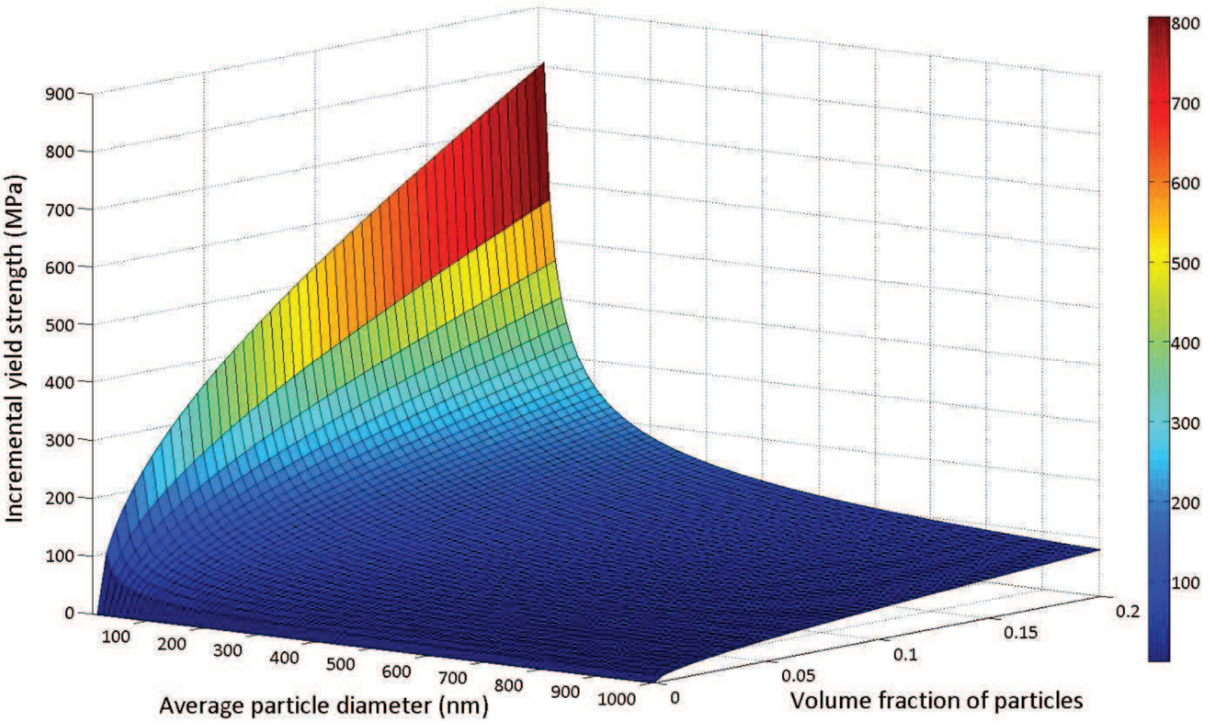

Figure 8.8: Incremental yield strength due to thermal mismatch as a function of average particle diameter and volume fraction of particles for as-extruded 6061Al/SiC composites according to Eqs. 8.8 and 8.9.

The modelled incremental yield strength due to the combined effect of Orowan strengthening and thermal mismatch for as-extruded 6061Al/SiC composite bars has already exceeded the experimental values according to Table 8.2. The above models all assume a fine microstructure with no defects. However, small amount of porosity is present in the as-extruded composites according to the microstructural characterization and from the fracture surface analysis of the as-extruded tensile samples, interfacial debonding also occurs during tensile tests (see Chapter 4). Porosity and interfacial debonding can result in the release of dislocations as well as ineffective load transfer from the matrix to the reinforcement particles, which is probably why the model overestimates the experimental data. In addition to Orowan strengthening and thermal mismatch, other strengthening mechanisms such as grain size refinement, modulus mismatch, are also effective strengthening mechanisms to improve the tensile strength of MMCs. The above calculations are far from comprehensive. They just provide some reference data to the individual strengthening mechanisms and how reinforcement type, shape, volume fraction and average size affect their contributions to the overall tensile strength of the composites. It is clearly observed that a great improvement is obtained when nano-sized particles are used as reinforcement particles.

8.3.2 Mechanical properties after cold rolling

8.3.2.1 Texture strengthening

According to Chapters 5 to 7, during cold rolling, the Al, 6061Al and the composite samples have developed crystallographic textures. The preferred orientations of the matrix grains have led to texture strengthening that is characterized by the Taylor factor, M, which is defined as the ratio between applied stress (σ) and resolved shear stress (τ_c) according to Eq. 8.10;

$$M = \frac{\sigma}{\tau_c} \tag{8.10}$$

M values are different for different orientations of crystals. In general, M varies from 2.3 to 3.674 for fcc [37]. A larger M value means that the grains in this orientation are harder to deform than the grains with a smaller M value. For randomly oriented fcc polycrystals, the value of M averaged over all orientations is 3.06 [37].

The Taylor factors of the Al matrix of the as-extruded strips and cold rolled samples studied in Chapters 5 to 7 are obtained from EBSD analysis by OIM software and the results are shown in Table 8.4. Due to the microstructure heterogeneity in the as-extruded 6061Al/SiC strips as observed in Figure 5.3 and only small areas of EBSD have been conducted, the Taylor factors for these samples are not provided since the obtained values cannot represent the rest of the sample.

Materials	**Taylor Factor (M)**		$\mathbf{M_{cold\ rolled}/M_{as\text{-}extruded}}$
	as-extruded	**cold rolled**	
Al	3.28	3.39	1.034
6061Al	3.21	3.35	1.044
6061Al/8.5SiC(SH)	-	3.03	-
6061Al/12.9SiC(SH)	-	3.10	-
6061Al/8.5NQX	3.15	3.26	1.035
6061Al/12.9NQX	3.14	3.21	1.022
Al/12.9Nb	3.17	3.34	1.054
6061Al/12.9Nb	3.15	3.33	1.057
6061Al/12.9Nb(SH)	3.05	3.30	1.082

Table 8.4: Averaged Taylor factors (M) estimated from OIM for the Al matrix of the as-extruded strip samples and cold rolled Al, 6061Al, 6061Al/SiC(SH), 6061Al/NQX and 6061Al/Nb samples.

It can be seen from Table 8.4 that except 6061Al/SiC(SH) composites, cold rolling has led to an increased Taylor factor while the additions of reinforcement particles have led to a decreased Taylor factor. According to Table 8.4, M values have increased by a factor of 1.022-1.082 when compared to the as-extruded strip samples due to texture strengthening. This strengthening mechanism is not very significant for fcc due to its abundant slip systems. However, for bcc or especially hcp metals, crystallographic texture has a large effect on mechanical properties.

For 6061Al/SiC(SH) composites, the texture and EBSD analysis in sections 5.1.3 to 5.1.5 show randomized texture after cold rolling due to the presence of SiC particles. For randomly oriented fcc metals, the M values should be close to 3.06 [37] which is consistent with the M values obtained from EBSD analysis according to Table 8.4. No texture strengthening has happened for cold rolled 6061Al/SiC(SH) composites.

8.3.2.2 Substructure strengthening

It has been discussed in section 8.2.2 that during cold rolling, the initial Al grains have been subdivided and smaller subgrains with low angles of misorientations separated by dislocation walls have been developed for the cold rolled samples. The appearance of subgrain boundaries due to dislocations has led to additional grain boundary strengthening. A simple Hall-Petch like relationship has been reported to model the yield stress without taking into account if the boundaries are low or high angle grain boundaries [38]:

$$\sigma_y = \sigma_0 + k_1 {D_B}^{-1/2} \tag{8.11}$$

where the boundary resistance is considered to be constant regardless of the boundary character and k_1 is approximately 0.14MPa $m^{1/2}$ for deformed Al [38]. According to the EBSD analysis from Chapters 5 to 7, elongated Al grains or subgrains with an approximately equivalent diameter of ~2μm in the as-extruded strips have subdivided into subgrains of diameter less than 1μm after cold rolling. Assume the cold rolled Al subgrain diameter is 1μm, then the improvement in strength due to substructure strengthening is estimated as ~41MPa according to Eq. 8.11. It should be noted that this is just a rough estimation since k_1 is suggested to vary with deformation degree and change with grain boundary angles [39]. However, the trend is clear that grain subdivision has led to improved strength of cold rolled samples.

8.3.2.3 Work hardening

Despite of texture strengthening and grain refinement, work hardening due to the increased dislocation density and interactions between dislocations is one of the most important strengthening mechanisms during plastic deformation.

According to the microhardness analysis from Chapters 5 to 7, the microhardness of all samples increases with increasing rolling strains with decreased work hardening rate. The reason for decreased work hardening rate is explained in detail in section 5.2.1. The simplest model, known as power law relationship (Eq. 5.1) [30] has been successfully utilised to model the increased microhardness as a function of rolling strains for the cold rolled Al, 6061Al(SH), 6061Al/SiC(SH), 6061Al/NQX and 6061Al/Nb samples in Chapters 5 to 7. The hardening coefficient K and strain hardening exponent n have been obtained from the fitted curves and the results are listed in Table 8.5.

Materials	**K**	**n**
Al	8.6	0.40
6061Al (SH)	64.1	0.10
6061Al/8.5SiC (SH)	42.1	0.15
6061Al/12.9SiC (SH)	37.4	0.15
6061Al/8.5NQX	24.9	0.40
6061Al/12.9NQX	24.6	0.38
Al/12.9Nb	10.8	0.30
6061Al/12.9Nb	24.8	0.32
6061Al/12.9Nb (SH)	40.6	0.16

Table 8.5: Hardening coefficient (K) and hardening exponent (n) values based on Eq. 5.1.

It can be seen from Table 8.5 that pure Al strip has a lowest K value and a highest n value and solutes have greatly increased K and lowered n values for the 6061Al alloy. K represents increment in strength due to work hardening when $\varepsilon=1$. Increased K values indicate that the additions of solutes promote work hardening during cold rolling, which is reported to be due to an increased rate of dislocation multiplication and a reduced rate of dynamic recovery [40]. The effect of reinforcement particles on the work hardening capabilities mainly depend on the nature of the particles. For shearable particles, literature suggests that the overall work hardening capabilities are reduced [30] while for non-shearable particles, very high initial work hardening rates are observed due to the additional dislocation loops stored around the particles [30, 41]. However, reduced K values have been obtained for 6061Al/SiC(SH) samples when compared to 6061Al(SH) possibly due to the increased amount of SiC particle cracking during cold rolling, causing localised strain softening and a decrease in the overall work hardening rates [42].

The strain hardening exponent n is a measurement of the persistence of hardening. With a low n, the work hardening rate is initially high and then decreases rapidly with strain. Generally speaking, high strength materials usually have lower n values than low strength materials [37] and MMCs with a harder matrix usually have lower n values than MMCs with a softer matrix [43], which is mostly the case in the present work. It should be noted from Table 8.5 that the Al or 6061Al based materials have n values from 0.30-0.40 while the solution heat treated materials have n values within the range of 0.10-0.16 despite the additions of different types of reinforcement, indicating that n values are largely controlled by the matrix.

8.4 References

[1] (16-04-2014). Available: http://www.goodfellow.com/E/Silicon-Carbide'.html

[2] N. J. Rounthwaite, "Development of bulk nanoquasicrystalline alloys for high strength elevated temperature applications," Doctor of Philosophy, Department of Materials, University of Oxford, 2012.

[3] Y. Yang, J. Lan, and X. C. Li, "Study on bulk aluminum matrix nano-composite fabricated by ultrasonic dispersion of nano-sized SiC particles in molten aluminum alloy," *Materials Science and Engineering A,* vol. 380, pp. 378-383, 2004.

[4] B. Avitzur, "Analysis of central bursting defects in extrusion and wire drawing," *Journal of Engineering for Industry-Transactions of the Asme,* vol. 90, pp. 79-90, 1968.

[5] G. I. Belchenko and S. I. Gubenko, "Deformation of non-metallic inclusions during steel rolling," *Russian Metallurgy,* pp. 66-69, 1983.

[6] J. H. Schmitt and J. M. Jalinier, "Damage in sheet-metal forming .1. Physical behavior," *Acta Metallurgica,* vol. 30, pp. 1789-1798, 1982.

[7] U. F. Kocks, C. N. Tomé, and H.-R. Wenk, *Texture and anisotropy : preferred orientations in polycrystals and their effect on materials properties*. New York ; Cambridge: Cambridge University Press, 1998.

[8] A. Poudens, B. Bacroix, and T. Bretheau, "Influence of microstructures and particle concentrations on the development of extrusion textures in metal-matrix composites," *Materials Science and Engineering A,* vol. 196, pp. 219-228, 1995.

[9] L. Q. Chen and N. Kanetake, "Finite element polycrystal model simulation of cold rolling textures in deformation processed two-phase Nb/Al metal-metal composites," *Transactions of Nonferrous Metals Society of China,* vol. 15, pp. 64-71, 2005.

[10] F. J. Humphreys, W. S. Miller, and M. R. Djazeb, "Microstructural development during thermomechanical processing of particulate metal-matrix composites," *Materials Science and Technology,* vol. 6, pp. 1157-1166, 1990.

[11] F. J. Humphreys and P. N. Kalu, "The plasticity of particle-containing polycrystals," *Acta Metallurgica Et Materialia,* vol. 38, pp. 917-930, 1990.

[12] L. C. L. Ko, "Particle stimulated nucleation: deformation around particles," PhD, Engineering and Physical Sciences, University of Manchester, 2014.

[13] F. J. Humphreys and M. Hatherly, *Recrystallization and related annealing phenomena*. Oxford: Pergamon, 1995.

[14] A. Kelly, "Processing of bulk hierarchical metal-metal composites," Doctor of Philosophy, University of Oxford, 2011.

[15] B. Bay, N. Hansen, D. A. Hughes, and D. Kuhlmannwilsdorf, "Overview no-96 - Evolution of fcc deformation structures in polyslip," *Acta Metallurgica Et Materialia,* vol. 40, pp. 205-219, 1992.

[16] J. G. Sevillano, P. Vanhoutte, and E. Aernoudt, "Large strain work-hardening and textures," *Progress in Materials Science,* vol. 25, pp. 69-412, 1980.

[17] F. J. Humphreys, P. B. Prangnell, J. R. Bowen, A. Gholinia, and C. Harris, "Developing stable fine-grain microstructures by large strain deformation," *Philosophical Transactions of the Royal Society a-Mathematical Physical and Engineering Sciences,* vol. 357, pp. 1663-1680, 1999.

[18] H. Jazaeri and F. J. Humphreys, "The transition from discontinuous to continuous recrystallization in some aluminium alloys I - the deformed state," *Acta Materialia,* vol. 52, pp. 3239-3250, 2004.

[19] S. K. Panigrahi and R. Jayaganthan, "Development of ultrafine grained high strength age hardenable Al 7075 alloy by cryorolling," *Materials & Design,* vol. 32, pp. 3150-3160, 2011.

[20] A. Mortensen, J. A. Cornie, and M. C. Flemings, "Columnar dendritic solidification in a metal-matrix composite," *Metallurgical Transactions a-Physical Metallurgy and Materials Science,* vol. 19, pp. 709-721, 1988.

[21] O. Beffort, S. Long, C. Cayron, J. Kuebler, and P.-A. Buffat, "Alloying effects on microstructure and mechanical properties of high volume fraction SiC-particle reinforced Al-MMCs made by squeeze casting infiltration," *Composites Science and Technology,* vol. 67, pp. 737-745, 2007.

[22] G. Mahon, J. Howe, and A. Vasudevan, "Microstructural development and the effect of interfacial precipitation on the tensile properties of an aluminum/silicon-carbide composite," *Acta Metallurgica Et Materialia,* vol. 38, pp. 1503-1512, 1990.

[23] B. Xiong, Z. Xu, Q. Yan, B. Lu, and C. Cai, "Effects of SiC volume fraction and aluminum particulate size on interfacial reactions in SiC nanoparticulate reinforced aluminum matrix composites," *Journal of Alloys and Compounds,* vol. 509, pp. 1187-1191, 2011.

[24] R. Mitra, V. S. C. Rao, R. Maiti, and M. Chakraborty, "Stability and response to rolling of the interfaces in cast Al-SiCp and Al-Mg alloy-SiCp composites," *Materials Science and Engineering A,* vol. 379, pp. 391-400, 2004.

[25] D. Poirier, R. A. L. Drew, M. L. Trudeau, and R. Gauvin, "Fabrication and properties of mechanically milled alumina/aluminum nanocomposites," *Materials Science and Engineering A,* vol. 527, pp. 7605-7614, 2010.

[26] M. Wang, D. Chen, Z. Chen, Y. Wu, F. Wang, N. Ma*, et al.*, "Mechanical properties of in-situ TiB_2/A356 composites," *Materials Science and Engineering A,* vol. 590, pp. 246-254, 2014.

[27] A. Sanaty-Zadeh, "Comparison between current models for the strength of particulate-reinforced metal matrix nanocomposites with emphasis on consideration of Hall-Petch effect," *Materials Science and Engineering A,* vol. 531, pp. 112-118, 2012.

[28] J. Ye, B. Q. Han, Z. Lee, B. Ahn, S. R. Nutt, and J. M. Schoenung, "A tri-modal aluminum based composite with super-high strength," *Scripta Materialia,* vol. 53, pp. 481-486, 2005.

[29] A. Kelly and R. Nicholson, *Strengthening methods in crystals*. Amsterdam ; London: Elsevier Pub. Co, 1971.

[30] R. N. Lumley, *Fundamentals of aluminium metallurgy : production, processing and applications*. Cambridge: Woodhead Publishing Ltd, 2011.

[31] X. G. Qiao, N. Gao, and M. J. Starink, "A model of grain refinement and strengthening of Al alloys due to cold severe plastic deformation," *Philosophical Magazine,* vol. 92, pp. 446-470, 2012.

[32] H. Sekine and R. Chen, "A combined microstructure strengthening analysis of SiCp/Al metal-matrix composites," *Composites,* vol. 26, pp. 183-188, 1995.

[33] M. Song, "Modeling the hardness and yield strength evolutions of aluminum alloy with rod/needle-shaped precipitates," *Materials Science and Engineering A,* vol. 443, pp. 172-177, 2007.

[34] Y. Wu and E. J. Lavernia, "Strengthening behavior of particulate reinforced MMCs," *Scripta Metallurgica Et Materialia,* vol. 27, pp. 173-178, 1992.

[35] R. J. Arsenault and N. Shi, "Dislocation generation due to differences between the coefficients of thermal expansion," *Materials Science and Engineering,* vol. 81, pp. 175-187, 1986.

[36] Z. Zhang and D. L. Chen, "Consideration of Orowan strengthening effect in particulate-reinforced metal matrix nanocomposites: A model for predicting their yield strength," *Scripta Materialia,* vol. 54, pp. 1321-1326, 2006.

[37] W. F. Hosford, *Mechanical behavior of materials*, 2nd ed. Cambridge: Cambridge University Press, 2010.

[38] N. Hansen, "Hall-Petch relation and boundary strengthening," *Scripta Materialia,* vol. 51, pp. 801-806, 2004.

[39] D. Abson and J. Jonas, "The Hall–Petch relation and high-temperature subgrains," *Metal Science,* vol. 4, pp. 24-28, 1970.

[40] G. E. Totten and D. S. MacKenzie, *Handbook of aluminum*. New York ; Basel: M. Dekker, 2003.

[41] L. M. Cheng, W. J. Poole, J. D. Embury, and D. J. Lloyd, "The influence of precipitation on the work-hardening behavior of the aluminum alloys AA6111 and AA7030," *Metallurgical and Materials Transactions a-Physical Metallurgy and Materials Science,* vol. 34A, pp. 2473-2481, 2003.

[42] M. T. Kiser, F. W. Zok, and D. S. Wilkinson, "Plastic flow and fracture of a particulate metal matrix composite," *Acta Materialia,* vol. 44, pp. 3465-3476, 1996.

[43] M. Soliman, A. El-Sabbagh, M. Taha, and H. Palkowski, "Hot deformation behavior of 6061 and 7108 Al-SiCp composites," *Journal of Materials Engineering and Performance,* vol. 22, pp. 1331-1340, 2013.

9. Conclusions

This thesis has studied microstructure and mechanical properties of Al or 6061Al alloy reinforced with nano-sized SiC particles (~500nm), micro-sized quasicrystalline alloy particles (<25μm) and micro-sized Nb particles (~130μm) fabricated by powder metallurgy routes followed by secondary processing techniques including extrusion and cold rolling. The main objective is trying to understand the effect of the matrix, reinforcements and the fabrication process on the microstructure and mechanical properties of the composites. The most important results from the experimental work and discussions are summarized as follows:

1. Powder metallurgy routes are effective methods to successfully fabricate Al alloy based composites with a homogeneous distribution of reinforcement particles. Secondary processing techniques including extrusion and cold rolling have been proven to be useful techniques to further consolidate the materials, reduce porosity and homogenize overall microstructure. No interfacial reaction products have been detected for the studied composites after extrusion and cold rolling, which is one of the advantages of powder metallurgy compared with liquid phase processing techniques that involve high temperatures [1]. However, damages, such as interfacial debonding and particle fracture, can happen during plastic deformation, especially cold rolling, mainly due to the different plasticity of the matrix and the reinforcement coupled with other factors. The damages can be minimised given the appropriate processing conditions.

2. Extrusion parameters, such as extrusion temperature and extrusion ratio, have found to largely influence the microstructure of the studied composites. A low extrusion temperature and extrusion ratio lead to a non-sufficient flow of the matrix alloy,

resulting in a non-homogeneous distribution of particles among the matrix alloy generating banded structures.

3. For the studied composites after extrusion into bars, A linear relationship between microhardness and tensile yield strength: $\sigma_y = (2.2 \pm 0.1) \times \mu HV_{500/200}$, has been found. 6061Al/SiC composites exhibit superior mechanical properties than either unreinforced alloys or composites reinforced with micro-sized particles with retained ductility while 6061Al/NQX and 6061Al/Nb composites show limited improvement in tensile strength mainly due to the size effect of the reinforcement and poor interfacial bonding. The particle size can significantly affect Orowan strengthening and thermal mismatch mechanisms, both of which increase with increasing reinforcement volume fractions while drop rapidly with increasing reinforcement diameter. In addition, the application of aging heat treatment results in enhanced mechanical properties due to precipitation hardening.

4. After extrusion into strips, pure Al and 6061Al strips have developed sharp β fibre textures with highest intensities near Brass. The additions of NQX and Nb reinforcement have led to a reduction in the texture intensities and the reduction extent generally increases with increasing reinforcement size and volume fractions due to the formation of particle deformation zones adjacent to the particles. The particle deformation zones have led to dynamic recrystallization due to PSN for NQX and Nb reinforced composites during extrusion while particle pinning and impeded recrystallization have been occurred for 6061Al/SiC composites due to the nano-sized particle.

5. After cold rolling, the weak and mostly random texture in the as-extruded strips has gradually evolved into stable orientations near β fibre with most intensities near Brass or Copper orientations for cold rolled NQX and Nb reinforced composites. The initially elongated Al matrix grains have been severely fragmented and subdivided into smaller subgrains with higher fractions of low angle misorientation boundaries. For SiC reinforced composites, however, the texture intensities have greatly reduced during cold rolling and a randomized texture with small equiaxed grains has achieved.

6. The mechanical properties of cold rolled composite samples exhibit some level of improvement when compared to the as-extruded composites in terms of microhardness, three-point bending tests and tensile tests. The tensile curves of cold rolled 6061Al/NQX, Al/Nb and 6061Al/Nb composites have an abrupt load drop in the middle of the tests and limited UTS values probably due to the microstructure defects formed during cold rolling and interfacial debonding.

7. Texture strengthening, substructure strengthening and work hardening are three main strengthening mechanisms responsible for the improved mechanical properties after cold rolling. Texture strengthening manages to increase the strength of cold rolled materials by a factor of 1.022-1.082 when compared to as-extruded strips (except 6061Al/SiC(SH) samples). Although it is not very effective for deformed fcc metals due to their abundant slip systems, it can be achieved without sacrificing other properties. Substructure strengthening due to the appearance of subgrain boundaries has led to additional grain boundary strengthening which can be expressed by a Hall-Petch like relationship. A rough estimation shows that the improvement in yield strength due to grain or subgrain refinement in the present work is around 40MPa. Work hardening behaviour can be

modelled by a simple power law relationship and it is largely affected by the matrix type, the additions of solutes and reinforcement particles.

8. The fabricated 6061Al/NQX composites in strip shape with an extrusion ratio of ER: 6, are not very successful. Interfacial debonding and Chevron cracking have been observed after extrusion and the cracks further grow into major cracks in sizes of hundreds of microns after cold rolling which seriously deteriorate the mechanical properties. Methods to improve the interfacial bonding and minimise the production defects, such as applying higher temperature and larger pressure during consolidation or high energy ball milling to break up the oxide layers around the particles should be further tested.

9. The fabricated Al/Nb and 6061Al/Nb composites develop into microstructures containing Al matrix and Nb planar fibres aligned parallel to the rolling plane during cold rolling. Limited improvement in mechanical properties of these rolled composites has been found since the Nb interparticle spacings are not close enough to act as effective barriers to mobile dislocations at the current rolling strains. Larger deformation should be carried out to further decrease the Nb interparticle spacing and the effect of closely aligned Nb filaments on the mechanical properties should be studied despite of the work hardening effect.

Based on the present work, several strategies for future development of new Al alloy based composites have been given: For matrix alloy, the use of heat treatable or non-heat treatable Al alloys should mostly depend on the composites' applications. Generally speaking, the heat treatable Al alloys have higher strength due to precipitation hardening. The 6xxx series Al alloys have a very good combination of high strength, formability, corrosion resistance and weldability which result in varieties of applications in different areas [2]. For reinforcements, the mechanical properties of the composites generally increase with increasing reinforcement volume fractions and decreasing reinforcement size. However, careful precautions need to be taken to avoid agglomerations. For composite fabrications, powder metallurgy has many advantages. The atomised raw powders generally have fine microstructure which is beneficial to mechanical properties. High energy ball milling is useful to fabricate nano-sized particulate reinforced MMCs with minimised clustering issues and strong interface bonding. Secondary processing techniques including extrusion and cold rolling are useful techniques to consolidate the materials and homogenize overall microstructure. Appropriate processing conditions, such as an appropriate extrusion ratio and temperature, should be investigated to avoid processing defects. For Al-SiC systems, composites extruded at 450-500°C with an extrusion ratio larger than 10 generally have a homogeneous microstructure with minimised defects. Cold rolling can significantly improve mechanical properties, however, generate damages as well. Methods, such as little rolling reductions per pass or inter-pass annealing, should be carried out to minimise the damages. All the processing steps should be carried out carefully such that no undesirable interfacial reactions can happen. For DPMMCs (e.g. Al-Nb systems), rolling only cannot have enough deformation strains to bring the reinforcement fibres close enough as effective barriers to mobile dislocations, larger deformation modes such as drawing, swaging or accumulative roll-bonding (ARB) are more suitable for producing DPMMCs for high strength purposes.

9.1 References

[1] A. Mortensen, J. A. Cornie, and M. C. Flemings, "Columnar dendritic solidification in a metal-matrix composite," *Metallurgical Transactions a-Physical Metallurgy and Materials Science,* vol. 19, pp. 709-721, 1988.

[2] (27-05-2014). Available: http://aluminium.matter.org.uk/content/html/eng/default.asp?catid=214&pageid=2144417085